## *Probing star formation and radio activity using faint galaxy redshift surveys*

Davies, Gregory Tudor

# Probing Star Formation and Radio Activity using Faint Galaxy Redshift Surveys

by Gregory Tudor Davies

A thesis submitted to the University of Durham
in accordance with the regulations for
admittance to the Degree of Doctor of Philosophy.

Department of Physics
University of Durham
October 2008

**Probing Star Formation and Radio Activity using Faint Galaxy Redshift Surveys**

Gregory Tudor Davies

## Abstract

In this thesis, we study the evolution of radio luminosity functions (RLF) for AGN and star forming galaxies (SFG), the colour-magnitude distributions of radio and X-ray sources at redshift $z \sim 1$, the star formation rate density in dwarf galaxies at $z \sim 1$ and investigate downsizing. In chapter 1 we give the background to our studies. We describe the Big Bang model before going on to examine different types of galaxies and looking at their star formation rates and the variation of their properties with their environments. We summarise the elements of modern astronomy methodology used throughout this thesis in chapter 2. In this chapter we describe the methods of measuring star formation rates, galaxy environments and luminosity functions.

In chapter 3 we match the AEGIS20 radio survey to the DEEP2 optical spectroscopic survey in the extended Groth Strip (EGS) to create a sample of radio-emitting galaxies that we separate into AGN and SFGs. We derive the RLFs of each of these at two redshift intervals and measure their evolution out to $z \sim 1$. We also compare the colour-magnitude distribution of the radio sources to that of the general galaxy population at this redshift and compare these to their local Universe equivalents. We found the evolution of the RLFs to be consistent with pure luminosity evolution with the form $L \propto (1+z)^{\alpha}$ where $\alpha = 1.0 \pm 0.9$ for the AGN and $\alpha = 3.7 \pm 0.3$ for the SFGs. We analyse the variations of these radio sources' properties with their environments in chapter 4. Using the projected $n^{th}$ nearest neighbour method to estimate the density of the environments, we find a strong trend of SFG numbers dropping with density.

The final science chapter is chapter 5 in which we describe the Redshift One LDSS3 Emission-line Survey (ROLES). This survey targets the [OII] emission line in dwarf galaxies with $\log(M_*/M_\odot) \lesssim 9.5$. We convert the [OII] luminosity to a star formation rate (SFR) and then proceed to analyse the mass-dependence of the global star formation rate at redshift $z \sim 1$. We find that SFR turns over with stellar mass at this redshift. By also comparing to similar studies in the local Universe, we investigate the empirical "downsizing" picture of galaxy evolution.

Finally, we present our conclusions and suggestions for future work in chapter 6.

# Contents

# List of Figures

# List of Tables

## Declaration

The work described in this thesis was undertaken between 2005 and 2008 while the author was a research student under the supervision of Professors Richard Bower and Ian Smail in the Department of Physics at the University of Durham. This work has not been submitted for any other degree at the University of Durham or any other University.

The author carried out all the work in this thesis with the exceptions of the parts listed below from chapter 5: George Hau did the target selection and Karl Glazebrook fitted the SEDs to derive the stellar masses. The final versions of the following are those done by David Gilbank, although the author worked on some of the earlier versions: the aperture corrections, the catalogue checks (section 5.2.4.3 and figure 5.6), the derivation of the $P_{OII}$ values (figure 5.7), the external flux calibration check (figure 5.8) the spectroscopic completenesses (section 5.3.2 and figure 5.9).

The majority of the text in section 5.1 is the author's edited version of an initial outline suggested by Karl Glazebrook. The majority of section 5.2 is based upon the author's own original text. However, much of it has been edited by collaborators to improve its flow. Subsections 5.2.4.3, 5.2.5, 5.3.2, the last two paragraphs of subsection 5.2.5.1 and the first paragraph of subsection 5.3.4 relate to work done by collaborators as described above and were predominantly written by them. The remainder of the text in this chapter is the author's own.

The author intends to submit the majority of the work in chapters 3 and 4 in the following paper:

- Davies G. T, Ivison R. J., Bower R. G., Smail I., Willmer C. N. A., Chapman S. C., Nandra K., "The Evolution of Faint Radio Sources in the AEGIS Survey"

and to submit the majority of the work in chapter 5 in the following paper:

- Davies G. T, Gilbank D. G., Glazebrook K., Bower R. G., Baldry I. K., Balogh M. L., Hau G., Li I. H., McCarthy P., Savaglio S., "A spectroscopic measure of the total Star Formation Density at z$\sim$1"

The author was supported through a PPARC/STFC studentship.

## Acknowledgements

Throughout my time in Durham, I have had the pleasure of meeting many people who have helped me no end with every aspect of academic life here. Chief among these is my principal supervisor, Richard Bower. His enthusiasm for all things astronomical is fantastic and I sincerely thank him for all his help over the years. His continued support and patience have been crucial to my PhD. My thanks also to Ian Smail for his support and advice, particularly with the work on the radio paper.

I have been lucky to have shared my two offices with outstanding office mates who have always been willing to help me with anything required and who have kept me entertained throughout. They are Raul Angulo, Phil Bett, Craig Booth, John Helly, Milan Raičević and Mark Swinbank and I thank them all.

I also have a long list of folk from Durham to thank for astronomical discussions and help, helping me to run the Physics Masterclass, being Astro 5-a-side team-mates and sometimes all of the above! They are Carlton Baugh, Rich Bielby, Shaun Cole, Rob Crain, Nigel Dipper, Pete Edwards, Vince Eke, Jim Geach, Jeanette Gladstone, Juan Gonzalez, George Hau, Bret Lehmer, Noam Liebeskind, Ian Manfren, Matt Middleton, Nigel Mitchell, Jim Mullaney, Mark Norris, Alvaro Orsi, Owen Parry, Tim Rawle, Darren Reed, Nick Ross, Allen Shone, John Stott, Dave Wake and Julie Wardlow. Special thanks also go to Lydia Heck and Alan Lotts for keeping the computers going and particularly for their patience with my computers! My thanks go to Glenda, Lynne and Pat for the friendly atmosphere every day in the coffee room.

I have also been most fortunate to meet astronomers from around the world whilst here in Durham. I would like to thank the following for their friendship and support: Garry Angus, Valeria Coenda, Julian Martinez and Chiara Tonini.

I also thank Jean Pope, my A-level Physics teacher who is in no small way responsible for my interest in Physics and my choosing to study it for the best part of the last 12 years.

I owe a huge thank-you to my family. My parents, Barbara and Peter, are chiefly responsible for my scientific proclivities. Without their support in so many ways, this thesis would simply not have been possible. My thanks also to my brother Dan for all his support and positivity that was always great motivation when the going got tough.

Finally, my fiancée Jo has kept me going throughout this time with her love, energy, patience and friendship. Without her in the Universe, it would not matter how many stars were formed!

# Chapter 1 | *Introduction*

During the past approximately ninety years, a wide range of astronomical observations and theoretical models have been made and developed in support of the "Big Bang" (BB) model of the Universe's evolution. According to the BB model, the Universe began at an extremely high temperature and density at a finite time, approximately 13.7 billion years ago. Over the course of its evolution, the Universe's appearance and the forms of its constituent parts have changed several times to form the distribution of galaxies, stars and planets which can be observed today. After approximately 9 billion years, our solar system was formed and astronomers became capable of measuring the Universe and developing and testing theories in respect of it.

Since the majority of modern astronomy (including the present work) is concerned with testing the properties and implications of the BB model, this thesis commences with an overview of the theories behind and the principal pieces of observational evidence in support of the BB model.

## 1.1 The Big Bang Model

Many of the dominant ideas in the BB model can be traced to Albert Einstein's Theory of General Relativity (Einstein, 1916). Einstein's theory described how the curvature of space-time is related to the energy and momentum of whatever matter and radiation are present in the Universe. Einstein used field equations do describe this relationship: the equations contain a cosmological constant $\Lambda$, which Einstein inserted to ensure a stationary Universe according to the prevailing consensus at the time. Thus, Einstein missed the opportunity to predict that the Universe was expanding, which would have been one of his most significant contributions to science. Over the next 19 years, Alexander Friedmann, Georges Lemaître, Howard Percy Robertson and Arthur Geoffrey Walker found an exact solution to Einstein's field equations under the assumptions of a homogeneous and isotropic universe (the Copernican, or Cosmological, principle). This resulted in the $FLRW metric$ which was developed in 1935 to describe the space-time interval between

two events in an expanding or contracting universe. The FLRW metric was first found by Friedmann in 1922 when he used it to deduce what are now known as the Friedmann equations that govern the expansion of space in a homogeneous and isotropic universe. Friedmann's equations are:

$$H^2 \equiv \left(\frac{\dot{a}}{a}\right)^2 = \frac{8\pi G}{3}\rho + \frac{\Lambda}{3} - \frac{kc^2}{a^2} \tag{1.1}$$

$$\frac{\ddot{a}}{a} = -\frac{4\pi G}{3}(\rho + 3p) + \frac{\Lambda}{3} \tag{1.2}$$

where $H$ is the Hubble parameter (whose present epoch value is denoted by Hubble's constant $H_0$) that characterises the expansion rate of the Universe. It is defined in terms of the universal expansion factor $a = a(t)$ which is normalised to unity at the present epoch (see Appendix A for this derivation and a formal definition of $H$). $G$ is Newton's gravitational constant and $c$ is the speed of light. The Universe is described as a fluid with pressure $p$ and density $\rho$. $k$ represents the curvature of the Universe and $\Lambda$ is Einstein's cosmological constant. The Newtonian derivations of these equations are given in Appendix A. Thus these equations predicted that the geometry and fate of the Universe are related to its density - this would have been a completely counter-intuitive notion before the publication of Einstein's work in 1916. Equation 1.1 implies the existence of a critical density $\rho_{crit}$ that yields $k = 0$ for any given expansion rate. To derive $\rho_{crit}$ we substitute $k = 0$ into equation 1.1:

$$\rho_{crit}(t) = \frac{3(H(t)^2 - \Omega_\Lambda H_0^2)}{8\pi G} \tag{1.3}$$

where $\Omega_\Lambda$ is defined by $\Lambda/3{=}\Omega_\Lambda H_0^2$ (see Appendix A). The ratio of the mean density and the critical density determines the geometrical future of the universe. If $< \rho > /\rho_{crit} > 0$, the Universe will eventually stop expanding and close in on itself into a big crunch (i.e. $a$ is bound). If $< \rho > /\rho_{crit} = 1$, then $a$ increases forever but to an asymptotic value. If $< \rho > /\rho_{crit} < 0$ then $a$ is unbounded and can increase forever. Astronomers often use the ratio $\Omega_x$ of the density to the critical for some quantity $X$:

$$\Omega_X = \frac{\rho_X}{\rho_{crit}} \tag{1.4}$$

where $X$ is likely to be baryons ($b$), cold dark matter ($c$), matter ($m = b + c$), radiation ($r$) or dark energy ($\Lambda$). We represent the total density parameter by $\Omega_0$.

Empirical evidence to support the idea of an expanding universe did not come until 1929. To understand it, we must first introduce the concept of redshift $z$. If a light-emitting body is moving away from an observer whilst it emits light, the wavelength of the observed light ($\lambda_{obs}$) will be longer than that as observed by an observer at rest with respect to the emitter ($\lambda_{em}$). Thus the observed light will appear redder or "redshifted". The difference between the two wavelengths is the relative distance travelled between the emitter and observer during the emission of one wavelength. Thus a light source moving away from the Earth will be redshifted by an amount that depends on the recessional velocity $v$. The redshift is defined as:

$$z \equiv \frac{\lambda_{obs} - \lambda_{em}}{\lambda_{em}} = \frac{v}{c} = \frac{1}{a} - 1 \tag{1.5}$$

where the second equation is derived in Appendix A and applies when $v \ll c$. The third equation is also derived in Appendix A. By 1929, after nearly a decade of observations, Edwin Hubble had compiled a list of the distances ($d$) to and recessional velocities ($v$) of 46 "spiral nebulae" (what we now know to be galaxies outside and separate to our own) (Hubble, 1929). He determined the values of $v$ from their redshifts and $d$ from, among other methods, the recent discovery that, for a certain type of variable star called a "Cepheid Variable Star", there was a tight correlation between its period of variability and its luminosity. Hubble found that many of the nebulae were outside the Milky Way and that $v$ was proportional to $d$, a relationship expressed by Hubble's law:

$$v = Hd \tag{1.6}$$

where $H$ is again Hubble's parameter with the present epoch value denoted by Hubble's *constant* $H_0$. From knowing that galaxies that are further away are moving away from us more quickly the logical deduction was that the Universe was expanding. This was the first piece of observational evidence that the Universe is expanding and provided support for Einstein's theory and the usefulness of Friedmann's equations. Further, if the Universe is expanding, it must have been smaller in the past. It was a similarly logical step to realise that it must have started at a finite time in the past in a state of increased density and temperature. This was indeed a controversial idea for many decades with several rival ideas proposed. Chief among these was the "Steady State" universe, as championed by Fred Hoyle and others. However, during the 20th century, more observational evidence gradually emerged to declare the BB model the firm favourite.

In the remainder of this section we briefly describe the main aspects of the BB model and how the theory has been adapted and improved to match the observations. We go through these aspects of the theory in the approximate chronological order in which they were most significant in the evolution of the Universe, starting with inflation theory.

### 1.1.1 Inflation

Despite the early successes of the BB theory, most notably in predicting the expansion of the Universe, there remained serious discrepancies between the theory's predictions and observations. In this section we outline three of these problems that would later be solved by modifying the hot BB model to include a period of universal inflation.

**The Flatness Problem** It has been known for a long time that the parameter $\Omega_0$, introduced in section 1.1, is very close to unity. More specifically, as shown in Appendix A,

$$\Omega_0 \equiv \Omega_M + \Omega_k + \Omega_\Lambda \simeq 1 \tag{1.7}$$

where $\Omega_M$, $\Omega_k$ and $\Omega_\Lambda$ (defined formally in Appendix A) are the contributions to the energy content of the Universe from matter, curvature and dark energy (discussed in section 1.1.5) respectively. This means that the Universe at the present epoch is very flat. However, the BB theory predicts that this is a most unlikely situation as the following analysis shows. From equations 1.1 and 1.3 we have:

$$\Omega_0 - 1 = \frac{kc^2}{\dot{a}^2 - \Omega_\Lambda \dot{a}_0^2} \tag{1.8}$$

Thus if $k = 0$ (i.e. the Universe is flat) then $\Omega_0 = 1$. If this is true at any time, it will remain true as the Universe expands. However, for any deviation of $k$ from 0, $\Omega_0$ will get further and further from unity, its observed value today. We can see this from considering the evolution of $a$ in a radiation dominated universe (as was the case in the fraction of a second after the big bang). In such a universe, $a \propto t^{1/2}$ (see Appendix A) and thus we get:

$$\Omega_0 - 1 \propto t \tag{1.9}$$

Equation 1.9 shows that, in such a non-flat universe, $\Omega_0$ gets further from unity as time progresses and thus that the flat universe is an *unstable* solution of Friedmann's equations. Since $\Omega_0$ is observed today to be $1.0002 \pm 0.020$ (Komatsu et al., 2008), we are again left with a contradiction. This is the flatness problem.

**The Horizon Problem** The Cosmological Principle, stated above, is that the Universe is homogeneous and isotropic. This principle was a fundamental tenet of General Relativity and states that, on the largest scales, it is the same everywhere and appears the same to observers regardless of the direction in which they look. To describe this issue in detail, we introduce the concept of the *observable Universe*. The observable Universe is the part of the Universe that we can actually see and thus its size is the distance that light has travelled during the lifetime of the Universe. Two parts of the Universe that are close enough together that at some time in the Universe's past a photon will have had time to travel from one to the other are said to be in causal contact. The observable Universe is filled with photons that comprise the cosmic microwave background (CMB, see section 1.1.3). These photons are a relic of the big bang itself and have been travelling throughout the Universe uninterrupted since decoupling (when they decoupled from the matter; decoupling is described in section 1.1.3). Importantly, this light is very nearly isotropic, with a spectrum of a black body with a temperature of 2.728K. This means that all these photons came from a region that was in thermal equilibrium and all parts of which were at some time in causal contact. Since opposite points of the sky (which, from the definition of the observable Universe, have never been in causal contact) appear to have been in thermal equilibrium at decoupling, there is a contradiction and this is known as the horizon problem.

**The Magnetic Monopole Problem** The Universe remained dominated by radiation for at least 1000 years. This is puzzling because the energy density of radiation drops off more quickly with the expansion of the Universe than does that of matter ($\rho_{rad} \propto a^{-4}$, $\rho_{dust} \propto a^{-3}$, see Appendix A). Thus, if the Universe started with just a small amount of non-relativistic matter, it would soon dominate the Universe. Most particles in the Early Universe, e.g. leptons and hadrons, interacted with the radiation field and thermalised, thereby slowing down their rise to dominance. However, combining the BB model with particle physics (for example in grand unified theories, GUTs) gives rise to predictions of other, more exotic par-

ticles being created in the Grand Unification Era ($10^{-43}$ to $10^{-36}$ seconds after the Big Bang). These exotic particles may not interact with the radiation field in the same way as baryonic matter and thus should dominate at later times. One example of these particles is the magnetic monopole, a stable heavy ($\sim 10^{16}$ times more massive than a proton) "knot" in the magnetic field. Such a particle has never been observed and this state of affairs has been termed the magnetic monopole problem.

All three of these problems can be solved if the Universe went through a period of exponential increase in size (inflation) between $10^{-36}$ to $10^{-32}$ seconds after the Big Bang, as proposed by Guth (1981). In such a theory, the cosmological constant $\Lambda$ was much greater at this time and caused the Universe to begin expanding rapidly. Below is a simple analysis to show how this solves the flatness problem. As the expansion proceeded, the first and third terms on the right hand side of equation 1.1 became diminished and the cosmological constant came to dominate:

$$\left(\frac{\dot{a}}{a}\right)^2 = \frac{\Lambda}{3} \tag{1.10}$$

Separating the variables in this equation and integrating yields:

$$a = e^{\sqrt{\Lambda/3}t} \tag{1.11}$$

Thus the expansion parameter increased exponentially with time. Differentiating equation 1.11 with respect to time and substituting into equation 1.8 gives:

$$\Omega_0 - 1 \propto e^{-\sqrt{4\Lambda/3}t} \tag{1.12}$$

This means that, during this phase of inflation, $\Omega_0$ was *driven towards* unity. It got so close that even all the subsequent expansion of the Universe between the end of inflation and the present epoch has been unable to move it away again.

Inflation solves the horizon problem by expanding the Universe very rapidly. This means that regions that were in causal contact before inflation can be moved so far apart that they are now further apart than the size of the observable Universe.

The magnetic monopole problem (and that of other exotic relic particles) is solved too. Their number density throughout the Universe is greatly reduced (necessarily more quickly than the cosmological constant) as the Universe expands. Thus we would no longer expect to find such particles (assuming no more of them have been formed since

inflation ended). The solution of this problem does provide one constraint on the theory of inflation: inflation cannot end before the Universe is cool enough to prevent more of these particles forming when it does so.

### 1.1.2 Nucleosynthesis

The production of nuclei heavier than $^1$H in the early Universe (Big Bang nucleosynthesis, BBN) took place in the period between 3 and 20 minutes after the Big Bang. This was the "Goldilocks" period for BBN when the temperature and pressure were not too high and not too low. At $\sim 10^{12}K$, amongst the photons, electron-positron pairs and neutrinos, there was also a smaller number of protons and neutrons. These baryons were constantly transforming into each other by the following reactions:

$$\begin{aligned} n &\rightleftharpoons p^+ + e^- + \bar{\nu}_e \\ n + e^+ &\rightleftharpoons p^+ + \bar{\nu}_e \\ n + \nu_e &\rightleftharpoons p^+ + e^- \end{aligned} \tag{1.13}$$

When the temperature had dropped to $\sim 3 \times 10^9 K$, it was cool enough for some neutrons and protons to combine to form deuterium:

$$n + p^+ \rightleftharpoons D + \gamma \tag{1.14}$$

However, the deuteron is only weakly bound and has a large photo-dissociation area (Boesgaard and Steigman, 1985) and is thus short-lived. It is not until the temperature has dropped below $10^9$K that the deuterium abundance can start to build up and provide the platform for the following nuclear reactions to start forming helium:

$$\begin{aligned} {}^2\mathrm{H} + {}^2\mathrm{H} &\rightleftharpoons {}^3\mathrm{H} + {}^1\mathrm{H} \\ {}^3\mathrm{H} + {}^2\mathrm{H} &\rightleftharpoons {}^4\mathrm{He} + n \\ {}^2\mathrm{H} + {}^2\mathrm{H} &\rightleftharpoons {}^3\mathrm{He} + n \\ {}^3\mathrm{He} + {}^2\mathrm{H} &\rightleftharpoons {}^4\mathrm{He} + {}^1\mathrm{H} \end{aligned} \tag{1.15}$$

The only other stable nuclei made in this primordial mixture were $^6$Li and $^7$Li. Unstable nuclei, including $^3$H, $^7$Be and $^8$Be, were also made but either decayed to or fused to make stable nuclei. No heavier nuclei could be made due to the absence of stable nuclei with 8 nucleons [1].

This theory also predicts the abundances of these nuclei and thus allows another direct test of the BB model. For example, the predicted abundance of He by mass is 22.5-26% depending on the baryon to photon ratio. This is well matched by observations (e.g. WMAP5) providing further strong evidence in support of the BB theory.

### 1.1.3 The Cosmic Microwave Background Radiation

The cosmic microwave background (CMB, first predicted by Alpher et al. (1948) and discovered, by chance, by Penzias and Wilson 1965) has already been mentioned in the discussion of the horizon problem in inflation theory above. In this section we describe briefly how the CMB was formed and observed and how it provides further evidence in support of the BB model.

After the period of nucleosynthesis, the Universe continued to expand and cool. With the density in radiation and relativistic matter declining as $a^{-4}$ and that of non-relativistic matter declining as $a^{-3}$, eventually, at about 60,000 years, the two were equal. At this time, the Universe is still ionised. At 400,000 years ($z \sim 1100$), this begins to change as electrons and protons begin to combine to form neutral hydrogen (the epoch of recombination). Before this epoch the baryonic plasma was locked to the photons by Thomson scattering but shortly after recombination is the period of decoupling when the photons become decoupled from the matter. After this time, the Universe became transparent since the photons could now travel uninterrupted. Since this was occurring throughout the Universe, we can picture a surrounding opaque "surface of last scattering" that hides the Big Bang from us. At this time the photons would have had a black-body spectrum and during the subsequent expansion of the Universe to the present epoch, the wavelength of this spectrum increased as $a(t)$ resulting in the present day CMB with a black-body temperature of $(2.725 \pm 0.0001)$K. The very discovery of this radiation is very strong evidence supporting the Big Bang model: it is only in a very hot, dense initial state that the photons could have been thermalised in a time less than the

[1] This bottleneck would be passed much later in the Universe's history in stellar cores using the triple-$\alpha$ process producing carbon. However it takes 10s of thousands of years to form a significant amount of carbon this way and thus this process negligibly affects the primordial mixture

age of the Universe.

The CMB is actually not *truly* isotropic. Even when the dipole term arising from the solar system's movement through it is removed, there remain fractional RMS anisotropies of the order $10^{-5}$. These are the seeds of structure formation sewn during inflation.

### 1.1.4 Dark Matter and Structure Formation

Zwicky (1933) proposed the existence of a new form of matter that could not be seen but whose presence could be inferred from the way it affected the gravitational field. Zwicky had been unable to account for the motions of galaxies in clusters using only the observable mass. This "dark matter" is today thought to account for $\sim 20.6\%$ of the Universe's energy budget (Komatsu et al., 2008). Although dark matter has never been directly observed, observational evidence for its existence has built up steadily over the past few decades (e.g. flat rotation curves (Ostriker et al., 1974) and gravitational lensing (Walsh et al., 1979) are both phenomena that require more mass than can be observed directly) to the point where very few astronomers doubt its existence. Nevertheless, the nature of dark matter remains somewhat of a mystery.

Potential dark matter constituents fall broadly into two categories: hot and cold (as determined by whether the velocities of the objects/particles at high redshift were relativistic or not). The most familiar hot dark matter candidate is the massive neutrino although this particle is not thought to be massive enough to account for all the missing mass. Additionally, hot dark matter theories have the disadvantage of predicting the inhibition of structure formation on small scales due to free-streaming motion out of the potential wells (described below). For this reason, theories of hot dark matter are favoured less than cold dark matter theories. Cold dark matter candidates could be weakly-interacting massive particles (WIMPS, non-baryonic material) or "MAssive Compact Halo Objects" (MACHOS). Examples of MACHOS would include black holes, neutron stars, brown dwarfs and very faint red dwarf stars. Thus MACHOS have the distinction of being the only dark matter candidates that have actually been observed! Although dark matter hasn't been directly observed and we don't know what it is, we can still know that it plays a crucial role in structure formation, the most widely accepted theory of which we describe next.

During the epoch of inflation, we recall that the Universe was expanding exponentially. As in any de Sitter universes (one in which the cosmological constant dominates), "empty" space was seething with quantum fluctuations: particles were continually pop-

ping in and out of existence. During inflation, these fluctuations were stretched out by inflation. Since this would have happened throughout inflation, the result was irregularities on a variety of scales. Hawking (1982), among others, predicted that the spectrum of these irregularities (or perturbations) would be that of a *nearly scale-invariant Gaussian random field*. A Gaussian random field is defined as one in which each value is drawn independently from a Gaussian probability density function.

The key process at work in forming the galaxies was gravitational instability. Once inflation had left some regions with higher densities (overdense) than the mean (averaged over a large enough volume that it can be considered homogeneous) and some with lower densities than the mean (underdense), gravity ensured that the overdense regions got denser and the underdense ones got less dense. Initially this process only applied to dark matter. This was because, until decoupling, the baryonic matter was tightly coupled to the CMB photons and so could not start to cluster. Thus dark matter had a head start on baryonic matter until $z \sim 1100$ and began to form halos, equilibrium configurations of collapsed dark matter satisfying the virial theorem. For a system of particles satisfying the virial theorem, their potential ($U$) and kinetic ($K$) energies are related by:

$$-2 < K >=< U > \tag{1.16}$$

When the baryonic matter became decoupled from the CMB, it simply started to fall into the dark matter potential wells that already existed. However, the response of the baryonic matter to the gravity-induced collapse was much less straightforward than that of the dark matter. As the hydrogen and helium atoms collided and the gas began to heat up, photons and free electrons were emitted. The gas lost a lot of its energy through this mechanism and thus fell ever deeper into the potential wells. As such the mass density at the centre of the halos soon came to be dominated by baryonic matter even though the halo's mass was dominated by dark matter. As the atoms and ions continued to radiate energy away, they fell ever further into the potential wells and the density continued to increase. Eventually the material became optically thick and the photons were trapped. After this point further collapse just heated the gas and eventually dynamical equilibrium was reached and the first stars formed. Many of these stars were very massive $M_* > 10M_\odot$ and they emitted a lot of UV radiation that may have contributed (along with quasars, discussed in section 1.2.3) to beginning to ionise the surrounding gas. By $z \sim 6$, nearly all the Universe was ionised and this brought to an end the period of *reionisation* and the Universe again became transparent.

Thus, out of the primordial perturbations to the density field grew all the structure we see in the Universe today. Astronomers have observed a rich, complex structure on the largest scales of voids and sheets of matter containing galaxies, clusters of galaxies and superclusters. Galaxies themselves are gravitationally bound, extremely complex structures, each containing up to $10^{12}$ stars. Galaxies are the building blocks of the Universe and come with a bewilderingly wide variety of shapes, sizes, colours and chemical properties. We look at different galaxies in more detail in section 1.2

### 1.1.5 The Cosmological Constant: Dark Energy?

The final protagonist in the BB model of the evolution of the Universe is dark energy. We have already seen that the Universe is expanding but in the late 20th Century the startling discovery was made that this expansion is *accelerating* (not for the first time!). This discovery was made from studies of Type Ia supernovae (SNe Ia, see Knop et al. 2003 and references therein). SNe Ia are usually formed when a white dwarf in a close binary system accretes enough mass from the secondary (red giant) star to initiate a runaway nuclear reaction. SNe Ia are extremely useful tools for astronomers because they are believed to be standard candles. Thus their true distance from Earth can be deduced from their measured fluxes. The above studies measured the fluxes from a sample of these supernovae at high redshift and found them to be fainter than those expected for a matter dominated universe ($\Omega_M$=1), forcing the conclusion that the Universe's expansion had been accelerating between the emission and detection of the photons. This result has since been corroborated by studies of the power spectrum of the CMB, e.g. Spergel et al. (2003).

So, something is causing the expansion of the Universe to accelerate. The nature of this mechanism is almost completely unknown and one of the most active areas of research in modern cosmology. The most popular is "Dark Energy", an undiscovered form of energy with an equation of state similar to:

$$p = w\rho \tag{1.17}$$

where $w$ is negative, causing the expansion to accelerate. Two possible forms of dark energy are a cosmological constant and quintessence. The cosmological constant can be pictured as the "energy of empty space". As the volume of the Universe increases, the energy of the vacuum increases since it is equal to $\rho V$, despite work being done to cause

the expansion. That is why the pressure must be negative. As its name suggests, dark energy in the form of a cosmological constant has the same energy density everywhere. The constant is denoted by $\Lambda$ in the equations above and in Appendix A and is currently the most popular theory for dark energy. When it is combined with the cold dark matter described above, it is known as the $\Lambda\ CDM$ paradigm of the evolution of the Universe. The most recent estimate of the value of $\Omega_\Lambda$ is $0.721 \pm 0.015$ (Komatsu et al., 2008). That means that ~72% of the energy budget for the whole Universe is tied up in dark energy. Quintessence is a form of dark energy that can evolve in both space and time. Quintessence generally predicts a slightly slower rate of expansion than the cosmological constant does. Although there has been no evidence yet found for quintessence, astronomers have not yet ruled it out.

## 1.2 Galaxies: types, properties and their spectra

Having described how we believe the first galaxies formed, we now turn our attention to the details of different types of galaxies. Astronomers have traditionally used a galaxy classification scheme based on the work of Hubble (1926). This system is based on the morphologies of the galaxies and is shown in the the classic "Hubble diagram" (or "tuning fork" diagram), shown in figure 1.1. Hubble separated galaxies into two broad groups. The first of these groups is elliptical galaxies which then has sub-divisions based on apparent eccentricity. The second group is spiral galaxies. This groups has two subgroups (the two "arms" of the Hubble diagram): one for galaxies with a bar at their centre and one for those without. There is a further sub-division based on the number of spiral arms and how tightly they are wound. Hubble coined the terms "early" and "late" to refer to galaxies towards the left and right respectively in the sequence. However, given the obvious temporal connotations of these words, Hubble has often been quoted as implying that galaxies evolved from left to right along this diagram. In fact, he did not mean to imply temporal evolution and merely intended his classification to separate galaxies according to their complexity (Baldry, 2008). We shall see later that it is possible for various events such as mergers to transform galaxies from one morphological class to another, usually moving to the left on the Hubble tuning fork. However, global evolution of galaxies from left to right on the diagram would not be possible. We can make this deduction from the fact that spiral galaxies rotate quite quickly whereas ellipticals do not and we know of no mechanism by which an elliptical could sponta-

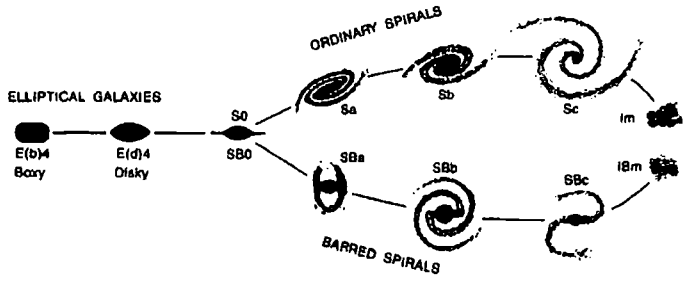


Figure 1.1: The famous Hubble "Tuning Fork Diagram" showing the classification of galaxies. This diagram is from Kormendy and Bender (1996) and shows their recommended amendments to the original idea. These include reclassifying ellipticals so as to be ordered by decreasing "boxiness" or increasing "diskiness", illustrating the two components of S0 galaxies and referring to non-barred spirals as "ordinary" spirals.

neously begin to rotate! In the remainder of this thesis, we shall follow the convention of calling elliptical galaxies early-types and spiral galaxies late-types although we shall bear in mind that the terms relate only to the galaxies' places in Hubble's sequence.[2] The Hubble sequence delineates a somewhat continuous trend of increasing complexity going from left to right. However, based on the galaxies' properties, it is possible to broadly classify them into just the two categories of early and late types. We hope to justify the claim that their properties support such a simple scheme in the following sections where we outline the properties of each type.

### 1.2.1 Early Type Galaxies

**Morphology** Early-type galaxies are typically smooth in optical appearance. They are centrally condensed objects with relatively high surface brightnesses. Early-type galaxies contain little or no disks and, where they do, the disk contributes very little to the total light output. The proportion of the disk, relative to the central bulge, increases as one goes from left to right along the Hubble sequence. The surface density profiles of early-type galaxies are well fit by a Sérsic profile based on the work of Sersic (1968):

[2]There is one further accident of history that complicates matters further: stellar classifications. Hot, relatively short-lived stars of types O and B are termed early types whereas cooler, longer-living stars of types K and M are termed late types. Ironically, the spectra of early-type galaxies are generally dominated by late-type stellar spectra and vice-versa! (Baldry et al., 2004)

$$I_m(R) = I_e \, e^{-b_m[(R/R_e)^{1/m}-1]} \tag{1.18}$$

where $I(R)$ is the surface brightness at radius $R$, $I_e$ is the surface brightness at the effective radius $R_e$ (defined as the radius that encloses half of the bulge's light), $b_m$ is a constant derived from the condition that comprises the definition of $R_e$ and $m$ is the Sérsic index. Many ellipticals are well fitted by $m = 4$ in which case they have a de Vaucouleurs (or $R^{1/4}$) profile (de Vaucouleurs, 1948).

**Gas, Stars and Star Formation Rates** Typically, early-types contain very little or no cool interstellar gas or dust. The stars within them are typically old with ages comparable to that of the Universe. This is due to the absence of gas from which new stars would form, a topic we shall return to throughout this thesis. In the majority of early-type galaxies, they formed their stars a long time ago. There is currently a consensus that the more massive of these galaxies formed their stars first, in the deepest potential wells in the $z >\sim 2$ Universe. Thereafter they switched off their star formation, most likely for a variety of reasons, producing the giant, red ellipticals in the local Universe. The quest to understand the time period of these galaxies' star formation, its dependence on the mass of the galaxy and on its surroundings will be one of the major thrusts of this thesis.

**Colour** Early-type galaxies are typically red in the optical and infrared. This is due primarily to their stellar content. As stated above, their stars tend to be relatively old. From the main-sequence lifetime-mass relationship (more massive stars burn their hydrogen more quickly than low mass stars do) they are therefore relatively low in mass and temperature (typically of spectral type K). Wien's law shows that the wavelength at which a black body's radiation peaks is inversely proportional to its temperature and the relatively cool stars, with effective temperatures of ~5000-7000K, peak around 6000Å. However, galaxies' colours are not simply determined by their stellar temperatures. Two other components that play a major role are metallicity (defined as the mass fraction of elements heavier than helium) and dust. The dependence of colour on metallicity is described by two trends. Firstly, metal rich stars tend to be bigger than metal poor ones and, secondly, stars with lower metallicity have fewer spectral lines in general and particularly at bluer wavelengths. Dust in the interstellar medium can affect a galaxy's colour very significantly. Dust particles whose sizes are similar to the wavelength of visible light

efficiently scatter and absorb ultra-violet (UV) and visible light produced by the stars and re-radiate the energy in the mid- and far-infrared. The efficiency with which this happens is a strong function of wavelength and can be approximated by $\propto \lambda^{-1}$. Thus the dust reddens and dims the light. We describe this reddening in detail in section 2.1.2.

**Spectra** As is commensurate with the description of early-type galaxies' stellar constituents above, their spectra peak in the rest-frame optical (5000Å to 7000Å ) and have a sharp drop-off below $\sim$ 4000Å. This is called the 4000Å break and results from the paucity of young, hot stars. Figure 1.2 shows the composite spectrum of some $\sim$ 2000 early-type spectra. It is dominated by the spectra of stars of spectral type K. Another notable feature is the density of absorption lines. These are caused by metals in the cooler stellar envelopes (usually in the photospheres) that absorb light emitted in the core in very narrow wavelength ranges.

### 1.2.2 Late Type Galaxies

**Morphology** Late-type galaxies contain a disk comprising gas, stars and dust. The appearance of this disk is dominated (at least in the optical and often at other wavelengths) by the spiral arms. These arms are sites of active star formation. Initially these arms were thought to be formed by the differential rotational velocity of the galaxy: stars further from the centre rotated around the centre of mass of the galaxy with a slower angular velocity than those nearer the centre. However, such a system would be short-lived. By the time the innermost stars had completed just two orbits, the arms would become very tightly wound. Since the orbital period of the stars is shorter than the age of the galaxy, this couldn't be the mechanism that produced the spiral arms and this problem became known as the "winding problem". The resolution of this problem is most likely to be similar to that proposed by Lin and Shu (1966) who suggested that spiral structure is caused by stationary density waves in the material in the disk (although we now know that these density waves are not stationary). That is, periodic regions of rarefaction and compression move throughout the disk in a similar way to a water wave propagating over the water's surface. These density waves rotate in such a way that every part rotates with the same angular velocity regardless of where it is in the galaxy. That is, when the galaxy is viewed in a certain non-inertial frame rotating with this angular velocity,

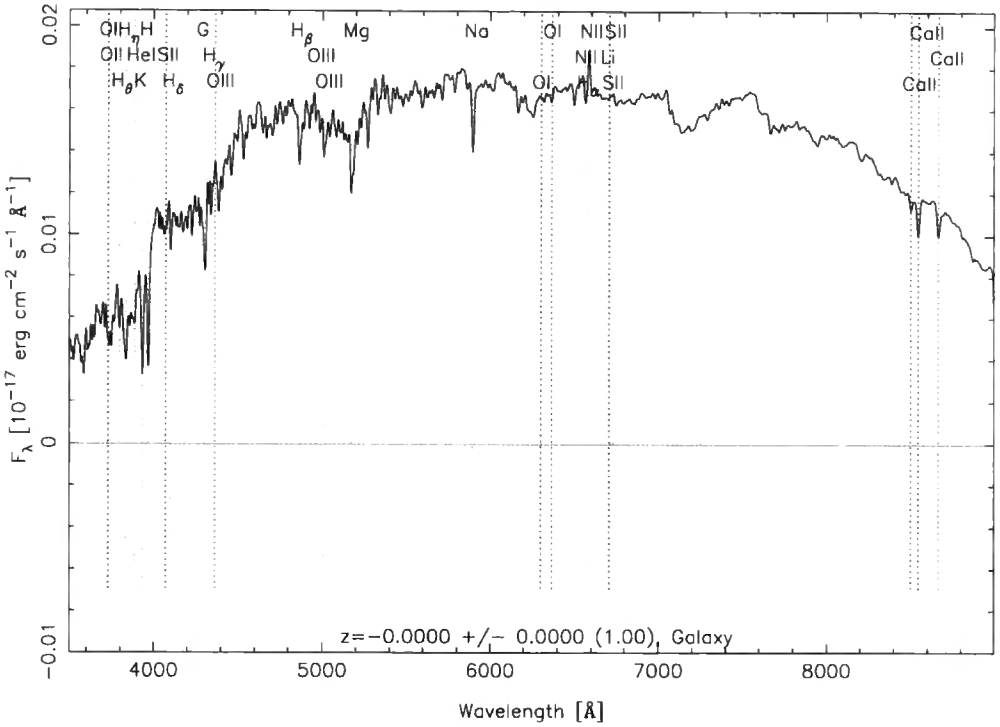


Figure 1.2: SDSS early-type galaxy composite template. This composite spectrum is based on the co-addition of ∼2000 spectra (see text for details). Note the sharp break in the spectrum at ∼ 4000Å and the forest of absorption lines, caused by the absorption of light from hot stellar cores in their cooler atmospheres. Figure from http://www.sdss.org/dr5/algorithms/spectemplates/index.html

the density waves appear stationary. The stars, gas and dust, of course, are not stationary, even in this frame. Stars and gas close to the galaxy's centre will move more quickly than the waves and, when seen in this non-inertial frame, will be seen to pass in and out the density waves. Stars and gas sufficiently far from the galaxy's centre will appear to be moving in the opposite sense to the inner stars when viewed in the non-inertial frame. Stars and gas at a certain distance from the galaxy's centre, the corotation radius, orbit at the same angular velocity as the density wave.

**Gas, Stars and Star Formation Rates.** As dust and gas clouds that are within the corotation radius overtake a density wave and enter a region of increased density, some of them become sufficiently dense to satisfy the Jeans criterion and start to collapse. The Jeans criterion can be expressed as a critical Jeans mass $M_J$ above which a

cloud with a given given temperature $T$ and density $\rho$ (assumed constant here for simplicity) will have so much gravitational potential energy that the thermal energy cannot prevent collapse. To derive $M_J$, we first find the gravitational potential energy $U$ of a spherical cloud of constant density and temperature:

$$U = -\int_0^R \frac{G\frac{4\pi}{3}\rho r^3 4\pi r^2 \rho dr}{r} = -\frac{3}{5}\frac{GM^2}{R} \tag{1.19}$$

where $R$ is the radius of the cloud, $G$ is the universal gravitational constant and $M$ is the mass of the cloud. Now the kinetic energy of the cloud $K$ is given by

$$K = \frac{3}{2}NkT = \frac{3}{2}\frac{M}{\mu m_H}kT \tag{1.20}$$

where $k$ is the Boltzmann constant, $\mu$ is the mean molecular weight and $m_H$ is the mass of the hydrogen atom. For the cloud to collapse, the virial equation (equation 1.16) gives the condition 2K<U. Substituting equations 1.19 and 1.20 into this condition, rearranging and remembering that $M = 4\pi R^3\rho/3$ yields the critical Jeans mass:

$$M_J = \left(\frac{5kT}{G\mu m_H}\right)^{3/2}\left(\frac{3}{4\pi\rho}\right)^{1/2} \tag{1.21}$$

Clouds with masses greater than the Jeans mass will then begin to collapse and form stars. When stars of spectral type O and B form, they will burn brightly and ionise the gas around them. They will often burn so brightly that they will not live long enough to fully overtake the region of overdensity. Thus this region (the spiral arm) will contain the vast majority of the galaxy's young stars and H II regions (regions of ionised hydrogen with the ionising radiation coming from the hot stars). H II regions and young stars will typically be distributed throughout the arms. On the other hand, smaller, redder stars can live much longer than one orbital period and will thus be dispersed evenly throughout the disk, even though they are most likely to be born in the arms. The density wave theory gives a similar explanation for the distribution of H I regions (neutral hydrogen) and dust. In regions of the galaxy inside the corotation radius, we have seen that the orbiting baryonic matter will approach the density wave from the inside (assuming the galaxy has *trailing* spiral arms). There will be a time lag of a few Myr between the clouds beginning to collapse and the young stars beginning to shine. Thus the

stars will be slightly displaced (a few hundred pc for a typical relative velocity between the gas and density wave of $\sim$ 100kms$^{-1}$) from the dust and H I. This is the theory's explanation for the observations of dust lanes on the insides of the spiral arms.

**Colour** Late-type galaxies are typically bluer than early-types. Although their mass is dominated by stars of spectral types F and G (which are themselves hotter and therefore bluer than most stars in early-type galaxies), late-type galaxies' light can be dominated by the O and B type stars. For resolved late-type galaxies, their colours are bluer towards their outer regions and in the spiral arms where the hottest stars reside.

**Spectra** Late-type galaxies typically have a continuum whose intensity increases almost monotonically with decreasing wavelength. This is a manifestation of their young, hot stars. As shown by the example in figure 1.3, their spectra are often dominated by emission lines from the H II regions (but including lines from helium and heavier elements) in the star-forming regions in the spiral arms. The dominant emission lines are those from the hydrogen Balmer series, and those from heavier elements such as oxygen and nitrogen. The hydrogen Balmer lines are denoted by $H_\alpha$ , $H_\beta$ and so on corresponding to lines due to photons from electron transitions from ever higher energy shells down to the $n$=2 level. The strength of a line may be parameterised by its equivalent width $EW$. In a plot of flux versus wavelength, $EW$ is defined as the width of a rectangular box in flux-wavelength space reaching up to the continuum (at the wavelength of the line) that has the same area as the spectral line. This is shown by equation 1.22:

$$EW = \int \frac{F_c - F_\lambda}{F_c} d\lambda \tag{1.22}$$

where $F_c$ is the flux of the continuum (usually assumed constant across the wavelength of the line), $F_\lambda$ is the total flux as a function of wavelength and the integral is done over the wavelength range of the line. The $H_\alpha$ line is a very important emission line in such galaxies since its strength is directly correlated with the intensity of the ionising flux from the hot stars. Thus the strength of the $H_\alpha$ line is an excellent tracer of star formation. The [OII] line is also used as a tracer of star formation although its strength is not directly linked to the ionising flux. The line

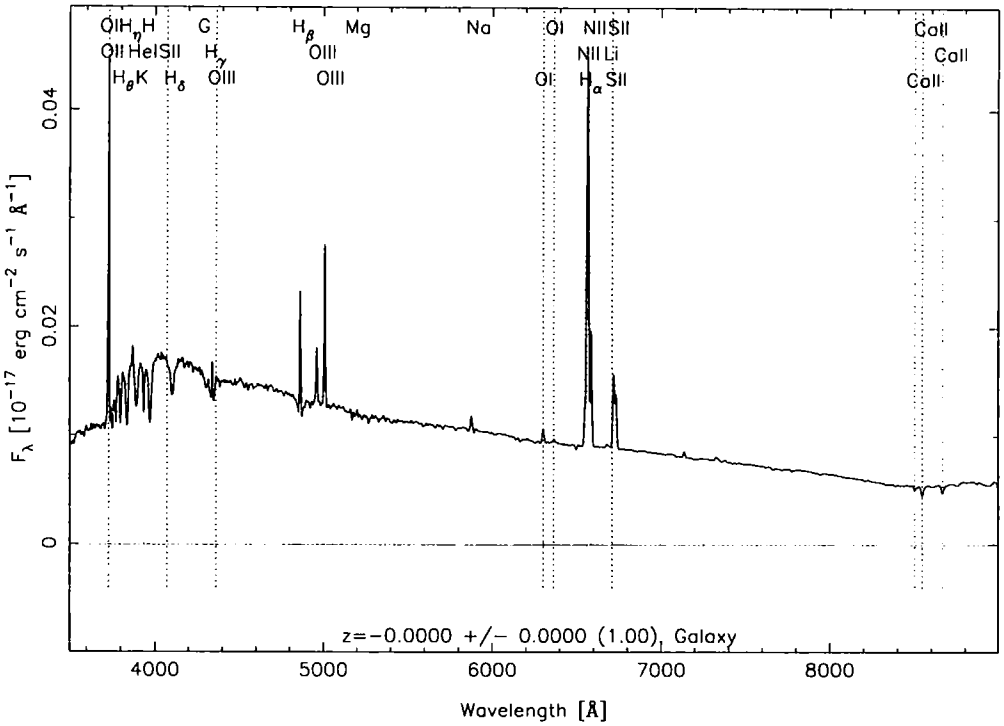


Figure 1.3: As figure 1.2 but for a late-type galaxy composite spectrum. Note the stellar continuum increasing with decreasing wavelength and the prominence of the hydrogen emission lines.

is forbidden in the sense that it cannot be produced in the laboratory on Earth. This is because even the hardest laboratory vacuums are so dense that the metastable excited states [3] would be collisionally de-excited. The detection of [OII] from H II regions therefore shows that, at least in parts, the gas must be very diffuse. The strength of the [OII] line has a complex dependency on the metallicity of the gas and this complicates its use a tracer of star formation. The measurement of star formation rates is discussed in greater detail in section 2.1. However, as we may infer from figure 1.3, heavy elements such as oxygen act as a major nebular coolant (Kewley et al., 2004) and thus the metallicity of the H II regions is critical to the energy balance of the gas.

[3] the [OII] line is actually a doublet, usually given the nominal wavelength of 3727Å. The two lines are formed by the transitions $_2D^{3/2} \rightarrow_4 S^{3/2}$ and $_2D^{5/2} \rightarrow_4 S^{3/2}$ that produce emission at 3726.1Å and 3728.8Å respectively

### 1.2.3 AGN

It is now thought that nearly every galaxy has a black hole at its core. Evidence for this is principally from the measured dynamics of stars orbiting the centre of a given galaxy. There is no known astrophysical system other than a black hole that is so small yet massive enough to provide the potential well for such orbits. Further, many galaxies have strong, non-stellar radiation (i.e. radiation other than that discussed above) from their centres. The centres of such galaxies are called active galactic nuclei (AGN) and the most plausible power source for them is accretion onto a massive black hole. AGN are characterised by a bright central nucleus, a wide continuum (wide in that it can cover 10 orders of magnitude in frequency) and temporal variability of the emission at different wavelengths. AGN can be characterised by the width of their emission lines, their radio emission and their X-ray emission. Observations of AGN vary a great deal resulting in many classifications:

**Seyfert 1** These are AGN with a very small nuclear region. Their spectra contain very broad emission lines including both allowed (from H I, He I and He II regions) and forbidden lines such as [OIII] . The broad widths are consistent with Doppler broadening that indicates the regions producing the lines are moving at speeds of $\sim 1000 - 5000\text{kms}^{-1}$ in the case of the allowed lines and $\sim 500\text{kms}^{-1}$ in the case of the forbidden lines. Seyfert 1s also emit highly variable X-ray radiation and can emit a small amount of radio radiation from the core.

**Seyfert 2** Seyfert 2 galaxies have the same narrow lines as Seyfert 1s but don't have the broad lines or the X-rays. They also have a continuum devoid of any emission lines, as Seyfert 1s do. However, the continuum is significantly less luminous in a Seyfert 2. Seyfert galaxies of both types are nearly always spirals.

**Radio Galaxies** Some AGN are found to be very bright in radio emission. They can be divided into broad- and narrow-line radio galaxies (BLRGs and NLRGs). These are analogous to Seyfert 1s and Seyfert 2s respectively and share with them a power-law continuum although not at UV and visible frequencies. However, morphologically, radio galaxies are different to Seyferts. BLRGs have a bright, starlike nucleus surrounded by a faint envelope of gas and are termed *N galaxies*. NLRGs are usually giant ellipticals. Radio galaxies often produce huge radio lobes, often several times the size of the galaxy itself, which are sometimes connected to the galaxy

by a collimated jet. They are also often bright in X-rays with the emission coming from both the galaxy and the jet. Radio galaxies are thought to be ~100 times less abundant than Seyfert galaxies.

**QSO / Quasar** Quasi-stellar objects (QSOs) are very luminous AGN, usually at very high redshift, that have a small, stellar-like nucleus and very high bolometric luminosity (up to $10^{48}$ erg $s^{-1}$). Most (indeed most AGN) are radio quiet and the term quasar is usually reserved for the few that are radio loud. QSOs are often bright in X-rays and UV. A measured excess in UV, giving rise to the *blue bump* is seen in most, but not all, QSO spectra. For this reason, they are also typically very blue objects. Their spectra are similar to those of Seyfert 1s: bright power-law continua and broad (both allowed and forbidden) emission lines. There may also be absorption lines, both from the QSO itself and from matter along the line-of-sight to the observer, most of them due to the hydrogen Lyman series and metals such as C IV and Mg II.

**Blazar** This final AGN classification is characterised by a high degree of linear polarisation at visible wavelengths and rapidly varying bolometric luminosity. A subdivision of these objects is the **BL Lacs**, named after the blazar BL Lacertae, found in the constellation of Lacerta (the Lizard). Their luminosity can change by a factor of 100 and by 30% in just 24 hours! In addition, their continua may be 30 – 40% linearly polarised. These continua, again like those of Seyfert 1s, are typically a power-law. They are almost devoid of emission lines although the few that are found usually place BL lacs at high redshift. Most BL Lacs ($\sim$ 90%) appear to reside in elliptical galaxies. A second sub division of blazars are optically violently varying quasars (**OVVs**). They are similar to BL Lacs although typically much more luminous and sometimes with broad emission lines.

#### 1.2.3.1 The Unified Model

As mentioned above, there is only one known astrophysical system that could act as the energy source of an AGN: accretion onto a black hole. Therefore, AGN are usually modelled as having fundamentally the same morphology. However, these AGN are highly anisotropic and can therefore appear very differently, in terms of the intensity of the flux at different wavelengths; it is the orientation of the AGN with respect to the line-of-sight to the observer that determines the classification of the AGN. Figure 1.4

shows schematically the structure of an AGN and how different sight-lines would give the different classifications described above. The basic picture is of a black hole (BH) at the centre surrounded by an accretion disk. The disk comprises matter that is orbiting the black hole but which, due to instabilities in the disk (these can be due to turbulence, viscosity or both), spirals in towards the BH, releasing gravitational energy as it does so. Beyond the disk there is a dusty torus that is opaque to visible, UV and possibly soft X-ray photons. Clouds of gas surround the black hole, both inside and outside of the torus. Those closer to the black hole move in a potential well with an enhanced gradient and move at the high speeds described above. Emission lines from these regions will be broad and the origin of the broadening is Doppler. Other clouds further from the centre of this system will not move so quickly and will thus only produce narrow lines.

#### 1.2.3.2 Radio Emission from AGN

Radio emission from an AGN is probably produced by synchrotron radiation. This inference is drawn from the power-law spectrum and highly polarised radio emission detected. Synchrotron radiation is emitted by electrons spiralling at relativistic speeds in magnetic fields. The spectra from individual electrons at different energies add up to give the power law spectrum (on a plot of log(flux) versus log(frequency), this is a straight line with negative gradient). The spectrum usually continues to increase with decreasing frequency down to a transition frequency below which it turns over and has a positive gradient. This is due to synchrotron self absorption when the plasma becomes opaque to its own synchrotron radiation. Since the particles are moving at relativistic speeds, the radiation is "beamed". This means that very little is emitted in directions other than that in which the particle is moving. In the case of an AGN, the required magnetic fields are generated by the highly conducting ionised accretion disk and rotate with it around the BH. The charged particles (possibly electrons and ions or an electron-positron plasma) are accelerated away from the nucleus. The energy source for this is likely to be the accretion mechanism onto the black hole (see below), the Blandford-Znajek (BZ) mechanism (Blandford and Znajek, 1977) or a combination of both. In the BZ mechanism, energy is effectively taken from the rotating black hole and given to the charged material. The rotating black hole is effectively a spinning conductor in a magnetic field and so acquires an EMF between its poles and equator with effective resistance of $\sim 30\Omega$. The BH then acts like a battery connected to a $30\Omega$ resistor and power is extracted from its rotational energy. The material is collimated, perhaps by a thick

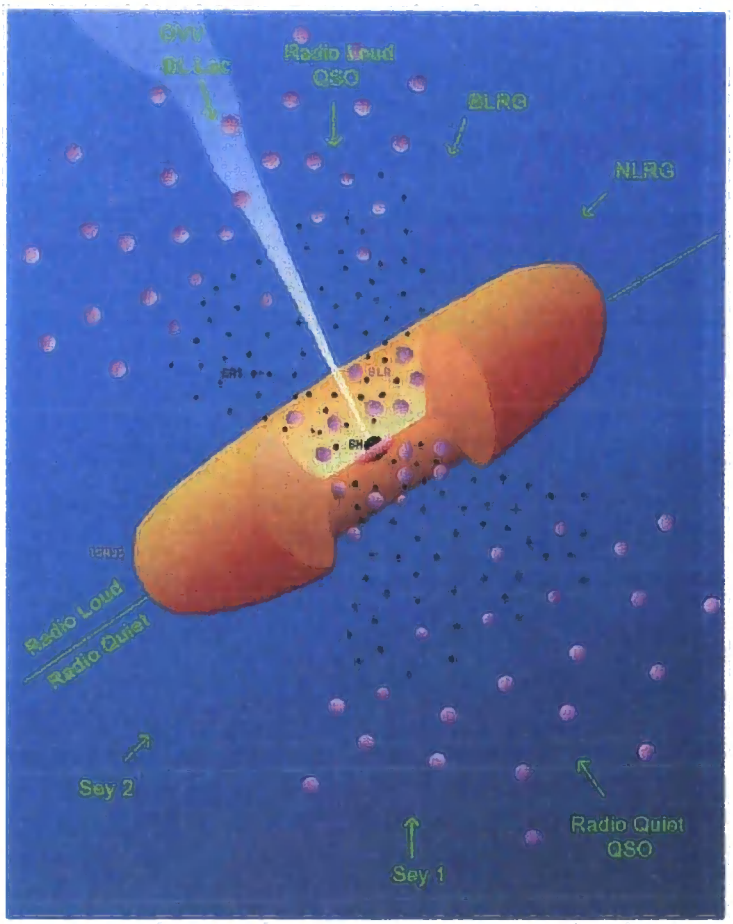


Figure 1.4: Cartoon showing anisotropic nature of an AGN in schematic form. The figure shows the basic picture is of black hole (BH), torus, gas clouds and, in the case of a radio-loud AGN, radio jet (see text for details). The classification given to the AGN is highly dependent on the angle at which it is viewed. The figure shows the viewing angles that would result in classification as Seyfert 1, Seyfert 2, Blazar (BL Lac), optically violently variable (OVV) quasars, radio loud/quiet QSO (quasi-stellar object, quasar), broad and narrow line radio galaxies (B(N)LRG). The small, black symbols represent clouds of gas moving at high velocity in the gravitational potential of the black hole. These clouds are the origins of the broad optical and UV emission lines. The larger, purple symbols represent clouds of gas moving at slower velocities and which produce emission lines with narrower widths. Note that, in this cartoon, the radio activity is only shown on one side of the AGN for the purpose of clarity and there is no implication that such features only appear on one side. Figure from Holt et al. (1991).

hot accretion disk (see below) or by the interaction of the plasma and the magnetic field, into a jet that interacts with the inter-galactic medium (IGM) to form giant radio lobes. These lobes still contain the magnetic field from the disk that was coupled to the ejected material. They can extend for several hundred kpc and can dominate the radio emission from the AGN.

Regions of active or recent star formation can also produce radio emission. This, along with methods of separating the radio emission from AGN and star formation, is discussed in section 2.1.9.

#### 1.2.3.3 Sub-classifications of Radio-Loud AGN and Accretion Disks

We now turn briefly to sub-classifications of radio-loud AGN and a possible explanation for the division between radio-loud and quiet AGN based on a qualitative description of the accretion disks around the BHs. Radio galaxies are traditionally categorised as either FR I or FR II (Fanaroff and Riley, 1974). FR I sources are typically low-powered radio galaxies with weak jets and edge-darkened radio lobes. Conversely, FR II sources are more powerful radio sources, have strong jets and have edge-brightened radio lobes caused by hot spots where the jets terminate in the ISM. Here we briefly discuss the possibility that morphological differences are due to different accretion modes and/or jet formation processes.

There are two broad classifications of accretion disks, based on their physical and radiative properties, that go some way to explaining some of the properties of AGN and thus merit a brief description here. The first is the Shakura-Syunyaev disk (hereafter SSD), based on the work of Shakura and Syunyaev (1973). This is a geometrically thin disk comprising cold gas. However, the disk is optically thick. This means that the mean free path of photons within it is short and photons can readily escape the disk so it radiates energy away very efficiently and becomes very luminous, especially at X-ray wavelengths. This radiation ionises the nearby broad- and narrow-line emitting regions.

The second type of disk is that which is consistent with advection-dominated accretion flow (ADAF). This type of disk, first predicted by Ichimaru (1977), is in many ways the opposite to the SSD. It is geometrically thick, even approaching a spherical profile, contains hot gas and is optically thin. This phenomenon can occur in systems with both high and low accretion rates. In rapidly accreting systems ($\dot{M} > \dot{M}_{Edd}$ where $\dot{M}_{Edd}$ is the Eddington limit), the photons within the disk are mostly trapped and the disk is radiatively inefficient. The heat therefore becomes trapped by the matter and the disk cools

by advection (the energy is transferred with the matter into the black hole). In systems of low $\dot{M}$, the accreting gas is so optically thin that the cooling time is longer than the accretion time and again the energy is advected with the matter (Abbassi et al., 2008). As a result of the low-luminosity disks, ADAFs are usually found in low-luminosity AGN (LLAGN).

The dependency of the differences in radio morphology on the accretion mode is currently an active area of research and authors disagree as to the extent to which there exists a one-to-one relationship between the two. For example, Wu and Cao (2008) find that, under certain assumptions, the same critical accretion rate (that divides the two modes of accretion) is predicted by the Ledlow-Owen relation (Ledlow and Owen, 1996) in the $Q_{jet} - M_{BH}$ plane that divides the FR I and FR II classes as is predicted by their model to be consistent with the ionisation luminosity of radio galaxies for the separation between FR I and FR II. They infer from this that most FR Is have a different accretion mode from FR IIs with most FR Is being in the ADAF accretion mode. On the other hand, Hardcastle et al. (2007) find there is no one-to-one relationship between accretion mode and FR class. However, they do suggest that a class of radio-loud AGN lacking in narrow lines, which they term low-excitation radio galaxies (LERGS), is fuelled by the accretion of the hot, X-ray emitting phase of the intergalactic medium (IGM) and that high-excitation radio sources are powered by accretion of cold material (i.e. SSD-type accretion).

#### 1.2.3.4 X-ray Emission from AGN

As mentioned in the descriptions of the various types of AGN, many of them produce X-rays. There are several possible sources of X-rays in AGN. Firstly, the synchrotron mechanism mentioned in section 1.2.3.2 can also produce X-rays in AGN. Additionally, the high frequency end of the continuum spectrum may account for some of the soft (low energy) X-rays and inverse Compton scattering of photons at lower energies off relativistic electrons can move these photons up to X-ray energies. This could happen in the disk or in the relativistic jets and lobes that are bright in radio emission. Thermal emission (i.e. radiation like that produced by stars in that it's not polarised and has a black-body spectrum) from galaxies can include X-rays too. For example, the spectrum of thermal bremsstrahlung (where an electron emits a photon in the vicinity of a positive ion - free-free emission) is also found in AGN.

#### 1.2.3.5 Visible Emission from AGN

There is one more important class class of AGN that are different to those discussed so far in that they have emission lines, some of which are in the visible part of the spectrum. Heckman (1980) found a class of galaxies with nuclear spectra that resembled those of H II regions. He called them low-ionisation nuclear emission regions (LINER) since the lines definitely didn't originate in the disk and the ionisation state of the gas is relatively low. For this reason, LINERs generally have less strong high-ionisation lines such as [OIII] , He II or [NeIII] lines than they do [OII] or [NII] . Although most authors regard LINERS as low-powered radio AGN, some authors believe LINERs to be powered by star formation rather than accretion onto a black hole (e.g. Shields (1992) who also claim the ionisation mechanism could be photo ionisation rather than shock heating). Sturm et al. (2006) found that luminous infrared galaxies (LIRGS) with LINERs in them tended to have mid-IR spectra consistent with them being starforming galaxies but that fainter ("normal") infrared galaxies with LINERs in them had much bluer mid-IR spectra and were not consistent with starforming galaxies.

## 1.3 Star Formation

As we have already mentioned, star formation is a central tenet of this thesis. Throughout, we will study the rate at which gas is converted into stars: how does this depend on galaxy type, mass and age? How does it vary throughout the history of the Universe? In this section, we describe the consensus picture of the star formation history of the Universe that has built up over the past decade or so. We leave the details of how star formation rates are measured to chapter 2.

### 1.3.1 The Star Formation History of the Universe

The $\Lambda\, CDM$ paradigm outlined in section 1.1 predicts a "bottom-up" picture of galaxy formation (e.g. Blumenthal et al. 1984) in which the least massive halos and galaxies form first. These then begin to merge over cosmic time producing more massive objects. However, this theory is, at least on first inspection, contradictory to a large body of observational evidence that the most massive galaxies in the Universe are actually the oldest. When this is coupled with observations that the most massive galaxies stopped forming stars first and that the masses of galaxies dominating star formation at a given epoch

appear to drop with cosmic time, we have the paradigm of "cosmological downsizing". This term was first used by Cowie et al. (1996) who carried out a spectroscopic study of ~400 objects over all redshifts up to $z \sim 1.7$ and found that the more massive galaxies formed at higher redshift and that the maximum $K$ luminosity (which is very sensitive to the galaxy's mass) of rapidly star forming galaxies has been declining smoothly with decreasing redshift since $z > 1$. This result has been backed up by many other studies (e.g. Juneau et al. (2005), Fontana et al. (2004), Mobasher et al. 2008). However, there is no one observation that actually contradicts the $\Lambda$ $CDM$ theory. It is a question of two trends that need to be either reconciled or disproved by further observations or theoretical refinements. The observational side of that quest is a substantial pillar of this thesis (see chapter 5).

There is also a large body of evidence that the global star formation rate has dropped significantly since $z \sim 1$ (e.g. Madau et al. 1996, Hopkins 2004, Cowie and Barger 2008, Hopkins and Beacom 2006). Many of these studies also show that that the global SFR actually peaked around $z \sim 1-2$ and drops either side of that redshift. Figure 1.5 shows the compilation of star formation rate density (SFRD) versus redshift points made by Hopkins and Beacom (2006).

The rate at which the global SFRD drops with redshift above $z \sim 3$ is still very uncertain, primarily due to the uncertainties in the corrections for the dust extinction, possible evolution in the distribution of the dust throughout the galaxy and cosmic variance (see section 5.3.5). We know that SFRD must drop with increasing redshift above some redshift since, by construction, there must be a delay between the beginning of star formation at the end of reionisation and the SFRD peak. However, in this thesis we are more concerned with the history of the global SFRD since $z \sim 1$. Throughout the remainder of this introduction chapter and this thesis as a whole, we discuss the possible reasons for the drop in SFRD with decreasing redshift since $z \sim 1$.

One of the currently favoured ideas to resolve these problems is that star formation is quenched by AGN (Bower et al. 2006, Croton et al. 2006). In the Bower et al. (2006) model, cooling flows (the flow of cold gas towards star forming regions) are stopped by heat from the AGN (this is known as AGN feedback). Consider a parcel of gas falling into the potential well of a galaxy. Assuming it starts out warm, it will need to cool if it is to be used in star formation, otherwise its thermal energy will enable it to remain in hydrostatic equilibrium. If the gas cools before it flows to the centre then the galaxy is being fed by an influx of cold gas and its cooling is so effective that it can't be heated up

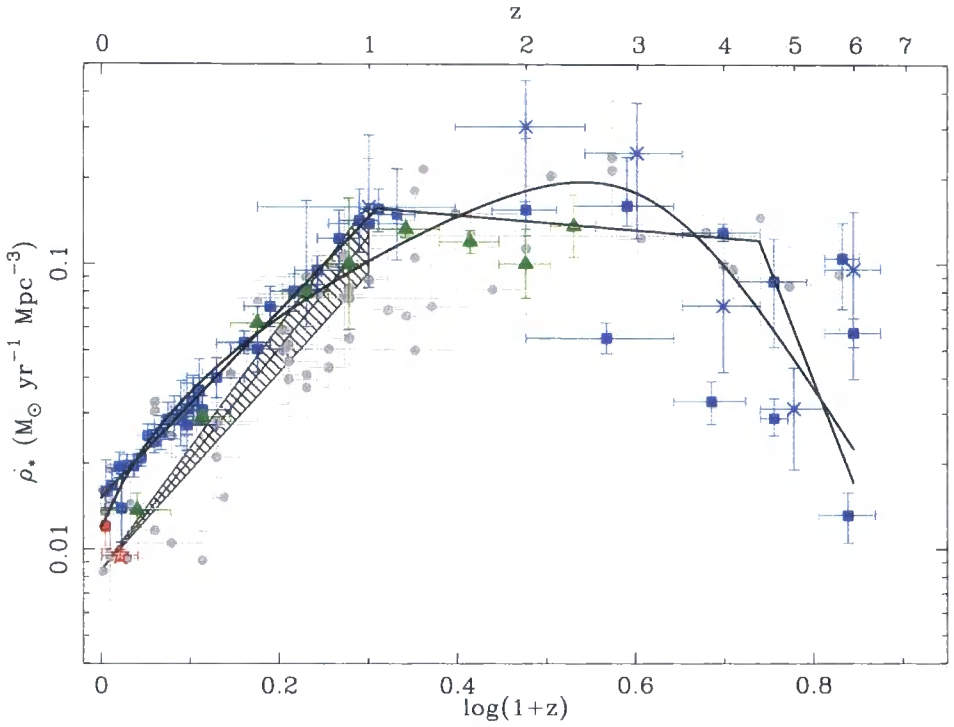


Figure 1.5: The evolution of SFRD with redshift (Figure from Hopkins and Beacom 2006). The data clearly show the rise and fall in SFRD with redshift and the large scatter at high redshift. The data here have been scaled assuming the SalA IMF. Star Formation Rate measurements are based on 24$\mu$m data (hatched region, green triangles), radio data (open red star), $H_\alpha$ data (filled red circle) and UV data (blue squares). The blue crosses are from the ultra-deep field and the solid lines are the best-fits (see Hopkins and Beacom (2006) for details).

by the AGN (the cooling efficiency increases rapidly as the system cools). However, if the parcel of gas cools more slowly than it flows to the centre, it is susceptible to the AGN heat input which can prevent the flow of cold gas and thus quench the star formation. This process could result in the global star formation rate density (SFRD) increasing with redshift (at least up to $z \sim 2$) for galaxies of all masses due to two reasons. Firstly, halos that collapsed at high redshift had lower cooling time/free-fall time ratios than those at low redshift due to the shallower potential wells at high redshift. Thus AGN feedback is less effective and galaxies can form more stars. Secondly, black holes are smaller at high redshift so even some cooling flows that are in hydrostatic equilibrium can form stars.

## 1.4 Galaxy Environments and their relationship with star formation

The final topic we discuss in this chapter is that of galaxies' environments and how this can affect their star formation rates. A galaxy's environment (more correctly its "environmental density") is simply the number density of galaxies in the part of the Universe in which that galaxy resides. Exactly how that is measured is a topic we leave until chapter 2. For now, we focus on the trends already discovered between various galaxy properties and their environmental density.

One of the hottest topics of debate in modern cosmology is the "nature versus nature" question applied to the evolution of galaxies. That is, what causes various galaxy properties to change over time? Which properties are affected more by the galaxy's environment and which are more affected by processes internal to the galaxy? Further, which properties are affected by both internal and external processes?

### 1.4.1 Galaxy trends with Environment

Dressler (1980) was the first to find galaxy trends with environment. He found that a galaxy's morphology followed a trend with environment. He found that elliptical galaxies were found more in denser environments and that spiral-shaped galaxies were more often found in less dense environments. As we shall see, this trend is consistent with our view of galaxy evolution and the relationship between star formation and environment. In fact, we have already seen that AGN feedback, which is more prominent in elliptical galaxies than spirals, is thought to quench star formation.

In the intervening years since Dressler's paper, many subsequent studies have found other galaxy trends with environment. For example, Balogh et al. (2004), looking at SDSS data, found a very strong trend of the fraction of galaxies that are red increasing with environment density in the local Universe. This trend was found for both bright and faint objects. This trend was also found at $z \sim 1$ by Cooper et al. (2006) (hereafter C06) in the DEEP2 data. As we have already seen, colour can be a useful way to characterise a galaxy. Although it doesn't contain as much information as the spectrum, the colour is quantifiable, reproducible and comparable to the star formation history via synthesis models. Therefore the above findings suggest that different types of galaxies reside in different environments. The obvious question to ask is whether these galaxies are different *because* they live in different environments. To examine this issue, we next look at the dependence of SFR on environment.

### 1.4.2 The dependence of SFR on Environment: Nature or Nurture?

Many studies have found the global mean star formation rate (SFR) to be suppressed in denser environments relative to less dense environments. For example, Hashimoto et al. (1998) found that star formation rates decreased with increasing environment density right across the range of densities studied ($\sim -2.3 < Log_{10}(3/(4\pi D^3/3)) < 1.3$ where $D$ is the 3-dimensional redshift space distance from a galaxy to its third nearest neighbour). They found this correlation even for fixed concentration index (measuring the degree to which a galaxy's light comes from its centre). The concentration index is used a quantitative proxy for Hubble type. Similar results have been found by Gómez et al. (2003) in the Sloan Digital Sky Survey (SDSS), who found SFR to decrease with increasing density above a characteristic density of $\sim 1h^{-1}$ comoving Mpc$^{-2}$. They found this trend was stronger for the more strongly star forming galaxies ($H_\alpha$ EW $> 5$Å ). However, below this characteristic density they found the SFR to be insensitive to density. Finally, Best (2004) (hereafter B04), using the 2dfGRS, found this trend to apply to radio galaxies too. B04 found the fraction of galaxies that are associated with star forming radio galaxies to drop with increasing environment density over the range $10^{-2} < \Sigma_{10}/\mathrm{Mpc}^{-2} < 10^3$ ($\Sigma_{10}$ is defined in equation 2.16 below).

A density of 1Mpc$^{-2}$ is below both the mean galaxy surface density at the virial radius of relatively rich clusters and that of galaxy groups (B04). Therefore, regardless of whether such a characteristic density as discussed above exists, the evidence implies that at least some of the physical processes responsible for this correlation are not intrinsic

to the cluster environment. The process most likely to turn a galaxy red that doesn't necessarily depend on the environment is simply the exhaustion of the gas supply to the star forming regions. However, some authors argue that this too can be exacerbated in the cluster environment which can trigger a starburst that rapidly consumes the gas (e.g. Poggianti et al. 1999).

An example of a process that *is* intrinsic to the cluster environment is ram-pressure stripping (e.g. Gunn and Gott 1972, Quilis et al. 2000) of the interstellar medium by the hot cluster gas. This is the process by which a galaxy loses some or all of its cold gas as it passes through the IGM in a cluster. The pressure on the gas is proportional to $\rho v^2$ (where $\rho$ is the density of the intra-cluster medium gas and $v$ is the relative velocity between the IGM gas and the galaxy) and the galaxy can have all its H I gas swept away in as little as 100Myr. The process is only effective where the gas around the galaxy has a sufficiently high density, namely in the cluster environment. With a reduction in or complete cessation of star formation, the galaxy's colour will turn red as the light becomes dominated by old stars.

Other processes that can cause a galaxy's colour to turn red in a dense environment are strangulation and mergers & harassment. Strangulation is the process by which a galaxy's flow of cold gas is cut off when the hot/warm gas is swept away (Kawata and Mulchaey, 2008). Alternatively two galaxies that pass each will interact with each other gravitationally. This may result in "harassment" (e.g. Moore et al. 1996) or a merging of the two galaxies that can result in at least one galaxy losing its supply of gas. Many studies (e.g. Balogh et al. 2000) have found gradients with cluster radius of galaxy colours and star formation rates with galaxies closer to the cluster centre being typically redder and with suppressed SFR compared to those galaxies further out.

A galaxy's environment may also affect the AGN, if one is present. For example, Hardcastle et al. (2007) suggest that high-powered (FR I class) radio AGN are more likely to be found in massive galaxies such as those that dominate groups and clusters. This is because these AGN are fuelled by hot-mode (ADAF) accretion and thus require a supply of hot gas. Conversely, low-powered radio AGN (FR II class) need a supply of cold gas and are therefore more likely to be found in systems that have recently undergone mergers. These systems are mostly found in mid-density environments where the galaxies get close enough together to interact (unlike in the field) but are not moving too quickly that they don't have time to interact (unlike in cluster centres).

## 1.5 Motivation for and Structure of this thesis

Having discussed the status of some of the aspects of modern astronomy relevant to star formation and radio galaxies, we now briefly discuss the questions this thesis attempts to answer before setting out the structure of the thesis. The first questions we tackle concern radio emission. Which of AGN and star formation dominate a galaxy's radio emission? How does this depend on galaxy type, radio luminosity and redshift? How well does a galaxy's radio emission trace its star formation and can it trace it over a significant period of the Universe's evolution? Further, how are these two radio-producing mechanisms affected by the galaxy's environment? Is it the galaxies' environments that causes the drop in the global star formation rate density since $z \sim 1$ (the "nature" versus "nurture" debate)? In this debate, there is growing evidence that star formation is only affected by environment when galaxy mergers and harassment are most common. We ask what properties such galaxies are likely to have and how they differ to other galaxies at the same redshift.

We will also turn our attention to the downsizing picture of the global star formation rate. What contribution do dwarf galaxies make to this rate at a redshift of $z \sim 1$ and how does that compare to the local Universe? Is the correct picture one of *only* the most massive galaxies forming stars at the highest redshifts with this trend being slowly reversed? Or, do all galaxies form stars at redshift $z \sim 1$ and it's just that the smallest ones have been too faint to be observed spectroscopically? Which galaxies dominate the global SFRD at which redshifts?

In chapter 2 we describe the "tools of the trade" required to carry out the research done in the rest of the thesis. These tools include luminosity functions, methods of measuring environmental density and descriptions of selected galaxy surveys.

We next measure the luminosity functions of radio AGN and star forming galaxies in chapter 3. By comparing these to their low-redshift counterparts we can measure their evolution and what type of galaxies dominate the global radio emission at different redshifts. Also in this chapter, we analyse the trends of X-ray emission with radio emission at $z \sim 1$ and test whether the colour-magnitude distribution for the radio sources is comparable to that in the local Universe.

Then in chapter 4, we analyse the environments of these radio sources and ask what trends, if any, are there of their properties with environment. Again, we compare these results to similar work done in the low-redshift Universe.

In chapter 5 we describe our own spectroscopic redshift survey at $z \sim 1$. This survey targets low mass galaxies and aims to measure their star formation rates and thus to infer the contribution to the global SFRD from these galaxies at this redshift. By comparing these results to those at $z \sim 0$, we can establish the downsizing theory by adding to our knowledge of which galaxies dominate the global SF at which redshifts.

Finally, in chapter 6 we present our conclusions and our suggestions for future work.

# Chapter 2

# *The Astronomer's Toolbox*

In this chapter we develop many of the tools we will use throughout the remainder of the thesis. We develop these tools here because some of the later chapters are written in paper format and are thus somewhat compressed, with the basic methodology excluded. In this chapter we describe general astronomical methods. In the later chapters we will describe the methods used as specific to the work in those chapters. We begin with one of the most important aspects of this thesis: measuring star formation rates.

## 2.1 Measuring Star Formation Rates

Information on a galaxy's star formation rate and history can be gleaned from observations, both spectroscopic and photometric, at a variety of wavelengths. Here, we outline the methods used and the principal measurements used in this thesis from which the above information is inferred.

It is difficult to infer a galaxy's SFR just from its flux at a given wavelength. To make the inference, we must also estimate the galaxy's star formation history, age and metal abundance. This information is estimated using synthesis models of galaxy spectra and broadband luminosities (e.g Larson and Tinsley 1978, Bruzual and Charlot 2003). The spectra of individual stars of differing masses at different ages are derived from stellar evolutionary tracks (e.g. in a Hertzsprung-Russell diagram). These templates are then added together. A part of this process is to weight them according to how many stars of each mass one would expect in a galaxy's makeup. This is done using the initial mass function (IMF, described in section 2.1.1). This gives synthesised spectra, luminosities, colours, etc of a single-age population as a function of age. Using these models to infer a galaxy's star formation rate from its colours or luminosity is problematic since it would require knowledge of its age, metallicity, reddening correction and star formation history (usually parameterised as a decaying exponential function of time). However, these

problems are avoided if the spectral measurements are dominated by young stars. At the blue wavelengths where this is the case, SFR scales linearly with luminosity.

Before we look at the individual parts of the spectrum from which we can infer star formation rates, it is first necessary to describe two issues one must be aware of when making these inferences. These are the IMF and reddening due to dust.

### 2.1.1 The IMF

The IMF is an empirical function describing the distribution of stars' masses with which they are born. In other words, it describes the relative probabilities of stars of different masses forming. In principle the shape of the IMF could be deduced by recording the masses of all the stars, correcting for their different lifetimes and allowing for the star formation histories of each star forming region. Salpeter 1955 was the first to do a version of this calculation. He measured the luminosity function (see section 2.3.1) of stars in the solar neighbourhood, converted to masses, corrected for main-sequence lifetimes and assumed the SFR had been constant for the last 5Gyr. Despite huge uncertainties, not least in the mass-to-light ratios, he derived a result that is still much used today: if $n_{\log M}\,\mathrm{d}\log M$ is the number of stars whose log(mass) is in the range log$M$ to log$M$ + dlog$M$ then plotting log $n$ versus log mass yields a straight line (a power law) with slope -1.35[1]. This power law index is usually denoted by $\Gamma$ (i.e. for a Salpeter IMF, $\Gamma$=1.35). This power law, along with the later IMFs of Miller & Scalo (Miller and Scalo, 1979), Scalo(1986, 1998) and Kroupa (Kroupa, 2001), is shown in figure 2.1, plotted as the mass fraction per logarithmic mass bin versus mass. We mention one other IMF that is not plotted in figure 2.1: the Kennicutt IMF (Kennicutt, 1983). This IMF has a slope of -1.5 for 1< $M/M_{\odot}$ <120 and is widely used to this day. Notice that the line for the Salpeter IMF in figure 2.1 has a slope of 1-$\Gamma$. This can be seen from the following analysis. From the definition of $n$ given above, we have:

$$n \propto M^{-\Gamma}. \tag{2.1}$$

where $M$ is the stellar mass in units of the solar mass, $M_{\odot}$ . The amount of mass in stars whose log(mass) is in the range log$M$ to log$M$ + dlog$M$ is $nM$. Since the integral of the IMF is normalised to unity, this is also the fraction of mass in this log(mass) range. We then have:

[1] this slope is only -1.35 with respect to logarithmic mass bins; it is -2.35 with respect to linear mass bins

$$nM \propto M^{1-\Gamma} \tag{2.2}$$

and

$$\frac{\mathrm{d}log(nM)}{\mathrm{d}log(M)} \propto 1 - \Gamma \tag{2.3}$$

Baldry and Glazebrook (2003) (hereafter BG03) derived a universal IMF by fitting spectral synthesis models with varying IMFs to the local ($z \sim 0.1$) luminosity densities in the range 0.2 to 2.2$\mu$m. They parameterised the IMF as a double power-law:

$$n_{\log m} \propto \begin{array}{ll} M^{-0.5} & \text{for } 0.1 < M < 0.5 \\ M^{-\Gamma} & \text{for } 0.5 < M < 120. \end{array} \tag{2.4}$$

Parameterising cosmic star formation history as

$$SFR \propto \begin{array}{ll} (1+z)^{\beta} & \text{for } z < 1 \\ (1+z)^{\alpha} & \text{for } z \geq 1, \end{array} \tag{2.5}$$

they found the best-fit universal IMF (universal in that it doesn't change with cosmic time or galaxy environment) over the range ($0.5 \leq \beta \leq 4.0$) and ($-2 \leq \alpha \leq 2$) was $\Gamma = 1.15 \pm 0.2$. This is the BG03 IMF that we will use to make SFR measurements in chapter 5.

### 2.1.2 Reddening Corrections

Before we cover individual star formation rate tracers in turn, it is important to mention another topic that will appear throughout this thesis and which we have already touched upon: interstellar reddening. As mentioned above, dust grains scatter and absorb UV and optical light, re-radiating it in the infrared. Thus short-wavelength radiation is dimmed and reddened by dust. This must be corrected for if we are to recover the intrinsic luminosities at UV and optical wavelengths. We define $A_\lambda$ to be the extinction (in magnitude) at wavelength $\lambda$. The amount of reddening is characterised by the colour excess $E(B-V)$, defined by the intrinsic ($i$) and observed ($o$) colours derived from the nebular gas emission lines:

$$E(B-V) = (B-V)_o - (B-V)_i \tag{2.6}$$

The most commonly used reddening law is that of Calzetti et al. (2000). This is an empirical law derived from starburst galaxies. It has the form:

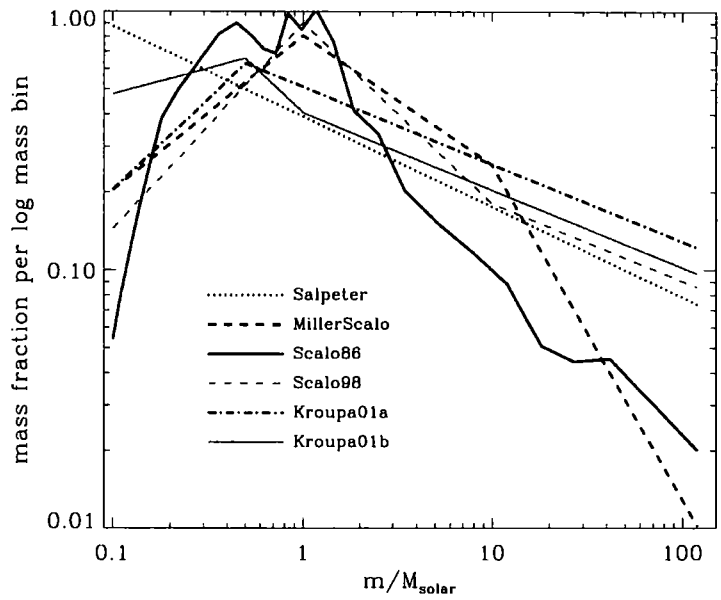


Figure 2.1: Stellar initial mass functions (IMF) plotted as mass fraction per unit logarithmic mass bin versus mass. The IMFs plotted are those of Salpeter (1955), Miller and Scalo (1979), Scalo (1986), Scalo (1998) and Kroupa (2001). All IMFs are assumed to be valid over the mass range $0.1 < M/M_{\odot} < 120$ and the integral of each curve is normalised to unity. The slopes of the curves are equal to 1-$\Gamma$ (see text for a proof of this) and the values of $\Gamma$ for $M > 1M_{\odot}$ for the IMFs listed above are 1.35, 1.5/2.3, ~2.05/1.5, 1.7/1.3 and 1.3 respectively. Figure from Baldry and Glazebrook (2003)

$$F_i(\lambda) = F_o(\lambda)10^{0.4E(B-V)k(\lambda)} \tag{2.7}$$

where $F_i(\lambda)$ and $F_o(\lambda)$ are the intrinsic and observed flux densities respectively and $k(\lambda)$ is given by:

$$k(\lambda) = \begin{array}{ll} 2.659(-1.857 + \frac{1.040}{\lambda}) + R_V & \text{for } 0.63\mu m \leq \lambda \leq 2.20\mu m \\ 2.659(-2.156 + \frac{1.509}{\lambda} - \frac{0.198}{\lambda^2} + \frac{0.011}{\lambda^3}) + R_V & \text{for } 0.12\mu m \leq \lambda < 0.63\mu m. \end{array} \tag{2.8}$$

where $R_V \equiv A(V)/E(B-V)$. Calzetti et al. (2000) find $R_V = 4.05$ for star forming galaxies. The curve from equation 2.8 is shown in figure 2.2. Also shown on the figure is the Milky Way extinction curve of Schlegel et al. (1998) for $R_V$=3.1. We shall use both of these curves to estimate reddening of our radio sources in section 3.3.2. The most striking feature of the Calzetti curve is the monotonic decrease in the extinction with increasing wavelength[2]. One advantage of this law is that it is relatively simple. It is almost a smooth curve and doesn't have the "blue bump" at 2175Å found in laws derived for the milky way. This bump is thought to be due to small graphite grains (e.g. Cardelli et al. 1989) as is seen when the line of sight passes through only diffuse parts of the ISM (Whittet et al., 2004).

### 2.1.3 $H_\alpha$

Having discussed the IMF and reddening that must be taken into account when inferring star formation rates, we now look at individual star formation tracers in turn. We begin with $H_\alpha$ .

When it is possible to measure it, the strength of the $H_\alpha$ line is perhaps the best diagnostic of a galaxy's current star formation rate. At a rest-frame wavelength of 6563Å, its major drawback is that it is redshifted out of the visible part of the spectrum at redshifts greater than $z \sim 0.4$ and into the infrared where strong sky emission lines make accurate measurements very difficult. Still, it remains very useful at lower redshifts. The reason behind its usefulness is that, in the ionised H II regions of star-forming galaxies discussed above, the strength of this line is directly correlated with the intensity of the ionising flux from the embedded stars. This is because $H_\alpha$ is a *recombination line*. In a

[2]For this reason, it would have made more sense to normalise extinctions relative to some long wavelength unaffected by dust such as the FIR or radio (e.g. in the definition of $R_V$). Historically, however, the $V$ band has been used and so authors use that convention today.

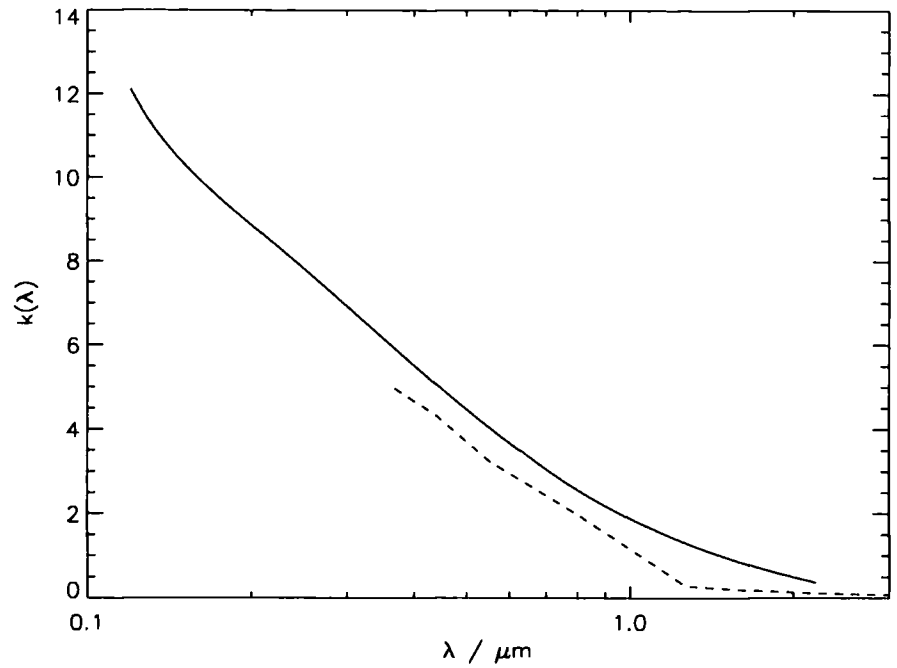


Figure 2.2: The Calzetti (solid line) and Schlegel (dashed line) reddening laws: $k(\lambda)$ as a function of $\lambda$. The respective values of $R_V$ are 4.05 and 3.1. See text for further details.

region of ionised hydrogen, the $H_\alpha$ line is formed when an electron recombines with a proton to form a neutral hydrogen atom. The electron can start at any quantum energy level in the atom but then cascades down through the energy levels, emitting photons as it does so as described by the Bohr model of the hydrogen atom. Approximately half the time, this cascade will include the $n = 3$ to $n = 2$ (where $n$ is the principal quantum number) transition when the emitted photon will contribute to the $H_\alpha$ line. Since the ionising flux is dominated by stars with high masses $> 10M_\odot$ and which therefore have very short lifetimes (< 20Myr), the $H_\alpha$ luminosity gives a near instantaneous measure of the SFR. The conversion used throughout this thesis is that of Kennicutt (1998) (hereafter K98):

$$SFR(M_\odot yr^{-1}) = 7.9 \times 10^{-42} L(H_\alpha)(ergs^{-1}) \tag{2.9}$$

This conversion rate assumes solar metallicity and the Salpeter 1955 IMF. $L(H_\alpha)$ must be corrected for dust reddening before being used in equation 2.9. The sensitivity of the conversion to this reddening correction is perhaps its most significant drawback. Many authors use an average correction of $A_{H_\alpha}$=1. For example, Kennicutt (1992) found this to

be a reasonable average extinction in local galaxies and Charlot et al. (2002) applied the same correction to all the galaxies in their sample in the Stromlo-APM Survey. We will also use this extinction correction in chapter 5.

### 2.1.4 [OII]

In the redshift range $0.4 < z < 1.5$, the [OII] line (with a rest-frame wavelength of 3727Å) is in the visible part of the spectrum and is thus relatively easy to measure. Although its strength is not directly related to the ionising flux, it can still be used as a tracer of star formation. This is because it can be calibrated empirically through $H_\alpha$ . This in turn is based on the observation that [OII] and $H_\beta$ are well correlated in star-forming galaxies (e.g. Gallagher et al. 1989). Under the assumption of case B recombination (Osterbrock, 1989), a theoretical Balmer decrement ($\equiv H_\alpha / H_\beta$ ) is derived to provide the final link between [OII] flux and SFR. K98 derive a calibration from the average of that of Kennicutt (1992) (based on 90 normal and peculiar galaxies) and Gallagher et al. (1989) (based on 75 blue irregular galaxies). The calibration of K98 is:

$$SFR(M_\odot yr^{-1}) = (1.4 \pm 0.4) \times 10^{-41} L([OII])(erg\ s^{-1}) \tag{2.10}$$

where the extinction correction is to be carried out in $H_\alpha$ . Implicit in this calibration is solar metallicity, no dust (the extinction correction remains to be made), the same Salpeter IMF as was used in equation 2.9 and case B recombination (which yields a Balmer decrement of 2.85). The main problem with this calibration is its dependence on the metallicity and the uncertainty in the dust reddening correction. This problem is analysed in detail in section 5.4.5.

### 2.1.5 Far-infrared

All the short-wavelength light emitted by young, hot stars and absorbed by dust is re-radiated in the far-infrared (FIR). Thus the radiation at that wavelength will act as another tracer of star formation. In the limiting case of the young stars dominating the UV and visible wavelengths and the dust opacity being high everywhere, the FIR luminosity measures the bolometric luminosity of the starburst. Such conditions roughly hold in the dense circumnuclear starbursts that power many IR-luminous galaxies (K98).

In practice, however, the situation is more complex. There are two components to a galaxy's FIR flux: a "warm" component ($\lambda \sim 60\mu m$) from the dust around the young star

forming regions and a cooler "infrared cirrus" component ($\lambda \geq 100\mu m$) from the dust heated by the interstellar radiation field. The former dominates the $40-120\mu m$ emission in early-type galaxies where the FIR luminosity correlates with other SFR tracers such as UV continuum and $H_\alpha$ (see, e.g. Buat and Xu 1996). In early-type galaxies, although often very luminous in the infrared, the emission is dominated by the cooler cirrus type. For starburst galaxies, K98 derive the following calibration:

$$SFR(M_\odot yr^{-1}) = 4.5 \times 10^{-44} L_{FIR}(erg\ s^{-1}) \tag{2.11}$$

Other authors have derived similar relationships from stellar synthesis models (e.g. Bell et al. 2005 using the models of Fioc and Rocca-Volmerange 1999). SFRs derived from the far-infrared are usually higher than those derived from [OII] or UV. Indeed, Conselice et al. (2007) analysing spectra of a $K$-band selected sample from the Deep Extragalactic Evolutionary Probe (DEEP2) survey found that the $24\mu$m -derived SFRs were always much higher than the [OII] -derived ones. However, Cowie and Barger (2008) found that, overall, their SFRs derived from $24\mu$m and UV were in good agreement. The disagreements found between the different tracers are most likely due to uncertainties in the dust correction (Daddi et al., 2007).

### 2.1.6 UV

The final calibration is perhaps the most original. It is based on the initial UV continuum produced by the hot stars. The optimal wavelength range is 1250-2500Å : this wavelength is short enough to restrict the emission to just the short-lived, young stars but long enough to avoid the Ly$\alpha$ forest and the Ly$\alpha$ line. The final calibration from K98 is:

$$SFR(M_\odot yr^{-1}) = 1.4 \times 10^{-28} L_\nu(erg\ s^{-1} Hz^{-1}) \tag{2.12}$$

The major drawback with this method is uncertainty in the inferred SFRs resulting from the extinction due to dust. As we have seen in figure 2.2, $k(\lambda)$ increases monotonically with decreasing wavelength. Thus the extinction at these UV wavelengths is likely to be an order of magnitude greater than that at $\sim 2\mu$m.

### 2.1.7 Star Formation and Radio Emission

In addition to the above correlations between SFR and emission at various wavelengths, there is strong evidence for a link between SFR and radio emission. As with the AGN ra-

dio emission, the mechanism responsible for the dominant component of radio emission (90%, Hodge et al. 2008) is synchrotron emission. The other 10% comes from free-free emission in H II regions. In the case of star formation, the electrons are accelerated to relativistic speeds in supernovae remnants (SNR, Condon 1992) from Types Ib and II supernovae. These electrons then gyrate around the lines of the ISM magnetic fields and emit the synchrotron radiation. The energy lost per unit volume varies as $n_e B^2$ where $n_e$ is the electron density and $B$ is the magnetic field strength (Binney and Tremaine, 2008). Since compression of the gas in the spiral arms of a late-type galaxy (where the hot stars and H II regions reside) would increase both $n_e$ and $B$ (the magnetic field is "frozen" into the interstellar gas), the synchrotron emission is greatly enhanced in the spiral arms. Also, only the most massive stars $\geq 8 M_{\odot}$ can produce the Type Ib and Type II supernovae required. For these reasons, this radio emission is correlated with the near-instantaneous SFR.

However, there are reasons why the SF tracers described above are usually preferred to radio emission. Firstly, the complex astrophysics linking the supernovae explosions and the emission of synchrotron emission is relatively poorly understood. Secondly, normal (by which we mean galaxies whose radio emission is not dominated by an AGN) radio galaxies were, until recently, below the sensitivity of most wide-area radio surveys, especially at high redshift. Thirdly, as we have seen, AGN also produce radio emission (and can do so in copious amounts). Separating the radio emission from SF from that from the AGN is a difficult problem that we discuss below. On the other hand, radio emission does have one major advantage over all the other tracers described thus far: it is totally unaffected by extinction due to dust. We have already seen the wavelength dependence of this phenomenon in the Calzetti reddening law. Despite these obstacles, SFR-radio calibrations have been derived. For example, Hodge et al. (2008) derived the following relationship for faint normal radio galaxies in the local Universe:

$$log(L_{1.4}) = (1.37 \pm 0.02) log(SFR) + (27.67 \pm 0.01) \tag{2.13}$$

where $L_{1.4}$ is the emission at 1.4GHz in ergs $s^{-1}$ $Hz^{-1}$ and SFR is measured in $M_{\odot}$ $yr^{-1}$. To examine the nonlinearity of this equation, and to test the validity of radio emission as an SFR tracer, we must first introduce what at first sight is a remarkable astrophysical trend: the FIR-radio correlation.

### 2.1.8 The FIR-Radio Correlation

The first correlation between emission in the far-infrared and the radio was discovered by van der Kruit (1971) analysing the nuclei of Seyfert galaxies at $10\mu m$ and 1.4GHz. Since then, this correlation has been found to hold for several orders of magnitude in radio luminosity (e.g. Bell 2003). At first, the tightness of this relation was the basis of an argument that both the FIR and radio emission vary linearly with SFR. Indeed, earlier radio-SFR calibrations (e.g. Condon 1992) assumed the relation to be linear. However, Bell (2003) found the FIR emission to only trace a small fraction of the SF in faint ($\sim 0.01L_*$) galaxies (see section 2.3.1 for the definition of $L_*$). Since the radio-FIR relationship is linear down to these luminosities, the radio emission too must trace only a small fraction of the SF in such faint galaxies.Bell (2003) therefore concluded that SFR-radio relation is non-linear and that the linearity of the FIR-radio relationship is a "conspiracy"!

### 2.1.9 Separating Radio Emission from Star Formation from that from AGN

As mentioned above, a galaxy's radio emission (and, to an extent, its optical emission) can originate either in its star forming regions or in the AGN. When using this emission to measure the galaxy's SFR, it's obviously imperative to only include that from the SF regions and thus we need a method to separate the two. In this thesis, this will be a particularly pertinent topic for chapter 3. Here we describe some possible separation methods.

**Emission line diagnostic diagram** The conventional method, where the required information is available, is to use an "emission line diagnostic diagram". In this scheme, the origin of the emission is revealed by the relationship between various ratios of emission line strengths: the origin of excitation is related to the level of excitation of different lines. This idea was first explored by Baldwin, Phillips and Terlevich (1981) and the resulting diagram is now known as the BPT diagram. It plots [OIII] 50007/$H_\beta$ versus [NII] /$H_\alpha$ (usually in log-log form). An example of such a plot from Brinchmann et al. (2004) is shown in figure 2.3. The blue and red lines on this plot separate the star forming galaxies (SFG) from the AGN. Between these two populations are the composites whose radio emission will have contributions from both SF and AGN. LINERs would be located towards the bottom right on this diagram and Seyferts towards the top right.

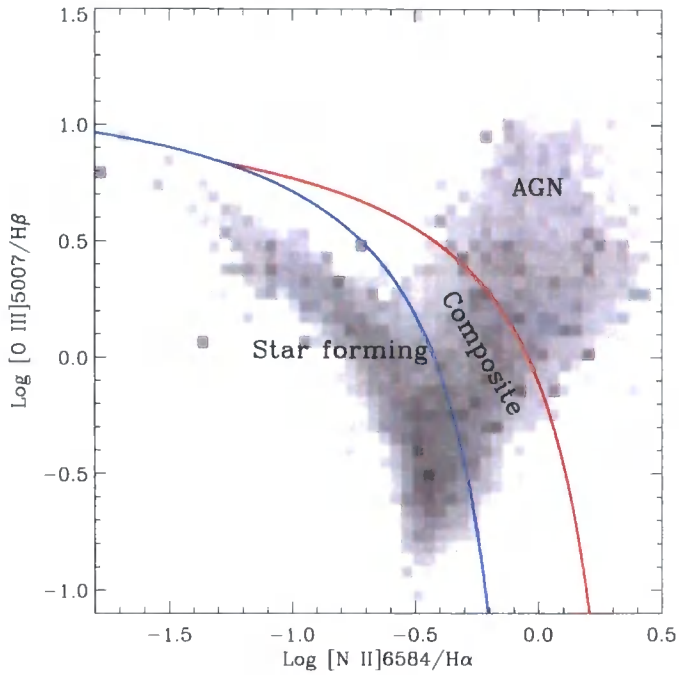


Figure 2.3: The BPT emission line diagnostic diagram for the sample of SDSS galaxies from Brinchmann et al. (2004). Every galaxy plotted here has S/N > 3 in all four lines. The upper, red separation line is from equation (5) of Kewley et al. (2001) and is an upper limit on starburst galaxies estimated using the Pégasé population synthesis code (Fioc and Rocca-Volmerange, 1999) and their own MAPPINGs photo ionisation and shock code. Their models allowed for wide ranges in metallicity, the ionisation parameter and dust extinction and for the effects of shock excitation by supernovae. The lower, blue line is taken from equation (1) of Kauffmann et al. (2003a). They found the line from Kewley et al. (2001) to be offset from the clear sequence of starforming galaxies and so chose a new demarcation (the lower curve in this figure). Figure from Brinchmann et al. (2004).

**Morphologies** As we saw in sections 1.3.1 and 1.4.2, AGN activity is more associated with early-type galaxies with lower star formation rates than with late-types with active H II regions. Therefore, in the absence of the spectral information required to construct a BPT diagram, the *likely* origin of the radio emission may be drawn simply by looking at images of the galaxy in any of the visible, infrared, UV and radio. Its shape in these wavelengths can be compared to the descriptions of early- and late- type galaxies given above. Also, one can compare the structure of the radio image to that of the visible. For example, if definite spiral arms are detected in the visible and IR and these coincide with the majority of the radio emission, it would be a strong bet that the radio emission is due to SF. Using the morphologies of galaxies will obviously not be as useful a diagnostic as the BPT diagram in the more marginal cases.

**Colours** A second useful estimator in the absence of spectral information is the galaxy's colour. For example, since we know that late-type galaxies are bluer and are more likely to have their radio emission dominated by SFR than early-types, simply using the galaxy's colour can give a useful indication as to the relative contributions of the AGN and SF to its radio emission. This method will have particular pertinence in chapter 3.

## 2.2 Measuring Galaxy Environment

In section 1.4 we discussed how various galaxy properties depend on the galaxy's environment density. In order to look for such trends we will need a method of measuring this density and in this section we discuss several methods of making this measurement. We also discuss the issues that affect the choice of method and limit its usefulness. We only consider those methods that give a continuous measurement, as opposed to those that rely on identifying galaxy groups and clusters. This is for two reasons. Firstly, using predefined classifications based, for example, on the number of galaxies in the group or cluster gives a poorly sampled range of galaxy environments. Secondly, at high redshift, denser regions are often under-sampled and clusters and groups are less numerous. Therefore a continuous, local measurement is more desirable.

### 2.2.1 Issues affecting Environment measures

In evaluating different methods of measuring environment density, there are several issues that will affect different issues by different amounts. We describe four of them here.

**Edge Effects** In any survey, only a finite fraction of the sky can be observed. Therefore every survey will have edges with no information available on the galaxies beyond those edges. However, the galaxies just beyond the edges of the survey will partly define the true environments of the galaxies just inside the survey. Therefore, any measurement of density must minimise these effects.

**Redshift-space distortions** Line-of-sight positions are inferred from the galaxies' redshifts. However, for a given cosmology, a galaxy's redshift is a monotonic function of its net recessional velocity from the observer. If this velocity were simply that of the Hubble flow, the redshift-inferred position would be its true position. However, galaxies also have peculiar velocities ($v_{pec}$) induced by their local gravitational fields and these affect its observed redshift ($z_{obs}$):

$$z_{obs} = z_{true} + \frac{v_{pec}}{c} \tag{2.14}$$

This effect causes clusters to become elongated in redshift-space, giving the "fingers of God" effect. Different methods of measuring the environmental density will be affected to different extents by these distortions, as discussed below.

**Accuracy across a range of environments** Peculiar velocities are naturally larger in denser environments such as clusters and rich groups but this is not the only issue that affects environment measures in a way that depends on the density of the environment. If we measure the distances to the galaxies around the galaxy whose environment density is being measured (the $n^{th}$ nearest neighbour measurement, described below), the choices of parameters will affect the accuracy of the density measurement by different amounts in different environments. For example, Cooper et al. (2005) (hereafter C05) found that, in the regions of higher density, choosing $n$=3 consistently reproduced the true environment density (as measured from the true distribution of galaxies in real space in mock catalogues, as discussed below) more accurately than had they chosen $n$=5. However, the opposite was true

in the lower density regions. Similarly, if foreground and background interlopers are rejected by only counting the galaxies within a velocity slice $\Delta v$, the choice of $\Delta v$ is important. In the higher density regions, the true density is reproduced better by larger values of $\Delta v$ (up to 2000kms$^{-1}$ for fixed $n$). Again the opposite is true in the lower density regions where a value of $\Delta$ v = 750kms$^{-1}$ would be preferred.

**Selection and observation completeness** Any spectroscopic survey carried out over a significant range of redshifts will have a selection completeness (fraction of galaxies for which a spectroscopic observation is attempted) that varies with redshift and an observation completeness (fraction of galaxies attempted for which a spectroscopic observation is successful) that depends on redshift, colour and magnitude. Both of these effects will affect the reproduction of the true environmental density in ways that vary with the above variables and must be accounted for. Determining the dependence of selection completeness on redshift is tricky but can be estimated by smoothing the observed number density of galaxies as a function of redshift then normalising according to an assumed dependence of the comoving number density of galaxies on redshift (C05). Alternatively, C05 suggest making an empirical correction to the densities using the median densities in discrete redshift bins and we follow this recipe in section 4.2.2.

### 2.2.2 Measures of Environment Density

We briefly describe three measurements of local density: the Voronoi Volume method, the counts in an aperture method and the $n^{th}$ nearest neighbour method. We outline their advantages and disadvantages based on the thorough comparisons of C05.

**Voronoi Volume** To calculate the environment density of a particular galaxy, the Voronoi Volume method includes the calculation of the volume $V$ of the polyhedron around that galaxy such that every point within the polyhedron is closer to that galaxy than any other. Thus the faces of the polyhedron are defined by the planes perpendicularly bisecting the vectors connecting the galaxy with all of its neighbours. C05 find that $V$ is not robust to the redshift space distortions. Further, the Voronoi volume method is severely affected by edge effects: there is a bias of large volumes being pushed to even larger volumes. For these reasons, we reject the Voronoi Volume method.

**Counts in an Aperture** This method involves counting the number $C$ of galaxies in a fixed volume. C05 report that this method can be made robust against edge effects (discussed in more detail in section 4.2.3 below) due to the fixed size of the aperture: by excluding galaxies within the aperture radius of the edge of the survey, the counts in an aperture method is devoid of any edge-induced biases. This method has traditionally been used when spectroscopic redshifts were not available for every galaxy. Use of photometric redshifts is likely to result in the inclusion of foreground/background interlopers and give a noisy estimate of the density. However, even when only spectroscopic sources are used, this method would only be suitable for surveys covering large areas on the sky. For example, even if the fixed volume is a comoving sphere of $1h^{-1}$ Mpc (some studies often use bigger volumes - e.g. Hogg et al. (2003) include an analysis using $8h^{-1}$ Mpc spheres in the SDSS), only 81% of these spherical apertures in a $30' \times 30'$ field (20 $h^{-1}$ comoving Mpc on a side, the approximate width of the Extended Groth Strip, EGS) would fit within the surveyed field (C05). Also, using this method effectively smooths the data on some adopted scale (the scale of the counting volume) and thus loses sensitivity on smaller and larger scales. C05 also report that the measure $C$ saturates at low densities, limiting its usefulness. Given these disadvantages, we choose not to use the counts in an aperture method.

**The $n^{th}$ Nearest Neighbour Estimate** An alternative to counting the number of galaxies in a fixed volume is to measure the volume out to a fixed number of galaxies. First used by Dressler (1980), this density measure measures the distance ($D_n$) from the galaxy whose environment density is to be measured to its $n^{th}$ nearest, spectroscopically observed neighbour. This distance can be measured in 3-d yielding a 3-dimensional density $\rho_n$:

$$\rho_n = \frac{3n}{4\pi D_n^3} \tag{2.15}$$

Alternatively, one can make a cut in velocity (this is an indirect cut in redshift) to exclude foreground and background objects and then measure $D_n$ as the *projected* distance to the $n^{th}$ nearest neighbour. This is then used to give a 2-dimensional surface density $\Sigma_n$:

$$\Sigma_n = \frac{n}{\pi D_n^2} \tag{2.16}$$

C05 used a DEEP2-selected sample of 12,636 galaxies drawn from a $120' \times 60'$ mock catalogue to test the the effectiveness of $\rho_n$ and $\Sigma_n$ in tracing environment density. They compared the $\rho_n$ and $\Sigma_n$, measured using the redshift-space galaxy positions, to $\rho_n$ measured using the real-space positions (their figure is shown in figure 2.4). The latter can be taken to be the true local environment density. They found that, in the higher density regions where redshift-space distortions are greatest, $\Sigma_n$ was significantly more effective at tracing the true environment than $\rho_n$. This is shown by the much higher value of the Spearman ranked correlation coefficient for $\Sigma_n$ than for $\rho_n$. Although $\Sigma_n$ also suffers from peculiar velocities and shows great scatter in this plot, it wins by virtue of $\rho_n$ failing badly to reproduce the real density in this regime as shown by the relatively flat distribution in the top left panel. $\rho_n$ was slightly more effective in the lower density regions but overall $\Sigma_n$ traced the true environment more effectively. C05 find that $\rho_n$ is strongly correlated with $V$ and the two methods share this disadvantage of not being robust to the redshift space distortion since they both directly use the line-of-sight information.

## 2.3 Measuring the Luminosity Function

Another tool that we will use in this thesis, particularly in chapter 3 is the luminosity function (LF). We therefore give a description of the LF and a method for constructing it here.

### 2.3.1 What is a Luminosity Function?

The LF is a function giving the relative numbers of galaxies of different luminosities in a given sample. More specifically, $\phi(L)\mathrm{d}L$ is the number density of galaxies in the sample with luminosities between $L$ and $L + \mathrm{d}L$. Schechter (1976) proposed the following form for $\phi(L)$:

$$\phi(L)\mathrm{d}L = \phi^*\left(\frac{L}{L^*}\right)^{\alpha} e^{-L/L^*}\frac{\mathrm{d}L}{L^*} \tag{2.17}$$

where $\alpha$ and $L^*$ are the two free parameters of the function when it is fitted to the data. $\alpha$ is the slope of the faint end of the LF and $L^*$ is a characteristic luminosity above which

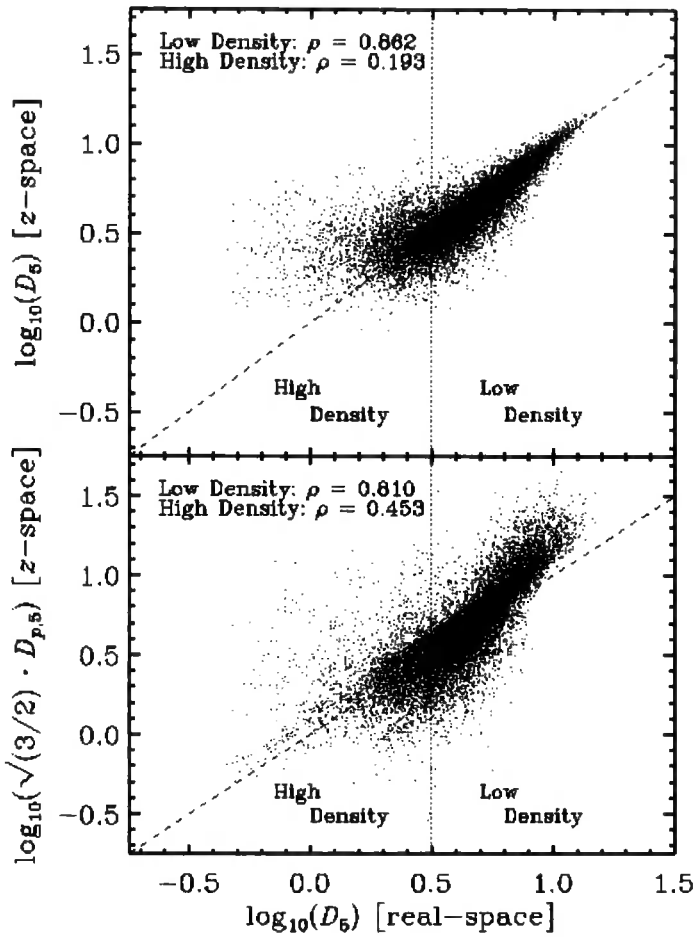


Figure 2.4: Environment density as measured from redshift space versus environment density as measured from real space. All measurements are computed in a $120' \times 60'$ DEEP2-selected mock catalogue. Top panel: the ordinate axis is the logarithm of the 3-d measure ($\equiv \rho_n$). Bottom panel: the ordinate axis is the logarithm of the 2-d measure ($\equiv \Sigma_n$) scaled by $\sqrt{3/2}$ to compare to the 3-d measure. In calculating the projected (2-d) measure, only galaxies within $\pm 1000 \mathrm{kms}^{-1}$ were considered. In both panels the abscissa is the logarithm of the 3-d measure in real space which is taken to be the true density. The values of $\rho$ in each panel are the Spearman ranked correlation coefficients. Figure from Cooper et al. (2005).

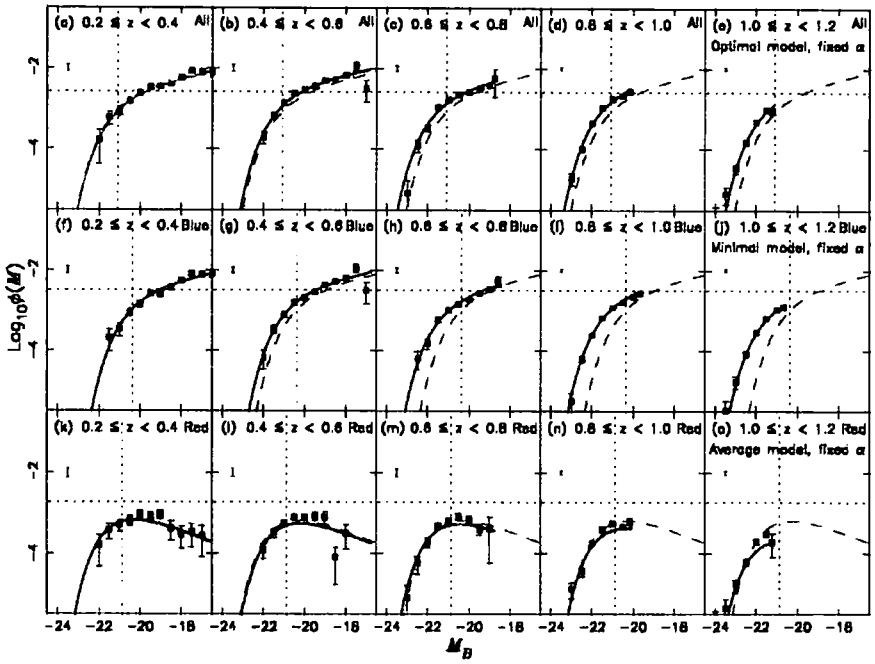


Figure 2.5: An example of luminosity functions with fitted Schechter functions. This figure shows the luminosity functions for galaxies in the DEEP2 redshift survey broken down into redshift bins and with red and blue galaxies shown separately. The points were calculated using the $1/V_{\rm max}$ method (see text for details) with fixed values of $\alpha$ of $\alpha$=-1.3 (All), $\alpha$=-1.3 (Blue) and $\alpha$=-0.5 (Red). The dotted lines show the values of $L^*$ and $\phi^*$ (a normalisation constant) evaluated in the low redshift interval for each colour. The dashed lines show the LF evaluated in the low redshift interval for each colour. The error bars in the top left of each panel show the errors due to cosmic variance. (This plot shows that red and blue LFs evolved differently: blue counts at a fixed absolute magnitude evolve strongly with redshift whilst red counts stay approximately constant). Figure from Willmer et al. (2006).

the LF drops rapidly with increasing luminosity. The units of $\phi$ would usually be the number of galaxies per unit volume per log($L$) bin. Examples of luminosity functions, fitted with functions of this form, are shown in figure 2.5.

There are two methods commonly used to construct LFs. The first is the stepwise maximum likelihood (SWML) method (e.g. Efstathiou et al. 1988, Loveday 2004). The likelihood to be maximised is the product of the probabilities $p$ that a galaxy at a partic-

ular distance has a luminosity in the range $L, L + \delta L$. The second method is the more intuitive $1/V_{\rm max}$ method. Since this is the method we use in chapters 3 and 5, we describe it in detail here.

### 2.3.2 The $1/V_{\rm max}$ method

If the sample for which the LF is to be constructed is volume-limited then the process is much simpler. In this case, one can simply count the number of galaxies in the volume. However, data does not "naturally" come in such a convenient form. The sample will more often be magnitude-limited. This means that only the brightest galaxies can be seen at greater distances meaning that the same volume has not been sampled for galaxies of all magnitudes. In the case of a magnitude-limited sample, simply counting the galaxies would not yield the true LF because the number of bright galaxies would be artificially increased relative to the number of faint ones. The way around this problem is to use the $1/V_{\rm max}$ method (e.g. Schmidt 1968). In this method, instead of counting galaxies and dividing by one volume, one measures the sum of each galaxy's $1/V_{\rm max}$ . Thus $V_{max}$ is effectively a weighting calculated for each individual galaxy. $V_{max}$ is the maximum volume of the Universe, in any part of which the galaxy could have been located and still have been included in the survey. Thus the $1/V_{\rm max}$ method gives a way to convert a magnitude-limited sample to a volume-limited one for the purposes of constructing an LF. Sometimes the only limit on the volume will be an upper limit defined by the flux limit of the survey. However, a bright flux limit would correspond to a lower limit on the volume. Sometimes other factors can complicate the calculation of $V_{max}$ such as the flux limit varying with some other galaxy property such as its colour or the wavelength of a particular feature of the spectrum if the survey is a spectroscopic one. The ratio $V/V_{max}$ is a measure of a galaxy's position within the observable volume. Thus the distribution of this ratio is a measure of the sample's uniformity: a uniform sample will have this ratio evenly distributed between 0 and 1 with a mean value of 0.5. When using the $1/V_{\rm max}$ method with constant $\log(L)$ bin width $\Delta L$, the value of $\phi$ in each bin would be calculated as:

$$\phi = \frac{1}{\Delta L} \sum_{i=1}^{N} \frac{1}{V_{max,i}} \tag{2.18}$$

where $N$ is the number of galaxies in the bin. The $1/V_{\rm max}$ method is the most commonly used method for constructing LFs and is the one we use in this thesis; we use it explicitly

in chapters 5 and 3.

## 2.4 Galaxy Surveys: Suitability for a Purpose

Finally in this chapter we describe a selection of galaxy surveys that are relevant to this thesis. We also discuss the properties of these surveys that make them more or less suitable for different measurements. Survey designers must always weigh up the survey's area on the sky, depth (i.e. what will be the minimum flux reached and at what wavelengths?) and cost in terms of telescope time. The primary goals of the survey will weight different priorities differently as we describe below.

There are some decisions that will affect the usefulness of a spectroscopic survey regardless of its primary goals and we describe three of them here. The first of these is cosmic variance. Since the largest structures in the Universe have grown out of the *random* primordial density fluctuations, the Universe is not homogeneous on the scales observed by an individual survey [3]. In other words, if an area on the sky towards an overdense region is surveyed, the results could be different (depending on what is measured) to those from surveying an underdense region of the sky. The errors from cosmic variance can be folded in to the error analysis (e.g. Somerville et al. 2004) but the best way to minimise these errors is to increase the area of the survey.

The second issue common to most surveys is completeness. In the case of a spectroscopic survey, this is the fraction of objects known to be in the field that are targeted for the spectroscopy (as defined previously, this is the *selection* completeness). The results of the survey will have to be adjusted to account for the survey's incompleteness and this can sometimes introduce very large uncertainties. As we have seen from the discussion of luminosity functions above, the vast majority of galaxies are relatively faint and therefore the completeness increases considerably as the depth of the survey is increased. Therefore, the more important the galaxy counts are (for example when constructing luminosity functions), the more important it is to increase the depth of the survey. For surveys measuring other properties such as the light from the brightest galaxies, this is less of an issue. However, the survey completeness can also have a big impact on studies of environment. This is because the completeness may be a strong function of environment thus heavily biasing the sample.

[3] This does not contradict the cosmological principle since that only applies to the largest scales of the Universe

Thirdly, the choice of filter that will limit the survey's depth can have quite subtle selection effects on the data, depending on the target redshift of the survey. As an example of this, we consider the selection of the DEEP2 survey and its effect on the colours of the final galaxy sample. This survey was selected in $R$ with a nominal limiting magnitude of $R_{AB} = 24.1$ although this did vary slightly between pointings. The central wavelength of this filter is $\sim$ 6400Å (rest-frame red light). Therefore, if the survey were targeted at $z = 0$, the faintest galaxies observed would have relatively strong emission at this wavelength: they would be red. However, the survey is carried out over the redshift range $0.2 \leq z < 1.4$ (at least in the EGS). At progressively higher redshifts, the spectra will be redshifted more and the $R$ filter will correspond to progressively bluer parts of the spectrum. Therefore the faintest galaxies observed will be bluer and the faintest red galaxies will be brighter than the faintest red galaxies observed at $z$=0. This effect is shown in figure 2.6 which is from Willmer et al. (2006). This figure shows the rest-frame colour-magnitude ($U - B$ versus $B$) plots in six different redshift bins of the galaxies observed in the DEEP2 survey. The line corresponding to the magnitude limit is a slanted line on this plot with its angle relative to the plot axes changing with redshift. In the bins closest to where $z \sim 0.4$ (where rest-frame light in the $B$ band is redshifted into the $R$ band), the line is nearly vertical since the faintest galaxies at this redshift could be any colour. This figure shows that one of the effects of selecting the survey in $R$ is to miss red galaxies at high redshift. This has obvious implications for measuring any properties where these galaxies would make a sizable contribution.

The area of the survey is most important when measuring galaxy environments. As discussed in section 2.2.1, many environment measures are susceptible to edge effects. The most common way of minimising these effects is to exclude any galaxies within a certain distance of the edge of the survey when it comes to measuring their environments (they are, of course, included when measuring the environments of the galaxies further from the survey edges). Therefore the size and shape of the area of the survey is a more important consideration for environment studies than it is for most other studies.

When measuring star formation rates and histories, the main consideration is at which wavelength to select the galaxies for observation. The observer's adage, *near-infrared light traces mass, while blue light traces star formation* (e.g. Binney and Tremaine 2008), bears closer inspection. We have already seen that the hot, young stars that dominate the H II regions in the spiral arms of starforming galaxies emit predominantly in the UV and the visible blue. Near-infrared emission (1-5$\mu$m) is mostly due to giant, old

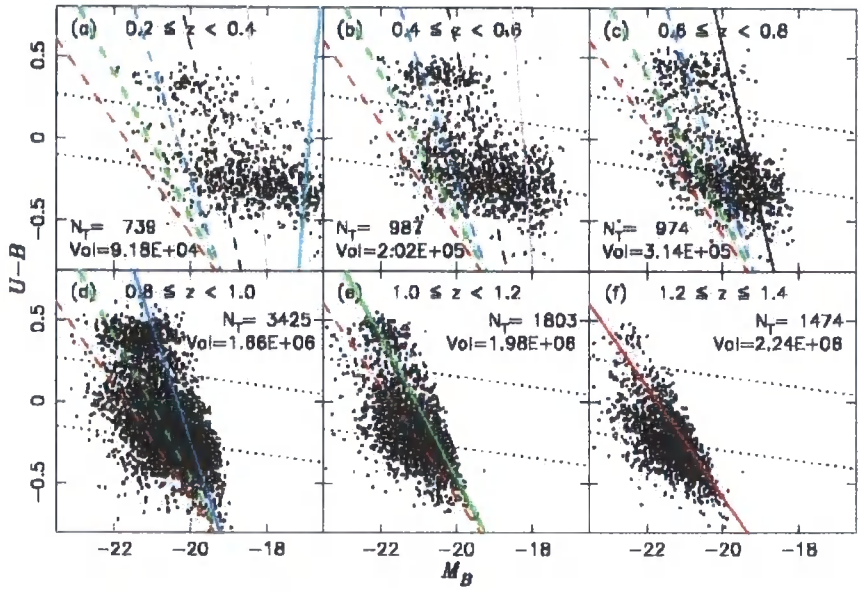


Figure 2.6: Rest-frame colour-magnitude diagrams in redshift bins from the DEEP2 survey. The solid line in each panel corresponds to the fixed apparent magnitude limit of $R_{Vega}$=23.88 ($R_{AB} \sim 23.94$) calculated at the upper limit of each redshift bin. The dashed lines represent these solid lines in other panels and the upper and lower dotted lines show the division between red and blue galaxies and between blue and very blue galaxies respectively. The numbers in each panel show the number of galaxies plotted in that panel and the co-moving volumes are in $\mathrm{Mpc}^3$ for a ($H_0$, $\Omega_M$, $\Omega_\lambda$)=(70, 0.3, 0.7) cosmology. Figure from Willmer et al. (2006).

stars. These stars are what become of the main-sequence dwarf stars that dominate the galaxy's mass.

Table 2.1 summarises the visible, radio and X-ray surveys used, either directly or indirectly, in this thesis. The table compares, among other things, the areas, depths and redshifts of the surveys. More details of individual surveys are given in the later chapters.

Table 2.1: Summary of spectroscopic surveys carried out by other authors (and the ROLES survey) that are relevant to this thesis. The DEEP2 and Chandra information refer only to the EGS. In the Chandra information, where a number is followed by another number in parenthesis, the first refers to the soft band and the one in parenthesis to the hard band. The Chandra limit is measured in erg $s^{-1}$ $cm^{-2}$. GDDS information refers to that part of the survey used to calculate star formation rate densities in Juneau et al. (2005). The FIRST information refers to the data from the April and May 1993 run. The SDSS information relates to the spectroscopic part of data release (DR) 6. * the main galaxy sample

| Name | Type | Wavelength/Energy | $z$ | Area/sq deg. | Limit | Exp time /ks | Resolution | No. of targets |
|---|---|---|---|---|---|---|---|---|
| DEEP2 | Visible | 6400-9100Å | 0.2-1.4 | 0.5 | $R_{AB}$=24.1 | 3.6 | 1.4Å | 17,600 |
| GDDS | Visible | 5500-9200Å | 0.8-2.0 | 0.15 | $K_{Vega}$=20.6 | 50-70 | 3.4Å | 207 |
| SDSS | Visible | 3800-9200Å | $\lesssim$0.2* | 7425 | $r_{Petrosian}$=17.77 | $\geq$2.7 | 1800-2200 | 790,860 |
| ROLES | Visible | 7000-8000Å | $\sim$1 | 0.015 | $K_{AB}$=24.0 | $\sim$17 | 11.4Å | 64 |
| AEGIS20 | Radio | 1.4GHz | $\sim$1 | 0.64 | 100 $\mu$Jy beam$^{-1}$ | 40 | 3.8″ | 1238 |
| FIRST | Radio | 1.4GHz | $\sim$0.1 | 300 | 1mJy | $\sim$8 | 5″ | 28,000 |
| NVSS | Radio | 1.4GHz | 0.001-3 | $\sim$34,000 | 2.5mJy | 0.023 | 45″ | 2,000,000 |
| Chandra | X-Ray | 0.5-2 (2-10) keV | $\sim$1 | 0.67 | 5.3(38) $\times$ $10^{-17}$ | 200 | 0.5-4.0(0.5-6.0)″ | 1325 |

# Chapter 3

# *The Evolution of the Radio Luminosity Function and the Colours of Radio Sources at $z \sim 1$*

## 3.1 Introduction

Recent models of galaxy formation have suggested that feedback from the growth of supermassive black holes plays a fundamental role in regulating the formation of galaxies and in shaping the galaxy luminosity function (Bower et al., 2006; Croton et al., 2006). These models make a crucial distinction between an optically bright mode of black hole accretion (the 'QSO mode') and an optically faint mode (the 'radio mode') in which the accretion energy is channelled into a powerful jet. The distinction between these modes has strong parallels in the behaviour of galactic black holes (Körding et al., 2006; Hardcastle et al., 2007) and can be explained in terms of dependence of the accretion disk structure on the accretion rate (Meier, 2001; Nemmen et al., 2007). However, the kinetic energy of the jet cannot be measured directly. In nearby clusters it can be estimated from the dimensions of the cavity seen in X-ray images (Bîrzan et al., 2004) but in general it must be inferred from the small fraction of the kinetic energy that is converted into radio synchrotron emission (Bîrzan et al. 2004; see McNamara and Nulsen 2007 for a recent review). In bright radio sources, the radio luminosity is typically estimated to be less than 1 per cent of the jet power.

Given the prominent role of these jets in recent galaxy-formation models, it is clearly important to determine the radio luminosity function (RLF), its environmental dependence and its evolution. Many galaxy properties have been found to change significantly with redshift: the star-formation-rate (SFR) density increases (Madau et al., 1996; Juneau

et al., 2005), as does the density of ultraluminous IR galaxies (ULIRGs; Blain 1999), X-ray-selected AGN (Hasinger, 2005) and luminous red galaxies (LRGs; Sadler et al. 2007, hereafter S07). A basic observational issue is to determine if these changes are matched by increased activity in the radio galaxy population.

In this chapter we investigate the evolution of the faint ($L_{1.4\,\mathrm{GHz}} \sim 10^{24}\,\mathrm{W\,Hz^{-1}}$) radio source population. At much brighter luminosities, it is already well established that the RLF evolves strongly. The most powerful radio galaxies are therefore found at high redshifts (Longair, 1966; Dunlop and Peacock, 1990; Jackson and Wall, 1999; Willott et al., 2001; Cowie et al., 2004). Such sources are, however, rare and the key issue is to determine the rate of evolution of the fainter – more numerous – radio galaxy population. At the fainter luminosities we target, however, we expect to find significant contributions from both 'radio mode' AGN and star forming galaxies (where the radio emission originates in supernova remnants, Condon 1992). In order to interpret the evolution of the radio luminosity function, it is crucial that we separate these two populations.

In the local Universe, Best et al. 2005 (hereafter B05) has shown that it is possible to effectively separate the two populations on the basis of their spectral shape. The bimodality of the galaxy population is evident in many indicators, such as the 4000Å break $D4000$ (as used by B05), colour and emission-line strength (e.g. Kauffmann et al. 2003a), and reflects two distinct populations of galaxies: a sequence of bluer galaxies that are still forming stars and a redder sequence dominated (at least at low redshift) by galaxies in which star formation has ceased. Relatively few galaxies lie between the two sequences: these may be systems in which star formation has recently been quenched, or systems with an unusually high degree of internal reddening.

At low redshift, the population of radio-detected galaxies can thus be cleanly divided into two classes following the bimodality of the overall galaxy population. In the blue-sequence systems, the radio emission is likely to be powered by star formation (see B05 for a detailed justification), while in the red-sequence systems there is insufficient star formation to account for the observed radio luminosity, and the radio emission must be powered by a central 'radio-mode' AGN. Both sequences place important constraints on galaxy formation models: in star forming galaxies the radio emission is not affected by dust, making it a robust probe of the SFR density (Condon 1992; Haarsma et al. 2000; Barger et al. 2007). In the AGN-powered population, the observations constrain the abundance and strength of 'radio-mode' feedback.

The aim of this paper is to trace the evolution of the radio emission from both galaxy

sequences as a function of redshift by applying the colour separation technique to radio sources detected in the All-wavelength Extended Groth Strip International Survey at 20 centimetres (AEGIS20, Ivison et al. 2007). For a statistical sample of these sources we obtain colours and redshifts from the DEEP2 spectroscopic redshift survey (Davis et al., 2005) allowing us to determine the source radio flux and assign a likely power-source to each galaxy. These two surveys have the depth and sky coverage required to trace the relative evolution of the SFG and 'radio-mode' AGN populations out to $z \sim 1$. We compare these high-redshift RLFs with the local RLFs derived by B05 and Mauch and Sadler (2007) (hereafter M07) using similar techniques.

This chapter is structured as follows. In §3.2, we briefly outline the survey data and the catalogue matching procedure. In §3.3, we describe the methodology for separating the catalogue into two classes of radio source and test the success of the technique. The results are presented in §3.4 starting with the combined radio source luminosity function and then an analysis of the colour distributions of matched sources. §3.5 contains our discussion and §3.6 our conclusions. We use magnitudes in the AB system throughout and assume a flat cosmology with $h = 0.7$ and $\Omega_\Lambda = 0.7$.

## 3.2 The AEGIS Survey

### 3.2.1 The optical, radio and X-ray surveys

The optical and radio data exploited here are part of the All-wavelength Extended Groth Strip International Survey (AEGIS). This survey also comprises optical imaging, X-ray, UV and near-, mid- and far-infrared (IR) datasets as described in detail by Davis et al. (2007). In this paper we draw on the radio, optical (both imaging and spectroscopic) and X-ray data. We leave analysis using the other data sets to future investigations.

The optical data comprise the fraction of the DEEP2 survey carried out in the Extended Groth Strip (EGS) using the DEep Imaging Multi Object Spectrograph (DEIMOS – Faber et al. 2003) spectrograph on the Keck-II telescope. The DEEP2 survey identifies galaxies out to redshift $z \sim 1.4$ and covers an area of $\sim 0.5\,\square^\circ$ in the EGS. The photometric redshift selection is described in Davis et al. (2007). We present a summary of the key points here. Imaging of the EGS was accomplished with the Canada-France-Hawaii Telescope's CFHT12K camera in the $B$, $R$ and $I$ filters and used to select targets for spectroscopic observation. To be an eligible target for spectroscopy, a source had to lie in the magnitude range $18.5 \leq R \leq 24.1$ and pass criteria concerning surface brightness

and its probability of being a galaxy. Each galaxy was given a weight, as described in Willmer et al. (2006), that was adjusted to ensure a good sampling over the range of luminosities and that approximately equal numbers of galaxies were selected above and below $z = 0.75$. The weight was then used in randomly selecting galaxies to satisfy DEIMOS slit-mask constraints. The probability of selection as a function of redshift is known to 1 per cent accuracy. The median probabilities of selection for each potential target were >70, 54 and 73 per cent in the redshift bins $z < 0.1$, $0.5 < z < 0.6$ and $z > 0.8$, respectively. The survey database contains a sample of 15,349 galaxies with reliable (redshift quality 3 or higher - > 95 per cent probability of being correct) spectroscopic redshifts and $K$-corrected $U$, $B$ and $R$ magnitudes. The database contains additional spectral properties such as line strengths and kinematics. Unfortunately, the $D4000$ spectra break index cannot be reliably measured from the data and so this is not available in the database. The problem is that different quantum efficiencies in the four CCD chip sets in DEIMOS is a major cause of systematic errors in $D4000$. Even after attempting to correct for this, there remained a significant wavelength dependence ($\sim \lambda^{0.6}$) of a throughput correction which is crucial in studying the evolution of $D4000$ with redshift (Renbin Yan, private communication).

The radio data are taken from the AEGIS20 survey (Ivison et al., 2007). The survey was carried out at 1.4 GHz using the National Radio Astronomy Observatory's Very Large Array (VLA) in its B configuration, yielding a near-circular synthesised beam with 3.8 arcsec FWHM. The $5\sigma$ limiting flux density in the deepest 150 arcmin$^2$ was $\sim$50 $\mu$Jy and the full area of the survey was 0.64□° to a depth of around 100 $\mu$Jy. The full AEGIS20 radio sample comprises 1,238 sources.

AEGIS20 and DEEP2 only partially overlap, due largely to the presence of the 23-Jy radio source, 3C 295, just to the south east of EGS. The overlapping area of 0.40 □° contains 10,189 DEEP2 sources (of which 5,007 have a redshift below 0.7 and 5,182 have a redshift above 0.7) and 758 radio sources. In figure 3.1 we show the sky-projection of the optical photometric and spectroscopic surveys, the radio survey and the X-ray survey.

In addition to the radio and optical data in these we draw on the deep CHANDRA X-ray catalogue presented in Laird et al. (2008). This survey covers $\sim$ 0.67□° and is almost exactly coincident with the DEEP2 spectroscopic survey on the sky. The survey contains 1325 sources of which 900 are in the overlap with the AEGIS20 radio survey. The survey's flux limits are $5.3 \times 10^{-17}$ erg cm$^{-2}$ s$^{-1}$ in the soft (0.5-2 keV) band and

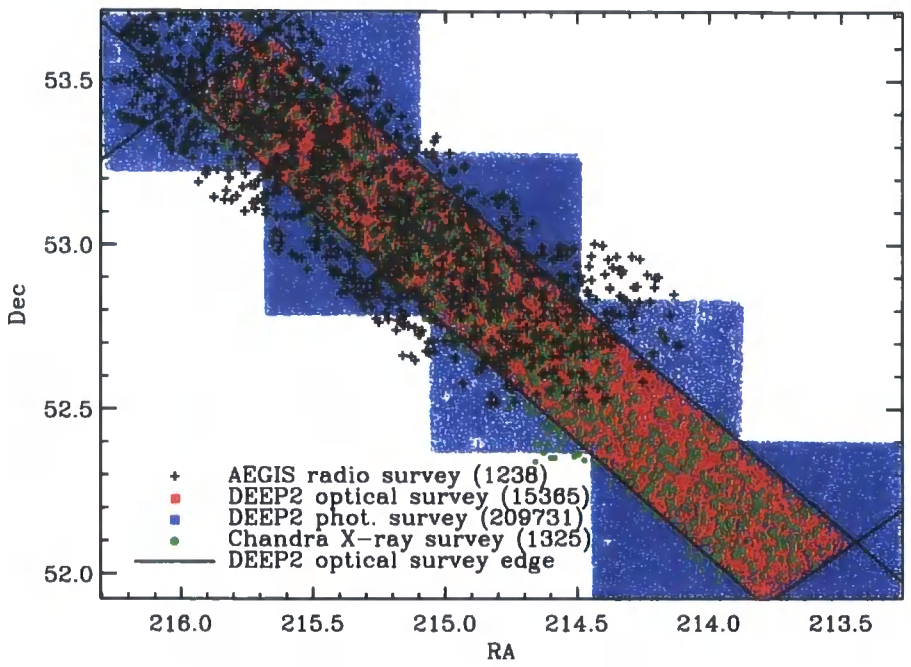


Figure 3.1: The sky-projection of the AEGIS surveys used in this chapter: the DEEP2 (optical) spectroscopic and photometric surveys, the radio survey and the X-ray chapter. The numbers in parenthesis show how many sources are in each survey. The edges to the DEEP2 spectroscopic survey are derived in section 4.2.3.

$3.8 \times 10^{-16}$ erg cm$^{-2}$ s$^{-1}$ in the hard (2-10 keV) band.

### 3.2.2 Matching the optical and radio surveys

Because the radio source and optical source need not be entirely coincident (the radio emission may come from a large-scale jet or off centred star forming region), some care is required in order to match the catalogues. We choose a matching radius (in $''$) around each radio source within which we would accept any optical source as a genuine match. We therefore need to choose this matching radius to be as large possible without introducing a statistically significant number of false matches into the sample. This problem is extensively discussed in B05 and S07. We assessed the level of contamination by randomly shifting the optical positions by a few arcmin and cross-correlating the false catalogue with the radio dataset. Since all matches from the false catalogue are obviously false, we were thus able to assess the level of contamination as a function of matching radius by comparing the number of matches from the real and false catalogues as a func-

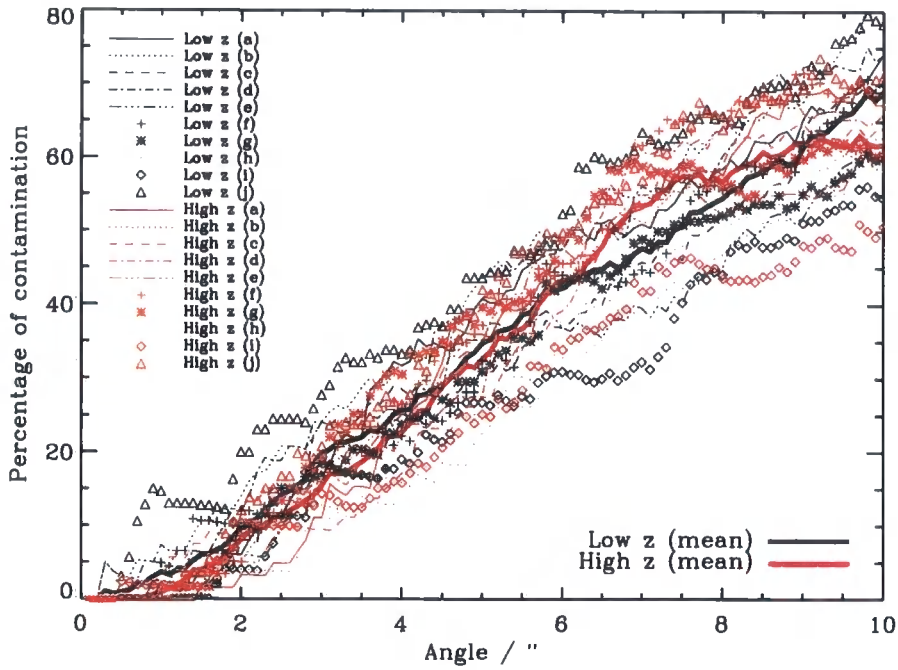


Figure 3.2: The contamination (fraction of false matches) of the radio sample versus matching radius (angle/″) as estimated from ten false catalogues (see text for details). Also plotted are the means at high and low redshift which differ little at any given matching radius. Low redshift refers to the $0.2 \leq z < 0.7$ epoch whilst high redshift refers to the $0.7 \leq z < 1.4$ epoch.

tion of matching radius. Since this is a noisy estimate, we did it 10 times and took an average. Figure 3.2 shows the level of contamination as a function of matching radius for each of the ten false catalogues (each of which was shifted by different amounts) and the averages we took in each of our redshift bins. Reducing the matching radius reduces both the number of true and false matches and increasing the matching radius increases both of these numbers. The *fraction* of matches that are false also increases with the matching radius. However, the rate of increase in this fraction with matching radius increases slightly above a matching radius of $\sim 2''$as shown in figure 3.2. We decided to pick a matching radius such that the expected fraction of false matches was 10%. This radius was 2.2″ in both our low and high redshift epochs.

We matched 141 (19%) of the radio sources in the overlap area with a DEEP2 source. However, when we combine our observations with the DEEP2 spectroscopic weighting system our completeness is significantly higher than this. This weighting system

accounts for incompleteness as a function of colour, magnitude and redshift and is described in Willmer et al. 2006. In this system (also described in more detail in section 4.3.2), each galaxy is weighted to account for galaxies of similar colour and magnitude that were not observed. Thus, each of these weights is $\geq 1$ and we can compare the sum of these weights to the total number of galaxies to measure the completeness. Within the overlap region of the radio and spectroscopic optical surveys, there are 390 (51%) radio sources that are matched to sources in the DEEP2 photometric catalogue. The total of the weights for our 141 sources is 345 giving us 88% completeness of the sources observed. This naturally leads one to ask what are the radio sources that we don't match to any optical sources? We assume that they are either matched to optical sources that are at a higher redshift than our sample or that they're matched to optical sources that are too faint for our sample. In the latter case, it is possible that we will be missing radio sources that would pass all criteria to get into the sample except that their optical counterpart is too faint. This would be a limitation of our method since the $1/V_{\rm max}$ method we employ below to construct the radio luminosity functions would not correct for this.

A consequence of the relatively small adopted limit for angular separation means that we may have failed to find matches for FR II galaxies (Bicknell, 1995) with extended radio emission from jets or lobes. We therefore visually searched for pairs of radio sources located either side of a DEEP2 galaxy. We found no pairs that could be matched plausibly in this way.

Within EGS there are 3,069 DEEP2 galaxies in areas common to the DEEP2, AEGIS20 and CHANDRA-X surveys with a redshift quality of 3 or higher and a restframe $B$ magnitude brighter than the completeness limit of -20.5 (the $B$ magnitude was chosen because it corresponds roughly to the observed $r$ magnitude in which the DEEP2 survey was selected). Of these, 125 are radio sources, 145 are X-ray sources and 25 of these are sources of both radio and X-ray radiation: 11 AGN and 14 SFGs, according to our classification.

### 3.2.3 Local comparison sample

B05 derived the RLFs for AGN and SFGs in the local Universe ($z_{\rm median} \sim 0.1$) by matching the main spectroscopic galaxy sample from the Sloan Digital Sky Survey (SDSS) with two radio surveys: the NRAO VLA Sky Survey (NVSS, Condon et al. 1998) and Faint Images of the Radio Sky at Twenty centimetres (FIRST, Becker et al. 1995). The NVSS and FIRST radio sources complement each other very well with very different beam sizes

and depths. NVSS has a beam size of 45″ and reaches a depth of 2.5mJy whilst FIRST has a beam size of ∼5″ and reaches a depth of 1mJy. The properties of both surveys are summarised in table 2.1 in chapter 2.

## 3.3 Separating the Radio Source Populations

### 3.3.1 Colour distribution

As we have already described, we expect both star formation powered and AGN powered radio sources to make significant contributions to the overall radio population in our sample. In the local Universe the radio source population falls into two distinct sequences that can be used as the basis of a classification system. We therefore begin by examining the colour distribution of the AEGIS radio sources.

Figure 3.3 (left panel) shows the distribution in colour-magnitude space of the radio sources compared to the general field population in the DEEP2 survey. This panel shows the radio sources to be redder and slightly brighter in the optical than the DEEP2 field population. We again mention that we are using restframe $(U - R)$ rather than $D4000$ since the latter is not available. Since radio galaxies are preferentially brighter than the general field population galaxies in DEEP2, comparing the colour distributions of the radio galaxies to that of their parent population requires us to limit our analysis to those field galaxies brighter than some absolute magnitude limit, $R = -21.5$ in this case.

Figure 3.3 shows that the radio sources do not have the same colour distribution as the general field population of DEEP2 galaxies. For the radio sources, the colour bimodality seen in the general field population is less prominent. The radio sample shows a far more uniform distribution redward of $(U - R) = 1.8$. In probing higher redshifts, it seems that a significant fraction of the radio sources have intermediate colours between the red sequence and blue galaxies of the general galaxy population. Furthermore, the blue sequence of radio galaxies (insofar as one exists) is not as blue as the blue sequence of the general field galaxies but occupies the space between the red and blue peaks of the general field population and forms an intermediate colour population (ICP). It is noticeable that these ICP radio galaxies in AEGIS have a similar spread in colours to the blue-sequence radio galaxies in the local Universe.

The equivalent plot from the local Universe using SDSS data is shown in the right hand panel of figure 3.3. In this panel, the radio data are from B05 and the general field population is a random sample of 10,000 galaxies satisfying our $R$ limit criterion from

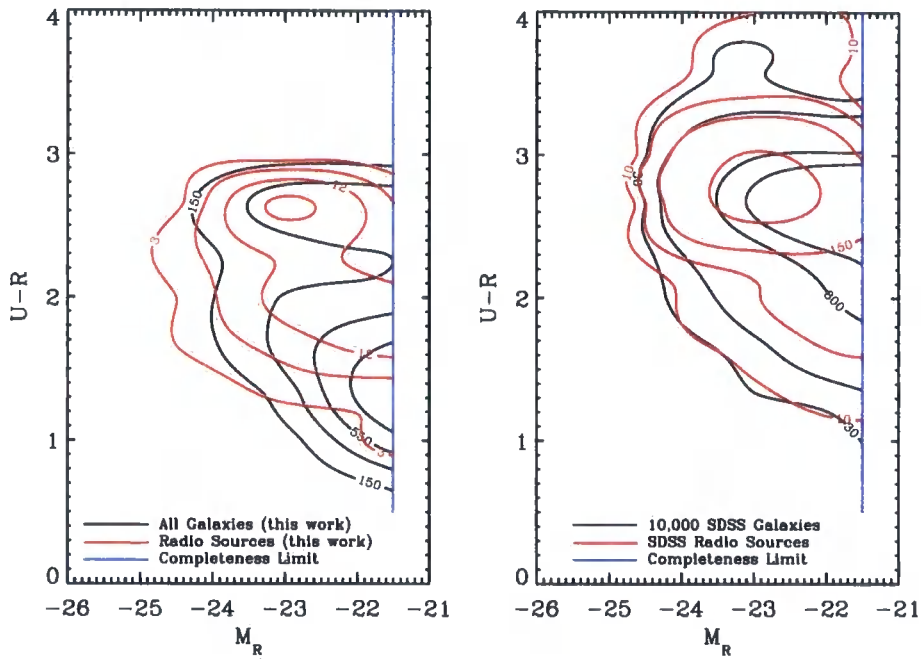


Figure 3.3: Left panel: the colour-magnitude diagram of DEEP2 galaxies in the form of a contour map (black lines). Over-plotted are the contours of the DEEP2 galaxies that we determined to be radio sources (red lines). The blue vertical line denotes the approximate limit of $R = -21.5$ that we use to compare the colours of the radio sources to those of the general field galaxy population from DEEP2. Right panel: the equivalent plot from the SDSS. Here, the background population is a random sample of 10,000 galaxies down to the same $R$ band limit of -21.5 .

the SDSS (Ivan Baldry, private communication). The completeness limit of $R = -21.5$ is shown in both panels. If we divide the sources into the blue and red sequences an interesting pattern emerges. Although the red sequence is over represented compared to the field, the colour-magnitude distribution for the remaining radio sources is similar to the general field. The situation is in stark contrast to the equivalent plot for AEGIS sources where the radio sources appear to be redder than the field and have a sizable ICP that is not seen in the field population.

We can quantify the differences in these distributions by projecting the sample to make a histogram of galaxy colours. For a valid comparison between the colours of the radio and general field population in AEGIS, we must allow for the fact that the survey is selected on observed $r$ band magnitude, which roughly corresponds to a restframe $u$ band. Therefore we will be incomplete in the faint red corner of each panel in figure 3.3 above a certain redshift for a given $R$ band limit. For the completeness limit of $R = -21.5$, we would only be complete out to a redshift of $\sim 0.9$. We therefore weight the colours with the spectroscopic completeness weights and our values of $V_{\rm max}$ described in section 3.4 in this test. Figure 3.4 shows these weighted U-R distributions for the radio and general field populations from DEEP2 (top panel) and from the SDSS (bottom panel). In each panel, the histograms have been normalised to have the same areas underneath. Comparing the colours of our radio matches to the general field population in DEEP2, it is now abundantly clear that they are different with a very prominent radio population between the red sequence and blue galaxies of the general field. Applying the $\chi^2$ test to the two colour distributions in AEGIS yields a value of $\chi^2$ such that the probability of such is too small to calculate. Applying the $\chi^2$ test to the radio population from DEEP2 to that from the SDSS (after renormalising the SDSS distribution so as to have the same area underneath as the the DEEP2 one) yields a similarly improbably large value of $\chi^2$.

### 3.3.2 Separating the two populations

Motivated by the bimodality of the galaxy population, B05 separated the two radio source populations by testing each galaxy to see if the system's star formation rate could account for the observed radio emission. If the star formation rate were sufficiently high, the system was classified as a star formation-powered and the galaxy would be termed a star forming galaxy (SFG). If the star formation rate was insufficient the source was classified as AGN powered. B05 were able to base their star formation rates on measured values of the $D4000$ index (this is effectively a narrow-band colour, sensitive

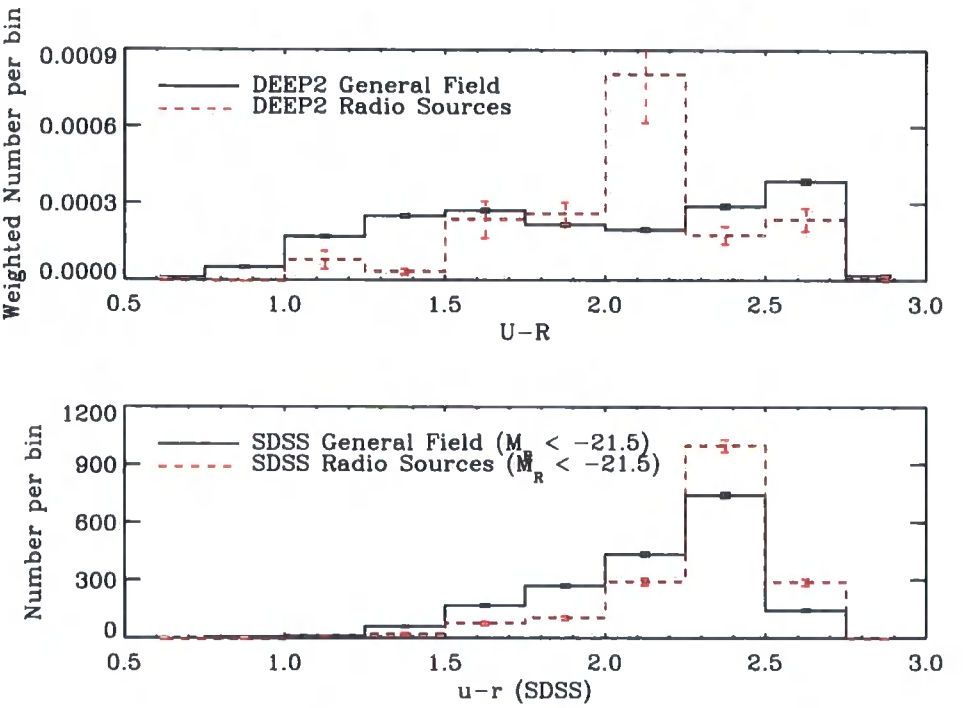


Figure 3.4: Top panel: Weighted histograms of the $(U - R)$ colours of the total general field galaxy population for the DEEP2 sample (black line) and those galaxies found to have radio emission (red line). Bottom panel: the equivalent plot for the local Universe using SDSS data. The radio sources in DEEP2 have a pronounced bump in their colour distribution at $U - R \sim 2.1$ compared to the general field that is not seen in the local Universe.

to the 4000Å break). Plotting $D4000$ versus $\log(L_{1.4\mathrm{GHz}}/M_*)$, where $L_{1.4\mathrm{GHz}}$ is the radio luminosity and $M_*$ is the stellar mass, they separate the two populations using the evolutionary track of a galaxy with an exponentially decaying SFR with $\tau = 3\,\mathrm{Gyr}$. In order to allow for the uncertainty in the SFR estimator they shifted the track redward by $D4000 \sim 0.2$ to establish a fiducial separation line. At low redshift, the radio source population is clearly bimodal in this space and the division of the population is relatively insensitive to the details of this fitting process.

In order to make our work comparable to that of B05, we have duplicated their method of separating the two populations as far as possible. Unfortunately, as described above, $D4000$ values are not available for AEGIS and we therefore use $(U-R)$ as a proxy for $D4000$. Although $(U-R)$ is clearly related to $D4000$, it is likely to be more susceptible to dust reddening because the two pass bands are further apart.

However, we can use galaxies from the SDSS to determine an empirical correlation between $D4000$ and $(U-R)$ colour. The colour data were taken from Baldry et al. (2006) while the $D4000$ values were downloaded from the public data archive (Kauffmann et al., 2006). The resulting relation is shown in Fig. 3.5 along with the line of best fit.

We used a Projet d'Étude des GAlaxies par Synthèse Évolutive model (Pégasé – Fioc and Rocca-Volmerange 1999) to estimate the stellar masses, based on absolute magnitudes and colour. As with B05, the galaxy employed had an exponentially decaying SFR with $\tau = 3\,\mathrm{Gyr}$. Extinction was appropriate for a galaxy with a disk geometry (inclination averaged) and there was no evolution in the stellar metallicity.

In figure 3.6 we plot $(U-R)$ versus $\log_{10}(L_{1.4\mathrm{GHz}}/M_*)$ for the AEGIS20 radio galaxies identified in DEEP2 and use this as the basis for separating the populations. $M_*$ was estimated for our galaxies by fitting a function to the $B-R$ colour, $R$ magnitude and $M_*$ for the galaxies in the Pégasé model and then interpolating to our $B-R$ and $R$. We also plot the $D4000$ versus specific radio-luminosity relation from B05, transformed to $(U-R)$ colour. The dashed line in this figure is the track of the starforming galaxy from B05 transformed from $(U-R)$ to $D4000$. The solid line is the dashed line shifted upwards in $(U-R)$ and is the line used for the actual separation in both B05 and this work. We reproduce the dashed line here because it serves as a cut-off for galaxies that are *most likely* to be SFGs (below it) to those that are likely to have an AGN component (above it). We take sources above the solid line to be *most likely* to be AGN. We take the galaxies between these two lines to be our intermediate colour population (ICP). We leave them

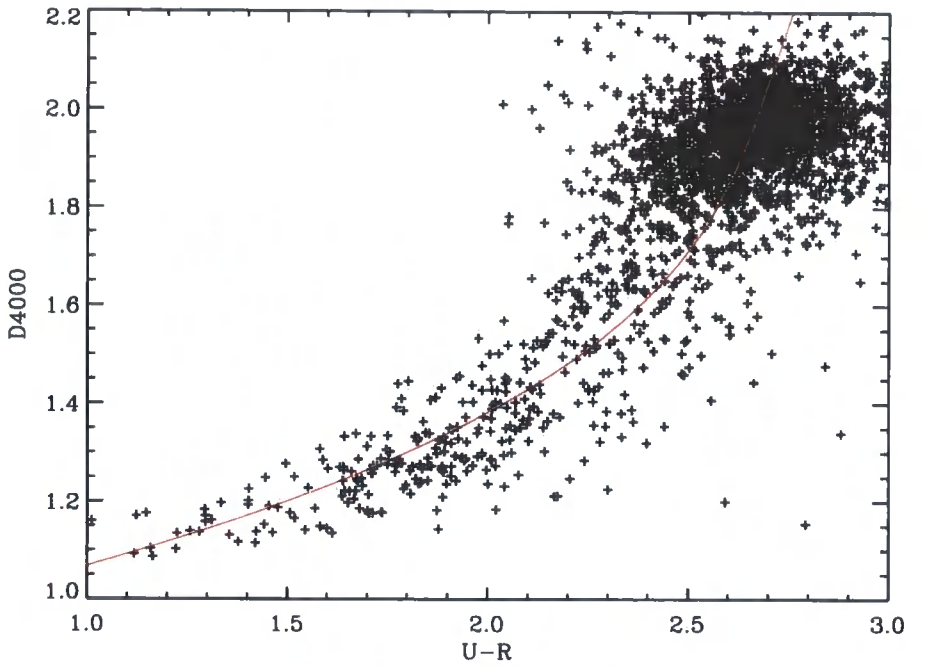


Figure 3.5: $D4000$ versus $(U - R)$ for SDSS radio sources (Baldry et al., 2006). The line is the line of best fit (of cubic form) to the data used in this work.

ostensibly as SFGs but investigate the effect of assuming they're AGN in section 3.4.3. At these redshifts ($0.2 < z < 1.4$), the separation of SFGs and AGN-powered radio sources is less clear-cut than that found locally by B05. However, although the AEGIS20 radio sources are not clearly bimodal in colour we can still use colour as a guide to the origin of the radio emission. We take AGN-powered sources to be galaxies lying above the transformed selection boundary from B05, as shown in Fig. 3.6; galaxies lying below this boundary are taken to be SFGs (and thus include the ICP). Of the 141 sources we matched in total, we designate 43 to be AGN on this basis and 98 to be SFGs.

Although the separation method described above has been shown to work well locally by B05, there are reasons why this may not be so effective at a redshift of unity. One of these is reddening of starburst galaxies due to dust (Poggianti and Wu, 2000). Since our separation depends on galaxy colours, dusty SFGs could in principle be misclassified as AGN. To investigate the likelihood of this, we compared the colour-colour distribution (in $(U - B)$ versus $(B - R)$ space) of our radio matches with that of the general field population of DEEP2 galaxies. The distribution is shown in figure 3.7. The AGN-powered radio source population lies close to the track defined by the field galaxy

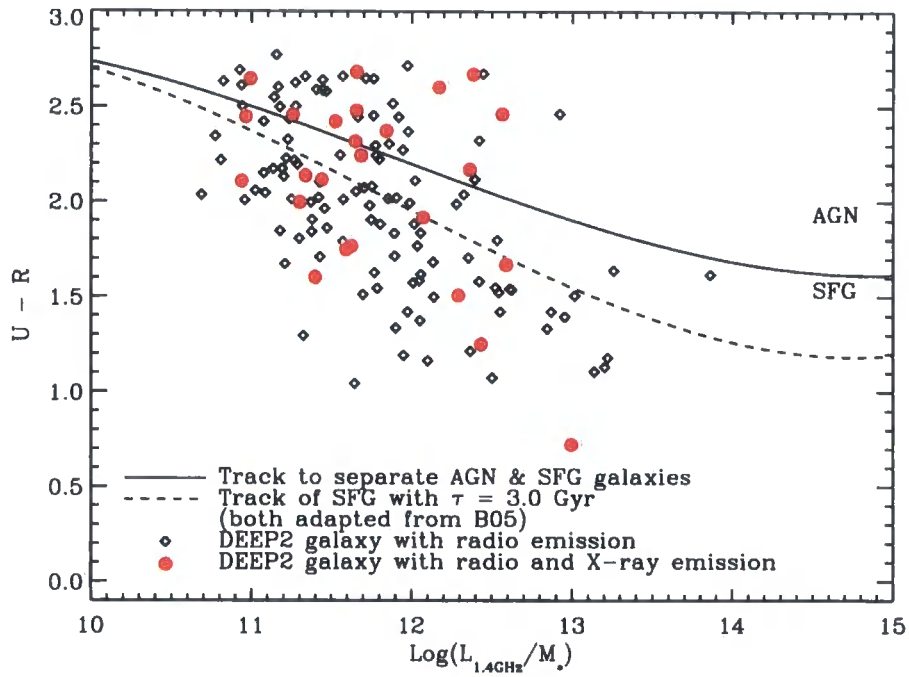


Figure 3.6: $(U - R)$ versus $\log(L_{1.4\mathrm{GHz}}/M_*)$ used to separate AGN- and star-formation-powered populations. We plot the optical galaxies for which a radio match was found. The solid line is the transformed selection boundary from B05. The dashed line is the track of the star forming galaxy used in B05 that is then shifted up by a constant amount in $D4000$ to make the solid line. The shift was an adjustment made by B05 so as to be most consistent with other methods that could have been used to separate the populations such as using a BPT diagram. The shift is 0.225 in $D4000$.

population. The directions of the reddening vectors derived from a sample of local starburst galaxies (Calzetti et al., 1994) and for Galactic reddening (Schlegel et al., 1998) are shown in figure 3.7. These two reddening laws are shown in figure 2.2. Since these two vectors point away from the track of the general field population, we would expect to find any of our radio sources that have been reddened away from the main track. Since they are nearly all very close to the track, we conclude that they are unlikely to have been reddened and thus will not have been misclassified for this reason. In contrast, some of the redder SFG radio sources could have suffered a high degree of reddening so that the colours are under-estimating their star formation rate.

Finally, we should be clear about the nature of the systems classified as SFG. Anything with sufficiently blue colour that we have designated it an SFG *potentially* has its star formation powered by star formation. However, while the colours may be consistent with the observed radio emission, we have been conservative in the classification (in the sense that we are unlikely to misclassify AGN powered systems) and the source might nevertheless obtain some of its radio power from an AGN. To test the accuracy of our colour based separation method, we compare it with other measures of AGN activity below. We note, however, that any other classification system has its own draw-backs. For example, an AGN that is detected on the basis of the BPT diagram may make little contribution to the radio flux.

### 3.3.3 Comparison with other measures of AGN activity

#### 3.3.3.1 X-ray and FIR

In figure 3.8 we compare the colour-magnitude distributions of the X-ray sources in the AEGIS field with that of the radio sources. It is interesting that the X-ray sources also have a substantial population of objects with intermediate colours as described in Nandra et al. (2007). Indeed the overall distribution of colours is strikingly similar and different to that of the field galaxy population. However, only 25 of the X-ray sources are actually matched with radio counter parts.

This is not surprising given that the emission mechanisms may require quite different accretion disk structure. Indeed, it is noticeable that very few of the star formation powered sources are matched to X-ray sources. Using the numbers in section 3.2.2, the fraction of our AGN found to be associated with an X-ray source is twice that of the SFGs. At the flux limit of the X-ray survey it is unlikely that we are detecting star forma-

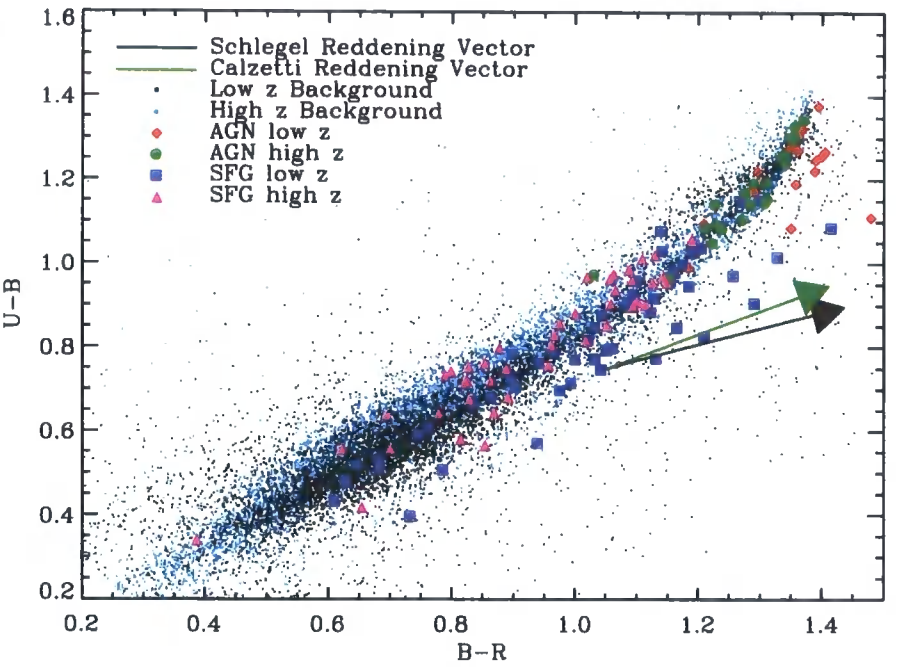


Figure 3.7: Colour-colour plot for our radio sources and the general field population of DEEP2 galaxies, with arrows showing the *directions* of the reddening vectors from Schlegel et al. (1998) and Calzetti et al. (1994). The radio sources – particularly those we have identified with the AGN-powered population – lie close to the track defined by the field galaxy population. The low redshift bin covers $0.2 \leq z < 0.7$ ($z_{\rm median} = 0.51$) and the high redshift bin covers $0.7 \leq z < 1.4$ ($z_{\rm median} = 0.93$). This plot shows that it's unlikely that the AGN in our sample have been significantly reddened since they're mostly very close to the path defined by the general field galaxies. On the other hand, some of the SFGs, especially at low redshift, may have been artificially reddened. We emphasise that the lengths of these vectors are arbitrary. The Schlegel reddening vector uses $R_V$=3.1. Having derived the vector using the values of $A/A(V)$ in the different passbands for this value of $R_V$, we multiplied its length by 0.75 to fit the plot then adjusted the length of the Calzetti reddening vector to be approximately the same.

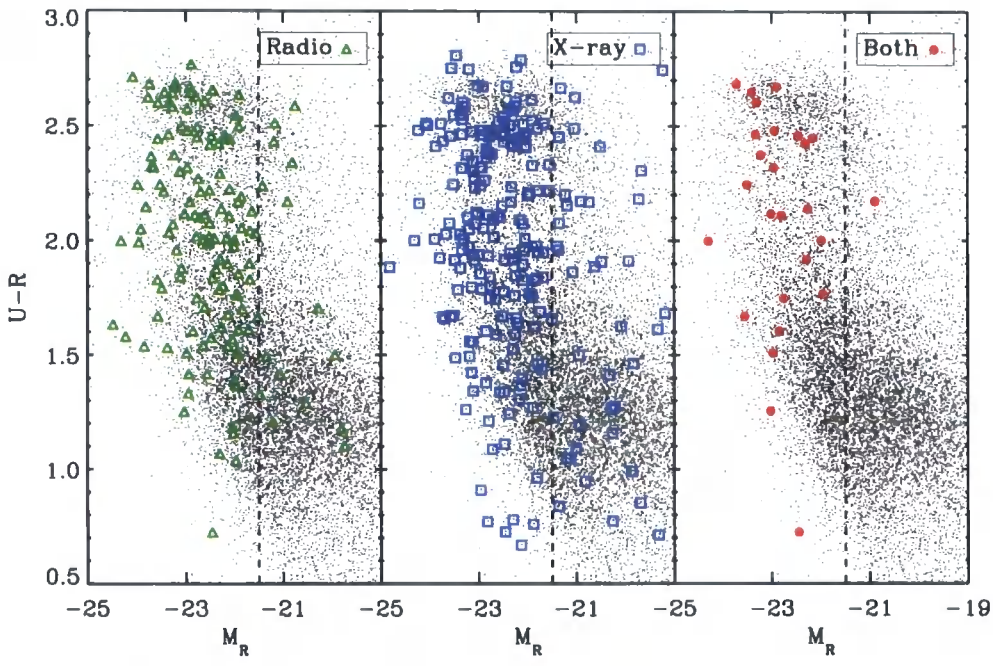


Figure 3.8: Colour-magnitude diagrams: we plot $(U - R)$ versus $R$ for the radio sources (left panel), for the X-ray sources (middle panel) and for those galaxies found to be sources of both radio and X-ray emission (right panel). On each panel, the black dots represent the general field galaxies from DEEP2. Neither the radio nor the X-ray sources follow the distribution of the general field galaxies with both having disproportionately large numbers between the red sequence and blue galaxies of the general field.

tion in these systems although we must conclude that a few SFGs will contain an AGN component. However, this match does *not* necessarily demonstrate that all, or even part, of the radio flux comes from the AGN. When constructing the luminosity functions below we will treat these sources cautiously. As we will show they make up only a small fraction of the total radio source population.

An additional or alternative strategy for separating the population of SFGs from the AGN-powered population would be to use the IR/radio correlation (Helou et al., 1985; Appleton et al., 2004; Seymour et al., 2008; Ibar et al., 2008). Galaxies with excess radio emission might then be identified as AGN-powered sources. The method does not give a clear-cut separation – some AGN-powered sources have flux ratios consistent with SFGs; however, the approach would allow us to estimate a lower limit to the fraction of sources we have classified as SFGs on the basis of their stellar mass and colour (figure 3.6) but which also have a significant AGN contribution to their radio luminosity.

#### 3.3.3.2 Optical spectroscopy

As a further diagnostic of the AGN population, we consider the optical spectroscopy. It is not possible to place all our sources in the [O III]5007/H$\beta$ versus [N II]6583/H$\alpha$ emission-line diagnostic diagram (Baldwin et al. 1981, hereafter BPT) since [N II]6583 and H$\alpha$ are redward of the observable wavelength range for many of our highest-redshift radio emitters. However, all our sources have spectra that include the [O III]5007 and H$\beta$ lines. The latter ratio is still useful in testing the accuracy of our separation, as we describe below.

Figure 3.9 shows the median spectrum for each population between 4750 and 5050Å, broken into two redshift bins covering $0.2 \leq z < 0.7$ ($z_{\rm median} = 0.51$) and $0.7 < z \leq 1.4$ ($z_{\rm median} = 0.93$). The 'radio-mode' AGN samples at low and high redshift do not display emission lines whose equivalent widths can be measured reliably. However the SFG (including the ICP) spectra show strong emission lines characteristic of a star-forming population. We measure [O III]5007/H$\beta$ ratios of $1.1 \pm 0.2$ and $1.2 \pm 0.8$ for the low- and high-redshift SFGs, respectively. We also measured the equivalent widths for the ICP to see whether the spectra could break the degeneracy based on colour alone for these objects. For the ICP, we measure equivalent width ratios of $3.2 \pm 1.2$ and $0.4 \pm 0.2$ for the low- and high-redshift galaxies, respectively. The results for the SFGs are consistent with them being star forming galaxies. In fact, given the equivalent widths of the SFGs and comparing to figure 2.3, we can conclude that these equivalent widths are more likely

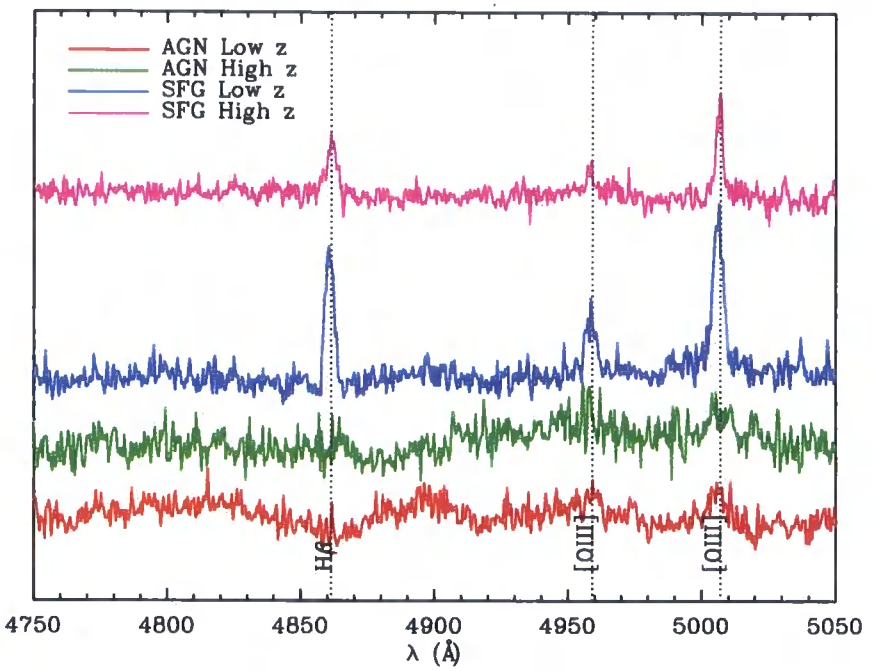


Figure 3.9: Median spectra of the low- and high-redshift AGN and SFGs. The spectra have been shifted by arbitrary amounts along the ordinate axis to separate them. The H$\beta$, [O III]4959, 5007Å emission lines have been marked. The low-redshift bin covers $0.2 \leq z < 0.7$ ($z_{\rm median} = 0.51$) and the high-redshift bin covers $0.7 \leq z < 1.4$ ($z_{\rm median} = 0.93$).

to come from star forming galaxies rather than AGN since they are ~1.0. However, we cannot say that they are inconsistent with being AGN either since we don't have [N II]6583/H$\alpha$ to break the degeneracy. The ICP result for the low-redshift sample is inconclusive, in part due to the large error bar and in part because its value puts it on a line in the BPT diagram with a large degeneracy between SFGs and AGN. The ICP high-redshift result is consistent with their radio emission being dominated by star formation.

#### 3.3.3.3 Optical morphologies

Last in our series of diagnostics, we compare the morphologies of the two populations as we have separated them. Figures 3.10 and 3.11 show *Hubble Space Telescope (HST)* Advanced Camera for Surveys (ACS) images of our AGN and SFG populations (where these images were available), respectively. In these figures, the images are ordered as follows. We use the parameter $\Delta(U-R)$ ($\equiv (U-R) - (U-R)_{cutoff}$ where, for a given

galaxy, $(U-R)_{cutoff}$ is the cutoff in $(U-R)$ between the AGN and SFGs evaluated at that galaxy's $\log_{10}(L_{1.4GHz}/M_*)$) as a proxy for the probability that the radio emission is AGN-powered. In each of figures 3.10 and 3.11 the images are ordered by increasing $\Delta(U-R)$ , starting in the bottom left hand corner and going along one row at a time. On inspection of these images, a clear trend emerges of the SFGs being, on average, more disk-like, with a smaller bulge-to-disk ratio than the AGN and often with visible spiral structure. As with the equivalent width analysis above, these morphologies couldn't be used as a sole method of separating the populations. For example, there are some similar images that appear in each category. However, these two plots do provide further circumstantial evidence that our separation method has been successful. For example, the majority of the small, bulge-dominated systems are classified as AGN and all those with visible spiral structure are classified as SFGs. Further, the few bulge-dominated systems classified as SFGs are near to the border in $\Delta(U-R)$ suggesting that, although the colour-based separation method appears to work well, there would be a case for lowering the separation line to bluer colours. These sources are included in the ICP so any errors in our measurements from any such misclassifications will be accounted for in the systematic errors calculated below by switching the ICP from the SFGs to the AGN. Nevertheless, we still wish to be cautious when describing our SFG population. As indicated by their morphologies, [O III]/H$\beta$ line ratios and as discussed below, it is plausible that some of them will contain AGN and yet have colours that are consistent with SFGs. Discerning which mechanism dominates the radio emission in such sources is beyond the current data set (see discussion in Ivison et al. 2007).

#### 3.3.3.4 Classification summary

To briefly summarise our classification system of SFGs and AGN, we have separated the two populations based primarily on their colour with redder sources being AGN and bluer ones being SFGs. We have allowed the colour-cutoff between the two to vary with the mass-to-radio luminosity ratio. This is to allow galaxies' colours to vary with different stages of evolution (as indicated by the mass-to-radio-light ratio). For example, consider two galaxies of equal *total* mass with similar, intermediate colours: one with AGN-powered radio emission and one with star formation-powered radio emission. The galaxy actively forming stars will have converted less of its mass into stars than a "red and dead" AGN galaxy and will thus have a higher $L_{1.4GHz}/M_*$ ratio. We have checked the accuracy of the separation using the X-ray emission, optical spectra

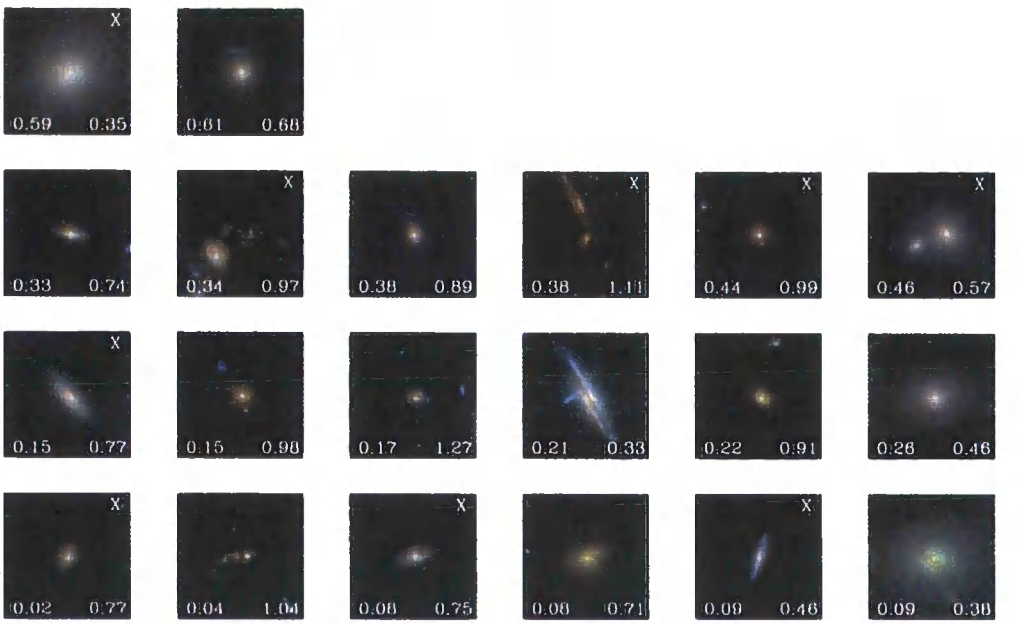


Figure 3.10: $6'' \times 6''$ *HST* ACS images of those galaxies that we have designated AGN. The plots are ordered by increasing $(U-R)$ - $(U-R)_{cutoff}$ (shown in the bottom left corner of each image) where the cutoff in $(U-R)$ is evaluated based on that galaxy's $L_{1.4GHz}$ and $M_*$ as described in the text. The redshift of each galaxy is given in the bottom right corner of each image. An X in the top right corner of an image denotes that that galaxy was matched to an X-ray source.

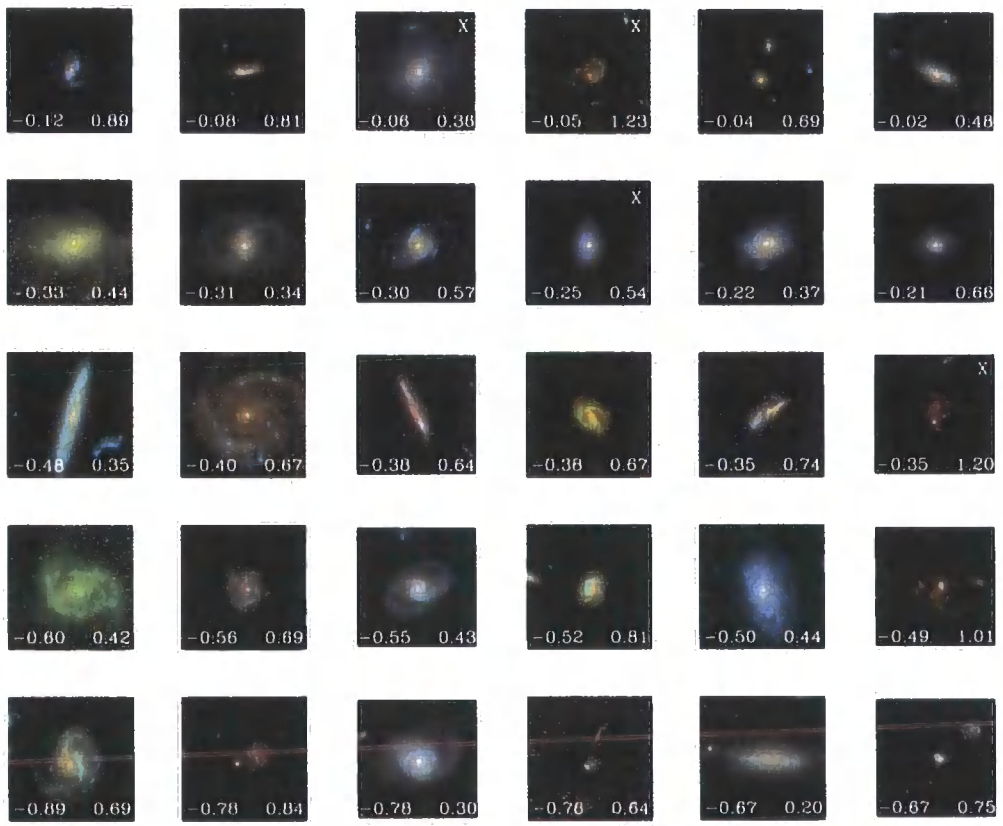


Figure 3.11: Same as figure 3.10 but for those galaxies that we have designated SFGs.

and optical images. It is unlikely that any of these methods could give perfect separation on their own (due to natural scatter in all the variables and because it seems likely that some sources have radio emission powered by star formation *and* AGN). However, they each provide evidence that the separation has been largely successful (as discussed above, the classification is not obviously systematically wrong). We shall incorporate the uncertainty in classifying the ICP into our systematic errors.

## 3.4 Radio Luminosity Functions

### 3.4.1 Constructing the radio luminosity function

We used the $1/V_{\rm max}$ method to calculate the RLFs of each population.

For a given galaxy, we compute $V_{\rm max}$ as the volume contained within the maximum redshift at which the galaxy would have been included in *both* the radio and optical catalogues. To determine $V_{\rm max}$ we allow for the optical and radio $K$-corrections as the source is redshifted. For consistency, we obtained the optical $K$-corrections by interpolating the function relating $K$-corrected magnitudes and colours at the redshifts of catalogued galaxies. These functions are illustrated in figure 3.12 which plots the limiting $B$ magnitude of the DEEP2 survey as a function of redshift. This limit was set to the faintest $B$ magnitude in the DEEP2 general field population at each redshift (within a redshift bin of 0.02). Since this is a very sensitive function of colour, we do this in very fine colour bins (with widths in $U-R$ of 0.02).

In determining the radio $K$-corrections, we assumed the radio spectra vary as $\nu^{-0.9}$ for the AGN and $\nu^{-0.7}$ for the SFGs (Carilli and Yun, 2000).

In order to calculate the RLFs, the values of $V_{\rm max}$ need to be weighted to account for the variations in targeting strategy and redshift success rates with galaxy colours and magnitudes in the DEEP2 survey. These weights, $w$, are described in Willmer et al. (2006). In non-cumulative form, the RLF in bin$_k$ (where there are $j$ bins) is given by

$$\phi_k = \frac{1}{b}\sum_{i=1}^{N_k}\frac{w_i}{V_{max,i}} \tag{3.1}$$

where $b$ is the bin width in $\log_{10}L_{1.4GHz}$, $N_k$ is the number of galaxies in bin $k$ and $1 \leq k \leq j$. The error on $\phi_k$ is given by:

$$\delta\phi_k = \frac{1}{b}\left[\sum_{i=1}^{N_k}\frac{w_i}{V_{max,i}^2}\right]^{1/2} \tag{3.2}$$

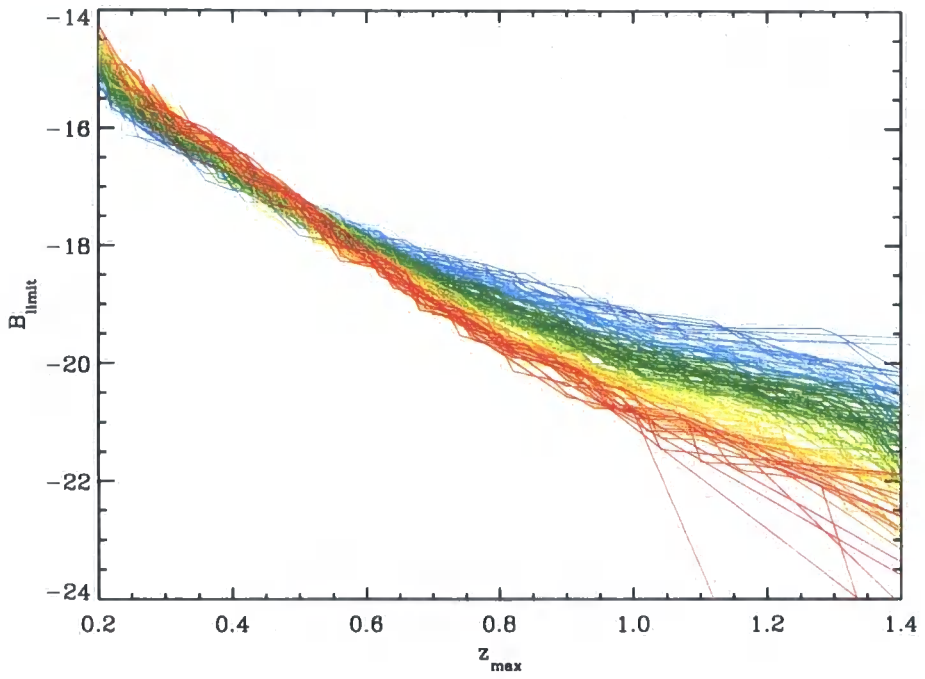


Figure 3.12: Limiting $B$ magnitude versus redshift for the DEEP2 general field population. In redshift bins of 0.02, we found the faintest $B$ magnitude of a galaxy in the survey. We did this as a function of colour with $U - R$ ranging from 0.5 to 2.8 in bins of width 0.02. The different coloured lines on this plot represent the different galaxy colours over the full $U - R$ range. This plot is used to k-correct the DEEP2 optical sources as we imagine them being moved to higher redshifts to calculate $1/V_{\rm max}$ .

Then cumulative RLF $\Phi_k$, which we use in this work, corresponding to luminosity $L_k$ is calculated as:

$$\Phi(> L_k) = b \sum_{i=k}^{j} \phi_i \tag{3.3}$$

and the error on $\Phi_k$ is given by:

$$\delta\Phi_k = b \left[ \sum_{i=k}^{j} \delta\phi_i^2 \right]^{1/2} \tag{3.4}$$

We show the RLFs in cumulative form to eliminate the effects of the choice of binning. The penalty for this choice is that the error bars on each point are not independent.

The stepwise maximum likelihood method that we rejected in favour of the $1/V_{\rm max}$ method has the potential advantage of being less susceptible to large scale structure than the $1/V_{\rm max}$ method. For example, if we lived in an underdense region of the Universe, the low luminosity galaxies would be more under-represented in a flux-limited sample than the high luminosity ones. Therefore the $1/V_{\rm max}$ method would be biased against the low luminosity end of the LF because those contributions of $1/V_{\rm max}$ would be missing. The SWML method, on the other hand assumes the LF is independent of redshift and thus it doesn't matter whether we live in an underdense region or not. However, we found our values of $V/V_{\rm max}$ to be uniformly distributed between 0 and 1 with a mean of 0.50 and thus conclude that the method has worked successfully.

### 3.4.2 The total radio luminosity function

Figure 3.13 shows the total (AGN and SFGs added together) cumulative RLF for the low-redshift epoch ($0.2 \leq z < 0.7$, $z_{\rm median} = 0.51$) and the high-redshift epoch ($0.7 \leq z < 1.4$, $z_{\rm median} = 0.93$). In this figure, we do not attempt to separate the contributions from the AGN and SFG populations so that we can compare the overall luminosity function with that measured at low redshift. The uncertainty is shown by the hashed region.

In order to compare with the local universe both panels show the combined AGN and SFGs RLFs from B05 at $z \sim 0.1$ and from M07 at $z = 0.04$. As can be seen from the comparison, there is significant evolution in the RLF. Given RLFs at three epochs ($z \sim 0.1$, 0.5 and 1.0), we can measure the amount by which each RLF has evolved. Evolution in the RLFs could take the following forms: pure luminosity evolution (PLE), in which the RLF is shifted horizontally to higher luminosities at higher redshifts, pure density

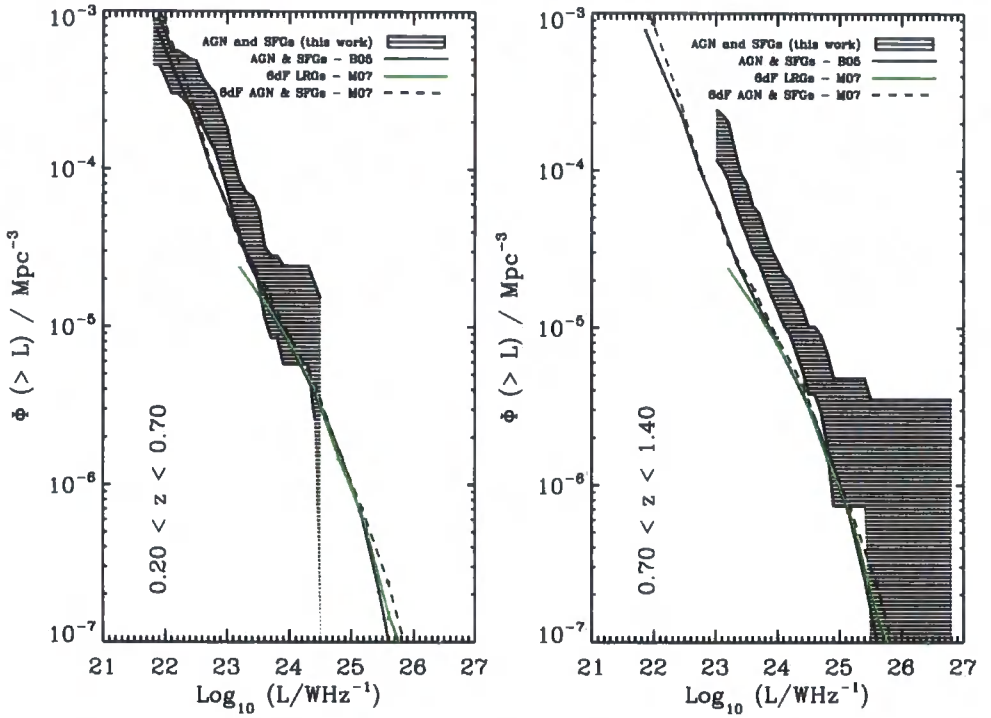


Figure 3.13: The cumulative, combined (AGN plus SFG) radio luminosity functions (RLF). The results of this work are shown by the black shaded areas. The shaded areas denote the region within the $1\sigma$ error bars. The left panel shows the RLF for the low-redshift epoch ($0.2 \leq z < 0.7$, $z_{\rm median} = 0.51$) and the right panel for the high-redshift epoch ($0.7 \leq z < 1.4$, $z_{\rm median} = 0.93$). We plot the AGN and SFGs combined RLF from Best et al. (2005), the AGN and SFGs combined RLF from M07, and the LRG RLFs from the 6dFGS (M07) against which we measure the evolution of the RLF.

evolution (PDE) in which the RLF is shifted vertically to higher densities at higher redshifts or a combination of the two. Neither of these simple extremes of pure evolution is well motivated physically and the aim of this chapter, given that we do not have enough data to differentiate between the above models, is to make a simple measurement of the evolution of the AGN, SFG and combined RLFs that can easily be compared to that of other studies. We have therefore adopted PLE as our model, measuring $\alpha$ in the PLE parameterisation of $L \propto (1+z)^{\alpha}$ (Boyle et al., 1988; Calura and Matteucci, 2003). $\alpha$ may be a luminosity-dependent parameter (i.e. the evolution is not *pure* luminosity evolution). For example, S07 found that LRGs have $\alpha = 2.0 \pm 0.3$ out to $z = 0.7$ and that more powerful LRGs undergo the most rapid evolution.

The values of $\alpha$ here and for the AGN and SFGs are measured as follows. For a section of the RLF that is well defined (i.e. the error regions are tight to the centre of the track denoting the RLF), we evolved the RLFs of B05 until they are as congruent as possible with our RLF. This is done separately for each of our two redshift epochs, as shown in figure 3.14 which shows the whole process of measuring $\alpha$. The value of $\alpha$ that best puts the RLF from B05 on top of ours is taken to be the measured value for that RLF type and epoch. We estimate an error on this value by considering what values of $\alpha$ would move the B05 RLF to the upper or lower limits of ours. Then, for a given RLF type (combined, AGN or SFG), we have two measured values of $\alpha$ (one for each redshift epoch) with errors on them. Then finally, for each RLF type, we take a weighted mean of those two values to be our measured value of $\alpha$ for that RLF type. We find that the evolution of the overall RLF is consistent with PLE of the form $L \propto (1+z)^{\alpha}$ where $\alpha = 2.2 \pm 0.5$.

### 3.4.3 AGN and SFG radio luminosity functions

Next, we explore the RLFs of AGN and SFGs separately. B05 made separate RLFs like these for the local Universe and we can thus measure the RLF evolution of each population, comparing our work with theirs. Figure 3.15 is similar to figure 3.13, but shows the RLFs of the AGN and SFGs separately. Also shown are the AGN and SFGs RLFs from B05 at $z \sim 0.1$ and M07 at $z = 0.04$.

We also plot the LRG RLF of Sadler et al. (2007) at $z \sim 0.5$. S07 measured the evolution of radio sources with 1.4GHz luminosities in the range $10^{24-25}\,\mathrm{W\,Hz^{-1}}$ using the 2SLAQ survey of red galaxies, i.e. radio galaxies lying close to the red sequence. We measured values of $\alpha$=1.0 $\pm$0.9 for the AGN and $\alpha$=3.7 $\pm$0.3 for the SFGs.

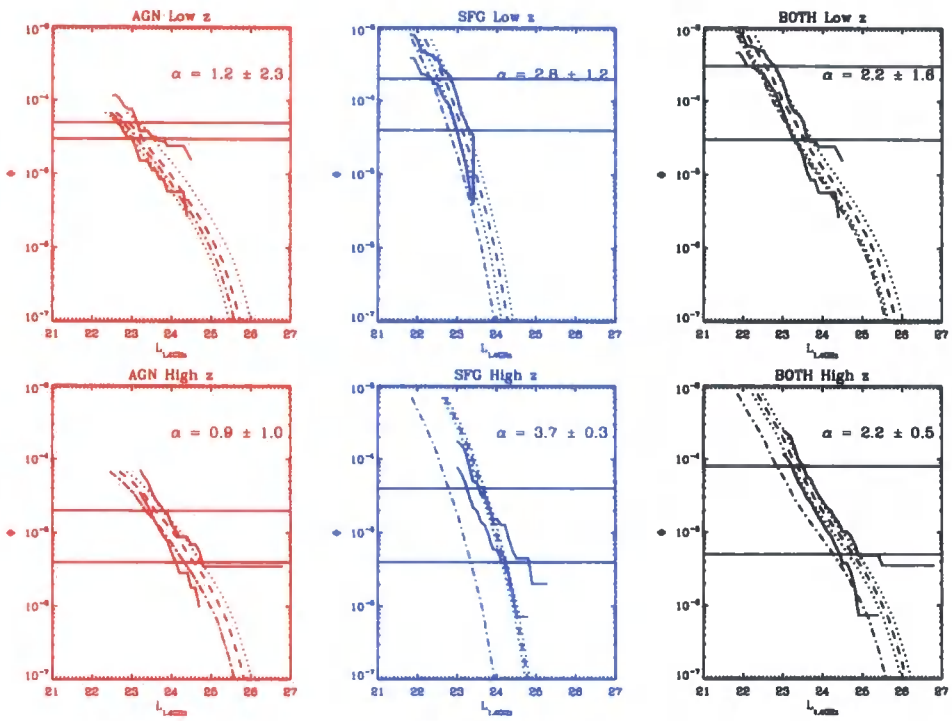


Figure 3.14: Measuring $\alpha$ for each RLF type. The left-most two panels (in red) are for the AGN RLFs; the middle two panels (in blue) are for the SFG RLFs and the right-most two panels (in black) are for the combined RLFs. The top panels show the evolution of the relevant B05 RLF required to match our low redshift RLFs and the bottom panels show the same for our high redshift RLFs. In each panel, the two horizontal, solid lines show the region of the RLF over which the fitting is being done. The diagonal, solid lines denote our RLFs as in figures 3.13 and 3.15. The dot-dash lines show the B05 RLFs as measured at $z \sim 0.1$; the dashed lines show the B05 RLF evolved with the given value of $\alpha$ in the top right corner of each panel and the two dotted lines show the B05 RLF evolved with the given value of $\alpha\pm$ the given error on $\alpha$. See text for details.

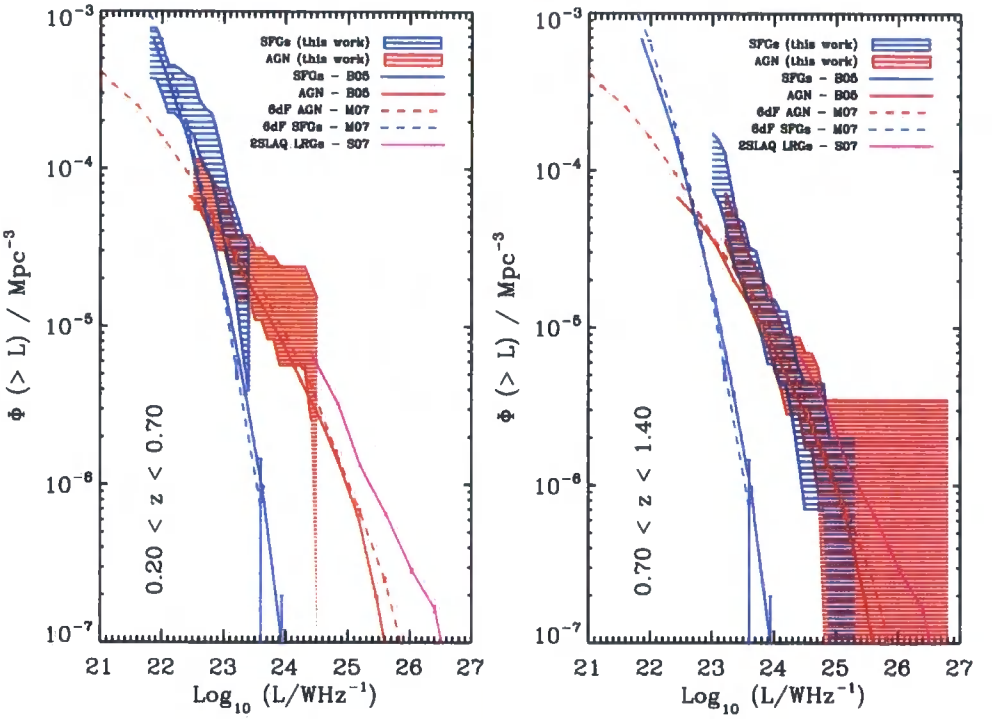


Figure 3.15: Cumulative AGN and SFG RLFs. The results of this work are shown by the red (AGN) and blue (SFGs) shaded regions. The ICP is included with the SFGs. The results in the left panel are for the low-redshift epoch ($0.2 \leq z < 0.7$, $z_{\rm median} = 0.51$) and those in the right panel for the high-redshift epoch ($0.7 \leq z < 1.4$, $z_{\rm median} = 0.93$). The shaded areas denote the regions within the $1\sigma$ error bars. Overlaid on each panel are red and blue solid lines (using the same colour coding as above) showing the results of Best et al. (2005) at $z = 0.1$, red and blue dashed lines (using the same colour coding as above) showing the results of M07 and the solid magenta line showing the LRG RLF from S07.

To see the impact of our classification system on these values of $\alpha$, we did the above analysis again but with the ICP included as AGN instead of SFGs. This yielded values of $\alpha$=2.1 $\pm$0.5 for the AGN and $\alpha$=2.7 $\pm$0.4 for the SFGs. This AGN value is not consistent with the value derived with the ICP as SFGs and shows the huge uncertainty in the evolution of the AGN RLF. It is either consistent with no evolution or consistent with the evolution of the LRGs of S07, depending on exactly where the line is drawn to separate the populations. On the other hand, the SFG evolution is just about consistent within the error bars with when the ICP was included with the SFGs. In either case, we find the evolution of the SFGs to be significantly stronger than that of the AGN. Finally, if we return to our original classification (ICP as SFGs) and remove the X-ray emitting sources from the SFG population, we measure $\alpha = 3.3 \pm 0.3$ for the SFGs and thus conclude that the X-ray population is not affecting our SFG results significantly.

## 3.5 Discussion

We have matched the AEGIS20 radio survey to the DEEP2 spectroscopic optical survey in the EGS to create a sample of 141 galaxies. We have separated these galaxies into AGN and star forming galaxies (SFGs) based primarily on their colours. Optical spectroscopy and imaging provide circumstantial evidence that that this separation method is an accurate one. We then constructed radio luminosity functions (RLFs) for the whole radio sample and the AGN and SFGs separately, at $z$ $\sim$0.51 and $z$ $\sim$0.93 and measured their evolution relative to other studies in the local Universe. We modelled the evolution as pure luminosity evolution (PLE) with $\alpha = 2.2 \pm 0.5$ for the whole radio sample, $\alpha$=1.0 $\pm$0.9 for the AGN and $\alpha$=3.7 $\pm$0.3 for the SFGs. However, there is a population with intermediate colours (the ICP, included in the SFGs above) whose classification is uncertain. We therefore remeasured the RLF evolution in the case that the ICP was switched to the AGN, measuring $\alpha$=2.1 $\pm$0.5 for the AGN and $\alpha$=2.7 $\pm$0.4 for the SFGs.

We also compared the colour-magnitude relations of the radio galaxies and the background population of DEEP2 galaxies at $z$ $\sim$1, the equivalent distributions at $z$ $\sim$0 and a sample of X-ray sources in the EGS at $z$ $\sim$1. We found that, at $z$ $\sim$1, both the radio and X-ray sources had prominent peaks at intermediate colours and were over represented there relative to the background population. We also found that, at $z$ $\sim$0, this population of radio sources at intermediate colours is not found.

We begin our discussion by comparing the evolution of the SFG RLF to the evolution

of the global star formation rate density (SFRD).

### 3.5.1 Comparison with SFRD evolution

We find that the radio luminosity function of the star forming galaxies evolves rapidly so that star forming galaxies match the AGN contribution to the radio luminosity function at $z \sim 1$. Such rapid evolution is also seen in other faint radio surveys: By combining several small survey regions, Haarsma et al. (2000) fitted a PLE model to SFG RLFs with a best fit of $\alpha = 2.74$. This agrees well with our value of $2.7 \pm 0.4$ from including the ICP with the AGN but is significantly less than our value of $3.7 \pm 0.3$ from including the ICP with SFGs. Although the samples are not directly comparable, it is also interesting to note that our result is consistent with Cowie et al. (2004) whose study of the RLF evolution of ULIRGs yielded $\alpha = 3$.

Rapid evolution is also seen in other star formation rate indicators. To explore this point further we compare the evolution we have measured with that of the global star formation rate density (SFRD). Hopkins and Beacom (2006) fit a function to SFRD versus $z$ with the parametric form from Cole et al. (2001):

$$\dot{\rho}_* = \frac{(a + bz)h}{1 + (\frac{z}{c})^d} \tag{3.5}$$

The fit for $0 < z < 1$ was done using SFRD measurements based on UV data from the SDSS as well as the Classifying Objects by Medium-Band Observations in 17 filters survey (COMBO17) and the *Galaxy Evolution Explorer (GALEX)*, corrected for obscuration using *Spitzer* far-IR measurements. Hopkins and Beacom (2006) derived the following values assuming the initial mass functions (IMFs) of Salpeter (1955) [Baldry and Glazebrook 2003]: $a = 0.0170\,[0.0118]$, $b = 0.13\,[0.08]$, $c = 3.3\,[3.3]$, $d = 5.3\,[5.2]$. The ratio of SFRD at $z = 0.91$ to that at $z = 0.1$ using this function is 4.5 [4.3], which is equivalent to the ratio derived assuming PLE with $\alpha = 2.7\,[2.6]$. This again agrees well with our measurement of $\alpha$ assuming the ICP is included with the AGN but less so if the ICP are included with the SFGs. However, we note that, around a redshift of unity, this line of best fit predicts less SFRD than is measured. Hopkins and Beacom (2006) find a better fit is that of a piecewise linear function:

$$a + b \log(1 + z) = \log(\dot{\rho}_*). \tag{3.6}$$

The best-fit parameters assuming the same IMFs as above are: $a = -1.82$ and $b = 3.28$.

If we assume pure luminosity evolution, $b$ is equivalent to $\alpha$, and thus the piecewise fit is about half way between our two measurements of $\alpha$ for the SFGs. Our separation of the two radio galaxy populations is thus consistent with work examining the evolution of SFRD via other SFR indicators. These comparisons suggest that AEGIS20 has traced star formation well and, conversely, that the optical samples are not missing significant star formation due to highly dust-obscured systems.

### 3.5.2 Star Formation, Radio and X-ray Emission

Given the similar distributions in colour-magnitude space of the radio and X-ray sources and the fact they are both so different to that of the general field population, we suggest that this is no coincidence and that there exists a causal relationship linking radio and X-ray emission to star formation amongst these galaxies. Major mergers amongst galaxies in groups or clusters could provide gas for both star formation and AGN activity (eg Nandra et al. 2007, Hopkins et al. 2005). At this stage the black hole would be obscured by gas and dust and the quasar would appear reddened. Eventually, the black hole would heat the gas to the point where it is driven from the galaxy in a superwind, the star formation would be quenched and the galaxy would move onto the red sequence. The fact that we see radio and X-ray sources on the red sequences (where the star formation has been quenched) at $z \sim 1$ indicates that ongoing star formation is not a prerequisite for AGN activity. Our results are consistent with this theory. For example, if an event such as a merger or harassment causes the spark for both the star formation and the AGN in a particular galaxy, then both forms of radio emission studied in this chapter will have been caused by the same event. This event will also start the chain of events that sees the galaxy migrate from the blue cloud to the red sequence as the star formation is eventually quenched.

An alternative theory as to how star formation is quenched by AGN activity is that the heating prevents the cooling flows of fresh gas to star forming regions (eg Bower et al. 2006, Croton et al. 2006). In the Bower et al. (2006) model, the AGN heating is limited by the black hole's Eddington limit and thus is ineffective at very high redshift ($\gtrsim 2$) when black holes have not had time to accrue sufficient mass and power. It is only at redshifts less than $\sim$1 that this feedback has become significant and has contributed to causing galaxies to migrate from the blue sequence to the red. In this work we might be seeing this migration happening.

As we have mentioned, it is possible that our ICP contains galaxies whose radio

emission is powered by *both* star formation and AGN. In this case, it would be more accurate to describe our SFG population as the population of radio sources not on the red sequence. This is because what we have designated as the SFG population is likely to contain both galaxies whose radio emission is powered by starbursts alone and those whose radio emission is powered by both starbursts and an AGN. In the latter case, the current dataset is unable to distinguish which of the starburst regions and AGN dominates the radio emission. The phenomenon of a population of radio sources with colours intermediate between the red and blue sequences is not seen in the local Universe (e.g. in the middle left panel of figure 9 of B05). This is consistent with the processes described above that cause galaxies to migrate from the blue sequence to the red being less effective at higher redshifts ($z \sim 1$) than in the local Universe.

### 3.5.3 Future Improvements

The uncertainty as to the correct classification of the objects in the ICP is perhaps the biggest drawback of this method. The most obvious improvement to the surveys would be to extend the optical spectroscopy out to $\sim 1.6\mu$m so as to include the [N II]6583 and $H_\alpha$ lines. With this information to hand, the most powerful discriminator between AGN and star forming galaxies, the BPT diagram, could be used.

Of course any survey would be improved by going deeper and/or wider. From the point of the radio luminosity functions presented in this chapter, their completeness would be particularly aided by deeper optical spectroscopy. At present, the RLFs may be incomplete due to not finding an optical match for some radio sources, even though they are within the redshift and radio luminosity ranges probed. With a deeper catalogue, we could be sure of including all such radio sources.

## 3.6 Conclusions

We have derived independent RLFs for galaxies whose radio emission is powered by AGN and SFGs, at two epochs ($0.2 \leq z < 0.7$, $z_{\rm median} = 0.51$) and ($0.7 \leq z < 1.4$, $z_{\rm median} = 0.91$) and compared them to similar work done in the local Universe. We have also explored the colour-magnitude diagram of these radio sources and compared it to that of a sample of X-ray-selected AGN and that of the general field population. Our results can be summarised as follows:

- The colour-magnitude distribution of AEGIS20 radio sources does not match that of the general field galaxy population from DEEP2 at $z \sim 1$. We find a prominent population of radio sources with colours between the red sequence and the blue general field population (an intermediate colour population, ICP). The radio sources are almost exclusively found in the colour region redward of rest-frame $(U - R) = 1.8$.

- Similarly, the colour-magnitude distribution of AEGIS X-ray sources is similar to that of the radio sources, suggesting they are triggered by similar mechanisms.

- We find the combined AGN and SFG RLF to evolve in a manner consistent with PLE of $L \propto (1 + z)^{\alpha}$ where $\alpha = 2.2 \pm 0.5$. In the case that the ICP is included with the SFGs, we measure $\alpha = 1.0 \pm 0.9$ for the AGN and $\alpha = 3.7 \pm 0.3$ for the SFGs. In the case that the ICP is included with the AGN, we measure $\alpha = 2.1 \pm 0.5$ for the AGN and $\alpha = 2.7 \pm 0.4$ for the SFGs. The SFG PLE is consistent with the evolution of the SFRD (Hopkins and Beacom, 2006). In the case of the ICP being included with the AGN, the AGN evolution is consistent with that of luminous red galaxies (LRGs) out to a redshift of 0.7.

# Chapter 4

# *The Environments of radio-powered AGN and star forming galaxies at $z \sim 1$*

## 4.1 Introduction

In this chapter, we examine the environmental dependence of the star formation rates, nuclear activity and radio luminosities of the radio sources we identified in chapter 3. We carry out this analysis at two epochs: an intermediate redshift one ($0.2 \leq z < 0.7$) and a high redshift one ($0.7 \leq z < 1.4$). In section 1.4.2 we discussed the results of Best (2004) (hereafter B04) who studied the environmental dependence of local galaxies with radio-powered star formation (star forming galaxies, SFG) and active galactic nuclei (AGN). We now have the opportunity to extend this study to higher redshifts using our samples of radio-powered SFGs and AGN found in chapter 3.

For example, one issue to address with such a study is whether the combination of the environment dependence of SFR and the increasing fraction of galaxies found in high density environments with cosmic time is responsible for the decline in the mean cosmic SFR since $z \sim 1$ (Madau et al., 1998). B04 found the percentage of galaxies with radio-powered star formation dropped with increasing environment density in the local Universe and we can now investigate whether this is also true in our two redshift epochs.

We also study the environments of the sample of radio-selected AGN. Black hole mass and galaxy bulge mass are strongly correlated (Magorrian et al. (1998), see Kormendy and Gebhardt (2001) for a review). This means that the mass build up of the black hole and of the galaxy's central bulge are fundamentally linked. It would be interesting to investigate whether the mechanism(s) that cause this relationship are affected

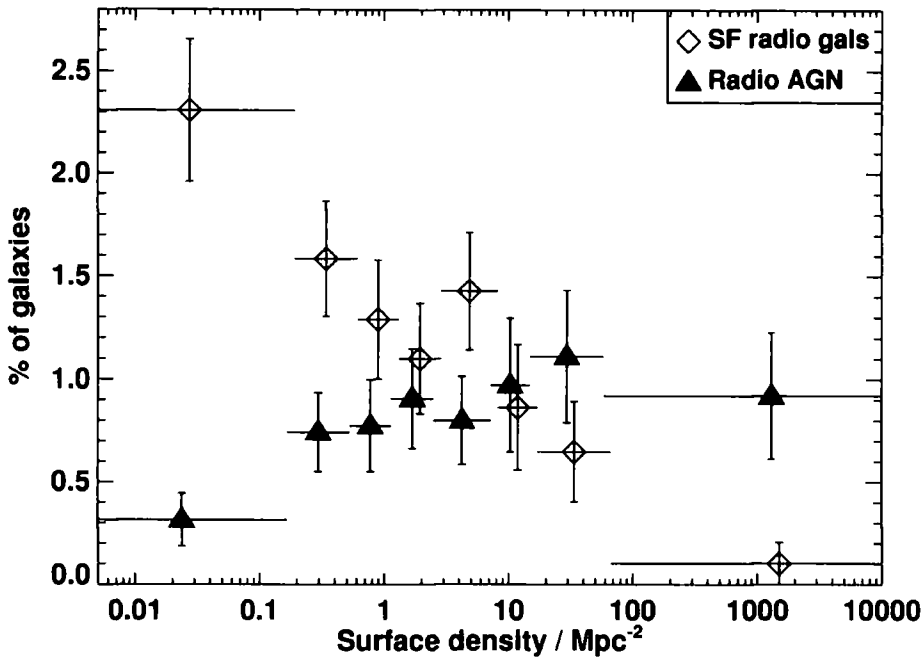


Figure 4.1: The fraction of galaxies within the 2dFGRS catalogue that are associated with radio sources classified as either AGN or star forming galaxies, as a function of projected surface density. The fraction of SFGs declines with density whilst that of AGN is independent of the density, with the possible exception of the lowest density bin. Note that, in this figure, the two data sets have been offset from each other by small, equal and opposite amounts along the $x$-axis for clarity. Figure from B04.

by the galaxy's environment, either in the local Universe or at higher redshifts. Thus we wish to measure the dependence of AGN activity on local environment density. B04 found the percentage of galaxies that are associated with radio-emitting AGN to be independent of the local overdensity over the range $10^{-1} < \Sigma_{10}/\mathrm{Mpc}^{-2} < 10^{3}$. However, the percentage did drop slightly below a density of $10^{-1}\mathrm{Mpc}^{-2}$. These results from B04 are shown in figure 4.1.

By investigating AGN activity as a function of environment density, we can also investigate the possible mechanisms that trigger AGN. B04 list three possible such mechanisms:

- The trigger is driven by the availability of cold gas. In this case, AGN activity should be suppressed in the densest environments where the gas has been swept

away by ram-pressure stripping.

- The trigger is driven by a function of the central black hole, in which case AGN activity should trace the distribution of galaxy bulges and be independent of environment. As stated above, B04 find no dependence of fraction of AGN on environment density with the possible exception of the percentage of AGN dropping in the lowest density bin.

- The trigger is a galaxy-galaxy interaction or merger. If this is the dominant AGN trigger, then AGN activity should trace the environments which are optimal for such interactions. This environment is that of groups, i.e. intermediate densities which provide high enough galaxy number densities yet low enough peculiar velocities to allow relatively frequent and significant galaxy-galaxy interactions (e.g. Heckman et al. 1986)

Further, Auger et al. (2008) investigated the environment dependence of AGN radio luminosities at moderate redshifts ($z \sim 0.3$). They found no significant trend between radio luminosity and environment. That is, at these redshifts, low and high luminosity AGN exist in the same environments. This is a different result to that found in the local Universe where limb-darkened, lower luminosity Fanaroff-Riley I (FR I, Fanaroff and Riley 1974) galaxies reside predominantly in rich clusters and limb-brightened, higher luminosity FR II galaxies tend to inhabit poor clusters or rich groups (e.g. Lilly and Prestage 1987). Auger et al. (2008) suggest that the appearance of this relationship in the local Universe is due to evolution of the density of the IGM (e.g. Maughan et al. 2006). Even at moderately high redshifts, the IGM is too dense for the larger, more powerful FR II galaxies to form their extended lobes. We are now in a position to find out whether the results found at moderate redshifts are also found at the higher redshifts we are investigating in the present work.

The rest of this chapter is structured as follows. In §4.2 we consider different ways in which to measure environment density and explain the reasons for our choice. We present the results in §4.3 and a discussion in §4.4. §4.5 contains our conclusions. We use $AB$ magnitudes throughout and assume a flat cosmology with $(\Omega_M, H_0/\mathrm{kms}^{-1})$ = (0.3, 70). Throughout this chapter we refer to the same redshift intervals we used in chapter 3 as *intermediate* ($0.2 \leq z < 0.7$) and *high* ($0.7 \leq z < 1.4$).

## 4.2 Analysis

### 4.2.1 Sample Selection

In this chapter we analyse the environments and environmental dependence of properties of the 141 radio sources identified in the DEEP2 survey in chapter 3. To calculate each galaxy's environment, we use the full spectroscopic catalogue of 15,365 galaxies in the EGS for which we calculated the restframe colours using the code kindly provided by Christopher Willmer (private communication). We make a magnitude cut at $B$=-21.0, only selecting galaxies brighter than this limit (regardless of whether we identify them as radio sources). This creates a volume-limited sample and is the same limit chosen by Cooper et al. (2006) (hereafter C06) in creating a volume limited sample (their sample B) from the DEEP2 survey. It is the faintest magnitude to which the DEEP2 survey is complete along both the red sequence and the blue cloud down at $z = 1.1$. We also use only those galaxies with redshift qualities of 3 or 4 (> 95% chance of being correct). This is the same selection criterion as used by C06 to make their sample B.

As in chapter 3, we use the parameter $\Delta(U-R)$ to distinguish between the active galactic nuclei (AGN) and star forming galaxies (SFG). For galaxy $i$, $\Delta(U-R)$ is defined as:

$$\Delta(U-R) = (U-R)_i - (U-R)_c \tag{4.1}$$

where $(U-R)_i$ is the (restframe) $(U-R)$ colour of galaxy $i$ and $(U-R)_c$ is the cutoff $(U-R)$ colour between AGN and SFG evaluated at the value of $\mathrm{Log}_{10}(L_{1.4GHz}/M_*)$ of galaxy $i$. $L_{1.4GHz}$ and $M_*$ are the galaxy's radio luminosity at 1.4GHz and stellar mass respectively. The separation between AGN and SFG is discussed at length in section 3.3. Radio sources with $\Delta(U-R) > 0$ are again designated as AGN here. However, as discussed in section 3.3.2, it is unlikely that all radio sources with $\Delta(U-R) < 0$ have their radio emission powered exclusively by star formation. Those with values of $\Delta(U-R)$ just below 0 are likely to contain radio contributions from AGN as well as star formation. Therefore, for the present work, we adopt as the sample of SFG those radio sources with $\Delta(U-R) < -0.4$ to give a pure sample of galaxies whose radio emission is powered by star formation. The intermediate colour population (ICP) identified in chapter 3 is not large enough to support a separate environment study of these galaxies alone.

In the present work, we use the $n^{th}$ nearest neighbour estimate of local environment density. This decision is based in part on C05's findings that this method doesn't suffer

from the effects of peculiar velocities as much as those methods that directly use the line of site information. It also gives a good reproduction of the density across a wide range of densities (given sensible choices of $n$ and $dv$, as discussed below) and is relatively robust to edge effects if galaxies within a sensible distance to the edge of the survey are omitted. Additionally, it is a relatively simple method that has already been used by many authors (e.g. Cowie and Barger 2008, C06, Balogh et al. 2004) and thus the results will be readily comparable to those of other authors.

We choose $n = 3$. This relatively low value helps to minimise the edge effects and C05 show it to be commensurate with the typical numbers of galaxies found in groups (as defined using the prescription in Yan et al. 2004) in the DEEP2 survey. We choose $\Delta v = 1000 kms^{-1}$. C05 show this value to be a good compromise between accurate reproduction of the density in high density environments (higher $\Delta v$) and in low density environments (lower $\Delta v$). We thus choose the 2-dimensional $n^{th}$ nearest neighbour method with $n = 3$ and $\Delta v = 1000 kms^{-1}$.

### 4.2.2 Selection completeness Correction

We now correct the density measurements for variations with redshift of the survey selection rate. In order to correct for this, we follow the recipe of C05 and apply an empirical correction to the measured values, $\Sigma_3$ to convert them to "overdensities" ($\delta_3$):

$$\delta_3 = \frac{\Sigma_3 - \Sigma_{3,med}}{\Sigma_{3,med}} \tag{4.2}$$

where $\Sigma_{3,med}$ is the median value of $\Sigma_3$ within a redshift bin of $\Delta z$=0.04. C05 shows that making this simple correction is at least as effective as using a redshift-dependent selection function.

### 4.2.3 Edge Effects

Following the discussion in section 2.2.1, we only calculated a density for the galaxies that were more than 1 $h^{-1}$Mpc from any edge of the survey (although, of course, we used the galaxies near the edges to measure the densities of the galaxies just inside of them). Using the value of $H_0 = 70 kms^{-1}$, this corresponds to a physical distance of 0.71Mpc at $z$=1. We modelled the survey on the sky as a parallelogram and fitted straight lines (parameterised as $\delta = a_0 + a_1 \times \alpha$ where $\alpha$ and $\delta$ are the right ascension and declination

| Edge | $a_0$ | $a_1$ |
|---|---|---|
| 1 | -1.73 | 0.707 |
| 2 | -1.69 | 0.697 |
| 3 | 3.00 | -0.560 |
| 4 | 3.26 | -0.617 |

Table 4.1: Coefficients $a_0$ and $a_1$ of the straight line fits to $\alpha$ and $\delta$ where $\alpha$ and $\delta$ are in radians.

respectively, measured in radians) to galaxy positions along each of the four edges. The values of $a_0$ and $a_1$ are given in table 4.1 and the edges are plotted on figure 3.1.

After removing the galaxies within 1 $h^{-1}$Mpc of the survey edges defined in table 4.1 (and following the magnitude cut above), there were 91 radio sources and 2,817 DEEP2 galaxies remaining.

### 4.2.4 A Test of the Environment Density Calculation

To check the accuracy of our density measurements, we plot the fraction of red galaxies versus environmental density in three redshift bins and compare the results to those of the sample B from C06. At $z > 0.75$, this sample B includes galaxies from all four DEEP2 fields but at $0.4 < z < 0.75$ they only draw them from the EGS. We copy their separation of red and blue galaxies using a separation line in restframe $U - B$ versus $B$:

$$U - B = -0.032(M_B + 21.52) + 0.454 - 0.25 + 0.81 \tag{4.3}$$

This equation has been adapted from van Dokkum et al. (2000) who fitted a straight line to the colour-magnitude (CM) relation of distant red early-type galaxies in clusters. We use the same colour cut for all our galaxies, regardless of their redshift. This is sensible since the colours of red galaxies in DEEP2 do not vary strongly with redshift (Willmer et al., 2006). The 0.25 mag shift in $U - B$ is to ensure the line passes through the valley between the red sequence and blue cloud (Willmer et al., 2006). The 0.81 mag shift converts from the $Vega$ to the $AB$ magnitude system.

Using this separation, we compute the fraction of red galaxies as a function of density in bins of $\Delta$ $\mathrm{Log}_{10}(1 + \delta_3) = 0.775$ (as required by using 4 density bins) in each of the following redshift bins: $0.40 \leq z < 0.75$, $0.75 \leq z < 0.85$ and $0.85 \leq z < 1.1$. We choose these redshift bins for this analysis since those are the ones used by C06 to which we

wish to compare. We will use different redshift bins in the remainder of this chapter, as described in section 4.3.1. Figure 4.2 shows our results and also those of C06. Both studies plot $\mathrm{Log}_{10}(1 + \delta_3)$ on the abscissa as the density measurement. The agreement between the results and those of C06 is reasonable in the low redshift bin and excellent in the middle redshift bin. However, in the high redshift bin, we find lower fractions of red galaxies at all densities. Given the difference in the two lines at high redshift, it does not appear that the measurements of the densities are systematically wrong: no horizontal shift of the line would bring much improved agreement with C06. Moreover, we appear to be finding fewer red galaxies and we put this down to a selection effect arising from the different DEEP2 survey fields. In the three fields other than the EGS, various cuts were made to select galaxies with redshifts $> 0.7$ but no such cut was made in the EGS (Davis et al., 2007). One of these selection criteria was apparent $R - I > 1.1$. For a galaxy observed at $z \sim 0.7$, apparent $R - I$ is close to restframe $U - B$ and therefore it appears that this selection effect is to include more red galaxies (in restframe $U - B$) in these other three fields. Although there are other possibilities such as cosmic variance, we think it most likely that the difference between our line and that of C06 in the high redshift panel of figure 4.2 is due to this selection effect. With this caveat in mind, we accept the accuracy of the density measurements and proceed to measure the properties of the radio sources against their local environment densities.

## 4.3 Results

### 4.3.1 The Relation between Environment Density and Radio Emission Mechanism

Figure 4.3 shows environment overdensity versus $\Delta(U-R)$ (the proxy for the probability that the galaxy's radio emission is AGN-powered) for the radio sources in each of the two redshift bins used in chapter 3: $0.2 \leq z < 0.7$ and $0.7 \leq z < 1.4$, along with a panel for the whole redshift range. In the intermediate redshift panel, we find a weak trend of the density increasing with $\Delta(U - R)$ . This trend is not found in the high redshift panel where a horizontal line would easily fit through the error bars although it is seen in the combined redshift interval but it is weaker even than in the intermediate redshift interval. We have thus found very weak trends that radio sources whose radio emission is most certainly produced by star formation reside in underdense environments and that those radio sources whose radio emission is most certainly produced by AGN reside

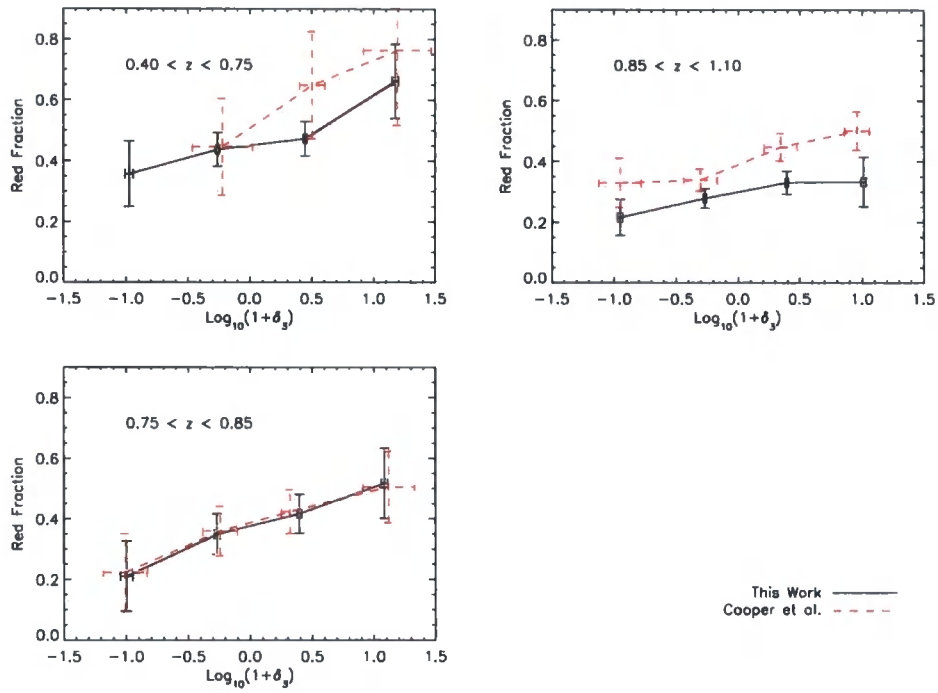


Figure 4.2: Fraction of red galaxies versus environmental overdensity for the current work (black, solid line) and for C06 (red, dashed line) in the same redshift bins used by C06 for their sample B. The points are plotted at the means in $x$ and $y$ of the galaxies in each bin. The error bars are the standard errors on the means. The agreement is reasonable in the lowest redshift panel and excellent at intermediate redshift. At high redshift, we find a lower fraction of red galaxies than C06 at all densities, probably due to a high-redshift selection effect. See text for details.

in overdense environments.

In each panel, we show the value of $\chi^2$ derived by comparing the graph with a horizontal line at the weighted mean of the ordinate values along with the probability that, in a $\chi^2$ distribution with the relevant number of degrees of freedom, a random variable $X$ would be more than the value of $\chi^2$ . This serves as a useful aide in assessing the significance of any trends shown on the plot. However, it shouldn't be believed blindly since, for example, it could be dominated by one bin with few galaxies in it if the values of the quantity being plotted are very close. The values of $\chi^2$ in figure 4.3 indicate that the trends described above are indeed weak since the probabilities of getting the values of $\chi^2$ are in excess of 0.05.

### 4.3.2 The Relation between Environment Density and Galaxy Colour

Next, we wish to find out whether the trends found in the local Universe by B04 of the percentage of SFGs and AGN dropping and staying constant with environment density respectively are present out to $z \sim 1$. We therefore plot these relationships in our two redshift intervals in figure 4.4. This figure shows the percentages of galaxies in each of three classes as a function of environment density. These three classes are: the radio sources we identify as being powered by AGN ($\Delta(U-R) > 0$), the radio sources we identify as being powered by star formation ($\Delta(U-R) <$ -0.4) and the entire radio sample (all values of $\Delta(U-R)$ , hereafter the *all* sample). Note that the third class is not simply the sum of the first two since it also includes those sources with -0.4$\leq\Delta(U-R)$ $\leq$0.0. We show this relationship at each of the redshift intervals used in figure 4.3. The values of $\chi^2$ and the meanings of the probabilities are also as in figure 4.3. The error bars in these plots are the standard errors of the means of the quantities in each bin. In the cases where there is only one galaxy in a bin, the error is estimated from those in the other bins in the following way: A straight line is fitted to the errors versus the number of galaxies in the bin which is then interpolated down to that for one galaxy.

In this plot, the percentages have been corrected for the effects of the DEEP2 redshift success rate varying with redshift, colour and magnitude in the following way. We use the weighting scheme presented in Willmer et al. (2006), kindly provided to us by private communication. For each spectroscopically observed galaxy, these weights are $\geq$1 and give the number of galaxies that that galaxy represents in a bin in apparent $R$ magnitude - apparent $(R-I)$ - apparent $(B-R)$ - redshift space. We use the weights in the "optimal" model in which the distribution of redshifts of red ($R-I > 1.03$) galaxies for which a

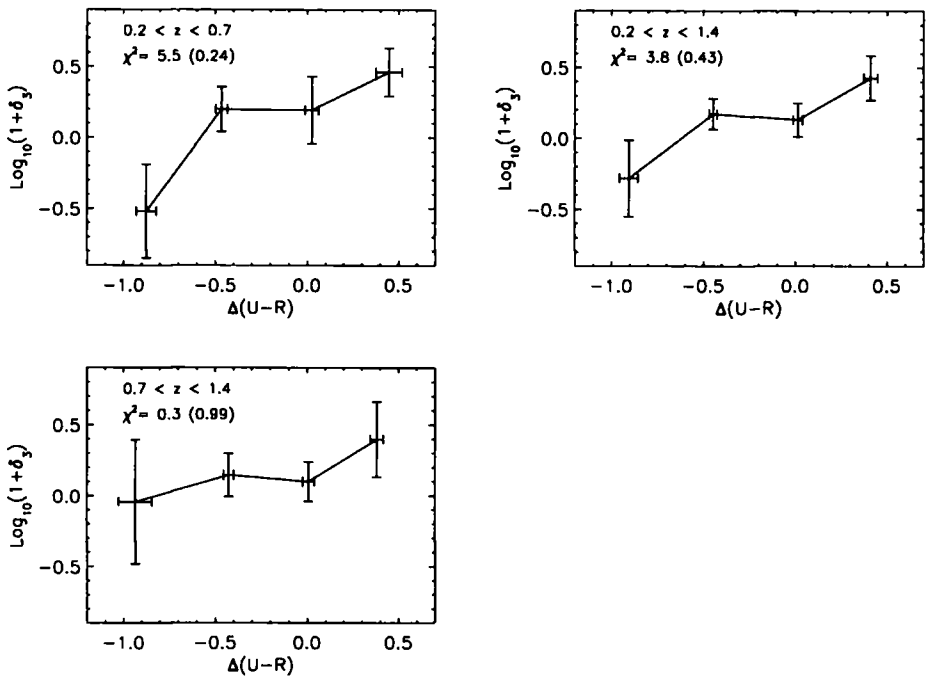


Figure 4.3: Environment overdensity versus $\Delta(U-R)$ (our proxy for the probability that a galaxy's radio emission is powered by an AGN; see text for details) in the intermediate and high redshift bins (top-left and bottom-left panels respectively) and in the combined redshift bin (top-right panel). The value of $\chi^2$ in each panel relates to the comparison between the graph and a horizontal line at the mean of the ordinate values. The numbers in brackets after each value of $\chi^2$ is the probability that, in a $\chi^2$ distribution with the relevant number of degrees of freedom, a random variable $X$ would be more than the value of $\chi^2$ . There is a very weak trend of increasing overdensity with increasing $\Delta(U-R)$ in the intermediate redshift panel but this trend is not seen in the high redshift panel and, in the combined redshift panel, is even weaker than that in the intermediate redshift panel.

redshift couldn't be obtained (the failures) is assumed to be that of those red galaxies that were observed (with redshift qualities of 3 and 4) and that the blue ($R - I < 1.03$) failures lie beyond the redshift range of the survey. We corrected the percentages plotted in figure 4.4 by multiplying the numbers of galaxies in each redshift-density-($U - R$) bin by the mean weight in that bin.

In the intermediate redshift panel, there is a fairly strong trend of the percentage of SFG decreasing with increasing density at low densities and being insensitive to the density at intermediate densities. There were no SFGs in the highest density regions at this redshift in our sample. On the other hand, the AGN percentage is insensitive to density at intermediate densities but increases in the highest density bin. In the high redshift panel, the SFG trend disappears and would be well-fitted by a horizontal line. The AGN trend is weaker than in the intermediate redshift bin. In the intermediate redshift panel, the *all* sample shows no consistent trend with density and would be well-fitted with a horizontal line. However, in the high redshift panel, it shows a weak trend of increasing with density. In the combined redshift panel, the trends found in the intermediate redshift panel are still seen although they are stronger in the case of the AGN and weaker in the case of the SFGs. The $\chi^2$ values backup the conclusion that the SFG trend in the intermediate redshift panel and the AGN trend in the combined redshift panel are strong ones and that all the others are weak. It is particularly noticeable that, in the combined redshift panel, the AGN and SFG samples do appear to have significantly different trends with environment density, given that the probability of each trend occurring by chance is $<0.2$.

### 4.3.3 The Relation between Environment Density and Radio Luminosity

Finally, in figure 4.5, we plot radio luminosity at 1.4GHz versus local environment density for the AGN and SFGs. We use the same redshift bins and meanings of $\chi^2$ as for figure 4.3. In the intermediate redshift panel, the SFG luminosities show no trend with density. The AGN luminosities are also insensitive to density apart from in the lowest density bin where they are lower. In the high redshift panel, the SFG luminosity graph is again consistent with a horizontal line. The AGN graph shows no consistent trend over the whole range of density but it does show significant deviation from a straight line. The sense of the deviation is that the AGN that reside in intermediate density environments have higher radio luminosities than those in the lowest and highest density regions. Looking at the two redshift periods together, the SFG luminosities again show

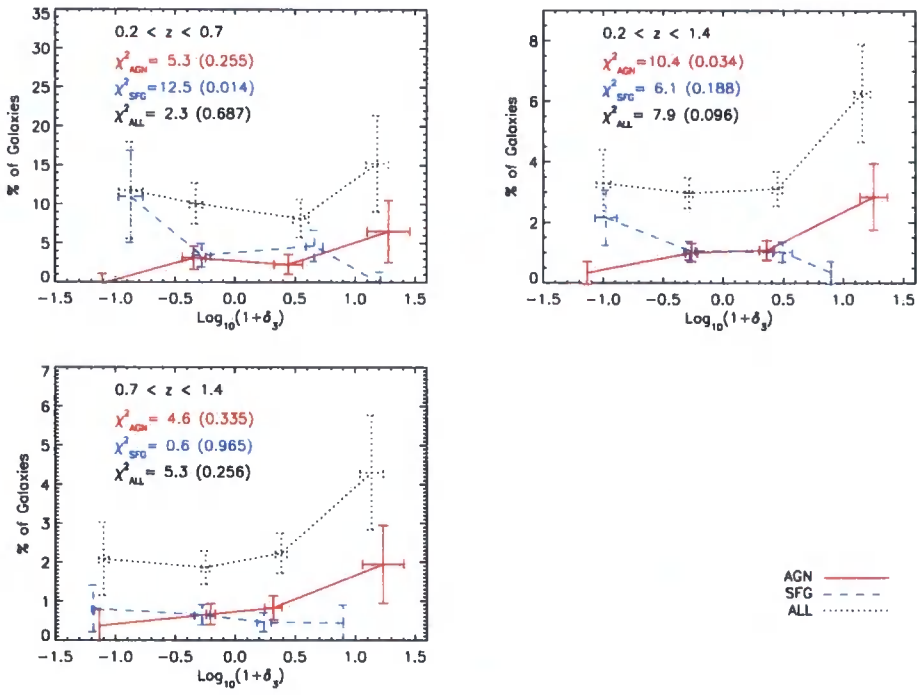


Figure 4.4: Percentage of galaxies we identify as radio-selected AGN, radio-selected SFGs and all the radio sources as a function of environment overdensity in the intermediate and high redshift bins (top-left and bottom-left panels respectively) and in the combined redshift bin (top-right panel). The samples labelled AGN and SFG are those galaxies with $\Delta(U-R) > 0.0$ and $< -0.4$ respectively (see text for details). The values of $\chi^2$ and the numbers in brackets are as for figure 4.3. In the intermediate redshift panel, both the SFG and AGN percentages show trends with density. The sense of the AGN trend is that there are more of them in the highest density regions and the trend is weak. The sense of the SFG trend is that there are more of them in the lowest density regions and the trend is strong. The *all* sample shows no dependence on density. However, in the high redshift panel, these AGN and SFG trends are not significant and the *all* sample is well fitted by a horizontal line. In the combined redshift panel the AGN and SFG trends can still be seen. Where the percentage in a given density bin was zero, we made a conservative estimate of the error on that percentage as the minimum error bar among those from that line on that plot where the percentage was non-zero.

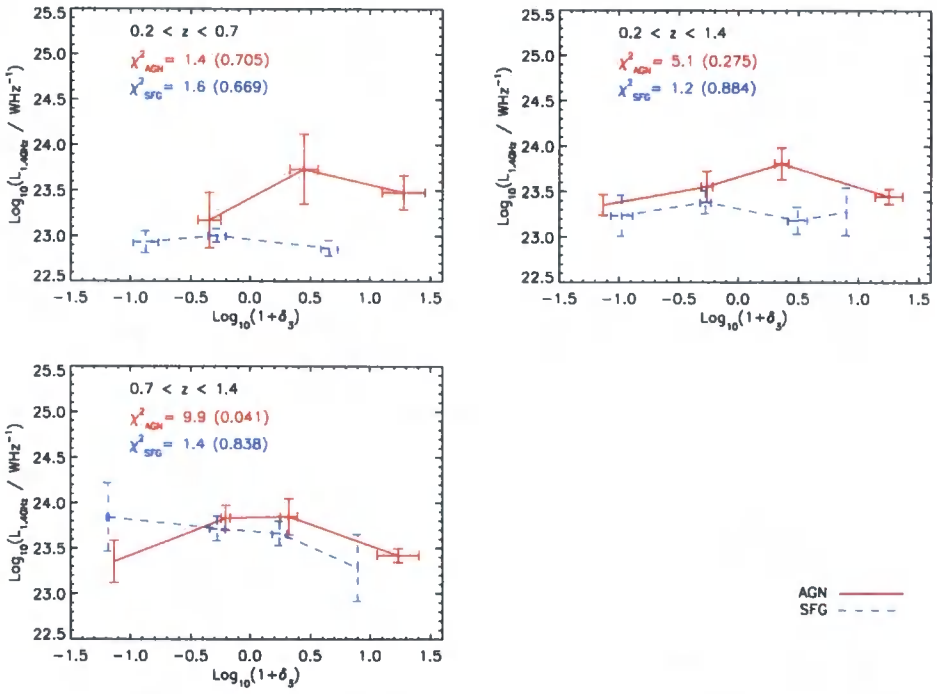


Figure 4.5: Radio luminosity versus environment overdensity in our intermediate and high redshift bins (top-left and bottom-left panels respectively) and in the combined redshift bin (top-right panel) for the same three samples shown in figure 4.4. The values of $\chi^2$ and the numbers in brackets are as for figure 4.3. In the intermediate redshift panel, none of the graphs deviate significantly from a straight line. In the high redshift panel, none of the samples show a continuous trend across the density range although the AGN luminosities are perhaps highest at the intermediate densities, dropping either side.

no dependence on density whilst the AGN still show a very weak trend of increased luminosity at intermediate densities. The values of $\chi^2$ for the SFGs are consistent with no trend in all three panels of figure 4.5. For the AGN, the only significant deviation from a straight line comes in the high redshift panel, as described.

## 4.4 Discussion

In this chapter we have taken the samples of radio-powered AGN and SFGs that we identified in chapter 3 and analysed the dependence of various properties of these galaxies upon the density of the environment in which they reside. We used three classes of

radio galaxies: (1) the AGN we identified in chapter 3, (2) the sample of SFGs we identified but with the removal of those galaxies most likely to contain a contribution to their radio emission from an AGN and (3) the whole sample of radio galaxies. We then further reduced these samples to include those brighter than a magnitude limit at which DEEP2 was complete in the red and blue. We checked the accuracy of our measure of environment against previous authors who used an almost identical data set and then carried out three studies using these environment density measures. These were to compare the densities to the probability of the radio emission being from an AGN or a star forming region, to plot the percentage of galaxies that are AGN or SFGs as a function of density and to compare the AGN and SFG radio luminosities to the densities.

Figure 4.3 shows very weak evidence that, the more likely a galaxy's radio emission is to be powered by an AGN, the denser is the environment in which it is likely to reside. Conversely, the more likely a galaxy's radio emission is to be powered by star formation, the less dense is the environment in which it is likely to reside. This trend, weak as it is, is only seen in the intermediate redshift interval. The trend is not strong enough to draw definite conclusions as to the environments of AGN and SFGs as shown by $\Delta(U - R)$ . We note, however, that in the intermediate redshift interval, this may be due to poor statistics rather than the lack of an inherent trend. It is possible that the trend is real but that it is masked by the large error bars. In the high redshift interval, this seems less likely since the line is flatter and we conclude that, if there is a trend, it gets weaker with increasing redshift.

Figure 4.4 shows that the percentage of galaxies that are star formation-powered radio sources decreases with environment density and that the fraction of galaxies that are AGN-powered radio sources increases with environment density. Both of these trends are stronger in the intermediate redshift interval than in the high redshift one where the SFG trend is not seen at all. The SFG trend in the intermediate redshift interval and the AGN trend in the combined redshift interval are particularly significant. These are interesting results because they mimic those of non-radio galaxies which show strong correlations between galaxy colour and environment density (e.g. Balogh et al. 2004, C06) and between star formation rates and environment density (e.g. Hashimoto et al. 1998, Gómez et al. 2003) found locally.

We see evolution in the SFG percentage-environment relationship. The sense of the evolution is for the trend to become weaker at higher redshifts. In the high redshift panel of figure 4.4, the error bars on the SFG line are no larger than those on the SFG line in

the intermediate redshift panel. The lack of a trend at high redshift, therefore, appears to be a conclusive result along with the strong trend found at intermediate redshift. This evolution adds weight to the argument that environment affects galaxies' star formation rates more as time progresses (the "nurture" picture of galaxy evolution). It also supports the idea that the combination of star formation being suppressed in dense environments and more galaxies residing in dense environments at later times is linked to the drop in the global mean SFR since $z \sim 1$.

Our trend for SFGs is in the same sense as that found locally by B04 (figure 4.1) though it is weaker in strength. B04 find the fraction of SFGs to vary by a factor of $\sim$20 over the full range of galaxy environments whereas, even in our intermediate redshift bin, we find the fraction to vary by only $\sim 6$. Taken together, the B04 result and our two redshift intervals show a progression of the SFG trend getting weaker with higher redshift.

The AGN evolution is inconclusive: our error bars are too large for us to be able to say whether or not the trend of AGN being found preferably in high density environments evolves. Even when combining our results with those of B04, we cannot conclude that the relationship evolves.

However, the AGN trend uncovered in this chapter does provide weak evidence that, at these redshifts, the triggering of an AGN is not driven so much by the availability of the cold gas as much as by the central black hole or by interactions and mergers according to the options discussed in section 4.1. This is because the one sure result we have for the AGN is that they are not suppressed in dense environments. If they were, this would be evidence that they required cold gas to be triggered since this cold gas has likely been swept away from these environments by ram-pressure stripping.

The absence of any dependence of SFG radio luminosity on environment in either of the redshift epochs is consistent with the result of Auger et al. (2008). The weak evidence that AGN radio luminosities are higher at intermediate densities at high redshift is intriguing. This could be due to the increased rate of mergers and interactions at these densities resulting from the best compromise between high number densities of galaxies and low velocity dispersions to maximise the frequency and significance of the interactions. Indeed, B04 found that AGN percentages were more dependent on group or cluster richness than local environment density and tended to be highest in galaxy groups and poor clusters.

In the local Universe, FR I sources are found preferentially in rich clusters whilst FR II

sources are more likely to be found in poor clusters or groups (e.g. Heckman et al. 1986). Since we have found no clear trends of radio luminosity across the whole density range explored, our results are consistent with a picture in which the IGM evolves to become less dense at later times. At high redshifts, a dense IGM would inhibit the formation of the giant radio lobes associated with FR II galaxies (e.g. Prestage and Peacock 1988) and thus reduce the strength of any trend of brighter radio sources being found in less dense environments.

## 4.5 Conclusions

The salient points of this chapter are summarised below. The intermediate redshift epoch refers to $0.2 \leq z < 0.7$ and the high redshift epoch to $0.7 \leq z < 1.4$.

- In the intermediate redshift epoch, there is a very weak trend of increasing local environment overdensity with increasing $\Delta(U-R)$, our proxy for the probability that the galaxy's radio emission is dominated by an AGN. This trend is especially strong in the lowest density environments. This trend is not seen in the high redshift epoch where the environment of a galaxy becomes insensitive to the origin of its radio emission.

- There is a weak trend of increasing AGN activity with increasing environment density in the intermediate redshift epoch. The results are inconclusive as to whether this trend evolves at higher redshifts. The dataset is too small and the error bars are too large.

- There is a strong trend of decreasing SF with increasing environment density in the intermediate redshift epoch, especially at the lowest densities. This trend disappears in the high redshift epoch where the SFR appears not to depend on the density. The lack of a trend at high redshift is also a significant result however and thus we find strong evidence for evolution in this trend with it getting stronger as cosmic time progresses.

- The luminosity of SFGs is independent of the density in both the intermediate and high redshift epochs.

- The radio luminosity of the AGN shows no continuous trend over the whole density range probed. However, there is weak evidence for increased AGN luminosity

at intermediate densities. This would be consistent with these AGN being associated with merging galaxies that are found preferentially at these densities.

# Chapter 5 | *The ROLES Survey*

The ROLES survey was initiated by Karl Glazebrook and Richard Bower. I have contributed to the project from the data reduction process onwards. In the declaration to this thesis I have described which elements of the work in this chapter have been done by other authors within the ROLES collaboration and which ones I have done.

## 5.1 Introduction

The assembly epoch of stellar mass in giant and dwarf galaxies remains a critical question in astrophysics and forms a key test confronting observations of galaxies at different redshifts with theory. It is now generally accepted that the assembly of cold dark matter (CDM, Blumenthal et al. 1984) follows a hierarchical bottom-up picture but this has long been at odds with the long standing observations that the most massive galaxies in the modern universe are the *oldest*, as measured by their stellar populations (e.g. Gallagher et al. 1984, Heavens et al. 2004). In recent years this issue has become known as *'cosmological downsizing'* where direct observations at high redshifts have shown that the most massive galaxies stopped forming stars at earlier epochs than less massive galaxies (e.g. Cowie et al. 1996, Juneau et al. 2005 (hereafter J05), Fontana et al. 2004, Mobasher et al. 2008). This is usually referred to as the 'top-down' paradigm.

This contradiction between the assembly of luminous and non-baryonic matter has been termed the 'Broken Hierarchy of Galaxy Formation' (Bower et al., 2006) and a major goal now of theoretical models is to explain this. There is no absolute contradiction between observations and theory: we do not find more galaxies or more baryons in galaxies at high redshifts than CDM halos could host for example. The key issue is what astrophysical and gas dynamical processes must operate to unwind the tight connection between baryons and dark matter laid down in the early Universe. Star formation must start earlier and proceed more efficiently in more massive halos but then be abruptly terminated at intermediate redshifts to make these objects red today.

Proposed solutions include intrinsic ones, such as using massive black holes known

to exist in active galactic nuclei (AGN) to quench star formation (e.g. Springel et al. 2005, Bower et al. 2006, Croton et al. 2006), and extrinsic ones, such as environmental forces on galaxies (Kauffmann et al. 2004, Menci et al. 2004). Exotic solutions actually modify the role of dark matter in driving galaxy formation, for example, making it self-interacting (Nusser et al., 2005). A critical observation to test these hypotheses is the direct measurement of star formation rate as a function of stellar mass in galaxies at different redshifts.

To date high redshift measurements have been focused on the most massive or the most highly star forming galaxies. Recent near-infrared selected spectroscopic surveys such as the Gemini Deep Deep Survey (GDDS, Abraham et al. 2004), K20 (Fontana et al., 2004) have pushed as deep as $K_{AB} \simeq 22.5$. These are desirable as the $K$-band allows a clean selection to be made on approximate stellar mass out to high redshifts and stellar mass is a robust quantity to compare with simulations. GDDS and K20 select $> 10^{11} M_{\odot}$ (stellar mass) galaxies to $z \simeq 2$ and $> 10^{10} M_{\odot}$ galaxies at $z \simeq 1$. Spectroscopic surveys serve to provide accurate redshifts and also to measure fluxes in nebular lines such as [OII] and H$\alpha$ which can be used to estimate star formation rates. However spectroscopy is generally not attempted for fainter continuum objects due to the much longer integration times required to assemble a large sample of objects. This results in a major limitation to earlier work such as J05 — the low mass bins at high redshifts are grossly incomplete, even though this is a relatively deep survey. Other spectroscopic work such as the Deep Extragalactic Evolutionary Probe (DEEP2, Davis et al. 2003, Willmer et al. 2006) and Virmos-VLT deep survey (VVDS, Le Fevre et al. 2003) are even shallower and only probe the most massive systems. The only studies of star formation in high- redshift low-mass systems either rely on photometric redshifts without spectral information (e.g. the Great Observatories Origins Deep Survey, GOODS, Dickinson et al. 2003) or use random Gamma Ray Burst events to select the spectroscopic targets (Savaglio et al., 2008).

In this chapter we report the first results from the 'Redshift One Emission Line Survey' (ROLES) which is the first survey to probe large numbers of $K$-selected and spectroscopically confirmed $10^8$–$10^9 M_{\odot}$ star forming dwarf galaxies at $z \simeq 1$ allowing critical measurements of the mass dependence of cosmic star formation history to be made. Such galaxies are as faint as $K_{AB} = 24, R_{AB} \sim 26$. This extra depth is achieved by three methods: firstly emission lines can be detected in spectra even when the spectral continuum cannot be. This then allows SFR measurements and the sample will not be biased by requiring the detection of the continuum. Secondly photometric redshifts in fields

with excellent multi-colour imaging allow pre-selection of galaxies in a redshift band near unity to very faint magnitude limits. Thirdly we use a matched band-limiting filter in our multi-slit spectroscopic observations to achieve a high- multiplex in a small area, thus we can tolerate a relatively low success rate for emission line galaxies.

We will therefore be in a position to add some more detail to the downsizing picture. In particular, we aim to answer the question of whether the global star formation rate density (SFRD) at $z \sim 1$ only has contributions from the most massive ($M_*/M_\odot \gtrsim 10^{9.5}$) galaxies. Alternatively, could there be a significant contribution from smaller galaxies that has thus far remained beyond the depth of spectroscopic studies at this redshift?

The structure of this chapter is as follows. In §5.2 we describe the ROLES project, the observations and the full data reduction pipeline. In §5.3 we describe our derivation of the star formation rates. Then §5.4 and §5.5 contain a discussion and our conclusions respectively. We adopt a flat cosmology with ($H_0$, $\Omega_m$) = (70, 0.3). All our magnitudes are on the AB system unless otherwise noted. $K_{\rm AB} = K_{\rm Vega} + 1.87$.

## 5.2 Method

### 5.2.1 Survey Design

ROLES (the Redshift One LDSS3 Emission line Survey) is designed to probe the SFRD in galaxies with stellar masses much lower than previously studied at redshifts of order unity. In order to do this efficiently, we adopt a novel survey strategy. We utilise fields with deep $K$-band photometry and photometric redshifts in order to pre-select galaxies which are most likely low-stellar mass systems at z$\sim$1. These galaxies are then followed up with multi-object optical spectroscopy in order to obtain both the redshift and star formation rate. To increase efficiency even further, we use a set of custom band-limiting filters to restrict the wavelength range (and hence the corresponding redshift range for a given rest frame wavelength) of our spectra and provide us with a high sampling density. We select $K$-faint ($22.5 < K \leq 24.0$) targets. Securing absorption line redshifts for galaxies this faint is extremely challenging and would require prohibitive amounts of telescope time. Indeed, one of the limitations of the GDDS work (J05) was that they required continuum detections for all their galaxies and this limited their depth. We therefore choose to use relatively modest exposure times ($\sim$ 4 hours on a 6.5-m telescope) and specifically target the [OII] emission line within our redshift window. With this approach, we will not obtain redshifts for galaxies without emission lines (to our

flux limit), but these do not contribute significantly to the SFRD. In this way, we obtain a mass-selected sample which, within the uncertainties of dust attenuation and the metallicity dependence of the conversion from [OII] flux to SFR (both discussed in section 5.4.5), is complete to a given SFR limit. Eventually, we aim to eliminate these uncertainties by extending the spectroscopic survey into the IR and measuring the star formation rates as traced by the IR emission and the $H_\alpha$ line.

Fields with both the depth and wealth of multi-colour imaging we require for this survey are currently scarce and were even scarcer at the outset of the programme. For ROLES, we use photometric catalogues and photometric redshifts from two imaging surveys in two different fields to select targets for follow-up spectroscopy: the *Chandra* Deep Field South (CDFS, Giavalisco et al. 2004, Mobasher et al. 2004), and the Faint Infra-Red Extragalactic Survey (FIRES, Franx et al. 2000, Förster Schreiber et al. 2006).

In this chapter, we present initial results from a subsample of our CDFS data. The observations upon which the present work is based were performed with the Low Dispersion Survey Spectrograph 3 (LDSS3) on the 6.5-m Clay telescope at Las Campanas Observatory. LDSS3 has a high throughput, as shown by the grism throughput curve in figure 5.1, taken from the LDSS3 website[1]) and by the filter transmission curve shown in figure 5.2. The mean throughput for the filter and grism is ~25%. LDSS3 also has a relatively large field of view (FOV) of diameter ~8.2′. It is thus well suited for obtaining spectra of large numbers of faint objects. The data were taken December 2006.

### 5.2.2 Sample selection & Spectroscopic Observations

For our LDSS3 spectroscopy, we obtained a set of four custom-band limiting filters to observe galaxies in well-defined redshift bins. In this work, we only consider the KG750 filter which covers approximately $(7500 \pm 500)$Å. Observations are on-going in both this filter and the KG650 [(6500±500)Å] and will be presented in future work. The transmission curve of the KG750 filter is shown in Fig. 5.2. Half-maxima occur at 7040 Å and 8010 Å and we adopt these as our wavelength limits. In targeting the [OII] line at 3727 Å, these limits correspond to a redshift range of $0.889 < z \leq 1.149$.

LDSS3 can perform multi-object spectroscopy (MOS) in nod-and-shuffle (N&S) mode (Glazebrook and Bland-Hawthorn, 2001), which allows extremely accurate sky-subtraction and thus allows us to reach lower flux limits than would otherwise be achievable with

[1] http://www.lco.cl/telescopes-information/magellan/instruments/telescopes-information/magellan/instruments/ldss-3/ldss-3-users-guide/users-guide

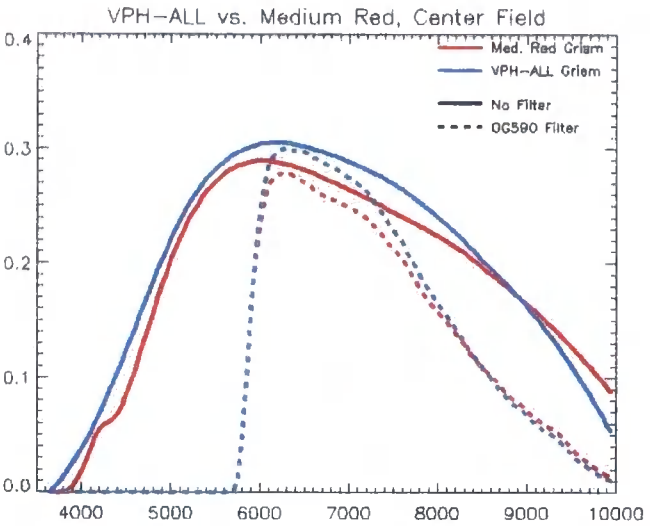


Figure 5.1: The throughput of the medium-red grism (the grism used in the present work; red, solid line) on LDSS3. The blue lines refer to a second grism not used in this work. The dotted lines show the grisms' throughput when they are used with a filter that only passes light above ~5900Å. Since this is not the filter used in this work, the only line relevant to this work is the red, solid one. Figure from LDSS3 website.

traditional MOS. This is particularly important in the wavelength window in which we are working, which is populated by numerous bright sky lines. We used the LDSS3 medium red grating (300 lines/mm, giving an average dispersion of $\sim 2.7$Å/pixel) and $0.8''$ wide slits which, with the plate scale of $0.189''$/pixel, gives a resolution of 11.4Å FWHM. Our N&S observations utilised $3''$ long slits, observing each target galaxy for 60s in one half of the slit and then nodding the telescope $1.2''$ and observing for another 60s at a second position within the slit. We refer to these two positions as A and B for convenience. By nodding within the slit, we observe the galaxy for the total time the detector shutter is open. Charge is shuffled along the detector between the A and B observations by 16 pixels (corresponding to the slit width of $3''$), so that we end up with two exposures for each galaxy, stored in different locations on the CCD. Because the telescope was nodded between exposures, the B exposure contains observations of the sky at the location of the galaxy in the A exposure and vice-versa. Thus sky-subtraction can be achieved simply by subtracting the A observation from the B. This process is described in more detail in the next section.

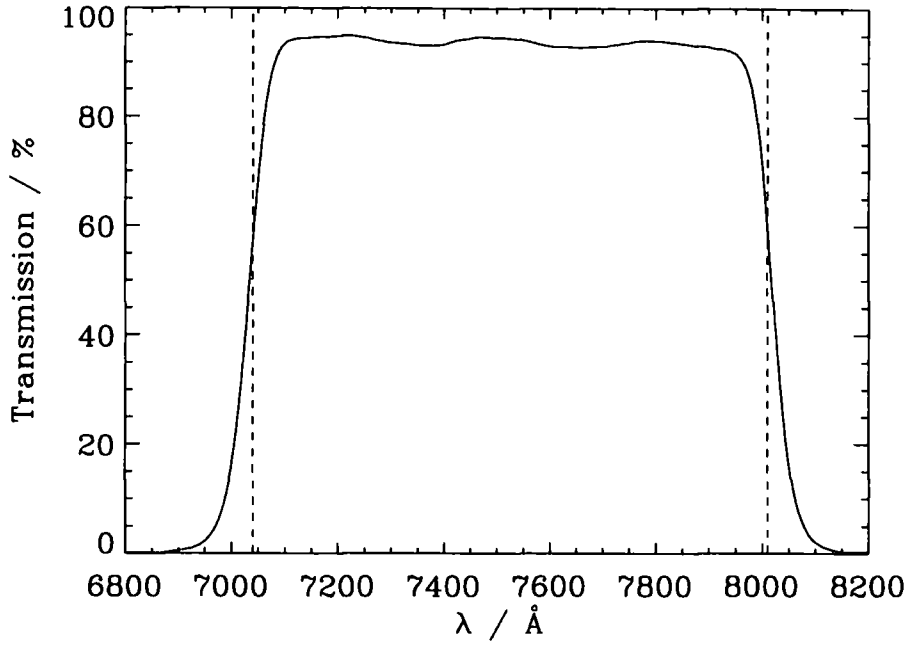


Figure 5.2: The transmission curve of the KG750 filter. The dashed lines at the half-maxima denote the minimum and maximum wavelengths used for line detection, 7040Å–8010Å.

With the above parameters, we can place an average of almost 200 objects in each mask over the ~8.2 arcmin diameter circular field of view of LDSS3. To select targets, we prioritised galaxies by assigning a weight to them based on their $K$-band magnitude, photometric redshift and its error. We primarily targeted galaxies in the range $22.5 < K \leq 24.0$. We used the photometric redshifts and 95% confidence intervals kindly provided by B. Mobasher and T. Dahlen to give higher weighting to those galaxies whose error bars placed them within (or overlapping with) our redshift window ($0.889 < z \leq 1.149$). We also gave higher priority to galaxies with smaller photometric errors. Once weights were assigned to each galaxy, slits were randomly allocated to objects, sorted by priority. Due to geometrical constraints, once all the highest priority targets were assigned, the mask was filled with lower priority targets (typically poorer photometric redshifts or $K$ magnitudes outside our main sample). The total weight for all targets allocated in the mask was then calculated and a Monte-Carlo technique used to design many realisations, keeping the version with the highest weight. Multiple masks at the same pointing position were then designed, giving highest priority to those galaxies not already observed in a previous mask (but repeats of some slits occur

Table 5.1: Summary of the observations. The CDFS field is centred on $\alpha$ = 03:32:27.600, $\delta$ = -27:45:00.00.

| Mask | Field | Number of exposures | Total exposure time /$ks$ | Obs. Date | Seeing / " |
|---|---|---|---|---|---|
| 4 | CDFS | 9 | 21.6 | 12/2006 | 0.6 |
| 5 | CDFS | 6 | 14.4 | 12/2006 | 0.5 |
| 6 | CDFS | 6 | 14.4 | 12/2006 | 0.5 |

and are useful for checking purposes, discussed later). The exact details of the object prioritising are not used to construct our completeness ratios because of complex interactions of geometric constraints. We therefore calculate our completeness *a posteriori* in §5.3.2. Moreover we eventually observe enough targets that we are highly complete for all galaxies within our $K$ magnitude range after ~6 masks. The main effect of the prioritisation is to ensure a relatively high completeness after only a few (~3) masks have been observed.

We exposed each mask for typically 20 N&S cycles of 60s exposures at each of the A and B positions, resulting in an exposure time of 40 minutes for each image. We typically took 6 exposures resulting in a total integration time of four hours. A log of the observations in given in Table 5.1.

### 5.2.3 Spectroscopic data reduction

#### 5.2.3.1 Pre-processing

In addition to standard spectral CCD data pre-processing (overscan subtraction, flatfielding, bad pixel masking etc.) a number of non-standard steps are necessary for our data, which we detail here. We used several routines from the Carnegie Observatories System for Multi-Object Spectroscopy 2 (COSMOS2[2]), but the majority were applied using custom written routines in IDL.

Firstly we used the COSMOS2 STITCH routine to combine the images from the two separate LDSS3 amplifiers into a single frame and convert the counts in the image into electrons. Overscan subtraction, bad pixel masking and flatfielding were then performed.

The repeated charge shuffling involved with N&S observations can cause artifacts which appear as short streaks along certain columns of the CCD. This is due to localised

[2]see http://users.ociw.edu/oemler/COSMOS2/COSMOS2.html.

defects ('charge traps') in the CCD which cause the charge to become smeared as it passes over them. This was partially removed by taking dark and flat frames in N&S mode and using these to flag affected areas in the bad pixel masks. However some of these charge traps still remained and we discuss how these were dealt with in §5.2.4.

Flexure within the instrument over an extended period of observations can cause small shifts (of the order of a few pixels) between exposures on the detector of a given feature. In order to correct for this, the positions of several bright emission lines visible in the raw frames were measured and the relative shifts found and corrected for.

#### 5.2.3.2 Sky-subtraction

For each individual exposure (see Fig. 5.3, panel a), N&S sky subtraction is performed by shifting the image by the shuffle distance (16 pixels) in the spatial direction and subtracting it from itself (Fig. 5.3, panel b). If we consider A-B, in the notation introduced in the previous section, every slit will now contain a positive image of galaxy spectrum A′ (where we use the prime to denote a sky-subtracted spectrum) and a negative image of spectrum B′ of the same galaxy, both with the sky removed. We next median-combine all our individual exposures with $5\sigma$ outlier-rejection to remove cosmic rays (Fig. 5.3, panel d). In order to be left with a positive, summed image of the galaxies, we can simply shift the sky-subtracted spectra by their separation (which is equal to the nod distance, 1.2″) and subtract them, A′-B′ (Fig. 5.3, panel e). We refer to the 2D, sky-subtracted and summed spectra obtained in this way as 'nod-folded' images. This then leaves us with the final, reduced 2D spectra from which we will make measurements such as line flux. However, in order to optimally detect emission lines in the first place, we will further process the images to produce optimally filtered versions. We also require an estimate of the noise in each pixel of our detection images to assess the significance of our detections, which we describe below.

#### 5.2.3.3 Noise estimation

By following a similar procedure to the sky-subtraction just described (i.e. shifting a copy of the image by the shuffle distance), but *adding* instead of *subtracting* the frames, we produce an image which contains a spectrum of the sky instead of the galaxy at the positions of the galaxies (A and B) in each slit (Fig. 5.3, panel c). By again median-combining the individual exposures our best estimate of the value of the sky at each

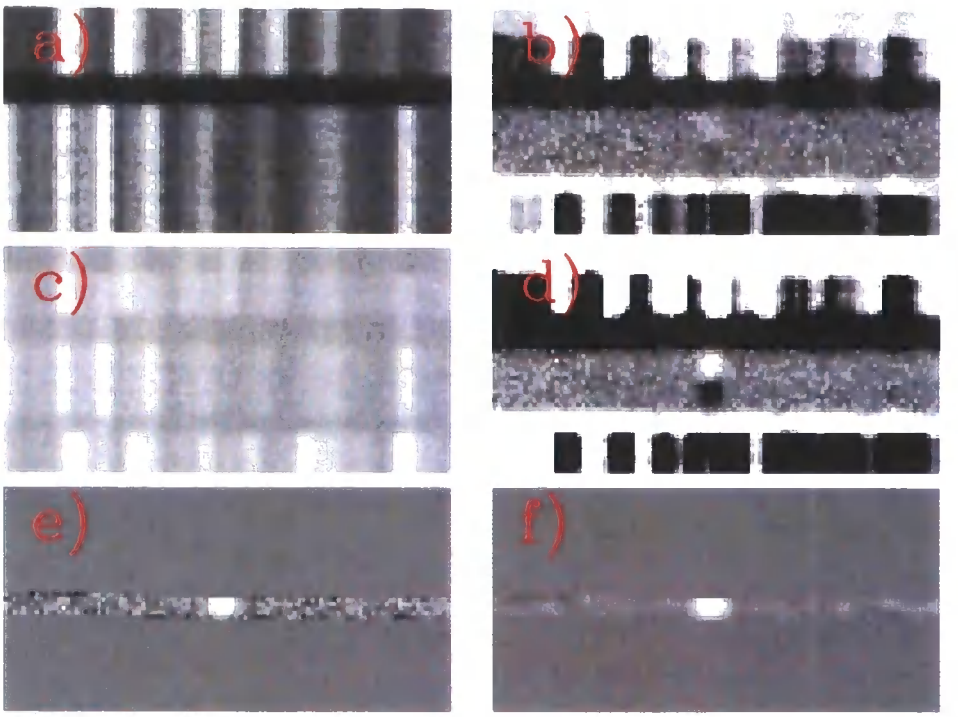


Figure 5.3: Examples of the various steps in the data reduction, showing a region centred on a bright emission line. The six panels each show a region of ~135 Å in the spectral (horizontal) direction by 25 pixels in the spatial (vertical) direction. Panel (a): the initial individual frame. Panel (b): the same frame after sky-subtraction (by shifting a copy of the image by 16 pixels and subtracting). The dipole signature of an emission line is now visible. Panel (c): the initial frame after adding instead of subtracting the two shuffled regions to produce an image of the sky. Panel (d): frames from step (b) after median combination of several exposures. Panel (e): co-addition of the positive and negative components of the dipole by 'nod-folding' and masking (see text for details). Panel (f): after convolution with the 2D Gaussian kernel.

pixel. We use this to estimate our noise, $N_{exp}$, in each pixel of each nod position in an individual exposure. The noise in the $i, j^{th}$ pixel is given by

$$N_{exp,ij} = \sqrt{| < sky > |_{ij} + 2R^2}, \tag{5.1}$$

where $< sky >$ is the median-combined sky frame, $R$ is the read noise of the detector (3.4 electrons), and the factor of 2 accounts for the fact that two readouts have been combined in the sky-subtraction/addition by using the two shuffle positions.

After stacking $n_{frames}$ exposures to form a mean, the noise in the $i, j^{th}$ pixel, $N_{com,ij}$, becomes

$$N_{com,ij} = N_{exp,ij}/\sqrt{n_{frames}}. \tag{5.2}$$

Once the combined frame is nod-folded to produce an image containing the sum of the objects, the noise in the $i, j^{th}$ pixel of the final combined science image is then

$$N_{ij} = \sqrt{N^2_{com_{A'},ij} + N^2_{com_{B'},ij}}, \tag{5.3}$$

which is just the quadrature sum of the A′ and B′ position noise values.

The following stages of the reduction pipeline (line detection onwards) require knowledge of where the slits lay on the detector. In order to map the slits, we ran all the data through COSMOS2[3], since this uses an optical model for the instrument to provide a convenient way to find and trace the slits and wavelength calibrate them to our He-NeAr reference arc. We used the mapping provided by COSMOS2 to convert spatial position and wavelength for each slit into $x$ and $y$ pixel coordinates on our IDL-reduced frames. We only use COSMOS2 for calculating this mapping rather than for completely reducing our data, since COSMOS2 would resample the data which would complicate line-detection by correlating the noise between neighbouring pixels. In this way, we stay with our original non-resampled pixels, but now possess a mapping between slit spatial and spectral and detector coordinates. We refine the mapping between detector coordinates and wavelength by fitting for a wavelength shift using the positions of several bright, isolated skylines. This resulted in an r.m.s. wavelength calibration accuracy of $\sim$3Å ($\sim$ 1 pixel or $\sim$ one quarter of the FWHM). Finally, pixel masks were created so that, for line detection, we only consider regions of the CCD occupied by slits. For these

[3]We used STITCH, ALIGN-MASK, MAP-SPECTRA, SPECTRAL-MAP, SFLATS, BIASFLAT, SUBSKY, EXTRACT-2DSPEC and SUMSPEC

slits we only use pixels within our wavelength limits (7040Å–8010Å) in the spectral direction and 5 high, centred on the expected object position within the slit in the spatial direction. All other pixels are flagged as 'bad' and not considered further.

### 5.2.4 Line Detection

#### 5.2.4.1 Optimal filtering

We wish to search our 2-d spectra for significant features consistent with emission lines from our target galaxies. Since the optimal detection kernel is the profile of the line itself, we start by finding several obvious bright lines, easily visible by eye, and measuring their profiles and assume that faint lines have the same profile. We find that they are typically well-approximated by elliptical Gaussians with FWHM of 5 pixels in the spectral direction and 3.5 pixels in the spatial direction. The kernel was normalised by setting its total to unity so as to conserve flux. We convolve our science images with this kernel, producing a signal frame, $S$ (Fig. 5.3, panel f).

This convolution changes the properties of the noise in each pixel from $N_{ij}$ to $N_{conv,ij}$ where

$$N_{conv,ij} = \sqrt{N_{ij}^2 \otimes k^2}, \tag{5.4}$$

where $k$ is the emission line-shaped kernel described above. $N_{conv,ij}$ is thus the quadrature sum of the contributions of each pixel in the kernel to the noise in the $i, j^{th}$ pixel.

Now, for the $i, j^{th}$ pixel, the significance, $\sigma$, is given by

$$\sigma_{ij} = \frac{S_{ij} - b_{ij}}{N_{conv,ij}} \tag{5.5}$$

where $b_{ij}$ is the local background (continuum) estimated from the mean of all pixels in two 1D side-bands, each 40 pixels wide, ranging from $i + 10$ to $i + 50$ pixels and $i - 10$ to $i - 50$ (or whatever number of pixels from these regions falls on pixels of the science spectrum flagged as good). It is appropriate to only measure the continuum in a 1D box (i.e. a line at the position of the $j^{th}$ pixel) in this way, since the image has already been convolved with a kernel in the spatial ($j$) direction and thus contains an estimate using values from multiple pixels in this direction.

We calculated the significance of each pixel in the science spectra and located the most significant peaks. If a peak lay closer than 2 pixels in the spatial direction or 1

pixel in the spectral direction to a more significant neighbouring peak, the former was rejected.

#### 5.2.4.2 Catalogue cleaning

A couple of different artifacts are present in our data which our line detection code also finds. These are residual charge traps (as described above) and weak galaxy continuum just above the noise limit of our data. The former is relatively easy to deal with in an automated way.

Since charge traps are only one pixel wide (in the row/spectral direction) they are easily identified with some form of sharpness criterion. They can be found quite simply by comparing the amplitude of the signal in the convolved frame with that in the original, unconvolved frame. In the case of charge traps, this ratio is low (since neighbouring pixels in the spectral direction do not contribute significant counts to the amplitude in the convolved frame, as they would for a real emission line). In order to maximise the difference, instead of using the full 2D convolution, we instead just convolve our science frame with a 1D version of the kernel, just in the spectral direction. In practice, we searched for the peak pixel in the unconvolved image in a 3×3 pixel box centred on the peak pixel of the convolved frame. This allowed for any possible mis-centring caused by the convolution. To remove charge traps, we adopted a threshold for the ratio of convolved-to-unconvolved peak amplitude $< 0.4$, and found that all lines in this category were clearly bright charge traps. Thus, such spurious lines are automatically rejected.

Dealing with spurious detections of weak continuum was harder to automate. Such cases are clear from the 1D spectra as very broad emission (many times broader than that expected for our emission lines). It appears that we only detect broad continua as emission for a small subsample of all continuum objects: where this feature falls between the two side-bands we use for estimating the continuum level, and thus does not get correctly subtracted. We only find perhaps half a dozen such cases per mask, and so it is feasible to objectively delete these by hand.

Figures 5.4 and 5.5 show examples of our convolved and un-convolved 2D and 1D spectra for a range of line significances. We visually inspected such plots, sorted by significance, for all objects. A reasonably clear cut-off in the reliability of lines was seen at $\sim 4.5\sigma$ in our units. Above this limit, the shapes of the lines in all the plots appeared broadly consistent with each other. There are several tests we can perform to assess the

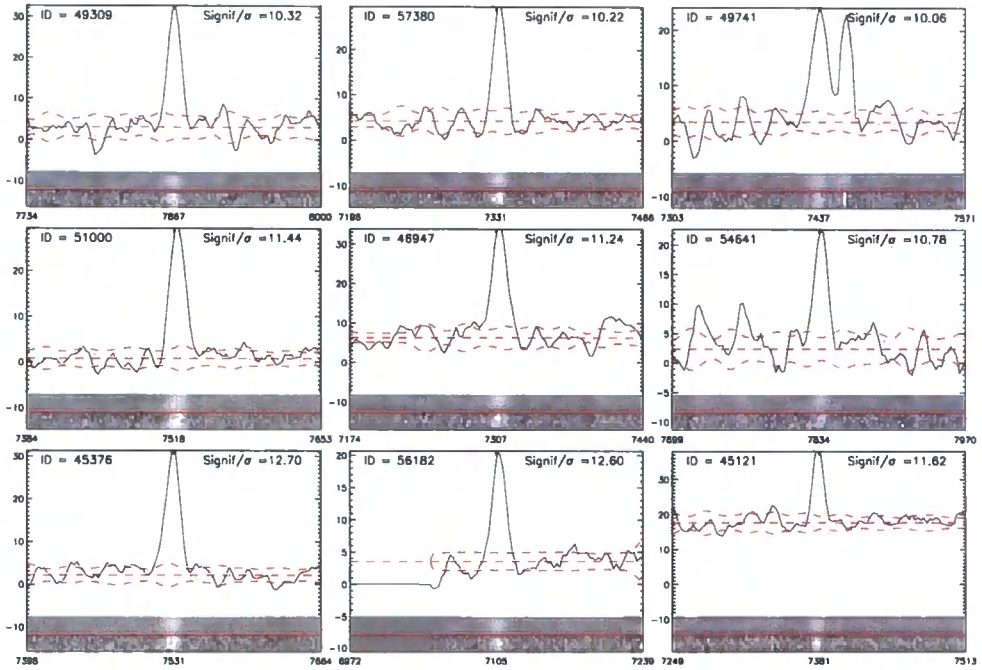


Figure 5.4: Examples of our 1- and 2-D spectra from mask 4 (CDFS). The lines are ordered according to their significance starting with the most significant in the bottom left corner and going left to right, row by row. The examples cover a range of line significances from ∼13 down to ∼10. The bottom 2-D spectrum is that from the unconvolved nod-folded signal frame and the top one from the convolved nod-folded signal frame (see text). The 1-D spectrum (black line) is taken from the middle row of the convolved frame. The red, dashed horizontal line shows the estimated continuum as described in the text and the red dashed lines either side of it show the 1 $\sigma$ deviations from the continuum as measured in the convolved masked nodfolded noise frame.

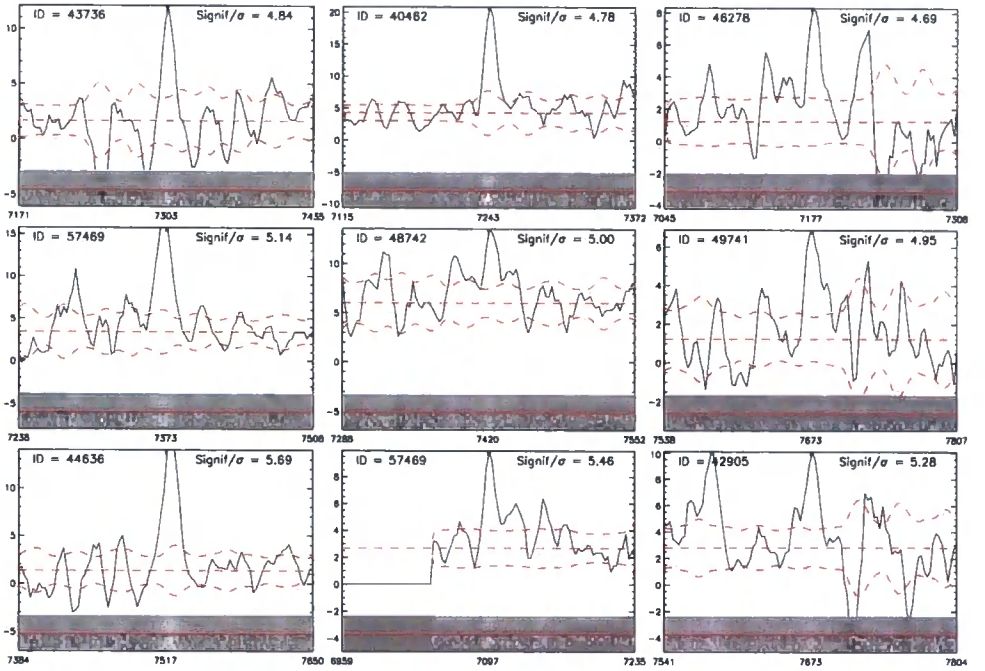


Figure 5.5: Same as figure 5.4 but for less significant lines (significance $< 6$).

reliability of our emission line catalogue.

#### 5.2.4.3 Tests of emission line catalogue

The most basic test we can do is to compare the properties of emission lines detected in our catalogue with repeat observations of the same galaxy observed in a different mask. Of all the detections in our $> 4.5\sigma$ catalogue, three galaxies observed in more than one mask show an emission line detection. All three of these have the emission line detection reproduced in the repeat observation, and the properties of the detection in terms of its measured wavelength, significance and line flux agree well. These measurements are tabulated in Table 5.2.

A second internal test of our catalogue is possible for those galaxies with multiple emission lines. We can attempt to measure redshifts from multiple lines and check that the wavelengths of the lines detected are consistent with a single redshift for the object. We do this by considering all possible combinations of common galaxy emission lines, compared with the observed wavelengths of our detected lines. We allow for an uncertainty in the observed wavelength of 3Å as suggested by our internal check in Table 5.2. Out of a sample of 64 objects with multiple lines $> 4.5\sigma$ significance, we don't find any

Table 5.2: Reproducibility of emission line properties for galaxies observed in more than one mask.

| mask | Galaxy ID | $\lambda_{em}$ | $\sigma$ | flux / erg cm$^{-2}s^{-1}$ |
|---|---|---|---|---|
| 4 | 41303 | 7429.60 | 7.3 | 3.79e-18 |
| 6 | 41303 | 7426.10 | 6.4 | 2.79e-18 |
| 4 | 42848 | 7421.20 | 13.4 | 7.65e-18 |
| 6 | 42848 | 7422.20 | 16.7 | 7.49e-18 |
| 4 | 46115 | 7602.00 | 7.0 | 1.39e-17 |
| 6 | 46115 | 7603.00 | 8.5 | 1.60e-17 |

which are inconsistent with a single redshift for the object.

As a further test for these multiple line objects, since the multiple lines uniquely define a redshift for the object, we can compare these redshifts from our data with others available from the literature. Where possible, we use spectroscopic redshifts. We use the compilation from Wuyts et al. (2008) and only consider secure redshifts (their quality flag 1.0). If a spectroscopic redshift is not available, we use their photometric redshift. This comparison is shown in Fig. 5.6 and we find excellent agreement between our multiple line redshifts and the independent spectroscopic or photometric redshifts.

#### 5.2.4.4 The Final Sample

The final cut is to only include objects with $22.5 \leq K_{AB} < 24.0$. This yields a final sample of 64 galaxies.

### 5.2.5 Line identification

For the majority of our emission line objects, we detect only a single line and thus the spectrum on its own gives an ambiguous redshift. Thus we must make use of additional data to determine a redshift. For a subsample of our objects, spectroscopic redshifts are available from public spectroscopy. We again use the compilation from Wuyts et al. (2008), considering only secure redshifts. For most of our objects, spectroscopic redshifts are not available and we must use photometric redshifts in order to determine the most likely identity of our emission line. Since our survey began, more accurate public photometric redshifts (FIREWORKS, Wuyts et al. 2008) for the CDFS have become available. They utilise many more filters and cover a wider wavelength range than those used in the Mobasher & Dahlen catalogues and hereafter we adopt these. The most probable

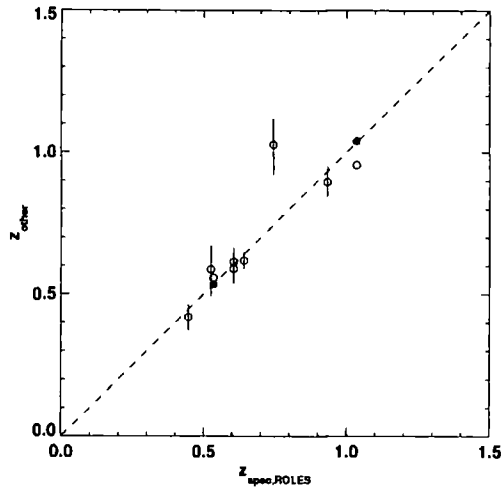


Figure 5.6: Comparison of secure spectroscopic redshifts from ROLES galaxies possessing multiple emission lines with independent redshift measurements from the literature. Open circles with error bars denote photometric redshifts from the FIREWORKS catalogue; filled circles denote secure spectroscopic redshifts from publicly available spectroscopy.

identities of strong emission lines in our survey are [OII] ($0.889 < z < 1.149$), H$\alpha$ ($0.073 < z < 0.220$) or one of H$\beta$ or [OIII] ($0.406 < z < 0.648$). Since we only care whether the line is [OII] we consider the likelihood that it is [OII] versus it is one of the other lines. In order to do this, we consider the probability distribution functions (PDFs) for the photometric redshifts kindly provided to us by S. Wuyts. We integrate the photo-z PDF over the redshift range for which we could detect [OII] and compare this with the PDF integrated over the three different redshift windows just described. The ratio then gives the probability that the line is [OII] ($P_{\rm OII}$). If the probability is $P_{\rm OII}$ <0.1 we set it to zero (i.e. assume it is not [OII] ) and for $P_{\rm OII}$ >0.9 we set it to unity (assume it is definitely [OII] ). The majority of our detections fall into one of these categories. For the few cases where $0.1 < P_{\rm OII} < 0.9$ we propagate this weighting through our analysis such that these galaxies contribute a fraction $P_{\rm OII}$ of their properties to the measurement under consideration (i.e. a galaxy with $P_{\rm OII} = 0.5$ would contribute half its [OII] flux to a measurement of the total [OII] flux). In Fig 5.7 we show examples of PDFs for the three different cases.

We summarise the properties of all our selected lines in Table 5.3.

Table 5.3: Our emission line catalogue: detections which we identify as [OII] . (Part 1)

| Galaxy ID | RA | Dec | $\lambda_{em}$ | $z_{em}$ | $\sigma$ | $f_{[OII]}$ | $P_{OII}$ | $K_{AB}$ | SFR | $\log(M_s)$ | comments |
|---|---|---|---|---|---|---|---|---|---|---|---|
| 41128 | 03:32:18.78 | -27:48:20.8 | 7449.9 | 0.9989 | 24.3 | 1.170e-17 | 1.00 | 22.99 | 1.340 | 9.208 | |
| 41318 | 03:32:35.70 | -27:48:15.5 | 7101.1 | 0.9053 | 35.9 | 1.070e-17 | 1.00 | 23.55 | 0.958 | 8.860 | |
| 41319 | 03:32:22.53 | -27:48:17.4 | 7307.9 | 0.9608 | 17.8 | 1.090e-17 | 1.00 | 22.12 | 1.140 | 9.558 | |
| 42009 | 03:32:30.98 | -27:47:54.2 | 7061.2 | 0.8946 | 6.9 | 2.360e-18 | 1.00 | 23.74 | 0.205 | 8.762 | |
| 42198 | 03:32:28.62 | -27:47:49.2 | 7815.9 | 1.0971 | 6.1 | 8.450e-18 | 1.00 | 23.39 | 1.220 | 9.133 | |
| 42704 | 03:32:39.88 | -27:47:38.1 | 7591.2 | 1.0368 | 11.4 | 1.560e-17 | 1.00 | 23.33 | 1.960 | 9.094 | |
| 42848 | 03:32:41.12 | -27:47:34.6 | 7422.3 | 0.9915 | 16.7 | 7.490e-18 | 1.00 | 23.30 | 0.840 | 9.061 | |
| 43649 | 03:32:39.39 | -27:47:14.3 | 7812.5 | 1.0962 | 26.6 | 2.910e-17 | 1.00 | 23.78 | 4.190 | 8.957 | |
| 44349 | 03:32:42.78 | -27:46:59.1 | 7901.2 | 1.1200 | 25.0 | 2.230e-17 | 1.00 | 22.62 | 3.380 | 9.494 | |
| 44370 | 03:32:36.45 | -27:46:58.3 | 7135.0 | 0.9144 | 6.5 | 3.010e-18 | 1.00 | 23.03 | 0.276 | 9.100 | |
| 44502 | 03:32:36.45 | -27:46:55.0 | 7052.2 | 0.8922 | 16.6 | 6.260e-18 | 1.00 | 22.94 | 0.541 | 9.115 | |
| 45277 | 03:32:35.47 | -27:46:37.1 | 7779.0 | 1.0872 | 16.1 | 1.560e-17 | 1.00 | 22.64 | 2.190 | 9.453 | |
| 45296 | 03:32:41.52 | -27:46:40.3 | 7812.5 | 1.0962 | 16.7 | 1.690e-17 | 1.00 | 23.13 | 2.420 | 9.246 | |
| 45376 | 03:32:15.74 | -27:46:32.4 | 7532.6 | 1.0211 | 12.7 | 1.090e-17 | 1.00 | 23.22 | 1.310 | 9.129 | |
| 45441 | 03:32:15.00 | -27:46:33.4 | 7858.0 | 1.1084 | 4.9 | 8.000e-18 | 1.00 | 23.50 | 1.180 | 9.092 | |
| 45603 | 03:32:12.82 | -27:46:27.7 | 7584.8 | 1.0351 | 12.4 | 1.120e-17 | 1.00 | 23.83 | 1.400 | 8.871 | |
| 45731 | 03:32:24.13 | -27:46:25.2 | 7515.9 | 1.0166 | 16.7 | 1.140e-17 | 1.00 | 23.17 | 1.360 | 9.145 | |
| 45952 | 03:32:24.31 | -27:46:21.9 | 7516.6 | 1.0168 | 23.1 | 1.720e-17 | 1.00 | 22.57 | 2.060 | 9.413 | |
| 46115 | 03:32:11.79 | -27:46:24.5 | 7603.1 | 1.0400 | 8.5 | 1.600e-17 | 1.00 | 23.02 | 2.020 | 9.237 | |

| Galaxy ID | RA | Dec | $\lambda_{em}$ | $z_{em}$ | $\sigma$ | $f_{[OII]}$ | $P_{OII}$ | $K_{AB}$ | SFR | $\log(M_s)$ | comments |
|---|---|---|---|---|---|---|---|---|---|---|---|
| 46278 | 03:32:36.96 | -27:46:15.7 | 7177.8 | 0.9259 | 4.7 | 2.500e-18 | 1.00 | 22.91 | 0.237 | 9.166 | |
| 46281 | 03:32:26.83 | -27:46:14.9 | 7061.2 | 0.8946 | 5.7 | 2.140e-18 | 1.00 | 23.38 | 0.187 | 8.924 | |
| 46747 | 03:32:25.98 | -27:46:04.1 | 7445.4 | 0.9977 | 35.9 | 2.270e-17 | 1.00 | 22.64 | 2.590 | 9.362 | |
| 46862 | 03:32:38.37 | -27:46:00.7 | 7594.1 | 1.0376 | 8.9 | 1.380e-17 | 1.00 | 23.12 | 1.730 | 9.190 | |
| 46947 | 03:32:32.55 | -27:45:59.9 | 7308.6 | 0.9610 | 11.2 | 7.830e-18 | 1.00 | 22.51 | 0.813 | 9.383 | |
| 47189 | 03:32:25.66 | -27:45:55.6 | 7584.1 | 1.0349 | 51.2 | 5.070e-17 | 1.00 | 22.60 | 6.320 | 9.421 | [OII] [NeIII] |
| 47961 | 03:32:40.42 | -27:45:38.2 | 7308.3 | 0.9609 | 8.2 | 6.500e-18 | 1.00 | 22.86 | 0.675 | 9.225 | |
| 48828 | 03:32:39.58 | -27:45:20.8 | 7540.5 | 1.0232 | 17.6 | 8.990e-18 | 1.00 | 22.97 | 1.090 | 9.242 | |
| 49167 | 03:32:37.90 | -27:45:08.1 | 7512.5 | 1.0157 | 12.3 | 6.710e-18 | 1.00 | 22.83 | 0.799 | 9.296 | |
| 49349 | 03:32:28.80 | -27:45:03.5 | 7364.6 | 0.9760 | 6.0 | 5.440e-18 | 0.82 | 23.49 | 0.587 | 8.963 | |
| 49369 | 03:32:24.02 | -27:45:04.1 | 7866.6 | 1.1107 | 10.1 | 1.210e-17 | 1.00 | 22.73 | 1.800 | 9.438 | |
| 49743 | 03:32:29.91 | -27:44:54.3 | 7362.3 | 0.9754 | 11.6 | 9.020e-18 | 1.00 | 23.44 | 0.972 | 8.986 | |
| 49793 | 03:32:29.29 | -27:44:55.6 | 7759.2 | 1.0819 | 5.4 | 6.260e-18 | 1.00 | 23.46 | 0.872 | 9.083 | |
| 49842 | 03:32:28.42 | -27:44:53.3 | 7358.6 | 0.9744 | 8.1 | 5.520e-18 | 1.00 | 22.65 | 0.594 | 9.335 | |
| 50081 | 03:32:23.35 | -27:44:48.0 | 7550.5 | 1.0259 | 4.5 | 3.750e-18 | 0.49 | 23.50 | 0.458 | 9.010 | |
| 50413 | 03:32:17.67 | -27:44:39.0 | 7143.9 | 0.9168 | 4.6 | 1.670e-18 | 1.00 | 22.83 | 0.155 | 9.192 | |
| 50602 | 03:32:15.80 | -27:44:34.5 | 7862.1 | 1.1095 | 16.0 | 1.820e-17 | 1.00 | 23.36 | 2.700 | 9.154 | |
| 50642 | 03:32:38.57 | -27:44:34.2 | 7308.3 | 0.9609 | 11.5 | 9.250e-18 | 1.00 | 23.60 | 0.961 | 8.898 | |
| 51000 | 03:32:24.21 | -27:44:26.7 | 7520.0 | 1.0177 | 11.4 | 1.230e-17 | 1.00 | 22.90 | 1.470 | 9.269 | |

| Galaxy ID | RA | Dec | $\lambda_{em}$ | $z_{em}$ | $\sigma$ | $f_{[OII]}$ | $P_{OII}$ | $K_{AB}$ | SFR | $\log(M_s)$ | comments |
|---|---|---|---|---|---|---|---|---|---|---|---|
| 51322 | 03:32:35.73 | -27:44:20.0 | 7205.4 | 0.9333 | 33.8 | 1.450e-17 | 1.00 | 22.78 | 1.400 | 9.232 | [OII] [NeIII] |
| 51725 | 03:32:14.28 | -27:44:09.8 | 7288.9 | 0.9557 | 14.3 | 8.110e-18 | 1.00 | 22.86 | 0.831 | 9.220 | |
| 51826 | 03:32:32.85 | -27:44:06.1 | 7589.3 | 1.0363 | 4.9 | 6.010e-18 | 1.00 | 23.45 | 0.753 | 9.044 | |
| 52667 | 03:32:32.34 | -27:43:45.8 | 7547.5 | 1.0251 | 17.3 | 9.190e-18 | 1.00 | 22.82 | 1.120 | 9.312 | |
| 52798 | 03:32:41.35 | -27:43:44.3 | 7381.0 | 0.9804 | 30.8 | 1.840e-17 | 1.00 | 23.04 | 2.010 | 9.168 | |
| 53880 | 03:32:26.39 | -27:43:21.7 | 7868.1 | 1.1111 | 19.5 | 2.340e-17 | 1.00 | 22.79 | 3.480 | 9.410 | |
| 54356 | 03:32:23.68 | -27:43:08.8 | 7381.7 | 0.9806 | 39.9 | 2.280e-17 | 1.00 | 23.26 | 2.490 | 9.067 | |
| 54692 | 03:32:43.40 | -27:42:59.1 | 7379.5 | 0.9800 | 7.6 | 3.100e-18 | 1.00 | 23.05 | 0.338 | 9.162 | |
| 54832 | 03:32:19.15 | -27:42:58.5 | 7520.3 | 1.0178 | 16.0 | 1.490e-17 | 1.00 | 22.61 | 1.780 | 9.396 | |
| 54871 | 03:32:27.02 | -27:42:56.4 | 7291.9 | 0.9565 | 12.5 | 8.320e-18 | 1.00 | 22.92 | 0.854 | 9.197 | |
| 55106 | 03:32:34.48 | -27:42:50.9 | 7776.4 | 1.0865 | 7.7 | 7.690e-18 | 1.00 | 23.68 | 1.080 | 8.989 | |
| 55404 | 03:32:23.55 | -27:42:42.2 | 7063.8 | 0.8953 | 14.4 | 5.010e-18 | 0.18 | 23.75 | 0.437 | 8.760 | |
| 56182 | 03:32:17.36 | -27:42:22.1 | 7106.6 | 0.9068 | 12.6 | 4.320e-18 | 1.00 | 23.89 | 0.389 | 8.712 | |
| 56594 | 03:32:21.96 | -27:42:14.1 | 7532.3 | 1.0210 | 15.4 | 1.090e-17 | 1.00 | 22.97 | 1.320 | 9.242 | |
| 56613 | 03:32:21.84 | -27:42:14.0 | 7537.9 | 1.0225 | 22.0 | 1.110e-17 | 1.00 | 22.97 | 1.350 | 9.243 | |
| 58506 | 03:32:34.40 | -27:41:27.0 | 7626.9 | 1.0464 | 4.7 | 5.590e-18 | 1.00 | 23.17 | 0.717 | 9.178 | |
| 59277 | 03:32:29.29 | -27:41:12.8 | 7154.3 | 0.9196 | 4.7 | 1.440e-18 | 1.00 | 22.37 | 0.134 | 9.399 | |
| 59317 | 03:32:29.91 | -27:41:06.8 | 7612.8 | 1.0426 | 5.0 | 4.140e-18 | 0.78 | 22.69 | 0.526 | 9.389 | |

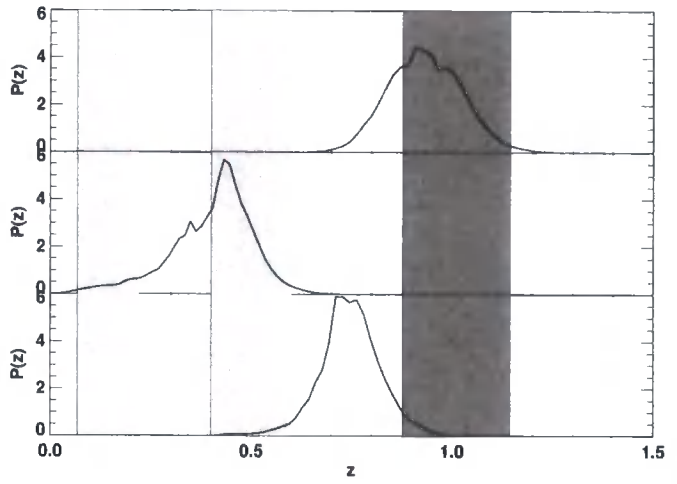


Figure 5.7: Photometric redshift probability distribution functions for three example galaxies. The probability is in arbitrary units. Shaded regions show the redshift windows for [OII] (rightmost line, darker shading); $H\beta$/[OIII] (centre shaded region); and H$\alpha$ (lowest redshift region). The top panel shows a galaxy where the detected emission line would be considered [OII] , the centre panel one which would be considered definitely not [OII] , and the lower panel shows a galaxy which falls between the two cases and has a probability $P_{\rm OII} \sim 0.3$.

#### 5.2.5.1 Flux measurement

We measure line fluxes from our science frames in a box $5 \times 5$ pixels around the centre of each emission line found. We actually use our full science frames (i.e. without masking) to allow for any small amount of misalignment in the masking process, which in some cases can incorrectly remove object flux. We subtract the background from the pixels where the emission lines lies then add up those pixels' counts to obtain the measured flux.

The measured flux is calibrated using observations of a spectrophotometric standard star, performing a smooth spline fit to the continuum and dividing the science observations by this fit. To compensate for absorption by telluric features, we isolate the A-band feature around 7600Å in our flux standard and measure the ratio of the observed flux to that expected from the smooth fit. Three different standard stars were observed on different runs and each time, the flux calibration agreed to within ~30%. We used a wider slit ($1''$) than for the our MOS masks for every standard, and thus the measurement should

be close to total flux for the stars.

Since we use 0.8″slits for our science targets, not all the light from each target galaxy will fall down the slit. We estimated the aperture correction to go from slit flux to total flux in the following way. We downloaded the public *HST ACS* $i$-band images[4] of a subsample of our target galaxies. We randomly selected 50 objects which met our $K$-band magnitude and photo-z selection criteria and measured their total magnitudes using a 0.5″radius aperture (this is much larger than the sizes of the galaxies). This image was then convolved to the ground-based seeing (0.6″) and a mask representing the 0.8″ box placed over the object. We used a box rather than a slit so as to account for the flux lost in both the dispersion and spatial directions, by our 5 ×5 pixel aperture. The magnitude was remeasured in the same way and the average difference corresponded to an aperture correction factor of 1.36. This correction is relatively small as our objects are typically seeing-dominated and the seeing FWHM is relatively small compared with the width of our slits. We multiplied our fluxes by this seeing-dependent aperture correction factor.

As a check of our flux calibration, we use ESO public 1D spectra[5] observed with FORS2 in the CDFS (Vanzella et al., 2008). We identify objects in common with our survey and measure line fluxes using a similar method to that used in ROLES (but on the 1D spectra). We plot the FORS2 fluxes against our [OII] fluxes in Fig. 5.8. It looks like we systematically underestimate flux by a factor of ∼2.5. The flux calibration of the ESO public data has been extensively checked against multi-band *ACS* photometry for a large sample of objects and there does not appear to be anything unusual about the objects in our overlapping subsample (E. Vanzella, private communication). Since we have no way of knowing whether there is this systematic error on our fluxes, we account for it by multiplying our fluxes by $\sqrt{2.5}$ and incorporate another factor of $\sqrt{2.5}$ into our error estimates (section 5.3.5). The origin of this discrepancy remains unresolved. Since we had many alignment stars ($\sim$ 6 per mask) and checked the centring of bright emission lines, we can rule out slit positioning errors as the cause.

[4]see: http://archive.stsci.edu/pub/hlsp/goods/v1/

[5]see: http://www.eso.org/science/goods/

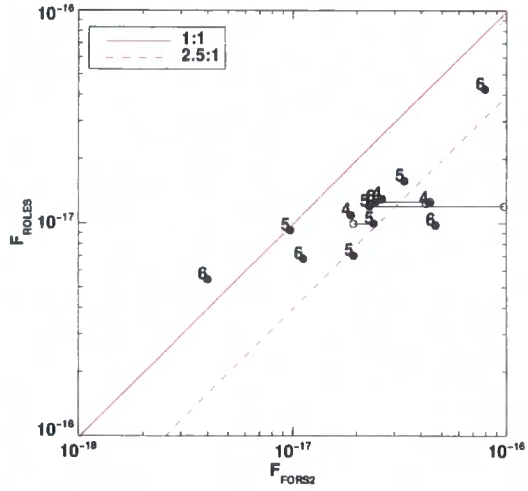


Figure 5.8: Comparison of line fluxes between Vanzella et al. (2008) (FORS2) and ROLES for all objects in common. Numbers indicate ROLES mask number. Open circles joined by lines to filled circles indicate repeat observations from the FORS2 spectra.

## 5.3 Analysis & Results

### 5.3.1 L([OII]) to SFR Conversion

We use the same conversion of L([OII]) to SFR as J05 which in turn was based on the calibration of Kennicutt (1998) (equation 2.10 in this thesis). We convert L([OII]) to L(H$\alpha$) assuming that ([OII]/H$\alpha$)$_{obs}$ = 0.5. We then correct for extinction in H$\alpha$ assuming average extinction of $A_{H_\alpha}$=1. Thus the extinction factor is 2.5 $\times$ 2 = 5 (where the factor of 2.5 accounts for one magnitude of extinction in H$\alpha$ and the factor of 2 accounts for our ([OII]/H$\alpha$)$_{obs}$ ratio) and the conversion is:

$$SFR(M_\odot yr^{-1}) = 5 \times \frac{7.9 \times 10^{-42}}{1.82} L([OII])(erg\ s^{-1}) \tag{5.6}$$

where the factor of 1.82 accounts for the conversion from a Salpeter IMF (Salpeter, 1955) to that of Baldry and Glazebrook (2003) (hereafter BG03).

### 5.3.2 Spectroscopic completeness

To calculate the completeness of our spectroscopy (i.e. the fraction of galaxies of interest on which we placed slits), we again use the FIREWORKS photometric redshift PDFs and public spectroscopy. If a secure spectroscopic redshift is available, we replace its photo-z

Table 5.4: Spectroscopic completeness as a function of $K$-band magnitude

| $K$ magnitude range | completeness |
|---|---|
| $22.50 < K < 22.75$ | 0.80 |
| $22.75 < K < 23.00$ | 0.75 |
| $23.00 < K < 23.25$ | 0.71 |
| $23.25 < K < 23.50$ | 0.61 |
| $23.50 < K < 23.75$ | 0.51 |
| $23.75 < K < 24.00$ | 0.34 |

PDF with a delta function located at the spectroscopic redshift. For every galaxy in our $K$-selected sample, in the area of our spectroscopic pointing, we sum their PDFs. This summation gives us the total redshift distribution of all galaxies in the sample (upper curve of Fig. 5.9). The number of galaxies in the $k^{th}$ magnitude bin in the redshift range, $z_0$ to $z_1$ is then

$$N_k = \sum_{bin} \int_{z_0}^{z_1} P_k(z) dz \tag{5.7}$$

where $P_z$ is the redshift probability density function, either given by the photo-z PDF or a delta function in the case of a secure spectroscopic redshift.

We then repeat this process for just the galaxies on which we placed slits. This gives the lower, thicker curve in Fig. 5.9. Since we are only interested in a specific redshift range (the shaded region in the figure), the completeness is given by the ratio of the integrals of the PDFs over this redshift range, i.e. the ratio of the area under the lower curve to the upper curve in this redshift range, i.e.

$$w_k = \frac{N_{slits}}{N_{phot}} \tag{5.8}$$

where $w_k$ is the completeness in the $k^{th}$ magnitude bin, $N_{slits}$ is the number of galaxies on which we placed slits and $N_{phot}$ is the number in the entire photometric catalogue, in the same field, and $N$ are calculated as given in equation 5.7.

Our overall survey completeness is 0.65. In practice, the completeness is a function of $K$-band magnitude, so we repeat this procedure in 0.25 magnitude bins. The results of this are tabulated in Table 5.4.

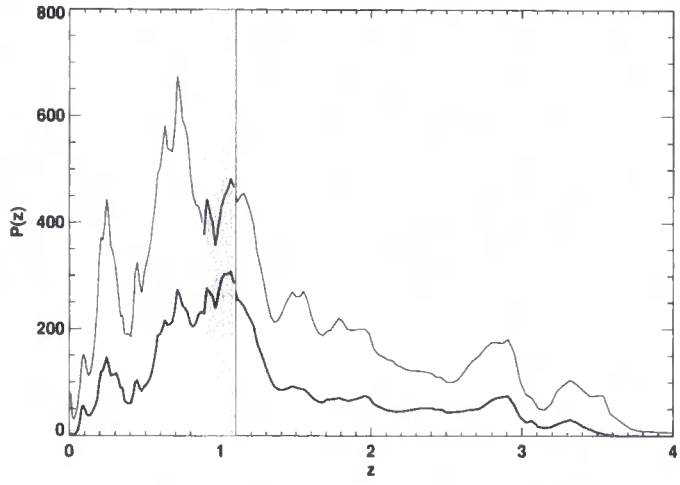


Figure 5.9: Redshift distributions used to calculate the completeness of our survey. These are constructed by simply summing the FIRE-WORKS photometric redshift P(z)s for individual galaxies (or delta functions for galaxies with spectroscopic redshifts). Plot shows distributions for all $22.5 < K \leq 24.0$ galaxies in our survey area (upper, thin line) and those on which we placed slits (lower, thicker line). Shaded region indicates redshift limits of our survey. The completeness is given by the ratio of the integral of the lower line to the upper line within this window. See text for details.

### 5.3.3 Survey volume

In order to calculate the SFRD we will use the $1/V_{max}$ method (equation 5.12), which requires an estimate of the volume from which each galaxy observed in our survey is drawn.

For each galaxy, the value of $V_{max}$ was determined by two limits: an [OII] line flux limit and a $K$-band flux limit. $V_{max}$ is the total volume in which the galaxy could be located and yield an [OII] flux above our flux limit at the observed wavelength and yield a $K$-band magnitude between our bright and faint $K$-band limits.

We calculate $V_{max}$ for the $i^{th}$ galaxy as

$$V_{max,i} = \Omega \int_{z_0}^{z_1} F_{vis,i}(z) \frac{dV_c}{dz} dz \tag{5.9}$$

where $\Omega$ is the angular area of our survey (53.9 arcmin$^2$ or $4.58 \times 10^{-6}$ steradians), $dV_c/dz$ is the differential comoving volume (e.g. Hogg 1999), and $F_{vis,i}(z)$ is a visibility

function for each galaxy which is 1 when both its $K$-band and [OII] fluxes are above our survey limit at that redshift (wavelength), and 0 otherwise. We outline the calculation of $F_{vis}(z)$ below. For reference, a galaxy which is visible at all redshifts (From $z_0 = 0.889$ to $z_1 = 1.149$) in ROLES would be drawn from a volume of $3.2 \times 10^4$ Mpc$^3$.

#### 5.3.3.1 $K$-band flux limit

For a galaxy observed at redshift $z_{obs}$ with $K$-band magnitude $K_{obs}$, we estimated the $K$-band magnitude at a given redshift $z$ to be:

$$K_z = K_{obs} + 5log(d_{obs}/d_z) + (k\text{-}corr_z - k\text{-}corr_{obs}) \tag{5.10}$$

where $d_{obs}$ and $d_z$ are the luminosity distances at the observed redshift and the redshift at which we wish to estimate $K$ respectively. $k\text{-}corr_{obs}$ and $k\text{-}corr_z$ are the $k$-corrections at the same redshifts. For simplicity we adopt the $K$-band $k$-correction of Glazebrook et al. (1995), which is based on an average model SED for normal galaxies:

$$k\text{-}corr(z) = \frac{-2.58z + 6.67z^2 - 5.73z^3 - 0.42z^4}{1 - 2.36z + 3.82z^2 - 3.53z^3 + 3.35z^4} \tag{5.11}$$

The $k$-correction in the $K$-band depends only slightly on the galaxy type (for z<1.5), and due to our narrow redshift slice the $k$-correction is constant to a good approximation. In practice, the effect of applying a $k$-correction or not only makes a $\sim$1% difference to the total volume probed.

#### 5.3.3.2 [OII] flux limit

Our [OII] line flux limit is not simply a constant flux limit (as is sometimes assumed in similar surveys), but is in fact a strong function of wavelength due to the numerous bright night sky lines. Since we have propagated an estimate of the noise in our detection images, $N_{conv,ij}$, it is a simple matter to calculate the average flux limit as a function of wavelength. We calculate the average noise spectrum for each mask and then take the shallowest mask as a conservative limit. The actual value we use is $4.5N_{conv,ij}$, since we adopt a $4.5\sigma$ detection threshold.

Figure 5.10 plots the fluxes of our [OII] lines versus their observed wavelengths. The solid line shows our $4.5\sigma$ [OII] limit. As we imagine a galaxy being moved further away and its [OII] flux dropping with the inverse square of its luminosity distance, it could pass in and out of our survey, depending on how bright it is. This is because there

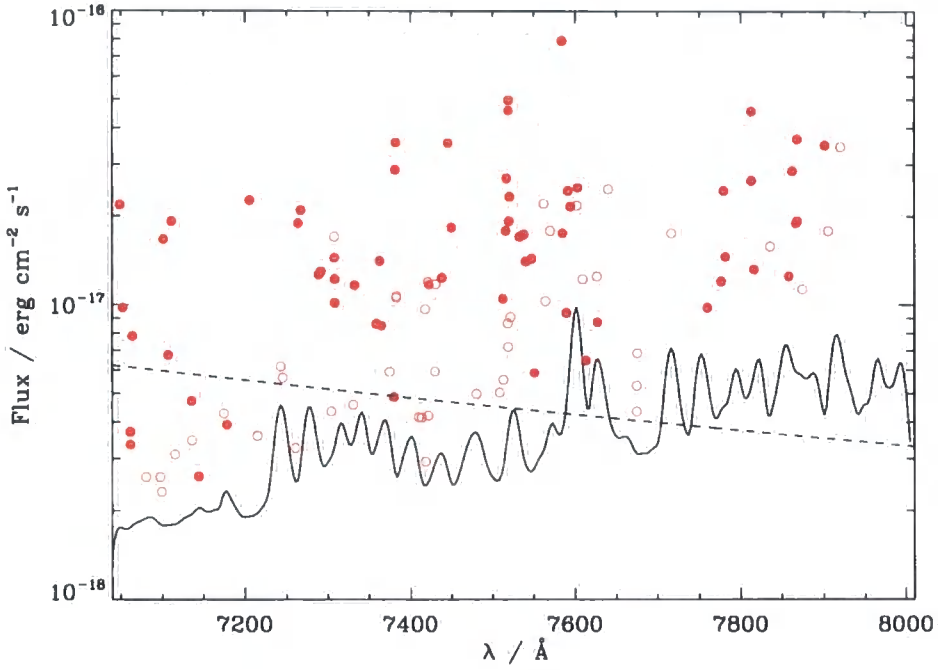


Figure 5.10: Flux versus wavelength for the lines with $P_{OII} > 0$ (i.e. most-likely [OII] detections, solid circles) and $P_{OII} = 0$ (open circles). The solid line is the $4.5\sigma$ flux limit derived from our average noise estimate in the detection images. The dashed line is the path traced out in flux-wavelength space by the galaxy observed at ~7380Å (this galaxy's point sits on the dashed line) if its redshift were increased or decreased. The galaxy would pass in and out of the survey before passing out of the survey for the final time at a distance at which [OII] would be observed at just under 7750Å. See text for details.

are peaks and troughs in the [OII] flux limit that we can detect. If a galaxy is initially visible to the survey (i.e. its position in flux-wavelength space is above the flux limit but its path takes it into a peak in the noise limit, it will be invisible to the survey in the volume covered by that peak. If the path emerges out of the peak above the flux limit at that wavelength, it will again be visible to the survey and this extra volume must be added to $Vmax$. This process is illustrated in figure 5.10 where the dashed line shows the path of a source observed at 7380Å with a flux of $4.90 \times 10^{-18}$ erg $\mathrm{cm}^{-2}s^{-1}$. This source would be visible to the survey all the way out to a distance corresponding to [OII] being observed at just under 7600Å at which point the path crosses under the telluric A-band feature. However, if the galaxy were moved away still further there would be two more regions where it would be visible to the survey before dipping below the flux limit for the last time at a distance corresponding to just under 7750Å.

Averaged over all of our [OII] lines, calculating the total $V_{max}$ in this way, using the detailed noise spectrum, gave a value 20% lower than had we calculated it assuming a constant flux limit of the flux in our faintest line.

### 5.3.4 Stellar Masses

The galaxies stellar masses are calculated using Karl Glazebrook's code which fits SED models to photometry given the redshift (we use the ROLES spectroscopic redshifts and the CDFS $UBVRIJHK$ photometry). This code is described, and used for mass fitting, in Glazebrook et al. (2004) (original GDDS masses), Baldry (2008) (where is it compared against other codes for SDSS) and Savaglio et al. (2008). It has been tested extensively. In short we use a two component star formation history model of a short burst superimposed on a range of older stellar populations (see Methods section of Glazebrook et al. (2004) for the parameterisation) and marginalise the mass over a range of extinction, metallicity and photometric errors (using a Monte-Carlo approach). In practice we find the masses are typically robust at the $\lesssim 0.2$ dex level whether or not the extra parameter spaces (bursts, dust and metallicity) are explored.

Figure 5.11 shows the mass function of the sample of galaxies in the CDFS photometric catalogue. To construct the mass function, the volume probed in each mass bin was estimated to be that volume between the minimum and maximum photometric redshifts of galaxies in that mass bin (since this is the mass function of the sample from the *photometric* catalogue, values of $1/V_{\mathrm{max}}$ are not available and thus we must estimate the volume in this way). The solid line shows the fitted Schechter function (equation 2.17)

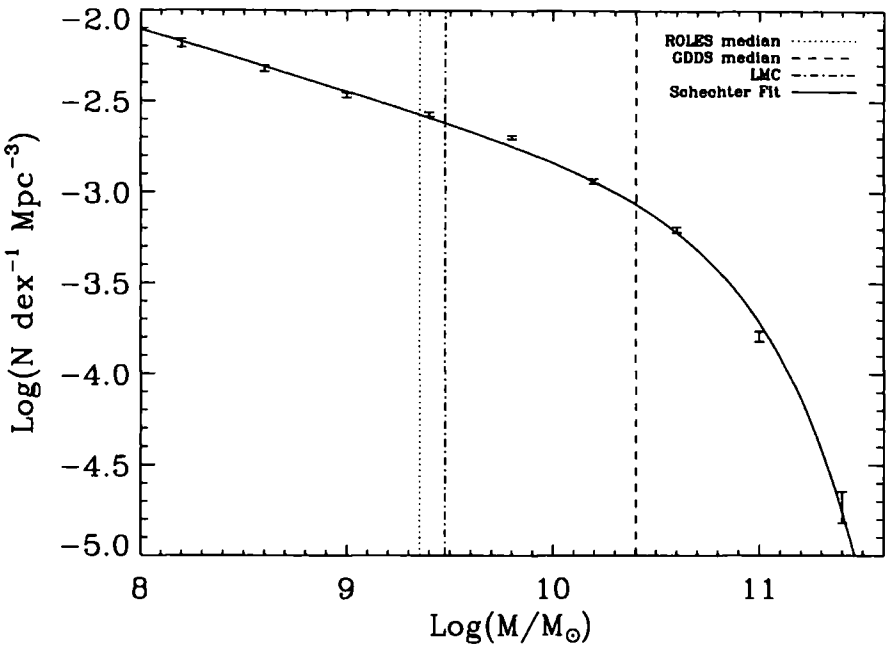


Figure 5.11: Mass function for the sample of galaxies in the CDFS photometric catalogue. The solid line is a fit of the Schechter form (as in equation 2.17 with $\alpha$=0.34 and $Mass^* = 7.2 \times 10^{10} M_\odot$ . The dotted and dash lines show the median masses of the ROLES sample and the GDDS sample used in J05 respectively. It is clear that ROLES samples down to much lower masses than GDDS. The dot-dashed line shows the mass of the Large Magellanic Cloud (LMC) for comparison. Even at its median mass, ROLES is observing systems smaller than the LMC.

with $\alpha = 0.34$ and $Mass^* = 7.2 \times 10^{10} M_\odot$ . Whereas the median GDDS mass is only just below this characteristic mass, the median ROLES mass is below that of systems like the LMC!

Figure 5.12 plots the [OII] fluxes of our sample versus the $K_{AB}$ magnitudes (top panel) and the stellar masses versus $K_{AB}$ (bottom panel). The points used in J05 (at $z \sim 1$) are added to both panels for comparison (these were kindly provided by Stéphanie Juneau in a private communication). The flux-$K_{AB}$ panel shows that we find a population with [OII] fluxes similar to the majority of J05 sources down to the $K_{AB}$ =24 limit. We also find a population with much lower [OII] fluxes (down to a limit of almost $\sim 1 \times 10^{-18}$ erg cm$^{-2}$ s$^{-1}$) across our $K_{AB}$ range which were not found in the GDDS.

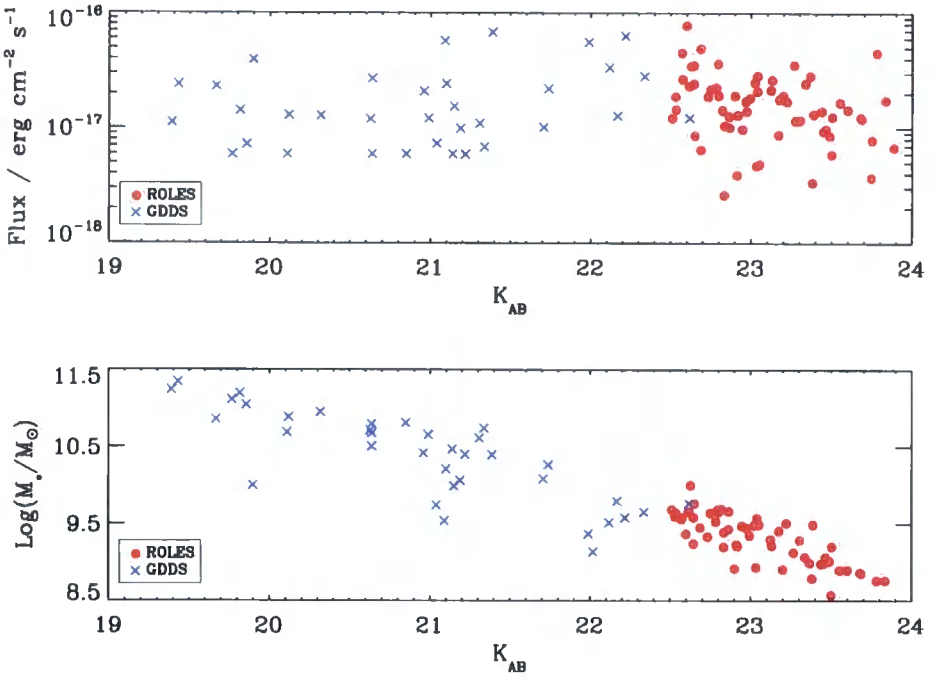


Figure 5.12: Top panel: [OII] flux versus $K_{AB}$ for the ROLES sources (red dots) and the GDDS sources (blue crosses) within the ROLES redshift range. Bottom panel: Stellar mass versus $K_{AB}$ for the same sources using the same colour code. By construction, there is minimal overlap in mass between the two surveys.

We explain this "extra" ROLES population as resulting from us not requiring that we were able to detect the continuum of our sources in order to measure the [OII] line flux and thus we are able to search to a lower flux limit. The bottom panel shows that the correlation between stellar mass and $K_{AB}$ continues down to our $K_{AB}$ limit and that it becomes tighter at the fainter magnitudes probed by ROLES.

### 5.3.5 Star formation rate density

For each mass bin, the star formation rate density (SFRD) was calculated using the $1/Vmax$ method as in equation 5.12.

$$SFRD = \sum_i \frac{P_{OII,i}\, SFR_i}{V_{max,i}\, w_i} \tag{5.12}$$

where $P_{OII}$ is the weighting due to the probability that the emission line is [OII] , $SFR_i$ is the star formation rate (derived from $L_{[OII]}$), $V_{max,i}$ is the maximum volume in which

Table 5.5: SFRD as a function of stellar mass. R and G denote the ROLES and GDDS surveys respectively

| Stellar Mass Range | Survey | SFRD / $M_\odot$ $Mpc^{-3}$ $yr^{-1}$ |
|---|---|---|
| $8.4 \leq \mathrm{Log}(M_*/M_\odot) < 9.0$ | R | $(1.99 \pm 1.3) \times 10^{-3}$ |
| $9.0 \leq \mathrm{Log}(M_*/M_\odot) < 9.8$ | R | $(5.50 \pm 3.3) \times 10^{-3}$ |
| $8.4 \leq M_*/M_\odot < 9.8$ | R | $(7.49 \pm 3.5) \times 10^{-3}$ |
| $8.4 \leq M_*/M_\odot < 11.5$ | R+G | $(2.44 \pm 0.51) \times 10^{-2}$ |

galaxy $i$ could be located and have been found in the ROLES survey and $w_i$ is the completeness in the $K_{AB}$ magnitude bin of galaxy $i$. Our results, split into different stellar mass bins, are given in table 5.5. The errors on the SFRD measurements in table 5.5 are calculated as follows. We begin by calculating the error $\delta_1$ defined as:

$$\delta_1(SFRD) = \sqrt{\left(\sum_i \frac{P_{OII,i}^2}{V_{max,i}^2\, w_i^2}\right)} \times \sigma(SFR) \tag{5.13}$$

where the subscripts again apply to the galaxies within a particular mass bin and $\sigma(SFR)$ is the standard deviation of the star formation rates in that bin. We then calculate a second error $\delta_2$ to account for the fact that the SFRD values may be a factor of $\sqrt{2.5}$ higher (see section 5.2.5.1). $\delta_2$ is defined such that:

$$\frac{SFRD + \delta_2(SFRD)}{SFRD} = \sqrt{2.5} \tag{5.14}$$

Thus $\delta_2 = \sqrt{2.5} - 1$. The final error is then the quadrature sum of $\delta_1$ and $\delta_2$. The SFRD measurements are not significantly affected by the choice of whether the stellar masses are calculated using the SExtractor *auto* or 3″ fixed aperture $K_{AB}$ magnitudes. By combining the ROLES and GDDS surveys at $z \sim 1$ we find the total [OII] -derived SFRD to be $(2.44 \pm 0.51) \times 10^{-2}$ $M_\odot$ $Mpc^{-3}$ $yr^{-1}$ . Thus 30% of this SFRD is in the galaxies of mass $\log(M_*/M_\odot)$<9.8 targeted by ROLES.

We estimate the cosmic variance using the method presented in Somerville et al. (2004). We make a conservative estimate by not including the completeness factor and by using the whole volume between our redshift limits: 64 /$3.2 \times 10^4 = 2 \times 10^{-3} Mpc^{-3}$ giving a bias of ∼1.3 (left panel of figure 3 from Somerville et al. 2004). This volume gives $\sigma_{DM} \sim 0.38$ (right panel of figure 3 from Somerville et al. 2004). Then 100%×1.3 × 0.38 =∼ 50%.

We estimate upper limits on our SFRD measurements by repeating the above analysis

but this time including every emission line whose photometric redshift was closer to that derived if the emission line was [OII] than to that derived if it was any other line. These SFRD upper limits were $4.2 \times 10^{-3}$ $M_\odot$ $Mpc^{-3}$ $yr^{-1}$ for the $8.4 \leq Log(M_*/M_\odot) < 9.0$ bin and $6.4 \times 10^{-3}$ $M_\odot$ $Mpc^{-3}$ $yr^{-1}$ for the $9.0 \leq Log(M_*/M_\odot) < 9.8$ bin. The points would also move up if instead we included every object where no flux was detected assuming their fluxes were on the flux limit of the survey.

Figure 5.13 plots the star formation rate density per logarithmic stellar mass bin. We have added the points at higher masses from the GDDS (J05, rebinned into slightly different mass bins to those used in that paper), DEEP2 (Conselice et al., 2007), Mobasher et al. (2008) and Cowie and Barger (2008) at $z \sim 1$ for comparison. The latter three include star formation tracers other than [OII] . It is immediately apparent from figure 5.14 that the star formation rate density, as a function of stellar mass, drops below stellar masses of $log(M_*/M_\odot) \sim 10^{10}$. Thus the trend found by J05 of star formation rate density increasing with lower and lower masses at $z \sim 1$ is not continued down to dwarf galaxy masses[6]. We discuss this point further in section 5.4.

## 5.4 Discussion

We have measured the star formation rate density in dwarf galaxies ($8.4 \leq Log(M_*/M_\odot) < 9.0$ ) at $z \sim 1$. The $1 \lesssim z \lesssim 2$ epoch is a very important epoch in the star formation history of the Universe. It is at this time that the global SFRD is beginning to drop and also when galaxies are beginning to migrate from the blue cloud to the red sequence. It is also the time at which the most massive galaxies ($M_*/M_\odot \gtrsim 11$) stop forming stars and thus some form of "downsizing" (discussed below) takes place in which the global SFRD becomes increasingly dominated by lower and lower mass galaxies. At this redshift, we have found the star formation rate density to drop as a function of mass at the masses of dwarf galaxies. In this section we discuss the results of this chapter in the context of other works. We begin by comparing our work to that of J05 from the GDDS.

### 5.4.1 Comparison with GDDS: Specific Star Formation Rates at $z \sim 1$

In the lowest mass bin of J05 ($9.0 \leq Log(M_*/M_\odot) < 10.2$ ) at $z \sim 1$, two thirds of the data have masses above 9.6, the approximate maximum mass of the ROLES sources.

[6]J05 include a factor in their SFRD calculation to account for their redshift completeness whereas we have not done so. This factor had a mean of 0.86 and thus doesn't affect the conclusions drawn here

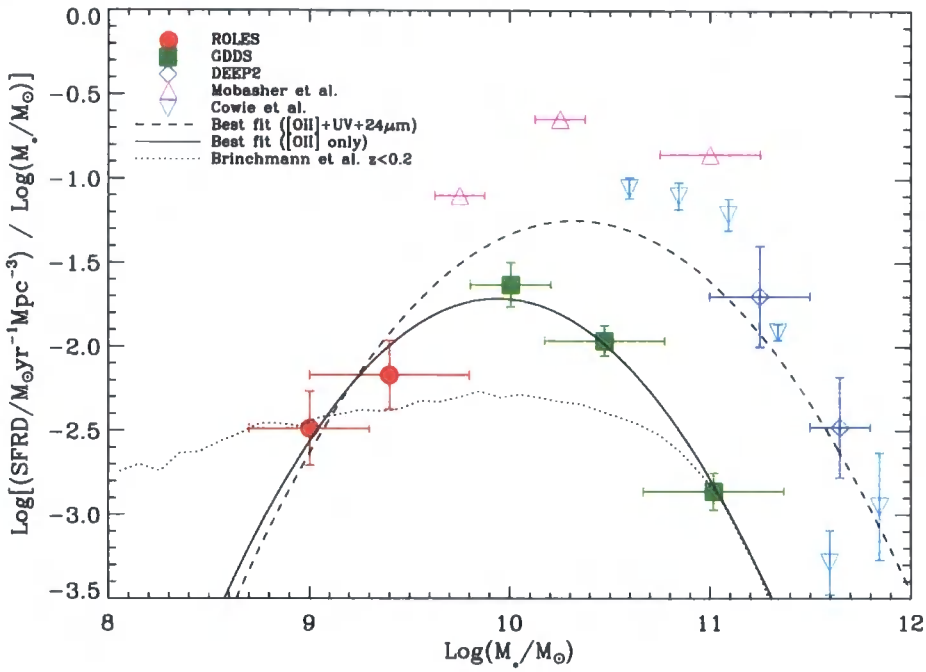


Figure 5.13: Star formation rate density per log(stellar mass) versus stellar mass at $z \sim 1$. Results are shown at different masses from ROLES, GDDS (J05), DEEP2 (Conselice et al., 2007) and the recent studies by Mobasher et al. (2008) and Cowie and Barger (2008). The dashed line is the second order polynomial line of best fit to all points. Given the huge scatter in the SFRD estimates using the different methods of SFR measurement, we think it prudent to mainly compare our results to those of GDDS (J05). With this in mind, the solid line is similarly fit just to ROLES and GDDS, the two surveys that only use [OII] lines to infer star formation rates. Neither the $x$- nor the $y$- error bars are included in the fits. ROLES is the first survey to show that the SFRD does not increase with ever decreasing stellar mass at this key redshift. The dotted line shows the relationship derived by Brinchmann et al. (2004) in the local Universe ($z < 0.2$). We see that the faint galaxies in the ROLES survey have comparable star formation rate densities to those of the same mass in the local Universe.

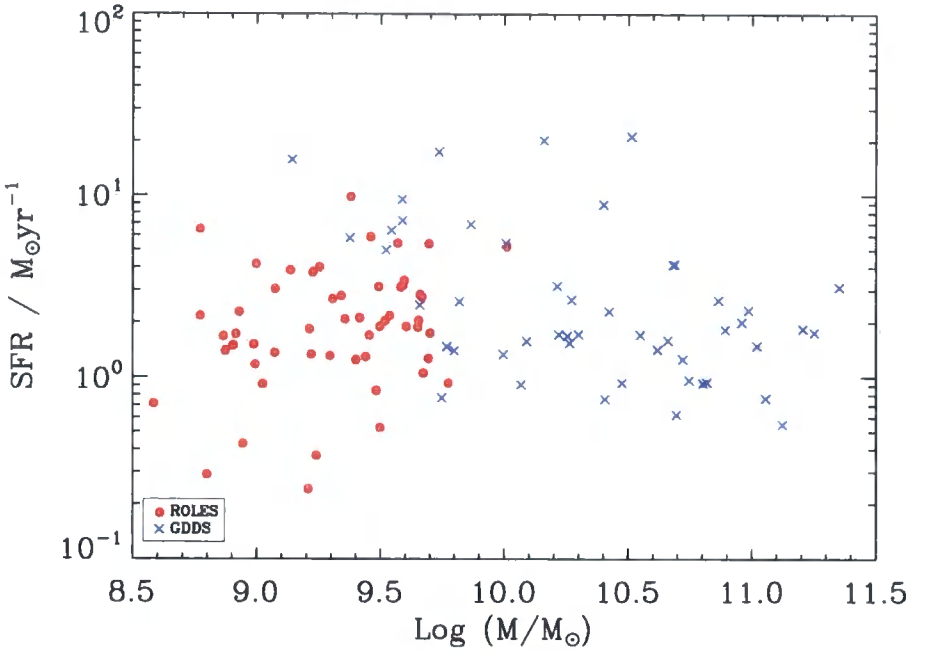


Figure 5.14: [OII] -derived star formation rate versus stellar mass for the ROLES (red, solid circles) and GDDS (blue crosses). There is little overlap in mass between the two surveys and they complement each other well.

Thus the two surveys complement each other very well with only a small overlap in $K_{AB}$ or stellar mass. ROLES is thus ideally placed to study both the continuation of the trends found by J05 down to lower stellar masses at $z \sim 1$ and to examine the mass dependence of galaxy properties such as star formation rates and specific star formation rates in a self consistent way across a wide range in stellar mass since ROLES almost reaches a stellar mass of $\log(M_*/M_\odot)$=8.5. Figure 5.14 plots the [OII] -derived SFRs from both ROLES and GDDS. As with the [OII] fluxes, the majority of the ROLES SFRs are comparable to those in GDDS although the galaxies found in GDDS with the highest star formation rates had no counterparts in ROLES. Also, ROLES has detected very low star formation rates (down to $\sim 2.5 \times 10^{-1}\ M_\odot\ \mathrm{yr}^{-1}$) across the mass range covered that are not found in GDDS. Perhaps the most interesting aspect of figure 5.14 is a lack of high mass ($\log(M_*/M_\odot) > 10.5$), high SFR ($\gtrsim 5 \times 10^{0}\ M_\odot\ \mathrm{yr}^{-1}$) galaxies in the GDDS. In part to examine this issue, we plot specific star formation rate (SSFR, star formation rate per unit stellar mass) versus stellar mass for the two surveys in figure 5.15. The slanted dashed lines on this plot are lines of constant SFR of 0.1, 1, 10 and 100 $M_\odot yr^{-1}$

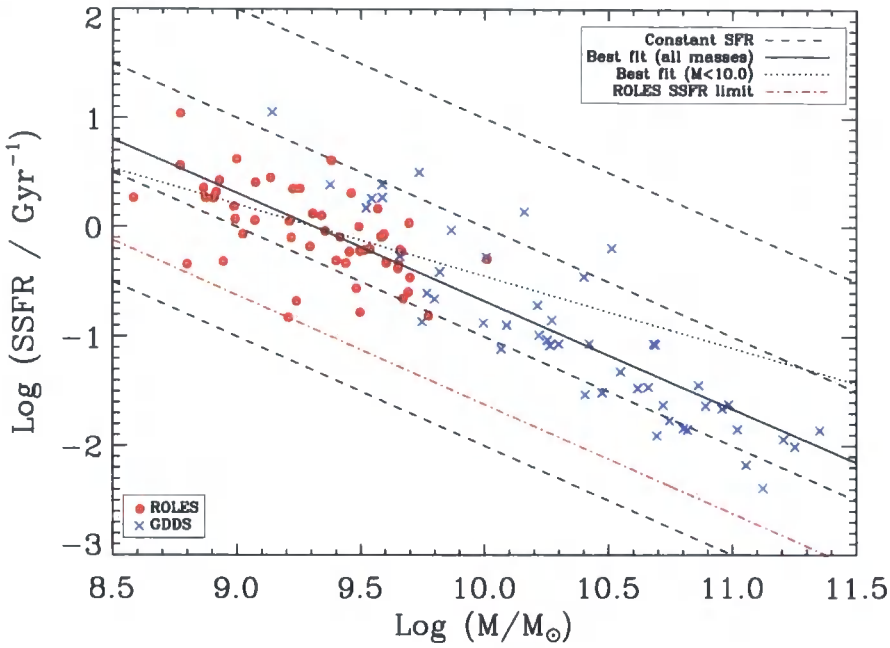


Figure 5.15: Specific star formation rate versus stellar mass for the ROLES (red, solid circles) and GDDS (blue crosses). The dashed lines are lines of constant SFR of 0.1, 1, 10 and 100 $M_\odot\ yr^{-1}$ from left to right. The SSFR limit was calculated using the minimum [OII] flux we measured for any source and the spectroscopic redshift of the source for which this flux was measured. This was also the source with the minimum flux, SFR and SSFR.

from left to right. The ROLES and GDDS points together are broadly consistent with being parallel to these lines of constant SFR (as shown by the solid line of best fit) which would indicate that galaxies of widely varying masses are all converting mass into stars at the same rate. However, for log stellar masses below ~10.0, the data are less consistent with this constant SFR and are more consistent with an SFR proportional to their mass (as shown by the dotted line of best fit for these galaxies being more horizontal). It is mainly the high mass galaxies' low SFRs, mentioned above, that give the impression of a constant SFR. Thus we find evidence that all but the highest mass ($\log(M_*/M_\odot)>$ 10.5) galaxies (which J05 infer were likely to have started forming stars in the "quiescent mode" at $z \sim 1.5$) were converting a similar fraction of their baryonic mass into stars in a given time period. This provides circumstantial evidence for a transition mass, discussed below, either side of which the SFRD varies differently with stellar mass.

Salim et al. (2007) analyses the specific star formation rates of star forming galaxies, AGN and composites of the two as a function of stellar mass in the local Universe. They also find the SSFR to drop as a function of mass above a mass of $\log(M_*/M_\odot)\sim 10.5$. However, this drop only occurs for the AGN and the composite galaxies. This suggests that there could be AGN components in the high mass galaxies in GDDS and that they're on their way to the red sequence with their star formation rates being quenched.

### 5.4.2 Star Formation Rate Density as a Function of Mass at z$\sim$ 1

Figure 5.13 compares the star formation rate density per logarithmic stellar mass from ROLES, GDDS, DEEP2 and recent studies by Mobasher et al. (2008) and Cowie and Barger (2008). The GDDS data are from J05 (we have slightly rebinned the lowest mass bin since the majority of their sources in this bin have $M_*/M_\odot > 9.6$); the DEEP2 data are taken from Conselice et al. (2007) and are based on a combination of [OII] and 24$\mu$m measurements. The data from Mobasher et al. (2008) and Cowie and Barger (2008) are derived from UV measurements. There is clearly a huge variation amongst the different studies of the star formation rate density for a given stellar mass, especially at higher stellar masses. In particular, we note that the UV- and 24$\mu$m-determined star formation rates are considerably higher than those determined from [OII] fluxes. Conselice et al. (2007) found that their 24$\mu$m- derived SFRs were always much higher than their [OII] -derived ones. We fit two 2-degree polynomial lines of best fit to the points: the solid line is just fitted to the [OII] points (ROLES and GDDS) and the dashed line is fitted to all the points. Both lines show that the global star formation rate density peaks at galaxies of $\sim 10^{10} M_\odot$ and declines with decreasing mass. The fit to all points peaks at $\log(M_*/M_\odot)$=10.3 and the fit to just the [OII] -determined points peaks at $\log(M_*/M_\odot)$=9.9. Thus we find that the trend found by J05 of SFRD increasing with ever decreasing galaxy stellar mass is not continued to masses lower than those in that study. This has important implications for measurements of the evolution of the global star formation rate.

In a sense, we have found a "transition mass", above and below which SFRD varies differently with stellar mass. Several studies have found similar transition masses in the local Universe. For example, Salim et al. (2007) find the (UV determined-) star formation to peak in galaxies of $\log(M_*/M_\odot) \sim 10.4$ in the local Universe. This is very close to a transitional mass found by Kauffmann et al. (2003b), again in the local Universe, of $\log(M_*/M_\odot) \sim 10.4$. This is a mass scale that divides many physical properties of galaxies either side of it. Below this mass, galaxies have younger stellar populations and

many have experienced recent starbursts suggesting SFR efficiency increases with halo mass for these low mass galaxies. This could be due to supernova feedback processes. For example, in the lowest mass systems, supernovae could prevent the gas from forming new stars by limiting the extent to which the gas can form dense molecular clouds. Above this transition mass, galaxies tend to have older stellar populations. This suggests that the SFR efficiency decreases with increasing stellar mass in these higher mass galaxies and that little star formation occurs in massive galaxies after they have assembled. This is a form of downsizing and may be due to the feedback processes discussed in section 1.3.1. It has long been assumed that SFR would peak and then fall back off in low mass galaxies due to a change in the feedback mechanism. We have found the first spectroscopic evidence for this phenomenon happening at $z \sim 1$.

The variation of SFR with stellar mass at this redshift has been looked at before using photometric redshifts. Drory and Alvarez (2008) studied SFR as a function of stellar mass and redshift in the FORS Deep Field and, as in this study, found SFR to turn over at lower masses. At progressively higher redshifts, this turnover mass increased (another sign of downsizing). At redshifts of $z \sim 1$, they found this mass to be $M_*/M_\odot \sim 10.8$, slightly higher than our transition mass, even when we include the non-[OII] points from figure 5.13.

We stress at this point that we have only measured the star formation in dwarf galaxies at $z \sim 1$ as traced by [OII] . A more complete measurement would be to add IR spectroscopy to the survey and add the 24$\mu$m - and UV-traced SFR to that traced by [OII] . We could then compare our results more meaningfully to the other studies shown in figure 5.13. We intend to present these results in future work. However, in section 5.4.3 we compare our [OII] -derived SFRs to those derived in the local Universe primarily based on $H_\alpha$ to test our flux-to-SFR conversion.

### 5.4.3 [OII] SFR versus total SFR: A study in the local Universe

In order to examine the effectiveness of our method of tracing SFR, we now look briefly at the results of Brinchmann et al. (2004) (hereafter B04) who derived total SFRD (primarily from $H_\alpha$ ) versus stellar mass from the SDSS. We included this relationship from B04 in figure 5.13. Comparing this line to ours provides yet more evidence of downsizing. There is a clear signal of the highest mass galaxies dominating the SFRD at high redshift, only for their dominance to be eroded with time such that, in the local Universe, the lowest mass galaxies contribute almost as much to the SFRD as the high mass galaxies.

In the top panel of figure 5.16 we plot SFRD versus stellar mass as found by B04 in the black, solid line (data kindly provided by Jarle Brinchmann, private communication). We removed the SFRD due to AGN, composite galaxies and unclassifiable sources from the total SFRD. We also plot this data as it was converted to the cosmology and dust-correction in J05 in the red, dashed line (figure 2 in J05). Finally, this plot shows the SFRD derived for the same galaxies but derived only from their [OII] fluxes and using our flux-to-SFR conversion in the blue, dot-dashed line (data from the NYU-VAGC low-$z$ sample and MPA Garching catalogue websites[7]). We find that the prominent, single peak in the plot found by B04 is not replicated when the data is converted to the form used in J05. Instead the distribution is much more uniform over the mass range $8.5 \lesssim \log_{10}(M_*/M_\odot) \lesssim 10.5$. The [OII] -derived SFRD is double-peaked with a high mass peak matching that found by B04 but with an extra, low-mass peak centred on $\log_{10}(M_*/M_\odot) \sim 9.2$. We note, however, that this distribution is sensitive to the aperture correction applied. To look into this second peak, we also show in the bottom panel of figure 5.16 the SFR versus stellar mass with both the SFRs from the B04 data and that derived using our flux-to-SFR conversion. Our conversion tends to give larger star formation rates at lower mass ($M_*/M_\odot \lesssim 9.8$) and smaller star formation rates at higher masses than B04. We conclude from this figure that our method is not missing significant contributions to the total SFRD. If anything, we may be systematically overestimating the SFRD at the lowest stellar masses probed although it is not straight forward to compare star formation rates derived in this way at such different redshifts. For example the required dust correction may change over cosmic time as the dust becomes progressively more evenly distributed throughout the star forming regions.

### 5.4.4 Downsizing

Throughout the discussion of the results in this chapter and of the results of other works, we have seen various hints of a downsizing picture of star formation. We briefly recall these pieces of evidence. Firstly, figure 5.13 shows that the global SFRD is dominated by higher mass ($\log(M_*/M_\odot) \sim 10.2$) galaxies at $z \sim 1$ than at $z \sim 0$ where galaxies of mass ($\log(M_*/M_\odot) \sim 9.0$) make an almost equal contribution. Secondly, figure 5.13 also shows that, whilst the contribution to the global SFRD from the most massive galaxies drops markedly over the redshift interval $\sim 0 < z < \sim 1$, that of the galaxies with mass

[7] http://sdss.physics.nyu.edu/vagc/ and http://www.mpa-garching.mpg.de/SDSS/DR4/ respectively

($\log(M_*/M_\odot)$ ~9.0) doesn't change (given the error bars on our measurements). Thirdly, Kauffmann et al. (2003b) found a transition mass in the local Universe above which SFR efficiency decreased with increasing stellar mass. Fourthly, Drory and Alvarez (2008), who found SFR to turn over with stellar mass, found that the mass at which this happens increases with redshift. A final glimpse of the downsizing picture is that we find any star formation at all in dwarf galaxies at $z$ ~1: this allows us to discount downsizing scenarios in which only more massive galaxies are forming stars at this redshift.

Summarising these results, we find evidence for a downsizing picture in which the SFRD is dominated by increasingly lower mass galaxies at lower redshifts although (with the possible exception of $\log(M_*/M_\odot)$>11.5 galaxies in the local Universe, Drory and Alvarez 2008) galaxies of all masses contribute at all redshifts.

Noeske et al. (2007) analysed star formation as a function of stellar mass and redshift using spectroscopic data from DEEP2. They claim to have uncovered what they call a "main sequence" of star formation that exists at least out to $z \sim 1.1$. That is, at a given redshift, the scatter in SFR, as function of stellar mass, is small. The main sequence moves to higher SFR at higher redshifts and has a lower limit of log(SFR / $M_\odot \mathrm{yr}^{-1}$)~ $3 \times 10^0$ for $\log(M_*/M_\odot)$~10 at $0.85 \leq z < 1.10$. Figure 5.14 provides evidence against this picture since ROLES clearly find SFR to be continuous at least down to $\sim 3 \times 10^{-1} M_\odot$ $\mathrm{yr}^0$ at all stellar masses. DEEP2 is incomplete for red galaxies at z>0.8 due to their $r_{AB} < 24.1$ limit as we saw in section 2.4. Thus we expect DEEP2 at z=1 to miss massive red galaxies with weak SFRs.

### 5.4.5 Metallicity and Reddening Effects

Our conversion of flux to SFR (equation 5.6), adapted as it is from Kennicutt (1998), assumes solar metallicity and no dust. We therefore assumed an extinction of $A_{H_\alpha}$=1 and applied this to every galaxy, regardless of the galaxy's mass or luminosity. These metallicity and reddening assumptions give a simple flux to SFR conversion that we can compare to other works (e.g. J05). However, both will introduce errors to our SFR measurements. Therefore, in this final section of the discussion, we attempt to quantify the effects metallicity and reddening due to dust will have on our results.

We estimate our metallicities ($Z$) using the mass-metallicity (M-Z) relationship derived by Savaglio et al. (2005) at z~0.7:

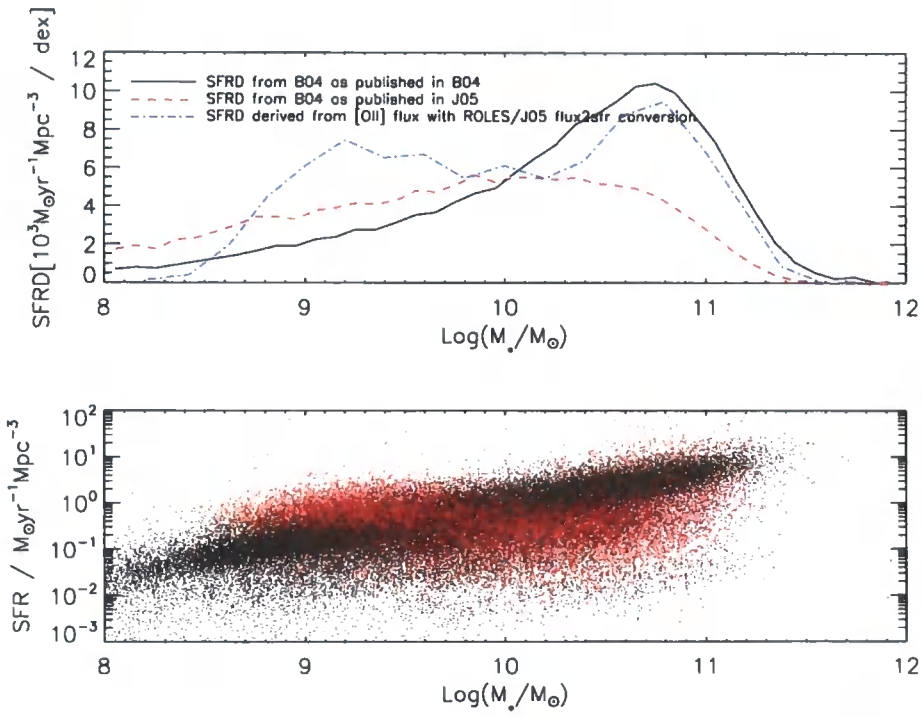


Figure 5.16: Top panel: SFRD versus stellar mass in the local Universe. The black, solid line is the total SFRD of B04. The red, dashed line is that same SFRD but converted to the cosmology and dust correction used in J05 (the same as that used in the present work). The blue, dot-dash line is the SFRD in the local Universe estimated from the [OII] fluxes using the flux-to-SFR conversion used here and in J05. Bottom panel: SFR versus stellar mass. The black points are those of B04 and the red ones those created by applying our flux-to-SFR conversion to the [OII] fluxes.

$$Z \equiv 12 + log(O/H)$$
$$= (0.478 \pm 0.058) Log(M_*/M_\odot) + (4.062 \pm 0.579) \tag{5.15}$$

where (O/H) is the number ratio of oxygen to hydrogen atoms. Equation 5.15 is derived from a sample of 56 galaxies from the GDDS in the redshift range $0.40 < z < 0.98$ whose spectra cover the [OII]$\lambda$3727, [OIII]$\lambda\lambda$4959, 5007 and $H_\beta$ lines. The metallicity is then calculated from these lines using the $R_{23}$ (Pagel et al., 1979) and $O_{32}$ diagnostics:

$$Log(R_{23}) = Log\left(\frac{f_{[OII]\lambda3727} + f_{[OIII]\lambda\lambda4959,5007}}{f_{H_\beta}}\right) \equiv x \tag{5.16}$$

$$Log(O_{32}) = Log\left(\frac{f_{[OIII]\lambda\lambda4959,5007}}{f_{[OII]\lambda3727}}\right) \equiv y \tag{5.17}$$

Then Z is defined using the relationship:

$$Z = 9.11 - 0.218x - 0.0587x^2 - 0.330x^3 -$$
$$+0.199x^4 - y(0.00235 - 0.1105x - 0.051x^2 - 0.04085x^3 -$$
$$+0.003585x^4) \tag{5.18}$$

Figure 5.17 shows the metallicities of our galaxies as a function of mass as calculated using equation 5.15.

Any alteration to the SFR([OII]) calibration depends on the way in which [OII]/$H_\alpha$ is related to the metallicity. Kewley et al. (2004) (hereafter K04) measure this relationship for a sample of 97 star forming galaxies covering every Hubble type and a wide range of magnitudes from the Nearby Field Galaxies Survey (NFGS, Jansen et al. 2000). K04 convert $R_{23}$ to Z using the relation from Zaritsky et al. (1994):

$$Z = 9.265 - 0.33R_{23} - 0.202R_{23}^2 - 0.207R_{23}^3 - 0.333R_{23}^4 \tag{5.19}$$

However, they also consider the relationship derived by Charlot and Longhetti (2001) for their "case F" method. In this case, the only spectral lines available for estimating $Z$ are [OII] , [OIII] and $H_\beta$. There is considerably larger scatter about the line of best fit

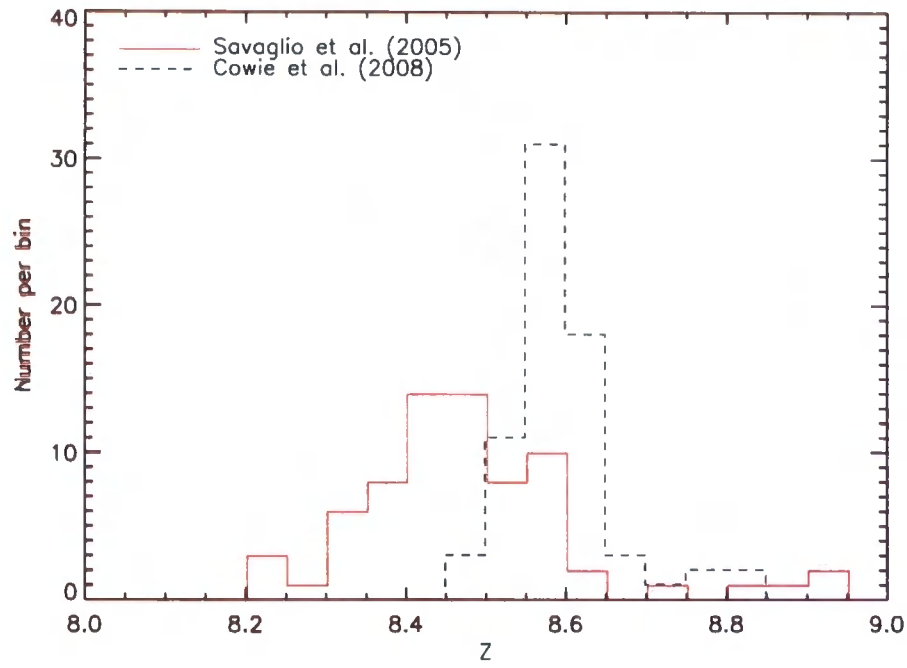


Figure 5.17: Metallicities (12 + Log[O/H]) of our sample. The metallicities are calculated using equation 5.15. The metallicities as calculated from the relation from Cowie and Barger (2008) are shown for comparison. This relation is $Z = 8.77 + 0.23M_{10}$ where $M_{10}$ is the galaxy mass in units of $10^{10}M_{\odot}$, and is based on the $R_{23}$ diagnostic.

to [OII]/$H_{\alpha}$ versus $Z$ as derived by Charlot and Longhetti (2001) than when derived by Zaritsky et al. (1994). Further, the Charlot and Longhetti (2001) method uses the [OIII]/$H_{\beta}$ ratio which K04 suggest may introduce a strong systematic effect into the abundance estimates, possibly due to its sensitive dependence on the ionisation parameter (defined below), rather than $Z$.

K04 then derived a straight line fit (with a negative slope) between [OII]/$H_{\alpha}$ and $Z$ based on the Zaritsky et al. (1994) relation. However, we must be careful in applying this metallicity-dependent correction to [OII]/$H_{\alpha}$ . K04 show the theoretical tracks of [OII]/$H_{\alpha}$ versus Z for different values of the ionisation parameter $q$:

$$q = \frac{S_{H^0}}{n} \tag{5.20}$$

where $S_{H^0}$ is the ionising photon flux per unit area and $n$ is the local number density of hydrogen atoms. These tracks show [OII]/$H_{\alpha}$ increasing with increasing $Z$ up to $Z \sim 8.5$ above which [OII]/$H_{\alpha}$ decreases with increasing $Z$. The shape of this curve can be un-

derstood from physical arguments: at low metallicity, the electron temperature $T_e$ is high and [OII] increases with $Z$ as one would perhaps intuitively imagine. At these temperatures, the thermal cooling is dominated by hydrogen free-free emission. However, at the temperatures typical of star forming regions (10000-20000K), the excitation energy between the two upper $_2D$ levels and the lower $_4S^{3/2}$ level of [OII] is of the order of the thermal electron energy, $kT_e$. The [OII] doublet is therefore closely linked to collisional excitations and de-excitations and thus to the electronic density $N_e$ and temperature $T_e$. As the abundance of $O$ increases, so does the rate at which the gas cools via the [OII] lines. Thus $T_e$ drops and the [OII] emission begins to drop with increasing metallicity.

The mean of the NFGS galaxies' ionisation parameters is $\sim 3 \times 10^7$ cm s$^{-1}$. Adapting the [OII]/H$_\alpha$ versus $Z$ track according to this value, we get a metallicity-corrected SFR calibration:

$$SFR([OII], Z)(M_\odot yr^{-1}) = 5 \times \frac{7.9 \times 10^{-42}}{1.82} \times \frac{L([OII])(erg\ s^{-1})}{-1857.24 + 612.693 \times Z - 67.0264 \times Z^2 + 2.43209 \times Z^3} \tag{5.21}$$

The black crosses in Figure 5.18 show the effect of making this correction to SFR assuming metallicities from equation 5.15. The SFRs have dropped by an average factor of $\sim 1.5$. There is very little scatter in this factor due to the small mass (and consequently $Z$) range of our galaxies and because our galaxies' masses place them near the peak of the [OII]/H$_\alpha$ versus metallicity curve so the [OII]/H$_\alpha$ ratio varies even less than for a sample with the same range of, but higher, metallicities. If this were the only issue affecting our results, it would be sensible to attempt an adjustment to our star formation results. However, we must first investigate the effects of reddening then see whether an adjustment is required.

Throughout this paper we have assumed a constant correction of $A_V$=1. If we assume $R_V = A_V/E(B-V) = 3.1$ (Cardelli et al., 1989) then this corresponds to $E(B-V) \sim 0.3$ and K04 show that such an assumption of constant reddening leads one to systematically overestimate SFR at low SFR and to systematically underestimate SFR at high SFR. Figure 5.19 shows the same effect in our data. K04 have evaluated $E(B-V)$ for each galaxy in their sample (they assume $R_V = 3.1$ and use the corresponding reddening curve from Cardelli et al. (1989) and assume an intrinsic $H_\alpha/H_\beta$ ratio of 2.85). They then use this to get a straight line fit to $E(B-V)$ versus the reddening-corrected (i.e. intrinsic)

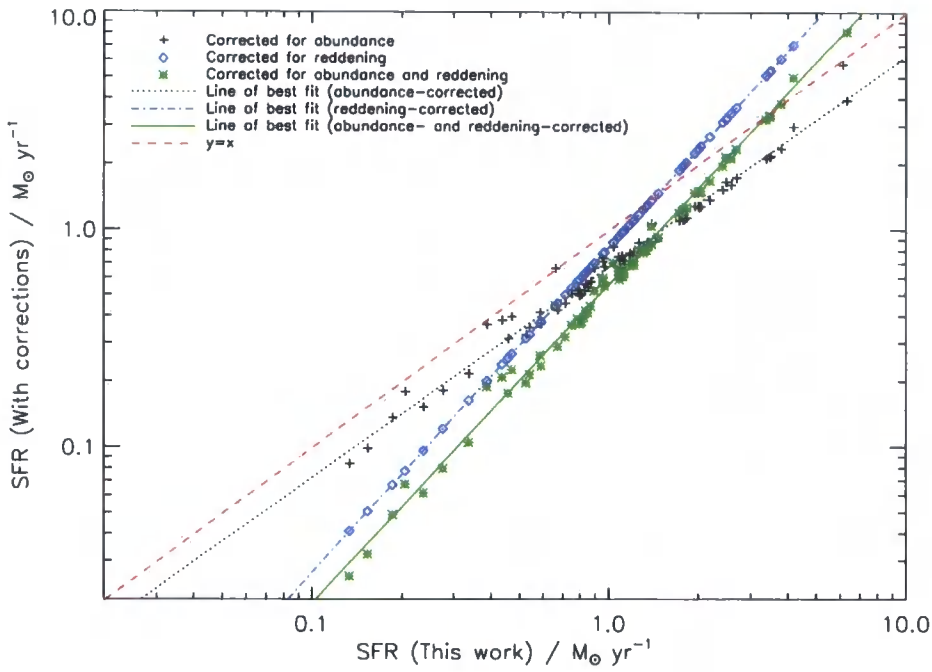


Figure 5.18: The effects on our SFR estimates after correcting for metallicity (black crosses, black dotted line of best fit), reddening (blue diamonds, blue dot-dash line of best fit) and both (green stars, green solid line of best fit). The red, dashed line in the line $y = x$. See text for details.

$L([OII]))_i$ and, using extinction correction from Calzetti et al. (2000), obtain the relation:

$$L([OII])_i = 3.11 \times 10^{-20} L([OII])_o^{1.495} \tag{5.22}$$

However, as cautioned by K04, this relationship must be applied with care. There is some evidence that such a reddening-luminosity relationship holds at high redshift. For example, Adelberger and Steidel (2000) measured $L_{bol,dust}$ (the bolometric dust luminosity) and $L_{1600}$ (the 1600Å luminosity) for galaxies in the local universe, at $z \sim 1$ and $z \sim 3$. The quantities $L_{bol,dust} + L_{1600}$ and$(L_{bol,dust}/L_{1600})$ give rough estimates of SFR and dust obscuration respectively. They found a correlation between $L_{bol,dust} + L_{1600}$ and $(L_{bol,dust}/L_{1600})$ at all three epochs. We use the relation expressed in equation 5.22 to estimate the correction to our SFRs for reddening. The blue diamonds in Figure 5.18 show the effect of applying only this reddening correction and no metallicity correction. Finally, we combine the reddening and metallicity corrections into one (the green stars in Figure 5.18):

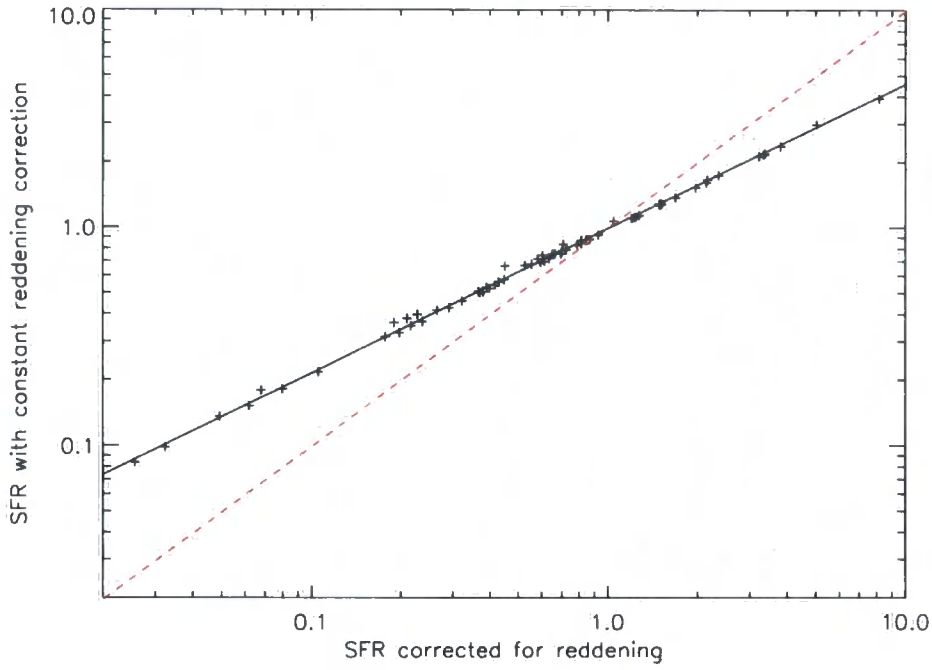


Figure 5.19: The effects of applying a constant reddening correction. In this figure we plot the SFRs corrected for abundance and reddening by assuming a constant reddening correction versus the SFRs corrected for abundance and the reddening correction as in equation 5.23. The effect is to overestimate the SFR at low SFR and to underestimate the SFR at high SFR.

$$SFR([OII],Z)(M_{\odot}yr^{-1}) = 5 \times \frac{7.9 \times 10^{-42}}{1.82} \times \frac{3.11 \times 10^{-20} L([OII])_o^{1.495} (erg\ s^{-1})}{-1857.24 + 612.693 \times Z - 67.0264 \times Z^2 + 2.43209 \times Z^3} \tag{5.23}$$

Thus, if we applied these corrections, our SFRs would mostly drop. The mean factor by which they would drop is 1.9. However, this factor is strongly correlated with the SFR itself so that the higher SFRs drop less and the highest ones would actually *increase*. The total SFR in our sample would drop by a factor of 1.2. Since this number is close to unity, we conclude that we do not need to adjust our results to account for metallicity and reddening effects.

## 5.5 Conclusions

We have designed and carried out the first survey capable of spectroscopically measuring the star formation rates of dwarf galaxies at $z \sim 1$. Our results are summarised as follows:

- We measure the total [OII] -inferred star formation rate density at $z \sim 1$ to be $(2.44 \pm 0.51) \times 10^{-2} M_{\odot}$ Mpc$^{-3}$ yr$^{-1}$ . This measurement is made over the mass range $8.4 \leq M_*/M_{\odot} < 11.5$ and includes the results from J05. In the mass range $8.4 \leq \mathrm{Log}(M_*/M_{\odot}) < 9.0$ we measure a SFRD of $(1.99 \pm 1.3) \times 10^{-3} M_{\odot}$ Mpc$^{-3}$ yr$^{-1}$ and in the mass range $9.0 \leq \mathrm{Log}(M_*/M_{\odot}) < 9.8$ we measure a SFRD of $(5.50 \pm 3.3) \times 10^{-3} M_{\odot}$ Mpc$^{-3}$ yr$^{-1}$ . These values are less than those found by other authors at the same redshift at higher stellar masses and, more pertinently, less than those found by J05 using the same method at higher masses at the same redshift. This implies a turnover in stellar mass of the global SFRD at this redshift, a result that has not been spectroscopically confirmed before.

- Our findings are consistent with there being a transition mass of $\log(M_*/M_{\odot}) \sim 10.3$, similar to that found in the local Universe. Above this mass, in the local Universe, star formation has almost finished and the galaxy's star formation is in a quiescent mode and the stellar population is older whilst below this mass, the stars are younger and the star formation rate is higher.

- We find evidence in support of the empirical "downsizing" picture of the evolution of the global star formation rate. In particular, in conjunction with other studies, we find that, with the possible exception of the most massive galaxies at $z \sim 0$, galaxies of all masses contribute to the global SFRD at all redshifts up to $z \sim 1$. However, the contribution of the most massive ($\log(M_*/M_{\odot}) \gtrsim 10.2$) galaxies has dropped off significantly since $z \sim 1$. On the other hand, the contribution of the smallest galaxies ($\log(M_*/M_{\odot}) \sim 9.0$) at $z \sim 1$ is consistent with that at $z \sim 0$ within the error bars of our measurements.

# Chapter 6

# *Conclusions and Future Work*

In this thesis we have derived radio luminosity functions for AGN and star forming galaxies, measured their evolution, charted the evolution of the colour-magnitude relation of radio sources, analysed the environments of radio sources and their evolution, measured star formation rates of dwarf galaxies at $z \sim 1$, and investigated downsizing. In this final chapter, we summarise the work that went into these endeavours and the conclusions we have drawn from this work. We then attempt to draw these different strands together and finally we look at what could be done in the future to extend this work.

## 6.1 Radio Luminosity Functions

In chapter 3 we derived a sample of radio sources in the redshift range $0.2 \leq z < 1.4$ by matching the AEGIS20 radio survey to the DEEP2 spectroscopic optical survey in the EGS. We then split this radio sample into two parts: those sources whose radio emission was star formation-powered and those whose radio emission was AGN-powered. This split was done primarily on the basis of the galaxies' colours following similar work done in the local Universe. We then constructed radio luminosity functions for each of these samples in each of two redshift intervals ($0.2 \leq z < 0.7$) and ($0.7 \leq z < 1.4$) and measured their evolution (which we modelled as pure luminosity evolution: $L \propto (1+z)^{\alpha}$) relative to the local Universe studies. We checked the accuracy of our population separation method using optical spectroscopy and imaging which provided circumstantial evidence that the method worked well at separating the two types of radio-emitting galaxies but there remained some uncertainty as to exactly where the cutoff line should be drawn. An intermediate colour population (ICP), probably containing both AGN and star forming galaxies and a few galaxies that had components of both, remained. This population is not seen in the local Universe and therefore it was less clearcut where to

put the dividing line than had been the case for other authors in the local Universe. Initially, following the local Universe studies, we included this ICP with the star forming galaxies. In this case, we found that the AGN luminosity function didn't evolve ($\alpha$=1.0 $\pm$0.9 ) over this redshift interval but that of the star forming galaxies evolved strongly ($\alpha$=3.7 $\pm$0.3 ). However, there is a systematic uncertainty in these results resulting from the potential misclassification of some of the ICP near the cut-off between the two samples. Deducing the relative contributions to the galaxies' radio emission from these two mechanisms was beyond the data set to hand. We therefore recomputed $\alpha$ with ICP reclassified as AGN. In this case, the AGN radio luminosity function now evolves considerably with $\alpha$=2.1 $\pm$0.5 whilst the star forming galaxies evolve as $\alpha$=2.7 $\pm$0.4 . We conclude that, within our uncertainties, the evolution in the star forming galaxies' radio luminosity function is consistent with the evolution in the global star formation rate density over the same interval. Also, in the case of the ICP being included with the AGN, the evolution in the AGN RLF is consistent with the evolution in the RLF of luminous red galaxies from the local Universe out to moderate redshifts.

## 6.2 The Colour-magnitude Distribution of Radio and X-Ray Sources at $z \sim 1$

With the sample of radio galaxies derived above, we were also able to construct the colour-magnitude diagram of radio sources at $z \sim 1$ and compare it to both the colour-magnitude diagram of radio sources in the local Universe and that of the general field population of galaxies at $z \sim 1$. Firstly, at $z \sim 1$, we find that the radio sources do not trace the general field population in this parameter space. Whereas the latter display the familiar colour bi-modality of a red sequence and blue cloud, the radio sources are found disproportionately in the "green valley" between these two. We find a similar result for X-ray sources from matching the Chandra survey in the EGS to DEEP2. We therefore conclude that at least some of the mechanisms responsible for causing galaxies to migrate from the blue cloud to the red sequence are also responsible for the radio and X-ray ignition in those galaxies. We hypothesise that one candidate for such a mechanism is major galaxy mergers. These can cause cold gas to be funnelled towards the star forming regions and towards the AGN, increasing the activity of both. When the black hole eventually drives the gas from the galaxy in a superwind, the star formation is quenched and the galaxy migrates to the red sequence.

We also find the colour-magnitude distribution of radio sources is different at $z \sim 1$ to what it is at $z \sim 0$. In the local Universe, the population of green valley radio sources is not seen from which we conclude that the mechanisms responsible for the galaxy migration and radio ignition were much more prevalent at higher redshifts than they are today.

## 6.3 The Environments of Radio Sources in DEEP2

We then analysed the environments of our sample of radio galaxies in chapter 4, estimating the environment density using the projected $n^{th}$ nearest neighbour method. At intermediate redshifts ($0.2 \leq z < 0.7$), we found that the galaxies with the highest values of $\Delta(U - R)$ (our proxy for the probability of the radio emission being AGN-powered) were more likely to be found in overdense environments whereas the galaxies with the lower values of $\Delta(U - R)$ were more likely to be found in underdense environments although the trend was very weak. Further, this trend was not seen at high redshift ($0.7 \leq z < 1.4$) indicating that environment effects are weaker at high redshifts. We then analysed the environment dependence of the fractions of galaxies that are either radio-powered star forming galaxies or AGN. We found a strong trend of the star forming galaxy fraction dropping with environment density in the intermediate redshift interval and a weaker trend at high redshift. When we compared to similar work done in the local Universe that found an even stronger trend, we saw consistent evolution of the relationship getting stronger as cosmic time progresses. We found weak trends of the AGN percentage increasing with environment density although the evidence for any evolution in the relationship was inconclusive. Thus our results for radio sources are similar to those of the general galaxy population where the fraction of red galaxies increases in denser environments with the trend getting weaker at higher redshifts.

## 6.4 The SFRD of Low-Mass galaxies at $z \sim 1$

In chapter 5 we described the ROLES survey in which we have targeted the [OII] emission line in dwarf galaxies ($\log_{10}(M_*/M_\odot) \lesssim 9.6$) at $z \sim 1$. We convert the [OII] flux to a star formation rate and plot SFRD versus stellar mass at this redshift, comparing to other studies at higher masses. We find the dwarf galaxies in our sample do contribute to the global SFRD, even at this high redshift but that the more massive galaxies (up to

$\log_{10}(M_*/M_\odot)$ ~10.3) in GDDS make a greater contribution. Above this mass, the SFRD drops with increasing stellar mass and we have thus identified a peak (the first to do spectroscopically) in SFRD with mass at this redshift.

Further, by comparing to similar work done in the local Universe, we analyse the evolution of the contribution to the global SFRD of galaxies of different masses. We find the contribution of small galaxies such as those in the ROLES sample is consistent with no evolution over the period $0< z <1$ whereas that of the more massive galaxies drops considerably. These results are qualitatively consistent with other authors and are evidence for the "downsizing" picture of the evolution of the global star formation rate.

## 6.5 Downsizing

These results have an impact on the picture of downsizing in galaxy formation. Firstly, our results rule out any picture in which the global star formation rate density is dominated solely by high mass galaxies at high redshift and by lower mass galaxies at low redshift. We find that dwarf galaxies make a contribution at $z$ ~1, albeit a less significant one than galaxies of mass $\log_{10}(M_*/M_\odot)$ ~10.3. We find that 30% of the SFRD in galaxies in the mass range $8.4 \leq \log(M_*/M_\odot) < 11.5$ is in galaxies with masses $\log(M_*/M_\odot) < 9.8$ which are the ones targeted by ROLES. In fact, in conjunction with other studies, we find that, with the possible exception of $\log(M_*/M_\odot) > 11.5$ galaxies in the local Universe, galaxies of all masses contribute at all redshifts.

By comparing to measurements in the local Universe, we also find that the evolution in the contributions to the global rate is itself mass-dependent. The more massive galaxies, which dominate at $z \sim 1$, stop forming stars relatively quickly over the redshift range $0 \lesssim z \lesssim 1$. On the other hand, we see very little evolution over the same period in the contribution from dwarf galaxies.

Further, we found evidence against what other authors had referred to as a "main sequence" of star formation. This main sequence is manifested as there being little scatter in the relationship between star formation rates and stellar masses at all redshifts out to $z$ ~1. That is, at any stellar mass and redshift, there is little variation in the star formation rates. By going to very faint [OII] fluxes (and thence very low star formation rates - at least down to $3 \times 10^{-1} M_\odot$ yr$^{-1}$), ROLES shows that, at $z$ ~1 in dwarf galaxies, star formation rates are measured at least down to this level.

## 6.6 Future Work

With regard to the radio methods and results described above, this work could be improved in future by a sample whose optical spectra cover the $H_\alpha$ and [NII] lines. This would enable the full BPT diagram to be used in separating the AGN population from the star forming one using the most reliable method. In that case, our results could be checked using samples whose purity should be higher and known with greater accuracy than ours and remove the systematic uncertainty in the evolution of our radio luminosity functions arising from possible misclassifications. Additionally, deeper and wider surveys will always improve statistics. In particular, a deeper optical survey in the EGS would improve the completeness of our radio luminosity functions by finding more optical sources to which more radio sources could be matched. If this were impractical, simply revisiting the field to improve the optical completeness would also be beneficial to this work for the same reason.

A wider survey (in both the radio and the optical) would have particularly aided our environment studies where the numbers of sources in some bins were small resulting in large error bars. A further improvement would be to implement a friends-of-friends (or other group finding) algorithm to identify groups in the data. It would then be interesting to see whether the AGN numbers (and luminosities) showed a more significant trend with group size than they do with local density, as has been found by other authors.

In the ROLES survey, we have so far only presented the results from one field using one star formation rate indicator. In future work, we aim to present similar results to these but adding the FIRES field to the CDFS field used here. This will of course help to reduce the errors due to cosmic variance. Additionally, we aim to do follow-up IR spectroscopy on the sources in which we have detected [OII] to measure the star formation as traced by the infrared light. The bulk of the IR luminosity from star formation that is re-radiated by dust in these galaxies would be emitted at $\sim 200\mu$m. This will make it visible to the submillimetre Herschel Space Observatory, due for launch in early 2009. Adding this to the [OII] -inferred star formation should provide quite a complete census of those galaxies' total star formation. Within the ROLES survey, there remains the unresolved issue of our [OII] fluxes disagreeing with those of other authors. It will be interesting to compare our [OII] fluxes in the FIRES field and the IR fluxes in both fields to those of in other studies to try to uncover any systematic error in our method.

In this thesis we have studied the relationships between galaxy mass, star formation

rate, colours, radio emission, X-ray emission and redshift for different galaxy types! We have shown the study of the evolution of galaxies to be a most complex one. Therefore the next generation of galaxy redshift surveys such as the Panoramic Survey Telescope & Rapid Response System (pan-STARRS) and the Large Synoptic Survey Telescope (LSST, due for first light in 2014) are designed to detect tens of billions of galaxies over wider areas and to greater depths than ever before. These surveys will study dark matter, dark energy, large-scale structure, gravitational lensing and faint galaxy distributions. Our understanding of the structure and evolution of the Universe is set to improve dramatically in the next decade or so.

# Appendix A | *Cosmography*

In this appendix, we derive a selection of cosmological and cosmographical relations used in this thesis. The majority of the derivations are based on Liddle (1999) and Hogg et al. (2003). We begin by relating Hubble's parameter $H$ to the expansion factor $a(t)$.

## A.1 Hubble's Parameter

The expansion factor $a(t)$ relates physical distances $r$ to comoving distances $x$:

$$r = a(t)\, x. \tag{A.1}$$

Note that equation A.1 gives $\dot{r} = \dot{a}\, x$ since distances are fixed in comoving coordinates so $\dot{x} = 0$. Hubble's parameter is defined in terms of the distance $d$ to an object and its recessional velocity $v$:

$$v = Hd. \tag{A.2}$$

Since $r$ is simply the physical distance between two points, we can replace $d$ in equation A.2 by $r$ and $v$ by $\dot{r}$. Then substituting equation A.1 into equation A.2 and cancelling factors of $x$ leads us to:

$$H = \frac{\dot{a}}{a}. \tag{A.3}$$

## A.2 Expansion factor, redshift and velocity of recession

From the definition of the expansion factor $a(t)$ in equation A.1, we can write $a(t)$ as the ratio of a given physical length at time $t$ to that in the present day: $a(t) = r(t)/r(0)$ since $a$ is normalised to unity at the present day. This length could be the wavelength of light as emitted ($\lambda_{em}$) and observed ($\lambda_{obs}$):

$$a = \frac{\lambda_{em}}{\lambda_{obs}} \tag{A.4}$$

However, from the definition of redshift $z$ (the first part of equation 1.5), we have $1/(1+z) = \lambda_{em}/\lambda_{obs}$ and therefore, from substituting in equation A.4:

$$a = \frac{1}{1+z} \tag{A.5}$$

Finally, the difference between $\lambda_{obs}$ and $\lambda_{em}$ exists because, during the time $\Delta t$ it takes for the photon to be emitted, its source is moving away from the observer at a speed $v$. Therefore, during this time and in the limit $v << c$, the source moves a distance $v\Delta t$ which is equal to the difference between the two wavelengths. Since $\Delta t \equiv 1/f = \lambda_{em}/c$ we have:

$$z = \frac{v}{c} \tag{A.6}$$

## A.3 The Friedmann Equations

We now give the Newtonian derivation of the Friedmann equations. We recall from chapter 1 the cosmological principle that states that the Universe is homogeneous and isotropic on large scales. In such a universe, no one place is any more special (in the sense of being the centre of the expansion) than any other and we can consider any place to be the centre. We now consider a particle of mass $m$ separated from an observer (who is at the centre of the expansion) by a distance $r$ in an expanding medium of density $\rho$. The particle will only feel a net gravitational force from the matter interior to it (which has mass $4\pi r^3\rho/3$). This matter exerts a gravitational force on the particle of

$$F_G = \frac{4\pi G\rho r m}{3} \tag{A.7}$$

giving the particle a potential energy of

$$V = -\frac{4\pi G\rho r^2 m}{3} \tag{A.8}$$

The particle's kinetic energy $T$ is given by

$$T = \frac{1}{2}m\dot{r}^2. \tag{A.9}$$

Its total energy $U$ is given by $U = T + V$ into which we substitute equations, A.9, A.8 and A.1 to give:

$$U = \frac{1}{2}m\dot{a}^2x^2 - \frac{4\pi}{3}G\rho a^2x^2m \tag{A.10}$$

Then substituting $kc^2 = -2U/mx^2$ and rearranging yields:

$$\left(\frac{\dot{a}}{a}\right)^2 = \frac{8\pi G}{3}\rho - \frac{kc^2}{a^2} \tag{A.11}$$

Finally, we add a term to account for cosmological constant $\Lambda$ and substitute in equation A.3 to yield equation 1.1:

$$H^2 = \left(\frac{\dot{a}}{a}\right)^2 = \frac{8\pi G}{3}\rho + \frac{\Lambda}{3} - \frac{kc^2}{a^2} \tag{A.12}$$

This is Friedmann's first equation. To derive the Friedmann's second equation (the "acceleration equation"), we first derive the "fluid equation" and begin with the first law of thermodynamics:

$$dE + pdV = TdS \tag{A.13}$$

where $V$ is a comoving volume of unit comoving radius, $E$ is the energy, $T$ the temperature and $S$ the entropy. Since the volume has physical radius $a$, using $E = mc^2$, the energy $E$ is given by

$$E = \frac{4\pi}{3}a^3\rho c^2. \tag{A.14}$$

Differentiating equation A.14 with respect to time yields:

$$\frac{dE}{dt} = 4\pi a^2\rho c^2\dot{a} + \frac{4\pi}{3}a^3\dot{\rho}c^2 \tag{A.15}$$

and differentiating $V = 4\pi a^3/3$ gives:

$$\frac{dV}{dt} = 4\pi a^2\dot{a}. \tag{A.16}$$

Substituting equations A.16 and A.15 into A.13, assuming a reversible expansion ($dS = 0$) and rearranging gives:

$$\dot{\rho} = 3\frac{\dot{a}}{a}\left(\rho + \frac{p}{c^2}\right) = 0 \tag{A.17}$$

This is the fluid equation which we will need on our way to deriving the acceleration equation. We next differentiate Friedmann's first equation (equation A.11) with respect to time to get:

$$2\frac{\dot{a}}{a}\frac{a\ddot{a}-\dot{a}^2}{a^2}=\frac{8\pi G}{3}\dot{\rho}+\frac{2kc^2\dot{a}}{a^3}. \tag{A.18}$$

We next use the fluid equation (equation A.17) to substitute in an expression for $\dot{\rho}$ and, after rearranging, we get:

$$\frac{\ddot{a}}{a}-\left(\frac{\dot{a}}{a}\right)^2=-4\pi G\left(\rho+\frac{p}{c^2}\right)+\frac{kc^2}{a^2} \tag{A.19}$$

Finally, we use Friedmann's first equation to substitute in an expression for $(\dot{a}/a)^2$ to get the acceleration equation:

$$\frac{\ddot{a}}{a}=\frac{-4\pi G}{3}\left(\rho+\frac{3p}{c^2}\right) \tag{A.20}$$

When we add the term to account for the cosmological constant to the right hand side of this equation, we have equation 1.2.

## A.4 Testing the Flatness of the Universe

In order to derive equation 1.7, we define a critical matter density $\rho_{crit,M}$ derived from equation A.12, by setting $k=\Lambda=0$ in the local Universe:

$$\rho_{crit,M}=\frac{3H_0^2}{8\pi G} \tag{A.21}$$

where, as throughout this appendix, the subscript 0 denotes the present day value of a parameter. We now define formally the different $\Omega$s referred to in section 1.1.1. These are the "observational parameters" whose values can only be fixed by observation. The first of these, $\Omega_M$ is the density parameter, covering baryonic matter, dark matter, radiation etc. It is defined by

$$\Omega_M=\frac{\rho_0}{\rho_{crit,M}} \tag{A.22}$$

We next define $\Omega_\Lambda$, which relates to the dark energy or cosmological constant. It is defined as:

$$\Omega_\Lambda=\frac{\Lambda}{3H_0^2} \tag{A.23}$$

For the purposes of consistency we also define $\Omega_k$ that relates to the curvature of the Universe:

$$\Omega_k = \frac{-kc^2}{a^2 H_0^2} \tag{A.24}$$

Then substituting equations A.22, A.23 and A.24 into equation A.12, having applied that equation in the present day yields:

$$\Omega_M + \Omega_\Lambda + \Omega_k = 1. \tag{A.25}$$

Equation A.25 shows that, if $\Omega_M + \Omega_\Lambda$=1, as discussed in section 1.1.1, then the Universe is flat since $\Omega_k$=0.

## A.5 The Evolution of the Hubble Parameter

We are now in a position to derive an expression for the evolution of the Hubble parameter $H$ in terms of observable parameters. We start by dividing the first Friedmann equation (equation A.12) by $\rho_{crit,M}$, substituting in equation A.22 and using $\rho = \rho_0/a^3$ (derived in section A.10) and rearranging to give:

$$H = H_0 \left[ \frac{\Omega_M}{a^3} - \frac{kc^2}{H_0^2 a^2} + \frac{\Lambda}{3H_0^2} \right]^{1/2} \tag{A.26}$$

Next, we apply the first Friedmann equation (equation A.12) to the present epoch to obtain:

$$H_0^2 = \frac{8\pi G \rho_0}{3} - kc^2 + \frac{\Lambda}{3} \tag{A.27}$$

which, after the substitution of equation A.23, rearranges to give:

$$\frac{kc^2}{H_0^2} = \frac{8\pi G \rho_0}{3H_0^2} + \Omega_\Lambda - 1 \tag{A.28}$$

We then substitute equation A.28 into equation A.26 and, after a little rearranging and substituting in equation A.5, obtain our expression for $H$ in terms of redshift and the observable parameters:

$$H = H_0 \left[ (1+z)^2 (1 + \Omega_M z) - \Omega_\Lambda z (2+z) \right]^{1/2} \tag{A.29}$$

## A.6 The Comoving Radial Distance $D_C$

We now use this expression for the Hubble parameter to derive the expression for the comoving radial distance out to a redshift $z$, starting with the Friedmann-Robertson-Walker (FRW) metric that describes the interval $ds$ between two events:

$$ds^2 = c^2dt^2 - a^2\left[\frac{dr^2}{1-kr^2} + r^2(d\theta^2 + sin^2\theta d\phi^2)\right] \tag{A.30}$$

where $\theta$ and $\phi$ are the altitude and azimuth angles respectively and $r$ is now the *comoving* distance. When the two events are the emission and detection of a photon (e.g. from a distant galaxy at redshift $z$), $ds$=0. We assume a flat universe ($k = 0$) and arrange the geometry such that $d\theta = d\phi = 0$. This leaves us with $a\ dr = c\ dt$ which we integrate between the emission and observation times of the photons, and use equations A.3 and A.5, to give:

$$r = \int_{t_1}^{t_0} \frac{dt}{a} = \int_{t_1}^{t_0} \frac{da}{a\dot{a}} \int_{t_1}^{t_0} \frac{da}{a^2H} \tag{A.31}$$

Differentiating equation A.5 gives $da = -a^2dz$. When we substitute this into equation A.31 we get the expression for the comoving distance $D_C$ out to redshift $z$:

$$D_C \equiv r = c\int_z^0 \frac{dz}{H} \tag{A.32}$$

where $H$ is given by equation A.29.

## A.7 The Angular Diameter Distance $D_A$

The angular diameter distance $D_A$ is a physical distance, defined as the ratio of the size of an object to the angle it subtends at the Earth $\theta$:

$$D_A = \frac{size}{\theta} \tag{A.33}$$

For example, in the case of an extended, resolved object such as a galaxy or a radio lobe, we can measure its size by considering two photons: one leaving each end of the object at the same time (the two events) and travelling the same distance $D_C$ to Earth where they are detected. We consider the space-like interval, $\int ds$ between these two events. This interval will be the size of the object. We apply the FRW metric (equation A.30) to this situation and choose the geometry such that $d\phi$=0 ($k$=0 still). $d\theta$ is the angle subtended at the Earth by the two ends of the object. We then have:

$$ds = a\, r\, d\theta \tag{A.34}$$

Integrating both sides of equation A.34, and again using equation A.5 gives the result that, per radian,

$$size = \frac{D_C}{1+z} \tag{A.35}$$

Then, by definition, in the case of $\theta$=1 radian, the size of the object will be equal to $D_A$. We thus have:

$$D_A = \frac{D_C}{1+z} \tag{A.36}$$

## A.8 The Luminosity Distance

The luminosity distance $D_L$ is the distance an object would be placed at given its intrinsic luminosity $L$ and the flux $f$ received from it:

$$f = \frac{L}{4\pi D_L^2} \tag{A.37}$$

If we model the emitting object as a spherical black body with temperature $T_{em}$, then its luminosity is given by Stefan's law:

$$L = 4\pi R^2 \sigma T_{em}^4 \tag{A.38}$$

where $\sigma$ is Stefan's constant and $R$ is the sphere's radius. The flux will be given by:

$$f = \sigma T_{obs}^4 \frac{R^2}{D_A^2} \tag{A.39}$$

where $T_{obs}$ is the observed temperature and is related to $T_{em}$ by:

$$T_{obs} = \frac{T_{em}}{1+z} \tag{A.40}$$

since the photons are redshifted between being emitted at redshift $z$ and observed at redshift 0. This relationship is justified in section A.10. Then substituting equations A.38 and A.39 into equation A.37 yields:

$$D_L = (1+z)^2 D_A \tag{A.41}$$

Or, substituting in equation A.36:

$$D_L = (1+z)D_C \tag{A.42}$$

## A.9 The Comoving Volume

Now that we have defined the comoving distance $D_C$ and the physical angular diameter distance $D_A$ we can define the element of comoving volume $dV_C$ in terms of the element of solid angle $d\Omega$ and the redshift interval $dz$:

$$dV_C = D_C(1+z)^2 D_A^2 \, d\Omega \, dz \tag{A.43}$$

Integrating this volume element in a flat universe yields the comoving, all-sky volume $V_C$ out to redshift $z$:

$$V_C = \frac{4\pi D_C^3}{3} \tag{A.44}$$

## A.10 The Evolution of the Expansion Factor and of the Energy Density

In the final section of this appendix, we derive the rates at which the expansion factor $a$ and the mass/energy[1] densities of dust (that is matter that exerts zero pressure, such as galaxies - we use *dust* synonymously with *matter*) and radiation, $\rho_{dust}$ and $\rho_{rad}$ respectively, drop off with time in radiation- and matter- dominated universes. We begin with the expressions for the variations of $\rho_{dust}$ and $\rho_{rad}$ with $a$ then derive the evolution of $a$ in the special cases of a radiation-dominated universe (up to ~3,000 years in the Big Bang model) and a dust-dominated universe.

Radiation exerts a pressure $p$ related to its energy density $\rho_{rad}$ by its equation of state:

$$p = \frac{\rho c^2}{3} \tag{A.45}$$

Substituting equation A.45 into the fluid equation (equation A.17) leads to the separable differential equation:

[1] we shall use these two terms interchangeably in this section since they differ only by the constant factor $c^2$ and only wish to derive the powers of $a$ or $t$ at which $\rho$ or $a4$ evolve

$$\dot{\rho} = \frac{4\dot{a}\rho}{a} \tag{A.46}$$

which can be separated, integrated and rearranged to give the evolution of the energy density of radiation with the expansion factor:

$$\rho_{rad} \propto \frac{1}{a^4} \tag{A.47}$$

We can combine equation A.47 with the energy density of radiation:

$$\rho_{rad}c^2 = \alpha T^4 \tag{A.48}$$

to give the evolution of temperature with the expansion factor:

$$T \propto \frac{1}{a} \tag{A.49}$$

This is a crucial relationship since it means the Universe cools as it expands. Equation A.49 also yields equation A.40.

In the case of dust, we have $p$=0. In this case, the fluid equation (equation A.17) can be rewritten as:

$$\frac{1}{a^3}\frac{d}{dt}(\rho a^3) = 0 \tag{A.50}$$

This can then be integrated to give the result that one would perhaps naively expect:

$$\rho_{dust} \propto \frac{1}{a^3} \tag{A.51}$$

### A.10.1 Evolution in a Radiation-dominated Universe

In a radiation-dominated Universe (where we still have $k$=0), Friedmann's first equation (equation A.11) reduces to:

$$\dot{a}^2 = \frac{8\pi G\rho_0}{3}\frac{1}{a^2} \tag{A.52}$$

where we have used equation A.47. This equation can be separated and integrated to give the evolution of the expansion factor in a radiation-dominated universe:

$$a \propto t^{1/2}. \tag{A.53}$$

Then substituting equation A.47 into equation A.53 yields the evolution of the energy density of radiation in a radiation-dominated universe:

$$\rho_{rad} \propto \frac{1}{t^2} \tag{A.54}$$

We can also see the evolution of the energy density of dust in such a universe by substituting equation A.51 into equation A.53:

$$\rho_{dust} \propto \frac{1}{t^{3/2}} \tag{A.55}$$

### A.10.2 Evolution in a Matter-dominated Universe

In a matter-dominated universe, the evolution of the expansion factor is governed by the dust. We therefore substitute equation A.51 into Friedmann's first equation (equation A.11) to yield:

$$\dot{a}^2 = \frac{8\pi G\rho_0}{3}\frac{1}{a} \tag{A.56}$$

This equation can be separated and integrated to yield the evolution of the expansion factor in a matter-dominated universe:

$$a \propto t^{2/3} \tag{A.57}$$

Then substituting equation A.51 into this equation yields the evolution of the energy density of dust in such a matter-dominated universe:

$$\rho_{dust} \propto \frac{1}{t^2} \tag{A.58}$$

Similarly, substituting equation A.47 into equation A.57 yields the evolution of the energy density of radiation in such a matter-dominated universe:

$$\rho_{rad} \propto \frac{1}{t^{8/3}} \tag{A.59}$$

# Bibliography


Abbassi, S., Ghanbari, J., and Najjar, S.: 2008, MNRAS **388**, 663

Abraham, R. G., Glazebrook, K., McCarthy, P. J., Crampton, D., Murowinski, R., Jørgensen, I., Roth, K., Hook, I. M., Savaglio, S., Chen, H.-W., Marzke, R. O., and Carlberg, R. G.: 2004, AJ **127**, 2455

Adelberger, K. L. and Steidel, C. C.: 2000, ApJ **544**, 218

Alpher, R. A., Bethe, H., and Gamow, G.: 1948, *Physical Review* **73**, 803

Appleton, P. N., Fadda, D. T., Marleau, F. R., Frayer, D. T., Helou, G., Condon, J. J., Choi, P. I., Yan, L., Lacy, M., Wilson, G., Armus, L., Chapman, S. C., Fang, F., Heinrichson, I., Im, M. e. a., Jannuzi, B. T., Storrie-Lombardi, L. J., Shupe, D., Soifer, B. T., Squires, G., and Teplitz, H. I.: 2004, ApJS **154**, 147

Auger, M. W., Becker, R. H., and Fassnacht, C. D.: 2008, AJ **135**, 1311

Baldry, I. K.: 2008, *ArXiv e-prints* 809

Baldry, I. K., Balogh, M. L., Bower, R., Glazebrook, K., and Nichol, R. C.: 2004, in R. E. Allen, D. V. Nanopoulos, and C. N. Pope (eds.), *The New Cosmology: Conference on Strings and Cosmology*, Vol. 743 of *American Institute of Physics Conference Series*, pp 106–119

Baldry, I. K., Balogh, M. L., Bower, R. G., Glazebrook, K., Nichol, R. C., Bamford, S. P., and Budavari, T.: 2006, MNRAS **373**, 469

Baldry, I. K. and Glazebrook, K.: 2003, ApJ **593**, 258

Baldwin, J. A., Phillips, M. M., and Terlevich, R.: 1981, PASP **93**, 5

Balogh, M. L., Baldry, I. K., Nichol, R., Miller, C., Bower, R., and Glazebrook, K.: 2004, ApJ **615**, L101

Balogh, M. L., Navarro, J. F., and Morris, S. L.: 2000, ApJ **540**, 113

Barger, A. J., Cowie, L. L., and Wang, W.-H.: 2007, ApJ **654**, 764

Becker, R. H., White, R. L., and Helfand, D. J.: 1995, ApJ **450**, 559

Bell, E. F.: 2003, ApJ **586**, 794

Bell, E. F., Papovich, C., Wolf, C., Le Floc'h, E., Caldwell, J. A. R., Barden, M., Egami, E., McIntosh, D. H., Meisenheimer, K., Pérez-González, P. G., Rieke, G. H., Rieke, M. J., Rigby, J. R., and Rix, H.-W.: 2005, ApJ **625**, 23

Best, P. N.: 2004, MNRAS **351**, 70

Best, P. N., Kauffmann, G., Heckman, T. M., and Ivezić, Ž.: 2005, MNRAS **362**, 9

Bicknell, G. V.: 1995, ApJS **101**, 29

Binney, J. and Tremaine, S.: 2008, *Galactic Dynamics: Second Edition*, Princeton University Press, Princeton, NJ, USA

Bîrzan, L., Rafferty, D. A., McNamara, B. R., Wise, M. W., and Nulsen, P. E. J.: 2004, ApJ **607**, 800

Blain, A. W.: 1999, MNRAS **304**, 669

Blandford, R. D. and Znajek, R. L.: 1977, MNRAS **179**, 433

Blumenthal, G. R., Faber, S. M., Primack, J. R., and Rees, M. J.: 1984, Nature **311**, 517

Boesgaard, A. M. and Steigman, G.: 1985, ARA&A **23**, 319

Bower, R. G., Benson, A. J., Malbon, R., Helly, J. C., Frenk, C. S., Baugh, C. M., Cole, S., and Lacey, C. G.: 2006, MNRAS **370**, 645

Boyle, B. J., Shanks, T., and Peterson, B. A.: 1988, MNRAS **235**, 935

Brinchmann, J., Charlot, S., White, S. D. M., Tremonti, C., Kauffmann, G., Heckman, T., and Brinkmann, J.: 2004, MNRAS **351**, 1151

Bruzual, G. and Charlot, S.: 2003, MNRAS **344**, 1000

Buat, V. and Xu, C.: 1996, A&A **306**, 61

Calura, F. and Matteucci, F.: 2003, ApJ **596**, 734

Calzetti, D., Armus, L., Bohlin, R. C., Kinney, A. L., Koornneef, J., and Storchi-Bergmann, T.: 2000, ApJ **533**, 682

Calzetti, D., Kinney, A. L., and Storchi-Bergmann, T.: 1994, ApJ **429**, 582

Cardelli, J. A., Clayton, G. C., and Mathis, J. S.: 1989, ApJ **345**, 245

Carilli, C. L. and Yun, M. S.: 2000, ApJ **530**, 618

Charlot, S., Kauffmann, G., Longhetti, M., Tresse, L., White, S. D. M., Maddox, S. J., and Fall, S. M.: 2002, MNRAS **330**, 876

Charlot, S. and Longhetti, M.: 2001, MNRAS **323**, 887

Cole, S., Norberg, P., Baugh, C. M., Frenk, C. S., Bland-Hawthorn, J., Bridges, T., Cannon, R., Colless, M., Collins, C., Couch, W., Cross, N., Dalton, G., De Propris, R., Driver, S. P., Efstathiou, G., Ellis, R. S., Glazebrook, K., Jackson, C., Lahav, O., Lewis, I., Lumsden, S., Maddox, S., Madgwick, D., Peacock, J. A., Peterson, B. A., Sutherland, W., and Taylor, K.: 2001, MNRAS **326**, 255

Condon, J. J.: 1992, ARA&A **30**, 575

Condon, J. J., Cotton, W. D., Greisen, E. W., Yin, Q. F., Perley, R. A., Taylor, G. B., and Broderick, J. J.: 1998, AJ **115**, 1693

Conselice, C. J., Bundy, K., Trujillo, I., Coil, A., Eisenhardt, P., Ellis, R. S., Georgakakis, A., Huang, J., Lotz, J., Nandra, K., Newman, J., Papovich, C., Weiner, B., and Willmer, C.: 2007, MNRAS **381**, 962

Cooper, M. C., Newman, J. A., Coil, A. L., Croton, D. J., Gerke, B. F., Yan, R., Davis, M., Faber, S. M., Guhathakurta, P., Koo, D. C., and Weiner, B. J.: 2006, *ArXiv Astrophysics e-prints*

Cooper, M. C., Newman, J. A., Madgwick, D. S., Gerke, B. F., Yan, R., and Davis, M.: 2005, ApJ **634**, 833

Cowie, L. L. and Barger, A. J.: 2008, *ArXiv e-prints* 806

Cowie, L. L., Barger, A. J., Fomalont, E. B., and Capak, P.: 2004, ApJ **603**, L69

Cowie, L. L., Songaila, A., Hu, E. M., and Cohen, J. G.: 1996, AJ **112**, 839

Croton, D. J., Springel, V., White, S. D. M., De Lucia, G., Frenk, C. S., Gao, L., Jenkins, A., Kauffmann, G., Navarro, J. F., and Yoshida, N.: 2006, MNRAS **365**, 11

Daddi, E., Dickinson, M., Morrison, G., Chary, R., Cimatti, A., Elbaz, D., Frayer, D., Renzini, A., Pope, A., Alexander, D. M., Bauer, F. E., Giavalisco, M., Huynh, M., Kurk, J., and Mignoli, M.: 2007, ApJ **670**, 156

Davis, M., DEEP Team, and Extended Groth Strip Collaboration: 2005, pp 1299–+

Davis, M., Faber, S. M., Newman, J., Phillips, A. C., Ellis, R. S., Steidel, C. C., Conselice, C., Coil, A. L., Finkbeiner, D. P., Koo, D. C., Guhathakurta, P., Weiner, B., Schiavon, R., Willmer, C., Kaiser, N., Luppino, G. A., Wirth, G., Connolly, A., Eisenhardt, P., Cooper, M., and Gerke, B.: 2003, in P. Guhathakurta (ed.), *Discoveries and Research Prospects from 6- to 10-Meter-Class Telescopes II. Edited by Guhathakurta, Puragra. Proceedings of the SPIE, Volume 4834, pp. 161-172 (2003).*, Vol. 4834 of *Presented at the Society of Photo-Optical Instrumentation Engineers (SPIE) Conference*, pp 161–172

Davis, M., Guhathakurta, P., Konidaris, N. P., Newman, J. A., Ashby, M. L. N., Biggs, A. D., Barmby, P., Bundy, K., Chapman, S. C., Coil, A. L., Conselice, C. J., Cooper, M. C., Croton, D. J., Eisenhardt, P. R. M., Ellis, R. S., Faber, S. M., Fang, T., Fazio, G. G., Georgakakis, A., Gerke, B. F., Goss, W. M., Gwyn, S., Harker, J., Hopkins, A. M., Huang, J.-S., Ivison, R. J., Kassin, S. A., Kirby, E. N., Koekemoer, A. M., Koo, D. C., Laird, E. S., Le Floc'h, E., Lin, L., Lotz, J. M., Marshall, P. J., Martin, D. C., Metevier, A. J., Moustakas, L. A., Nandra, K., Noeske, K. G., Papovich, C., Phillips, A. C., Rich, R. M., Rieke, G. H., Rigopoulou, D., Salim, S., Schiminovich, D., Simard, L., Smail, I., Small, T. A., Weiner, B. J., Willmer, C. N. A., Willner, S. P., Wilson, G., Wright, E. L., and Yan, R.: 2007, ApJ **660**, L1

de Vaucouleurs, G.: 1948, *Annales d'Astrophysique* **11**, 247

Dickinson, M., Giavalisco, M., and The Goods Team: 2003, in R. Bender and A. Renzini (eds.), *The Mass of Galaxies at Low and High Redshift*, pp 324–+

Dressler, A.: 1980, ApJ **236**, 351

Drory, N. and Alvarez, M.: 2008, ApJ **680**, 41

Dunlop, J. S. and Peacock, J. A.: 1990, MNRAS **247**, 19

Efstathiou, G., Ellis, R. S., and Peterson, B. A.: 1988, MNRAS **232**, 431

Einstein, A.: 1916, *Annalen der Physik* **354**, 769

Faber, S. M., Phillips, A. C., Kibrick, R. I., Alcott, B., Allen, S. L., Burrous, J., Cantrall, T., Clarke, D., Coil, A. L., Cowley, D. J., Davis, M., Deich, W. T. S., Dietsch, K., Gilmore, D. K., Harper, C. A., Hilyard, D. F., Lewis, J. P., McVeigh, M., Newman, J., Osborne, J., Schiavon, R., Stover, R. J., Tucker, D., Wallace, V., Wei, M., Wirth, G., and Wright, C. A.: 2003, in M. Iye and A. F. M. Moorwood (eds.), *Instrument Design and Performance for Optical/Infrared Ground-based Telescopes. Edited by Iye, Masanori; Moorwood, Alan F. M. Proceedings of the SPIE, Volume 4841, pp. 1657-1669 (2003).*, Vol. 4841 of *Presented at the Society of Photo-Optical Instrumentation Engineers (SPIE) Conference*, pp 1657–1669

Fanaroff, B. L. and Riley, J. M.: 1974, MNRAS **167**, 31P

Fioc, M. and Rocca-Volmerange, B.: 1999, *ArXiv Astrophysics e-prints*

Fontana, A., Pozzetti, L., Donnarumma, I., Renzini, A., Cimatti, A., Zamorani, G., Menci, N., Daddi, E., Giallongo, E., Mignoli, M., Perna, C., Salimbeni, S., Saracco, P., Broadhurst, T., Cristiani, S., D'Odorico, S., and Gilmozzi, R.: 2004, A&A **424**, 23

Förster Schreiber, N. M., Franx, M., Labbé, I., Rudnick, G., van Dokkum, P. G., Illingworth, G. D., Kuijken, K., Moorwood, A. F. M., Rix, H.-W., Röttgering, H., and van der Werf, P.: 2006, AJ **131**, 1891

Franx, M., Moorwood, A., Rix, H.-W., Kuijken, K., Röttgering, H., van der Werf, P., van Dokkum, P., Labbe, I., and Rudnick, G.: 2000, *The Messenger* **99**, 20

Gallagher, J. S., Hunter, D. A., and Bushouse, H.: 1989, AJ **97**, 700

Gallagher, III, J. S., Hunter, D. A., and Tutukov, A. V.: 1984, ApJ **284**, 544

Giavalisco, M., Ferguson, H. C., Koekemoer, A. M., Dickinson, M., Alexander, D. M., Bauer, F. E., Bergeron, J., Biagetti, C., Brandt, W. N., Casertano, S., Cesarsky, C., Chatzichristou, E., Conselice, C., Cristiani, S., Da Costa, L., Dahlen, T., de Mello, D., Eisenhardt, P., Erben, T., Fall, S. M., Fassnacht, C., Fosbury, R., Fruchter, A., Gardner, J. P., Grogin, N., Hook, R. N., Hornschemeier, A. E., Idzi, R., Jogee, S., Kretchmer, C., Laidler, V., Lee, K. S., Livio, M., Lucas, R., Madau, P., Mobasher, B., Moustakas, L. A., Nonino, M., Padovani, P., Papovich, C., Park, Y., Ravindranath, S., Renzini, A., Richardson, M., Riess, A., Rosati, P., Schirmer, M., Schreier, E., Somerville, R. S., Spinrad, H., Stern, D., Stiavelli, M., Strolger, L., Urry, C. M., Vandame, B., Williams, R., and Wolf, C.: 2004, ApJ **600**, L93

Glazebrook, K., Abraham, R. G., McCarthy, P. J., Savaglio, S., Chen, H.-W., Crampton, D., Murowinski, R., Jørgensen, I., Roth, K., Hook, I., Marzke, R. O., and Carlberg, R. G.: 2004, Nature **430**, 181

Glazebrook, K. and Bland-Hawthorn, J.: 2001, PASP **113**, 197

Glazebrook, K., Peacock, J. A., Miller, L., and Collins, C. A.: 1995, MNRAS **275**, 169

Gómez, P. L., Nichol, R. C., Miller, C. J., Balogh, M. L., Goto, T., Zabludoff, A. I., Romer, A. K., Bernardi, M., Sheth, R., Hopkins, A. M., Castander, F. J., Connolly, A. J., Schneider, D. P., Brinkmann, J., Lamb, D. Q., SubbaRao, M., and York, D. G.: 2003, ApJ **584**, 210

Gunn, J. E. and Gott, J. R. I.: 1972, ApJ **176**, 1

Guth, A. H.: 1981, Phys. Rev. D **23**, 347

Haarsma, D. B., Partridge, R. B., Windhorst, R. A., and Richards, E. A.: 2000, ApJ **544**, 641

Hardcastle, M. J., Evans, D. A., and Croston, J. H.: 2007, MNRAS **376**, 1849

Hashimoto, Y., Oemler, A. J., Lin, H., and Tucker, D. L.: 1998, ApJ **499**, 589

Hasinger, G.: 2005, in R. Bender and A. Renzini (eds.), *Multiwavelength Mapping of Galaxy Formation and Evolution*, pp 68–+

Hawking, S. W.: 1982, *Phys.Lett. B* **115**, 295

Heavens, A., Panter, B., Jimenez, R., and Dunlop, J.: 2004, Nature **428**, 625

Heckman, T. M.: 1980, A&A **87**, 152

Heckman, T. M., Smith, E. P., Baum, S. A., van Breugel, W. J. M., Miley, G. K., Illingworth, G. D., Bothun, G. D., and Balick, B.: 1986, ApJ **311**, 526

Helou, G., Soifer, B. T., and Rowan-Robinson, M.: 1985, ApJ **298**, L7

Hodge, J. A., Becker, R. H., White, R. L., and de Vries, W. H.: 2008, AJ **136**, 1097

Hogg, D. W.: 1999, *ArXiv Astrophysics e-prints*

Hogg, D. W., Blanton, M. R., Eisenstein, D. J., Gunn, J. E., Schlegel, D. J., Zehavi, I., Bahcall, N. A., Brinkmann, J., Csabai, I., Schneider, D. P., Weinberg, D. H., and York, D. G.: 2003, ApJ **585**, L5

Holt, S. S., Neff, S. G., and Urry, C. M.: 1991, *Testing the AGN Paradigm (AIP Conference Proceedings)*, AIP Press

Hopkins, A. M.: 2004, ApJ **615**, 209

Hopkins, A. M. and Beacom, J. F.: 2006, ApJ **651**, 142

Hopkins, P. F., Hernquist, L., Cox, T. J., Di Matteo, T., Martini, P., Robertson, B., and Springel, V.: 2005, ApJ **630**, 705

Hubble, E.: 1929, *Proceedings of the National Academy of Science* **15**, 168

Hubble, E. P.: 1926, ApJ **64**, 321

Ibar, E., Cirasuolo, M., Ivison, R., Best, P., Smail, I., Biggs, A., Simpson, C., Dunlop, J., Almaini, O., McLure, R., Foucaud, S., and Rawlings, S.: 2008, MNRAS **386**, 953

Ichimaru, S.: 1977, ApJ **214**, 840

Ivison, R. J., Chapman, S. C., Faber, S. M., Smail, I., Biggs, A. D., Conselice, C. J., Wilson, G., Salim, S., Huang, J.-S., and Willner, S. P.: 2007, ApJ **660**, L77

Jackson, C. A. and Wall, J. V.: 1999, MNRAS **304**, 160

Jansen, R. A., Franx, M., Fabricant, D., and Caldwell, N.: 2000, ApJS **126**, 271

Juneau, S., Glazebrook, K., Crampton, D., McCarthy, P. J., Savaglio, S., Abraham, R., Carlberg, R. G., Chen, H.-W., Le Borgne, D., Marzke, R. O., Roth, K., Jørgensen, I., Hook, I., and Murowinski, R.: 2005, ApJ **619**, L135

Kauffmann, G., Heckman, T. M., De Lucia, G., Brinchmann, J., Charlot, S., Tremonti, C., White, S. D. M., and Brinkmann, J.: 2006, MNRAS **367**, 1394

Kauffmann, G., Heckman, T. M., Tremonti, C., Brinchmann, J., Charlot, S., White, S. D. M., Ridgway, S. E., Brinkmann, J., Fukugita, M., Hall, P. B., Ivezić, Ž., Richards, G. T., and Schneider, D. P.: 2003a, MNRAS **346**, 1055

Kauffmann, G., Heckman, T. M., White, S. D. M., Charlot, S., Tremonti, C., Peng, E. W., Seibert, M., Brinkmann, J., Nichol, R. C., SubbaRao, M., and York, D.: 2003b, MNRAS **341**, 54

Kauffmann, G., White, S. D. M., Heckman, T. M., Ménard, B., Brinchmann, J., Charlot, S., Tremonti, C., and Brinkmann, J.: 2004, MNRAS **353**, 713

Kawata, D. and Mulchaey, J. S.: 2008, ApJ **672**, L103

Kennicutt, Jr., R. C.: 1983, ApJ **272**, 54

Kennicutt, Jr., R. C.: 1992, ApJ **388**, 310

Kennicutt, Jr., R. C.: 1998, ARA&A **36**, 189

Kewley, L. J., Geller, M. J., and Jansen, R. A.: 2004, AJ **127**, 2002

Kewley, L. J., Heisler, C. A., Dopita, M. A., and Lumsden, S.: 2001, ApJS **132**, 37

Knop, R. A., Aldering, G., Amanullah, R., Astier, P., Blanc, G., Burns, M. S., Conley, A., Deustua, S. E., Doi, M., Ellis, R., Fabbro, S., Folatelli, G., Fruchter, A. S., Garavini, G., Garmond, S., Garton, K., Gibbons, R., Goldhaber, G., Goobar, A., Groom, D. E., Hardin, D., Hook, I., Howell, D. A., Kim, A. G., Lee, B. C., Lidman, C., Mendez, J., Nobili, S., Nugent, P. E., Pain, R., Panagia, N., Pennypacker, C. R., Perlmutter, S., Quimby, R., Raux, J., Regnault, N., Ruiz-Lapuente, P., Sainton, G., Schaefer, B., Schahmaneche, K., Smith, E., Spadafora, A. L., Stanishev, V., Sullivan, M., Walton, N. A., Wang, L., Wood-Vasey, W. M., and Yasuda, N.: 2003, ApJ **598**, 102

Komatsu, E., Dunkley, J., Nolta, M. R., Bennett, C. L., Gold, B., Hinshaw, G., Jarosik, N., Larson, D., Limon, M., Page, L., Spergel, D. N., Halpern, M., Hill, R. S., Kogut, A., Meyer, S. S., Tucker, G. S., Weiland, J. L., Wollack, E., and Wright, E. L.: 2008, *ArXiv e-prints* 803

Körding, E. G., Jester, S., and Fender, R.: 2006, MNRAS **372**, 1366

Kormendy, J. and Bender, R.: 1996, ApJ **464**, L119+

Kormendy, J. and Gebhardt, K.: 2001, in J. C. Wheeler and H. Martel (eds.), *20th Texas Symposium on relativistic astrophysics*, Vol. 586 of *American Institute of Physics Conference Series*, pp 363–+

Kroupa, P.: 2001, MNRAS **322**, 231

Laird, E. S., Nandra, K., Georgakakis, A., Aird, J. A., Barmby, P., Conselice, C. J., Coil, A. L., Davis, M., Faber, S. M., Fazio, G. G., Guhathakurta, P., Koo, D. C., Sarajedini, V., and Willmer, C. N. A.: 2008, *ArXiv e-prints*

Larson, R. B. and Tinsley, B. M.: 1978, ApJ **219**, 46

Le Fevre, O., Vettolani, G., Maccagni, D., Mancini, D., Mazure, A., Mellier, Y., Picat, J. P., Arnaboldi, M., Bardelli, S., Bertin, E., Busarello, G., Cappi, A., Charlot, S., Chincarini, G., Colombi, S., Dantel-Fort, M., Foucaud, S., Garilli, B., Guzzo, L., Iovino, A., Marinoni, C., Mathez, G., McCracken, H., Pello, R., Radovich, M., Ripepi, V., Saracco, P., Scaramella, R., Scoreggio, M., Tresse, L., Zanichelli, A., Zamorani, G., and Zucca, E.: 2003, in P. Guhathakurta (ed.), *Discoveries and Research Prospects from 6- to 10-Meter-Class Telescopes II. Edited by Guhathakurta, Puragra. Proceedings of the SPIE, Volume 4834, pp. 173-182 (2003).*, Vol. 4834 of *Presented at the Society of Photo-Optical Instrumentation Engineers (SPIE) Conference*, pp 173–182

Ledlow, M. J. and Owen, F. N.: 1996, AJ **112**, 9

Liddle, A. R.: 1999, *An Introduction to Modern Cosmology*, John Wiley & Sons Limited, Baffins Lane, Chichester, West Sussex PO19 1UD, UK

Lilly, S. J. and Prestage, R. M.: 1987, MNRAS **225**, 531

Lin, C. C. and Shu, F. H.: 1966, *Proceedings of the National Academy of Science* **55**, 229

Longair, M. S.: 1966, MNRAS **133**, 421

Loveday, J.: 2004, MNRAS **347**, 601

Madau, P., Ferguson, H. C., Dickinson, M. E., Giavalisco, M., Steidel, C. C., and Fruchter, A.: 1996, MNRAS **283**, 1388

Madau, P., Pozzetti, L., and Dickinson, M.: 1998, ApJ **498**, 106

Magorrian, J., Tremaine, S., Richstone, D., Bender, R., Bower, G., Dressler, A., Faber, S. M., Gebhardt, K., Green, R., Grillmair, C., Kormendy, J., and Lauer, T.: 1998, AJ **115**, 2285

Mauch, T. and Sadler, E. M.: 2007, MNRAS **375**, 931

Maughan, B. J., Jones, L. R., Ebeling, H., and Scharf, C.: 2006, MNRAS **365**, 509

McNamara, B. R. and Nulsen, P. E. J.: 2007, ARA&A **45**, 117

Meier, D. L.: 2001, ApJ **548**, L9

Menci, N., Cavaliere, A., Fontana, A., Giallongo, E., Poli, F., and Vittorini, V.: 2004, ApJ **604**, 12

Miller, G. E. and Scalo, J. M.: 1979, ApJS **41**, 513

Mobasher, B., Dahlen, T., Hopkins, A., Scoville, N. Z., Capak, P., Rich, R. M., Sanders, D. B., Schinnerer, E., Ilbert, O., Salvato, M., and Sheth, K.: 2008, *ArXiv e-prints* 808

Mobasher, B., Idzi, R., Benítez, N., Cimatti, A., Cristiani, S., Daddi, E., Dahlen, T., Dickinson, M., Erben, T., Ferguson, H. C., Giavalisco, M., Grogin, N. A., Koekemoer, A. M., Mignoli, M., and Moustakas, L. A. e. a.: 2004, ApJ **600**, L167

Moore, B., Katz, N., Lake, G., Dressler, A., and Oemler, A.: 1996, Nature **379**, 613

Nandra, K., Georgakakis, A., Willmer, C. N. A., Cooper, M. C., Croton, D. J., Davis, M., Faber, S. M., Koo, D. C., Laird, E. S., and Newman, J. A.: 2007, ApJ **660**, L11

Nemmen, R. S., Bower, R. G., Babul, A., and Storchi-Bergmann, T.: 2007, MNRAS **377**, 1652

Noeske, K. G., Weiner, B. J., Faber, S. M., Papovich, C., Koo, D. C., Somerville, R. S., Bundy, K., Conselice, C. J., Newman, J. A., Schiminovich, D., Le Floc'h, E., Coil, A. L., Rieke, G. H., Lotz, J. M., Primack, J. R., Barmby, P., Cooper, M. C., Davis, M., Ellis, R. S., Fazio, G. G., Guhathakurta, P., Huang, J., Kassin, S. A., Martin, D. C., Phillips, A. C., Rich, R. M., Small, T. A., Willmer, C. N. A., and Wilson, G.: 2007, ApJ **660**, L43

Nusser, A., Gubser, S. S., and Peebles, P. J.: 2005, Phys. Rev. D **71(8)**, 083505

Osterbrock, D. E.: 1989, *Astrophysics of Gaseous Nebulae and Active Galactic Nuclei*, Universtiy Science Books, Mill Valley, CA, USA

Ostriker, J. P., Peebles, P. J. E., and Yahil, A.: 1974, *ApJL* **193**, L1

Pagel, B. E. J., Edmunds, M. G., Blackwell, D. E., Chun, M. S., and Smith, G.: 1979, MNRAS **189**, 95

Penzias, A. A. and Wilson, R. W.: 1965, ApJ **142**, 419

Poggianti, B. M., Smail, I., Dressler, A., Couch, W. J., Barger, A. J., Butcher, H., Ellis, R. S., and Oemler, A. J.: 1999, ApJ **518**, 576

Poggianti, B. M. and Wu, H.: 2000, ApJ **529**, 157

Prestage, R. M. and Peacock, J. A.: 1988, MNRAS **230**, 131

Quilis, V., Moore, B., and Bower, R.: 2000, *Science* **288**, 1617

Sadler, E. M., Cannon, R. D., Mauch, T., Hancock, P. J., Wake, D. A., Ross, N., Croom, S. M., Drinkwater, M. J., Edge, A. C., Eisenstein, D., Hopkins, A. M., Johnston, H. M., Nichol, R., Pimbblet, K. A., de Propris, R., Roseboom, I. G., Schneider, D. P., and Shanks, T.: 2007, MNRAS **381**, 211

Salim, S., Rich, R. M., Charlot, S., Brinchmann, J., Johnson, B. D., Schiminovich, D., Seibert, M., Mallery, R., Heckman, T. M., Forster, K., Friedman, P. G., Martin, D. C., Morrissey, P., Neff, S. G., Small, T., Wyder, T. K., Bianchi, L., Donas, J., Lee, Y.-W., Madore, B. F., Milliard, B., Szalay, A. S., Welsh, B. Y., and Yi, S. K.: 2007, ApJS **173**, 267

Salpeter, E. E.: 1955, ApJ **121**, 161

Savaglio, S., Glazebrook, K., and Le Borgne, D.: 2008, *ArXiv e-prints* 803

Savaglio, S., Glazebrook, K., Le Borgne, D., Juneau, S., Abraham, R. G., Chen, H.-W., Crampton, D., McCarthy, P. J., Carlberg, R. G., Marzke, R. O., Roth, K., Jørgensen, I., and Murowinski, R.: 2005, ApJ **635**, 260

Scalo, J.: 1998, in G. Gilmore and D. Howell (eds.), *The Stellar Initial Mass Function (38th Herstmonceux Conference)*, Vol. 142 of *Astronomical Society of the Pacific Conference Series*, pp 201–+

Scalo, J. M.: 1986, *Fundamentals of Cosmic Physics* **11**, 1

Schechter, P.: 1976, ApJ **203**, 297

Schlegel, D. J., Finkbeiner, D. P., and Davis, M.: 1998, ApJ **500**, 525

Schmidt, M.: 1968, ApJ **151**, 393

Sersic, J. L.: 1968, *Atlas de galaxias australes*, Cordoba, Argentina: Observatorio Astronomico, 1968

Seymour, N., Dwelly, T., Moss, D., McHardy, I., Zoghbi, A., Rieke, G., Page, M., Hopkins, A., and Loaring, N.: 2008, *ArXiv e-prints* 802

Shakura, N. I. and Syunyaev, R. A.: 1973, A&A **24**, 337

Shields, J. C.: 1992, ApJ **399**, L27

Somerville, R. S., Lee, K., Ferguson, H. C., Gardner, J. P., Moustakas, L. A., and Giavalisco, M.: 2004, ApJ **600**, L171

Spergel, D. N., Verde, L., Peiris, H. V., Komatsu, E., Nolta, M. R., Bennett, C. L., Halpern, M., Hinshaw, G., Jarosik, N., Kogut, A., Limon, M., Meyer, S. S., Page, L., Tucker, G. S., Weiland, J. L., Wollack, E., and Wright, E. L.: 2003, ApJS **148**, 175

Springel, V., White, S. D. M., Jenkins, A., Frenk, C. S., Yoshida, N., Gao, L., Navarro, J., Thacker, R., Croton, D., Helly, J., Peacock, J. A., Cole, S., Thomas, P., Couchman, H., Evrard, A., Colberg, J., and Pearce, F.: 2005, Nature **435**, 629

Sturm, E., Rupke, D., Contursi, A., Kim, D.-C., Lutz, D., Netzer, H., Veilleux, S., Genzel, R., Lehnert, M., Tacconi, L. J., Maoz, D., Mazzarella, J., Lord, S., Sanders, D., and Sternberg, A.: 2006, ApJ **653**, L13

van der Kruit, P. C.: 1971, A&A **15**, 110

van Dokkum, P. G., Franx, M., Fabricant, D., Illingworth, G. D., and Kelson, D. D.: 2000, ApJ **541**, 95

Vanzella, E., Cristiani, S., Dickinson, M., Giavalisco, M., Kuntschner, H., Haase, J., Nonino, M., Rosati, P., Cesarsky, C., Ferguson, H. C., Fosbury, R. A. E., Grazian, A., Moustakas, L. A., Rettura, A., Popesso, P., Renzini, A., Stern, D., and The Goods Team: 2008, A&A **478**, 83

Walsh, D., Carswell, R. F., and Weymann, R. J.: 1979, *Nature* **279**, 381

Whittet, D. C. B., Shenoy, S. S., Clayton, G. C., and Gordon, K. D.: 2004, ApJ **602**, 291

Willmer, C. N. A., Faber, S. M., Koo, D. C., Weiner, B. J., Newman, J. A., Coil, A. L., Connolly, A. J., Conroy, C., Cooper, M. C., Davis, M., Finkbeiner, D. P., Gerke, B. F., Guhathakurta, P., Harker, J., Kaiser, N., Kassin, S., Konidaris, N. P., Lin, L., Luppino, G., Madgwick, D. S., Noeske, K. G., Phillips, A. C., and Yan, R.: 2006, ApJ **647**, 853

Willott, C. J., Rawlings, S., Blundell, K. M., Lacy, M., and Eales, S. A.: 2001, MNRAS **322**, 536

Wu, Q. and Cao, X.: 2008, *ArXiv e-prints* 807

Wuyts, S., Labbe, I., Forster Schreiber, N. M., Franx, M., Rudnick, G., Brammer, G. B., and van Dokkum, P. G.: 2008, *ArXiv e-prints* 804

Yan, R., White, M., and Coil, A. L.: 2004, ApJ **607**, 739

Zaritsky, D., Kennicutt, Jr., R. C., and Huchra, J. P.: 1994, ApJ **420**, 87

Zwicky, F.: 1933, *Helvetica Physica Acta* **6**, 110